Supporting Information

Recognition of Higher Fullerene Isomers with Low-Symmetry Coordination Cages

Xiao-Qing Guo[1]†, Pengwei Yu[3]†, Li-Peng Zhou[1], Shao-Jun Hu[1], Xiao-Fang Duan[1,2], Li-Xuan Cai[1], Lipiao Bao[3], Xing Lu[3]*, Qing-Fu Sun[1,2]*

Affiliations:

[1]State Key Laboratory of Structural Chemistry, Fujian Institute of Research on the Structure of Matter, Chinese Academy of Sciences, Fuzhou 350002, PR China.

[2]University of Chinese Academy of Sciences, Beijing 100049, PR China.

[3]State Key Laboratory of Materials Processing and Die & Mould Technology, School of Materials Science and Engineering, Huazhong University of Science and Technology, 1037 Luoyu Road, Wuhan, 430074, PR China.

*Corresponding author. lux@hust.edu.cn; qfsun@fjirsm.ac.cn.

†These authors contributed equally to this work.

Table of Content

1. Materials and Methods

Materials. Unless otherwise stated, all chemicals and solvents were purchased from commercial companies and used as received. Deuterated solvents were purchased from Adamas, J&K scientific and Sigma-Aldrich. Fullerenes isomers (D_2-C_{76}, C_{2v}-C_{78}, and C_{2v}'-C_{78}) were synthesized by arc-discharge method and separated by multi-stage HPLC process with toluene as the eluent (See section 9 for detailed synthetic details).

NMR measurements. 1D and 2D-NMR spectra were measured on Bruker-Biospin Avance III HD (400 MHz) and JEOL ECZ600S (600 MHz) spectrometer. Variable-temperature ^{1}H-NMR spectra were measured on JEOL ECZ600S spectrometer. ^{1}H-NMR chemical shifts were determined with respect to residual signals of the deuterated solvents used.

MS measurements. ESI-TOF-MS were recorded on an Impact II UHR-TOF mass spectrometry from Bruker, with tuning mix as the internal standard. Data analysis was conducted with the Bruker Data Analysis software (Version 4.3) and simulations were performed with the Bruker Isotope Pattern software.

Cavity volume calculation. The cavity volumes of the complexes were calculated based on MoloVol calculations (https://molovol.com/)[S1] using single probe mode (Small probe radius: 2.4 Å; Grid resolution: 0.2 Å; Optimization depth: 4). For fullerene molecules, the program parameters were set as follows: small probe radius: 1.2 Å; Grid resolution: 0.2 Å; Optimization depth: 4. The corresponding graphics were generated with PyMOL software.[S2]

Enantiomeric separation. HPLC analyses were performed on the SHIMADZU LC-20A instrument with a chiral Enantiopak®SDMP column (4.6*250 mm, 5μm). Racemic C_3-**1** was separated on a Waters Prep 150 LC instrument with a chiral Enantiopak®SDMP column (10.0*250 mm, 5μm).

2. X-ray Crystallography

Single crystal X-ray diffraction data for ligand C_3-**1**, empty cages *T*-**3** and **4** were collected on a Bruker D8 VENTURE photon II diffractometer with Iμs 3.0 microfocus X-ray source using Mo Kα radiation (λ = 0.71073 Å). Data reduction was performed with the saint and SADABS package.[S3] The X-ray diffraction for *P*-**1** was carried out on a micro-focus metal jet diffractometer using Ga Kα radiation (λ = 1.3405 Å). Data reduction was performed with the CrysAlisPro package.[S4] Limited to the very weekly diffraction of the giant supramolecular assembly in nature, the X-ray diffraction studies for host–guest complexes $C_{60}\subset S_4$-**4** and $C_{70}\subset S_4$-**4** were carried out on BL17B macromolecular crystallography beamline in Shanghai Synchrotron Radiation Facility (SSRF). The collected diffraction data were processed with the HKL 3000 software. The structures were solved by direct methods and refined by full-matrix least-squares

on F^2 with anisotropic displacement using the SHELXTL software package.[S5] Carbon-bound hydrogen atoms have been positioned in accordance with idealized parameters and subjected to refinement utilizing a riding model. Disorder was modelled using standard crystallographic methods encompassing constraints, restraints and rigid-body modeling where necessary. Details on crystal data collection and refinement were summarized in Table S15–S22. CCDC: 2307962-2307967 contains the supplementary crystallographic data for this paper. These data can be obtained free of charge via www.ccdc.cam.ac.uk/conts/retrieving.html (or from the Cambridge Crystallographic Data Centre, 12 Union Road, Cambridge CB21EZ, UK; fax: (+44) 1223-336-033; or deposit@ccdc.cam.ac.uk).

2.1 Crystal data for C_3-**1**:

Triclinic space group *P*-1, a = 9.276(4) Å, b = 17.092(7) Å, c = 20.259(8) Å, α = 102.897(12)°, β = 90.871(12)°, γ = 105.056(12)°, V = 3014(2) $Å^3$, Z = 2, T = 140(2) K. Anisotropic least-squares refinement for the framework atoms and isotropic refinement for the other atoms on 10613 independent merged reflections (R_{int} = 0.1521) converged at residual wR_2 = 0.3390 for all data; residual R_1 = 0.0942 for 5830 observed data [$I > 2\sigma(I)$], and goodness of fit (GOF) = 1.104.

Specific refinement details:

Suitable crystals of the racemic ligand C_3-**1** for X-ray diffraction were obtained by slowly volatilizing a mixed solution of ligands in n-hexane/isopropanol (v/v = 1/1) at room temperature. Upon retrieval from the mother liquid, the crystal is expeditiously enveloped in crystal oil, followed by the swift acquisition of data within an environment purged with liquid nitrogen. The utmost attainable resolution of the diffraction data is 1.0 Å when the signal-to-noise ratio exceeds 1.8. The asymmetric unit was found to comprise one complete C_3-**1** and two bonded water molecules.

Due to significant thermal motion within the structure, thermal parameter restraints (SIMU, DELU) were applied to all atoms. Adding H-atoms onto isolated oxygen atoms led to A-level alerts (indicating proximity to surrounding atoms). As a result, we chose not to add H-atoms during the refinement process.

CheckCIF gives two B-level alerts, all of which result from missing H-atoms on isolated oxygen atoms.

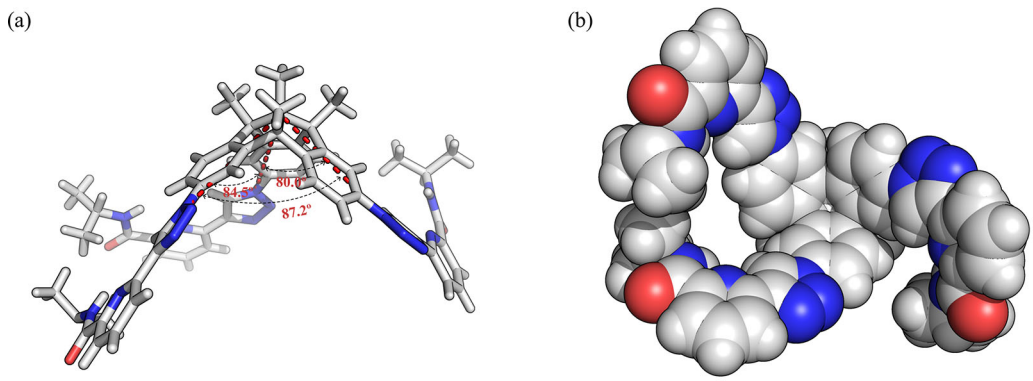

Fig. S1. (a) Cone-shaped 3D stereostructure of C_3-**1**. (b) Space-filling representation of C_3-**1**. Solvents are omitted for clarity.

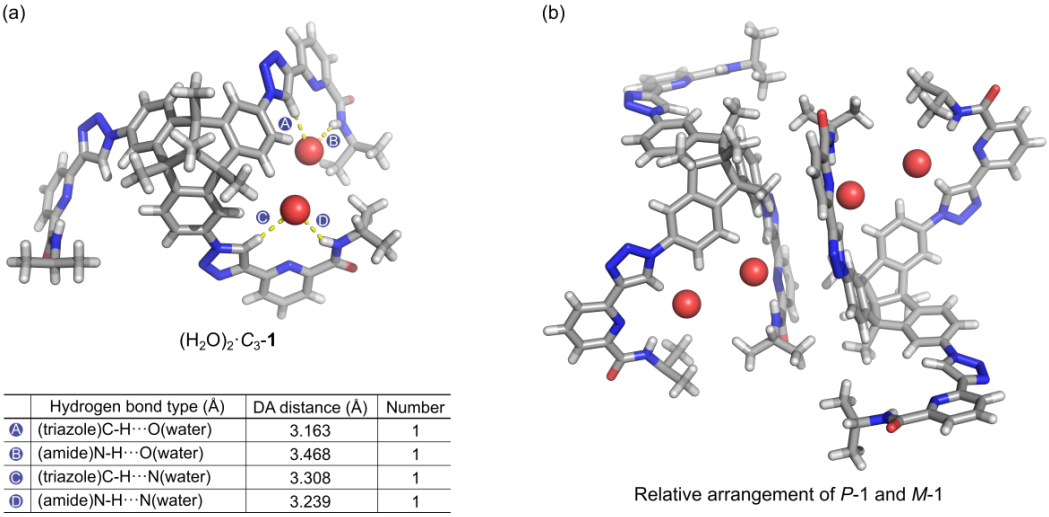

	Hydrogen bond type (Å)	DA distance (Å)	Number
Ⓐ	(triazole)C-H···O(water)	3.163	1
Ⓑ	(amide)N-H···O(water)	3.468	1
Ⓒ	(triazole)C-H···N(water)	3.308	1
Ⓓ	(amide)N-H···N(water)	3.239	1

Fig. S2. (a) C_3-**1** binds two water molecules via multiple H-bond interactions. (b) Coexistence of *P* and *M* configuration ligand C_3-**1** in the unit cell.

2.2 Crystal data for homochiral *P*-**1**:

Trigonal space group *R*3, a = 23.5481(9) Å, b = 23.5481(9) Å, c = 12.9841(5) Å, α = β = 90°, γ = 120°, V = 6235.3(5) $Å^3$, Z = 3, T = 293(2) K. Anisotropic least-squares refinement for the framework atoms and isotropic refinement for the other atoms on 4155 independent merged reflections (R_{int} = 0.1529) converged at residual wR_2 = 0.3883 for all data; residual R_1 = 0.1572 for 2980 observed data [$I > 2\sigma(I)$], and goodness of fit (GOF) = 1.468.

Specific refinement details:

Crystals of the homochiral C_3-symmetric *P*-**1** for X-ray diffraction were obtained by slow volatilization of the chloroform solution of ligand at room temperature. To establish the absolute configuration of the crystal, distinct diffraction experiments employing Cu or Ga Kα radiation were conducted. Regrettably, the data derived from the Cu Kα radiation exhibited limited diffraction resolution (> 1.2 Å), coupled with a

large Flack parameter (0.288). In contrast, the employment of Ga Kα radiation yielded a resolution of 1.0 Å and more lower Flack value (0.047), elucidating the absolute *P* configuration. The asymmetric unit was found to comprise one third of *P*-**1**, one third of a chloroform molecule, and two free chloroform molecules.

Due to the thermal motion of the free chloroform molecules, thermal parameter restraints (ISOR) were applied to confine the refinement of chlorine atoms to an approximately isotropic manner. Bond length and angle restraints were also applied to the three free chloroform molecules.

CheckCIF gives seven B-level alerts, all of which result from the disorder of the free chloroform molecules (high R1 and wR2 value, large average Ueq of residue around chloroform atoms) and the limited resolution (sine(theta_max)/wavelength < 0.575, low bond precision).

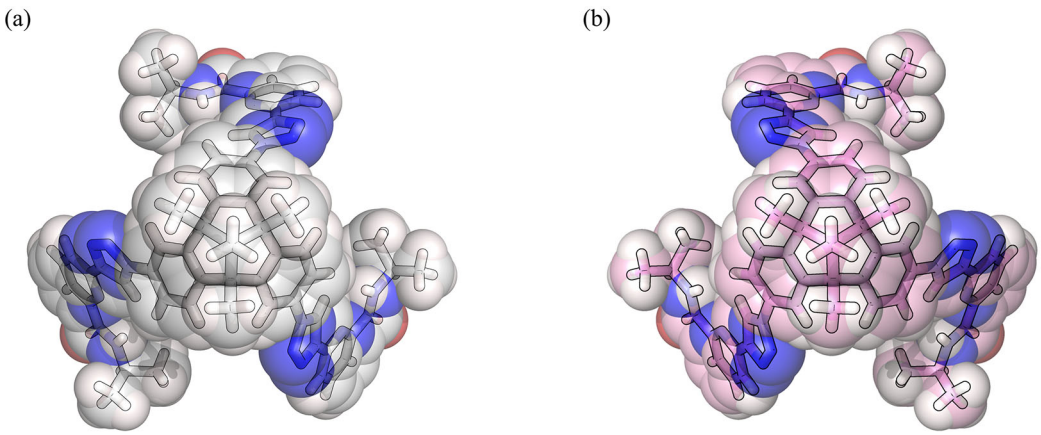

P-**1** *M*-**1**

Fig. S3. (a) Space-filling and stick representations of *P*-configuration crystal structure of ligand C_3-**1**. Solvents are omitted for clarity. (b) Space-filling and stick representations of *M*-configuration molecular modeling of ligand C_3-**1**.

2.3 Crystal data for *T*-**3**:

Orhombic space group *Pccn*, a = 22.156(2) Å, b = 23.722(3) Å, c = 80.692(9) Å, α = β = γ = 90°, V = 42411(8) $Å^3$, Z = 4, T = 273(2) K. Anisotropic least-squares refinement for the framework atoms and isotropic refinement for the other atoms on 21539 independent merged reflections (R_{int} = 0.2216) converged at residual wR_2 = 0.3254 for all data; residual R_1 = 0.1056 for 10971 observed data [$I > 2\sigma(I)$], and goodness of fit (GOF) = 0.970.

Specific refinement details:

The crystals for empty cages *T*-**3** were obtained by slow diffusion of dichloromethane vapor into the corresponding complexes solution (CH_3CN/MeOH, v/v 4/1) at room temperature over one month. Upon isolating the crystal from the mother liquid, it will be rapidly weathered. Consequently, we sealed the crystal in a capillary tube filled with

the mother liquid before testing. The completeness of the diffraction data can reach 97%. The asymmetric unit was found to comprise two complete C_3-**1** molecules and associated counterions.

Owing to substantial thermal motion within the structure, we imposed constraints (SAME) on the bond lengths and angles of chemically identical organic ligand pairs to ensure their mutual similarity. Additionally, thermal parameter restrictions (SIMU, DELU) were extended to all atoms, excluding lanthanum. Bond length and angle limitations (DFIX) were also administered to the peripheral isopropylamine groups and middle TBTQ skeletons. Furthermore, the pyridine and triazole components were modeled as rigid groups to enhance structural accuracy, employing the specific constraints (AFIX 66, AFIX 56).

Because of the large number of amorphous solvents and highly-disordered counterions existing in the unit cell, which occupy as much as 52.6% of the unit cell for *T*-**3** according to PLATON/SOLV calculation, the final R factor was slightly high. The residual electron intensities arising from these amorphous solvents and highly-disordered counterions were removed using the PLATON/SQUEEZE routine.[S6, S7]

CheckCIF gives two A-level alerts, one stems from the inherent weak diffraction ability of the crystal, and the remaining one arises from the high beamstop theta(min) limit set. Additionally, CheckCIF reports five B-level alerts, all of which result from the limited resolution of the data (high Rint value), thermal motion (or minor unresolved disorder) of counterions (large average Ueq of residue around sulfur atoms on counterions).

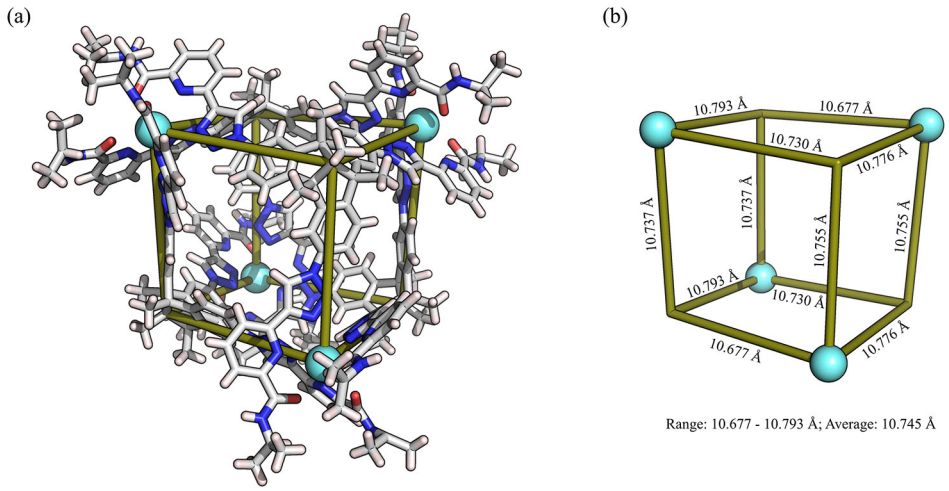

Fig. S4. (a) Cationic part of the crystal structure of *T*-**3**. (b) Simplified pseudo-cube from *T*-**3**. Counterions are omitted for clarity. (Δ handedness La centers, pale cyan sphere)

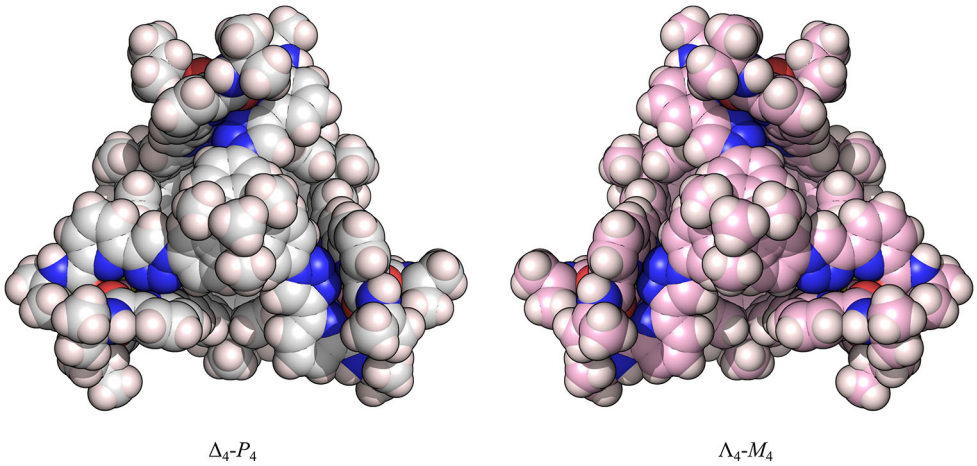

Fig. S5. Space-filling representations of the enantiopure Δ_4-P_4 and Λ_4-M_4 within the crystal structure of *T*-**3**. Counterions are omitted for clarity.

2.4 Crystal data for **4**:

Monoclinic space group *C2/m*, a = 62.910(10) Å, b = 36.326(6) Å, c = 36.322(5) Å, α = 90°, β = 125.26°, γ = 90°, V = 67780(18) $Å^3$, Z = 4, T = 278 K. Anisotropic least-squares refinement for the framework atoms and isotropic refinement for the other atoms on 13201 independent merged reflections (R_{int} = 0.327) converged at residual wR_2 = 0.4721 for all data; residual R_1 = 0.1581 for 6363 observed data [$I > 2\sigma(I)$], and goodness of fit (GOF) = 1.569.

Specific refinement details:

The crystals for empty cages **4** were obtained through the slow diffusion of dichloromethane vapor into the corresponding complexes solution (CH_3CN/MeOH, v/v 4/1) at room temperature over one month. Upon isolating the crystals from the mother liquid, they will be rapidly weathered. To counteract this, we sealed the crystal in a capillary tube filled with the mother liquid before testing. During the data collection process, the crystals exhibited very weak diffraction ability. The highest resolution of the crystal can only reach about 1.5 Å (Fig. S6), whether utilizing the Bruker D8 VENTURE photon II diffractometer with Iμs 3.0 microfocus X-ray source or the Shanghai Synchrotron Radiation Facility (SSRF). Fortunately, even at this low resolution, the built-in SHELXTL automatic parsing program in APEX III[S56] can generate a rough structure. On this basis, we further refined the data to derive the resulting structure. The asymmetric unit was found to comprise one complete and two incomplete (one-third) C_1-**2** molecules.

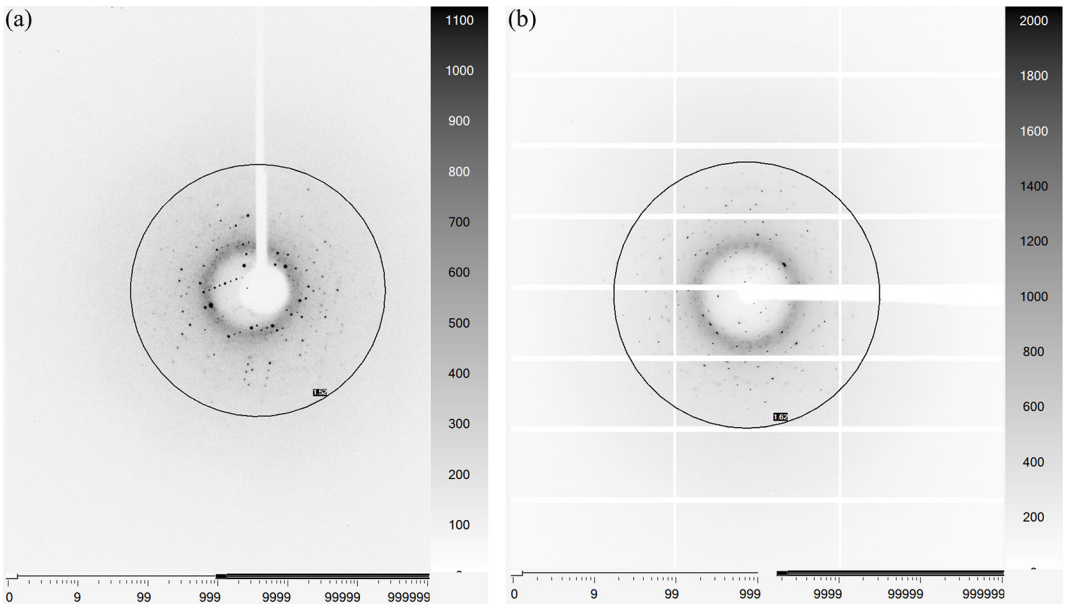

Fig. S6. Representative diffraction frames of crystals for **4** on Bruker D8 VENTURE photon II diffractometer (a) and SSRF (b).

The crystallographic analysis of **4** reveals a notable degree of disorder. Among the three triazole-pyridine-amide (TPA) chelating groups on ligand C_1-**2**, two can adopt two positions. Consequently, the pseudo-cube accommodates two metal centers with unambiguous stereoconfigurations (Δ and Λ), while the remaining two can be modeled as disordered with both Δ and Λ stereoconfigurations. As a result, three possible stereoisomers (ΔΔΔΛ, ΔΛΛΛ, and ΔΔΛΛ) coexist in the crystal structure. The inherent weak diffraction ability of crystal for **4** might be attributed to the presence of these isomers, a phenomenon similar to a recent report from the Nitschke group.[S8]

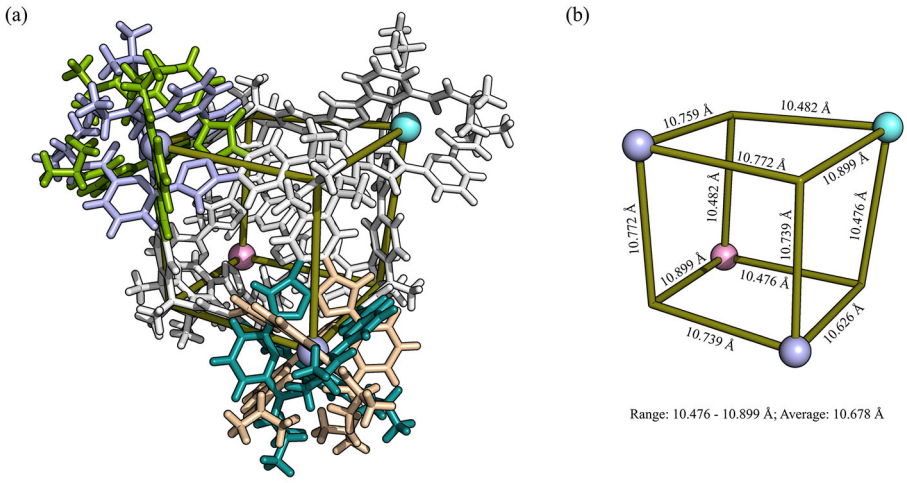

Fig. S7. (a) Cationic part of the crystal structure of **4** showing the arrangement of the disordered TPA chelating groups on two possible positions. (b) Simplified pseudo-cube from **4**. (Δ handedness La centers, pale cyan sphere; Λ handedness La centers, pink sphere; Δ/Λ handedness La centers, lightblue sphere)

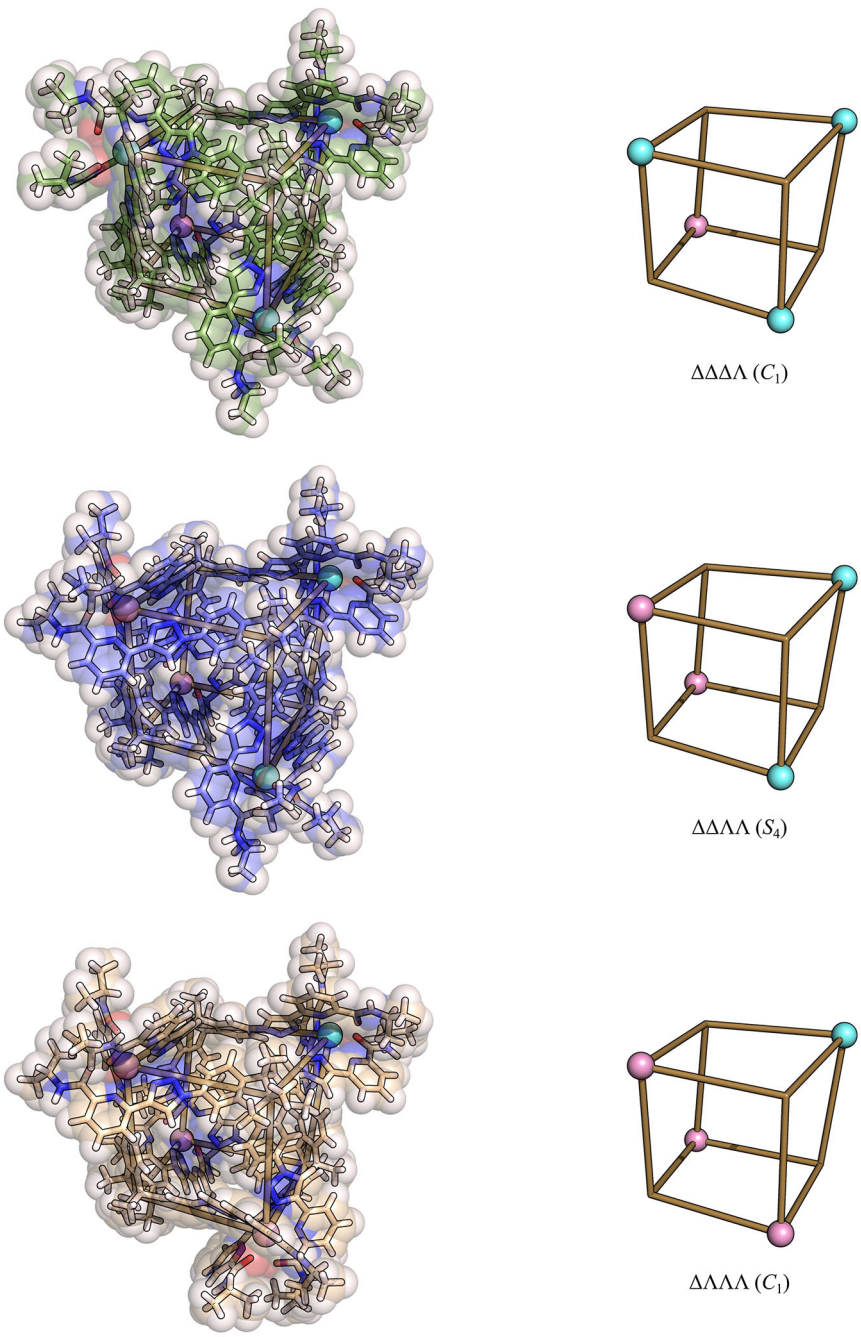

Fig. S8. Possible diastereomers present in the crystal structure of **4**. (Δ handedness La centers, pale cyan sphere; Λ handedness La centers, pink sphere)

Owing to the limited resolution and the substantial thermal motion within the structure, we imposed constraints (SAME) on the bond lengths and angles of chemically identical TPA chelating groups to ensure their mutual similarity. Additionally, thermal parameter restrictions (SIMU, DELU, ISOR) were extended to all atoms, excluding lanthanum. Bond length and angle limitations (DFIX, DANG, SADI) were also administered to the peripheral isopropylamine groups and middle TBTQ skeletons. Furthermore, benzene and triazole components were modeled as rigid groups to enhance structural accuracy, employing the specific constraints (FLAT, AFIX

66, AFIX 56). Due to substantial disorder, segments of the TPA chelating groups exhibit proximity or spatial intersection. Therefore, given the connectivity, certain hydrogen atoms on the pyridine or peripheral isopropylamine groups cannot be added via the HFIX instruction.

Too low resolution is insufficient to support the determination of counterions or solvents. Because of the large number of amorphous solvents and highly-disordered counterions existing in the unit cell, which occupy as much as 75.1% of the unit cell (67780(18) $Å^3$) for **4** based on PLATON/SOLV calculation, the final R factor was high. The residual electron intensities arising from these amorphous solvents and highly-disordered counterions were removed by the PLATON/SQUEEZE routine.[S6, S7]

CheckCIF gives four A-level alerts, all of which result from the crystal's inherent weak diffraction ability, the substantial thermal motion or disorder of counterions, and the presence of various isomers.

2.5 Crystal data for $C_{60}\subset S_4$-**4**:

Monoclinic space group *C2/c*, a = 39.925(8) Å, b = 41.557(8) Å, c = 41.117(8) Å, α = 90°, β = 95.23(3)°, γ = 90°, V = 67935(24) $Å^3$, Z = 8, T = 293(2) K. Anisotropic least-squares refinement for the framework atoms and isotropic refinement for the other atoms on 47013 independent merged reflections (R_{int} = 0.0624) converged at residual wR_2 = 0.3921 for all data; residual R_1 = 0.1210 for 28575 observed data [$I > 2\sigma(I)$], and goodness of fit (GOF) = 1.353.

Specific refinement details:

After standing for more than two weeks, purple flaky crystals for $C_{60}\subset S_4$-**4** appeared near the liquid level on the inner wall of the NMR tube. Upon retrieval from the mother liquid, the crystal is expeditiously coated with crystal oil, followed by quickly acquiring data within a nitrogen-purged environment. The utmost attainable resolution of the diffraction data is 1.0 Å when the signal-to-noise ratio exceeds 2.1. The asymmetric unit was found to comprise one complete S_4-**4** cage, one C_{60} molecule, and eight associated counterions.

The C_{60} guest exhibits very high levels of disorder. In order to establish a reasonable model for C_{60}, we employed the disordered structure refinement (DSR) program,[S9] utilizing a full set of bond distance and angle restraints (SADI, FLAT, RIGU, SIMU, SAME, FLAT) to achieve semi-automatic modeling. The C_{60} molecular fragment in the database of DSR was used to fit the desired position in the unit cell.

Due to the significant thermal motion of counteranions, we introduced constraints (SAME) on the bond lengths and angles of chemically identical counteranions to ensure their mutual similarity. Thermal parameter limitations (SIMU, DELU) were also applied to all atoms except for lanthanum. Furthermore, we employed bond length and angle restraints (DFIX, SADI) to the peripheral isopropylamine groups and middle TBTQ skeletons for reasonable structure. The pyridine and triazole components were

treated as rigid groups to enhance structural accuracy, utilizing specific constraints (AFIX 66, AFIX 56).

Because of the large number of amorphous solvents and highly-disordered counterions existing in the unit cell, which occupy as much as 36.0% of the unit cell for $C_{60}\subset S_4$-**4** based on PLATON/SOLV calculation, the final R factor was slightly high. The residual electron intensities arising from these amorphous solvents and highly-disordered counterions were removed by the PLATON/SQUEEZE routine.[S6, S7]

CheckCIF gives four B-level alerts, all of which result from the thermal motion through the structure, disordered guest/counterions/solvents molecules, and the limited resolution.

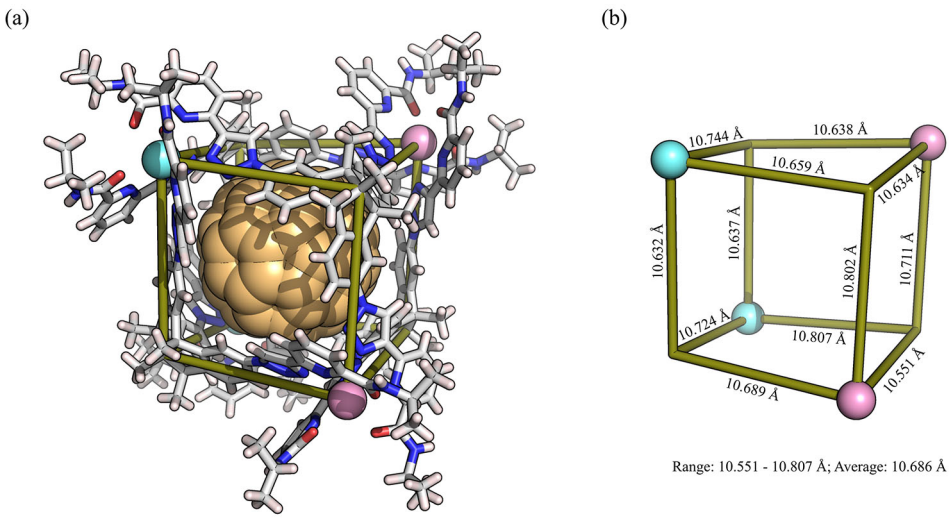

Fig. S9. (a) Cationic part of the crystal structure of $C_{60}\subset S_4$-**4** showing the guest bound within the cage cavity (one C_{60} molecule) in space-filling representation. (b) Simplified pseudo-cube from $C_{60}\subset S_4$-**4**. Counterions are omitted for clarity. (Δ handedness La centers, pale cyan sphere; Λ handedness La centers, pink sphere)

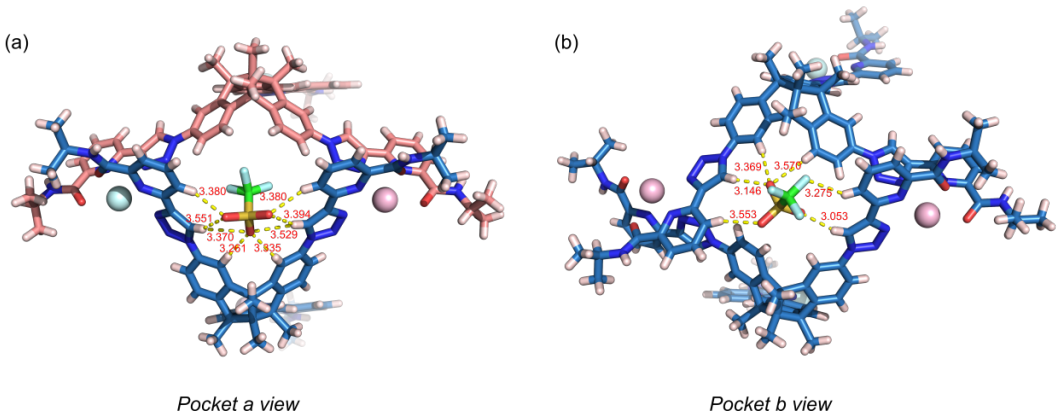

Fig. S10. Two types of pockets in $C_{60}\subset S_4$-**4** bind OTf⁻ anions through multiple H-bond interactions. Pocket *a* consists of one *P*-**2** and one *M*-**2** (a), while pocket *b* consists of two *P*-**2** (b).

2.6 Crystal data for $C_{70}\subset S_4$-**4**:

Monoclinic space group *C2/c*, a = 40.408(8) Å, b = 42.122(8) Å, c = 41.136(8) Å, α = 90°, β = 96.44(3)°, γ = 90°, V = 69574(24) Å^3, Z = 8, T = 293(2) K. Anisotropic least-squares refinement for the framework atoms and isotropic refinement for the other atoms on 47685 independent merged reflections (R_{int} = 0.041) converged at residual wR_2 = 0.3877 for all data; residual R_1 = 0.1437 for 33359 observed data [$I > 2\sigma(I)$], and goodness of fit (GOF) = 1.575.

Specific refinement details:

After standing for more than two weeks, brown flaky crystals for $C_{70}\subset S_4$-**4** appeared near the liquid level on the inner wall of the NMR tube. After separating from the mother liquid, the crystal is promptly coated with crystal oil. Subsequently, data acquisition was carried out rapidly in an environment purged with liquid nitrogen. The highest achievable resolution for the diffraction data stands at 1.0 Å, provided the signal-to-noise ratio surpasses 2.1. The asymmetric unit has been identified to consist of a complete S_4-**4** cage, one C_{70} guest molecule, and eleven corresponding counterions.

Similar to the C_{60} guest in $C_{60}\subset S_4$-**4**, the C_{70} guest exhibits a very high level of disorder in $C_{70}\subset S_4$-**4**. Therefore, the disordered structure refinement (DSR) program[S9] was utilized to establish a semi-automatic modeling equipped with a comprehensive range of bond distance and angle restraints (SADI, FLAT, RIGU, SIMU, SAME, and FLAT). We utilized the C_{70} molecular fragment from the DSR database to fit the desired position in the unit cell.

Due to the significant thermal motion exhibited by the counteranions, we introduced constraints (SAME) on the bond lengths and angles for chemically identical counteranions to ensure their congruence. Thermal parameter limitations (SIMU, DELU) were also applied to all atoms, except for lanthanum. Moreover, we implemented restrictions (DFIX, SADI) on bond lengths and angles for the peripheral isopropylamine groups and middle TBTQ skeletons. To heighten the precision of our structure, the pyridine and triazole components were treated as rigid groups, employing specific constraints (AFIX 66, AFIX 56).

Owning to the presence of numerous solvents and disordered counterions within the unit cell, constituting a considerable 37.8% portion for $C_{70}\subset S_4$-**4** according to PLATON/SOLV calculation, a slightly elevated final R factor was observed. The residual electron intensities originating from these amorphous solvents and disordered counterions were successfully eliminated by utilizing of the PLATON/SQUEEZE routine.[S6,S7]

CheckCIF gives one A-level alert and four B-level alerts, all of which result from the thermal motion through the structure, disordered guest/counterions/solvents molecules, and the limited resolution.

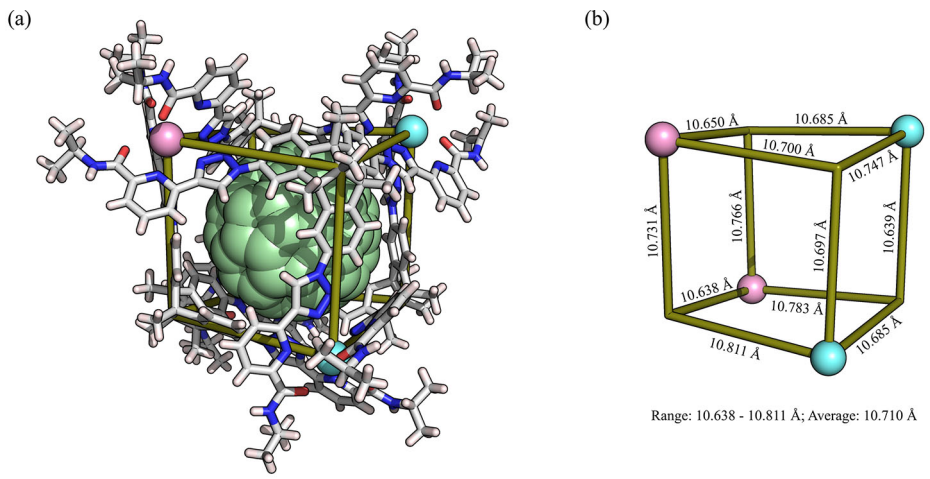

Fig. S11. (a) Cationic part of the crystal structure of $C_{70}\subset S_4$-**4** showing the guest bound within the cage cavity (one C_{70} molecule) in space-filling representation. (b) Simplified pseudo-cube from $C_{70}\subset S_4$-**4**. Solvents and counterions are omitted for clarity. (Δ handedness La centers, pale cyan sphere; Λ handedness La centers, pink sphere)

3. Synthesis and Characterization

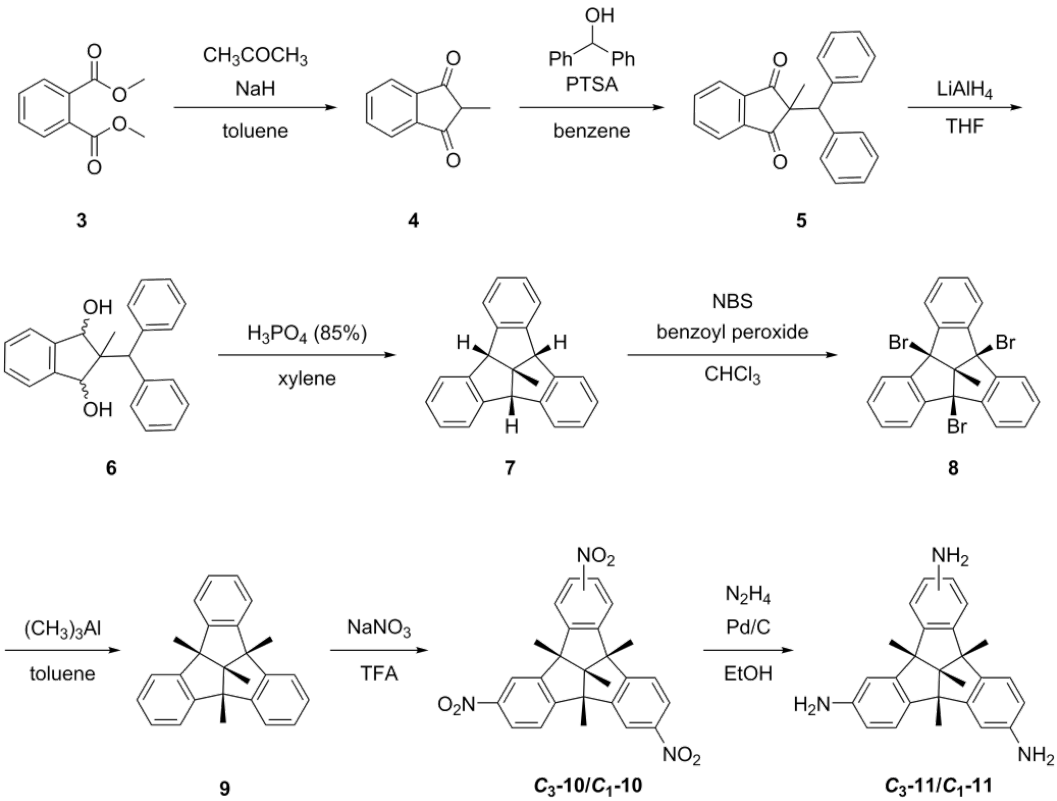

Scheme S1. Synthetic route of precursors C_3-**11**/C_1-**11**.

3.1 Synthesis of ligands

3.1.1 Synthesis of ligand C_3-**1**

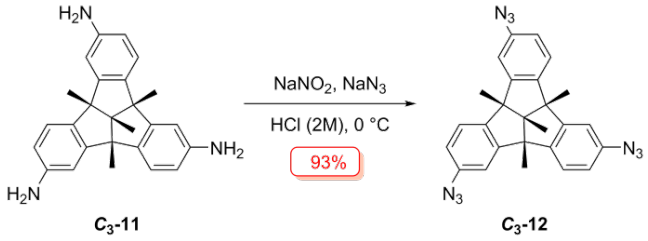

The precursor C_3-**11** was synthesized based on reported methods.[S10-S12] Aqueous sodium nitrite (174 mg, 2.52 mmol, for a 3/1 ratio of nitrite to amino group) was added to a cooled solution of C_3-**11** (105 mg, 0.28 mmol, 1.0 equiv) in dilute hydrochloric acid (2 M, 15 mL) to create the diazonium salt in an ice bath. After stirring for 0.5 h, an aqueous solution of sodium azide (182 mg, 2.80 mmol, 10.0 equiv) was added dropwise to the diazonium salt. The mixture was stirred for another 2 h. The precipitate was recovered by filtration and further purified by column chromatography on silica gel with petroleum ether. Off-white powder C_3-**12** was obtained after drying *in vacuo* (120 mg, 93%).

^{1}H NMR (400 MHz, $CDCl_3$, 298 K) δ = 7.30 (d, J = 8.2 Hz, 3H), 6.92 (d, J = 2.1 Hz, 3H), 6.88 (dd, J = 8.2, 2.1 Hz, 3H), 1.61 (s, 9H), 1.34 (s, 3H). ^{13}C NMR (101 MHz, $CDCl_3$, 298 K) δ = 150.47, 144.57, 137.40, 125.53, 119.70, 113.66, 69.68, 62.94, 25.00, 15.52. ESI-TOF-MS for $C_{26}H_{21}N_9$ $[M + Na]^+$: calcd, m/z = 482.1812; found: 482.1803.

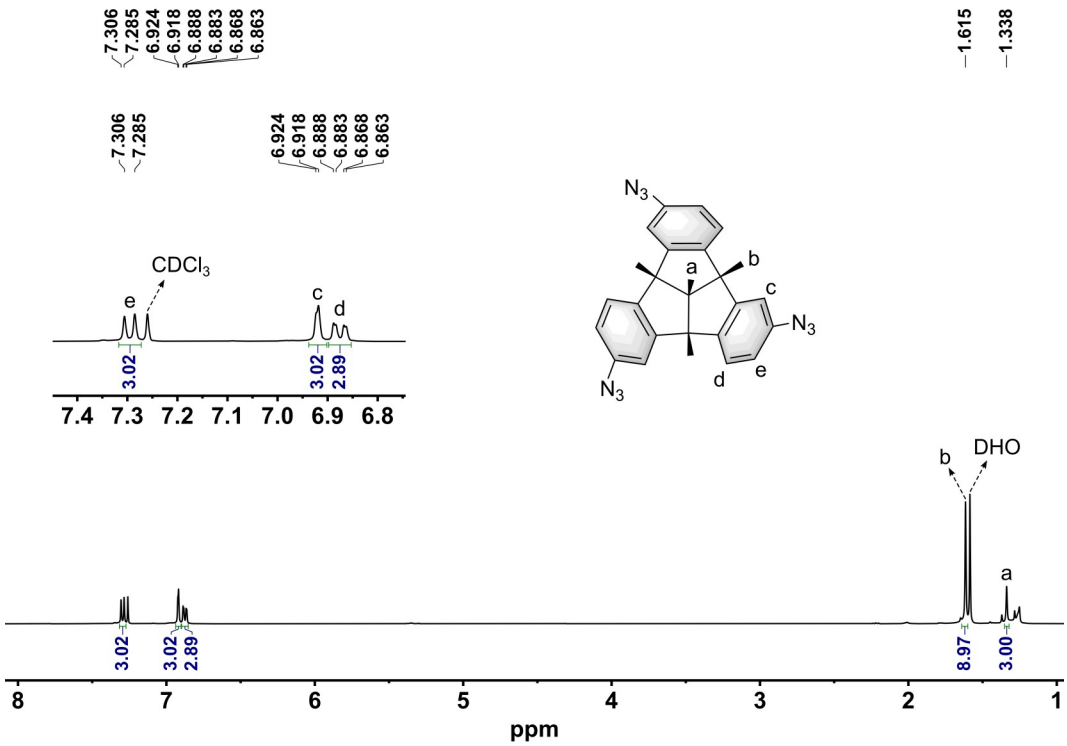

Fig. S12. ^{1}H NMR spectrum of C_3-**12** (400 MHz, 298 K, $CDCl_3$).

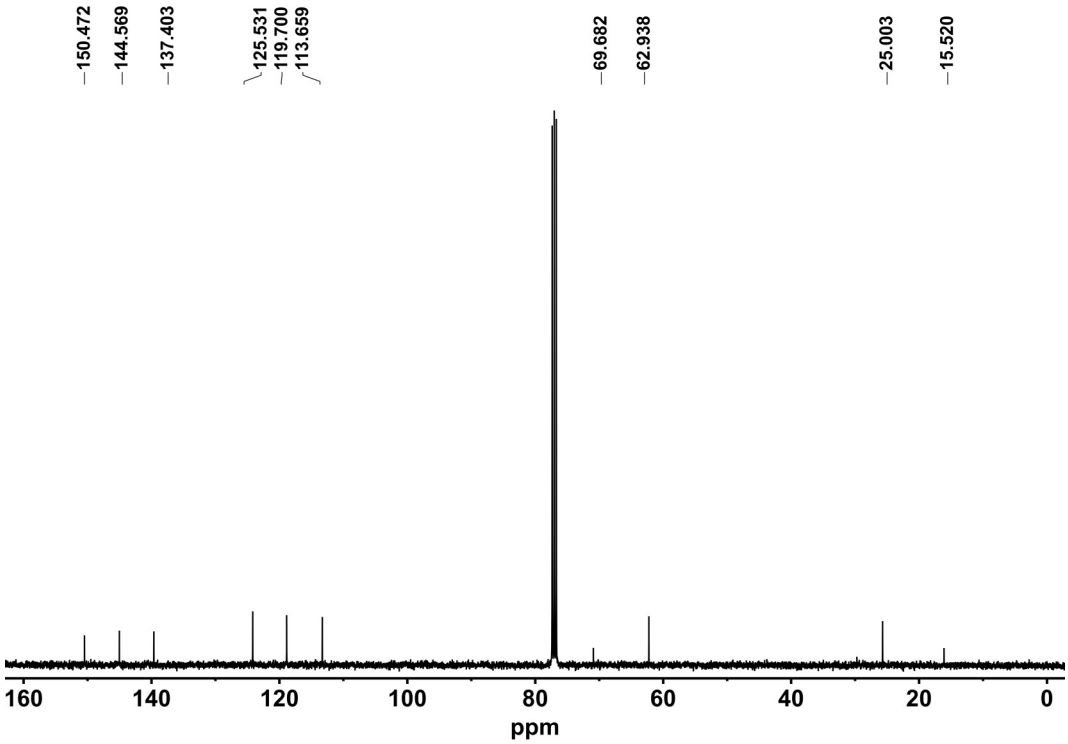

Fig. S13. ^{13}C NMR spectrum of C_3-**12** (101 MHz, 298 K, $CDCl_3$).

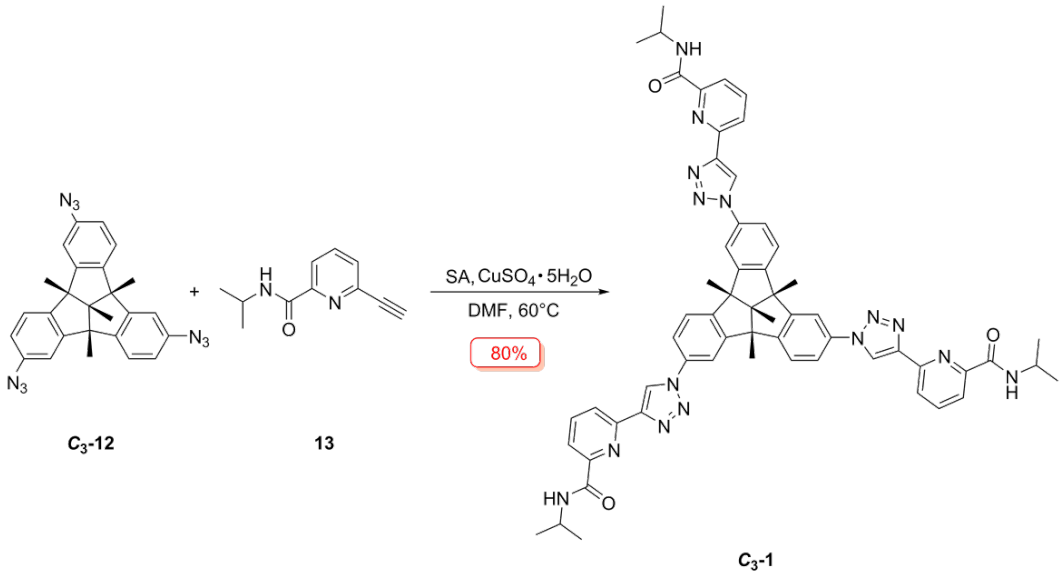

The precursor **13** was synthesized based on reported methods.[S13] C_3-**12** (120 mg, 0.26 mmol, 1.0 equiv), **13** (162 mg, 0.86 mmol, 3.3 equiv), sodium ascorbate (SA, 109 mg, 0.55 mmol, 2.1 equiv) and $CuSO_4{\cdot}5H_2O$ (58 mg, 0.23 mmol, 0.9 equiv) were added into a solution of DMF (40 mL). The reaction mixture was stirred at 60 °C for 48 h. After that, the reaction solution was cooled to room temperature, and the solvent was removed under reduced pressure. Then, 50 mL of EDTA saturated aqueous solution was added and stirred for 1 h. The solution was extracted with mixed organic solvents (50 mL × 3, DCM/MeOH v/v = 10/1), and the organic phase was washed with distilled

water (30 mL × 2) and dried with anhydrous Na_2SO_4. The solvents were removed under reduced pressure to afford a crude product which was further purified chromatographically (SiO_2, DCM/MeOH, v/v = 100/1). White powder C_3-**1** was obtained after drying *in vacuo* (213 mg, 80%). The racemic C_3-**1** can be further separated into *P*-**1** and *C*-**1** by chiral HPLC (See section 8 for details of the enantioseparation).

^{1}H NMR (400 MHz, $CDCl_3$, 298 K) δ = 8.47 (s, 3H), 8.36 (d, *J* = 7.9 Hz, 3H), 8.20 (d, *J* = 7.7 Hz, 3H), 8.02 – 7.94 (m, 6H), 7.77 (d, *J* = 8.2 Hz, 3H), 7.66 (d, *J* = 8.3 Hz, 3H), 7.56 (d, *J* = 8.3 Hz, 3H), 4.36 – 4.26 (m, 3H), 1.85 (s, 9H), 1.53 (s, 3H), 1.30 (t, *J* = 6.7 Hz, 18H). ^{13}C NMR (101 MHz, $CDCl_3$, 298 K) δ = 163.17, 150.37, 150.17, 149.15, 148.50, 148.36, 138.54, 137.15, 124.51, 121.95, 120.69, 120.35, 116.25, 100.00, 71.17, 62.90, 59.60, 41.57, 38.22, 31.31, 29.79, 25.87, 22.92. ESI-TOF-MS for $C_{59}H_{57}N_{15}O_3$ $[M + Na]^+$: calcd, m/z = 1046.4661; found, 1046.4655.

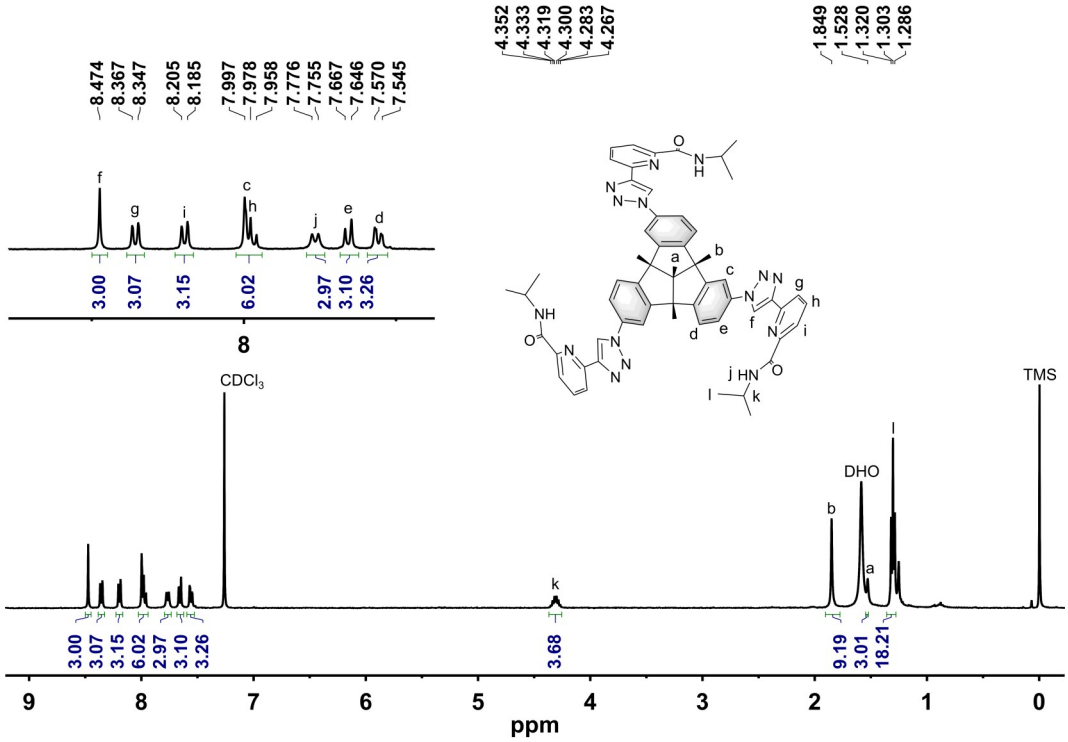

Fig. S14. ^{1}H NMR spectrum of C_3-**1** (400 MHz, 298 K, $CDCl_3$).

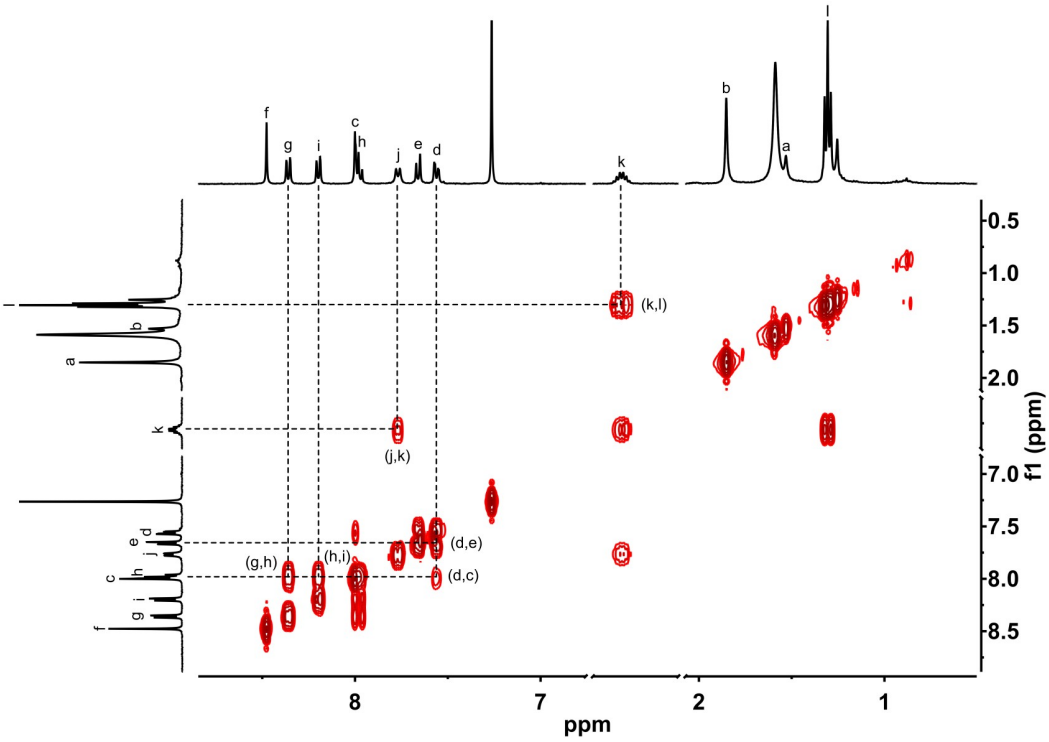

Fig. S15. Partial ^{1}H-^{1}H COSY spectrum of C_3-**1** (400 MHz, 298 K, $CDCl_3$).

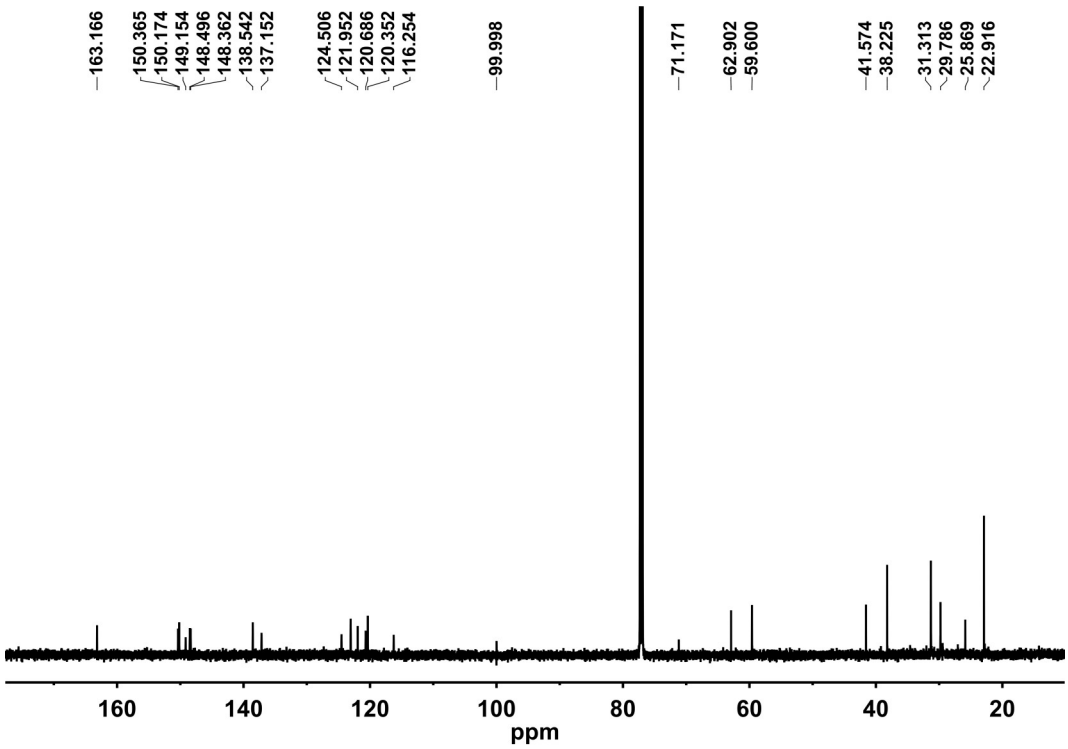

Fig. S16. ^{13}C NMR spectrum of C_3-**1** (101 MHz, 298 K, $CDCl_3$).

3.1.2 Synthesis of ligand C_1-**2**

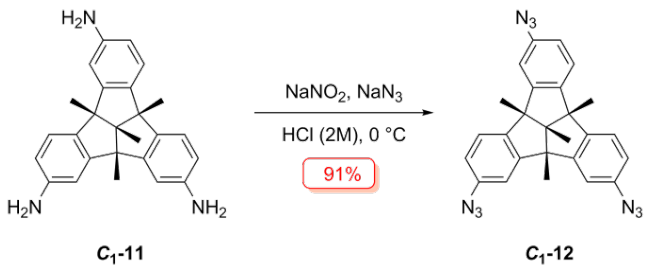

Similar to C_3-symmetric **11**, the C_1-symmetric precursor **11** as a by-product was synthesized based on reported methods.[S10-S12] Aqueous sodium nitrite (652 mg, 9.45 mmol, for a 3/1 ratio of nitrite to amino group) was added to a cooled solution of C_1-**11** (400 mg, 1.05 mmol, 1.0 equiv) in dilute hydrochloric acid (2 M, 30 mL) to create the diazonium salt in an ice bath. After stirring for 0.5 h, an aqueous solution of sodium azide (683 mg, 10.50 mmol, 10.0 equiv) was added dropwise to the diazonium salt. The mixture was stirred for another 2 h. The precipitate was recovered by filtration and further purified by column chromatography on silica gel with petroleum ether. Off-white powder C_1-**12** was obtained after drying *in vacuo* (439 mg, 91%).

^{1}H NMR (400 MHz, $CDCl_3$, 298 K) δ = 7.32 – 7.27 (m, 3H), 6.95 – 6.82 (m, 6H), 1.61 (s, 9H), 1.34 (s, 3H). ^{13}C NMR (101 MHz, $CDCl_3$, 298 K) δ = 150.30, 150.08, 149.91, 145.58, 145.43, 145.18, 140.39, 139.56, 139.48, 70.92, 62.55, 62.23, 61.91, 31.52, 29.72, 25.77, 25.70, 25.63, 16.10. ESI-TOF-MS for $C_{26}H_{21}N_9$ $[M + Na]^+$: calcd, m/z = 482.1812; found: 482.1815.

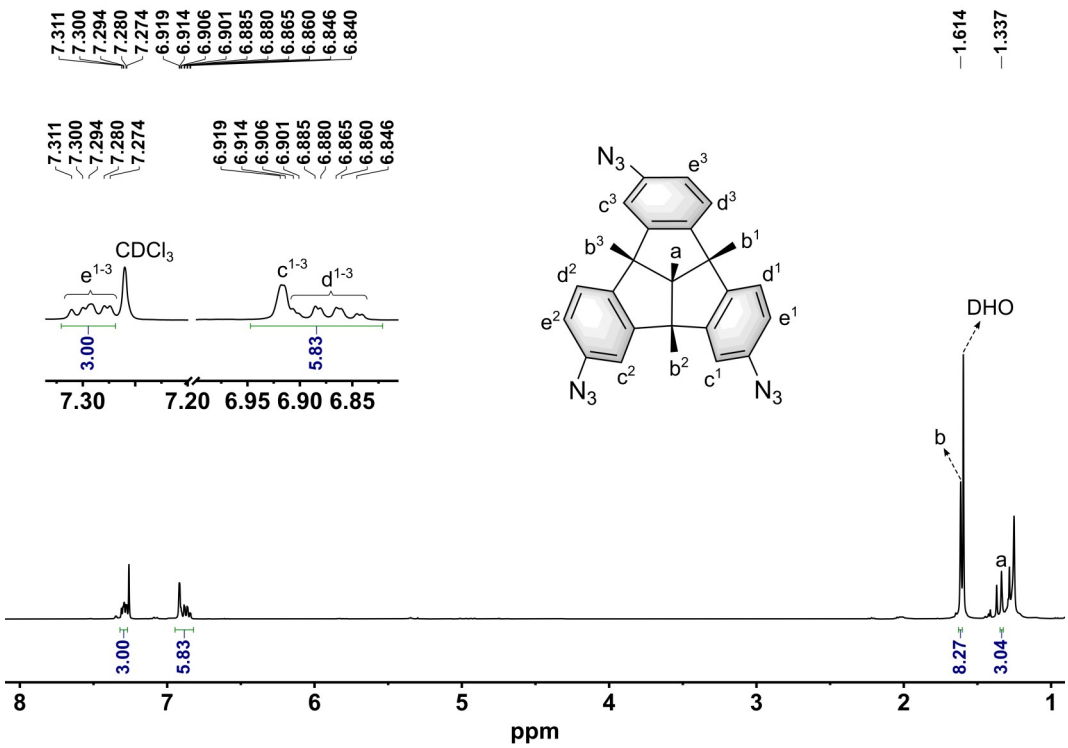

Fig. S17. ^{1}H NMR spectrum of C_1-**12** (400 MHz, 298 K, $CDCl_3$).

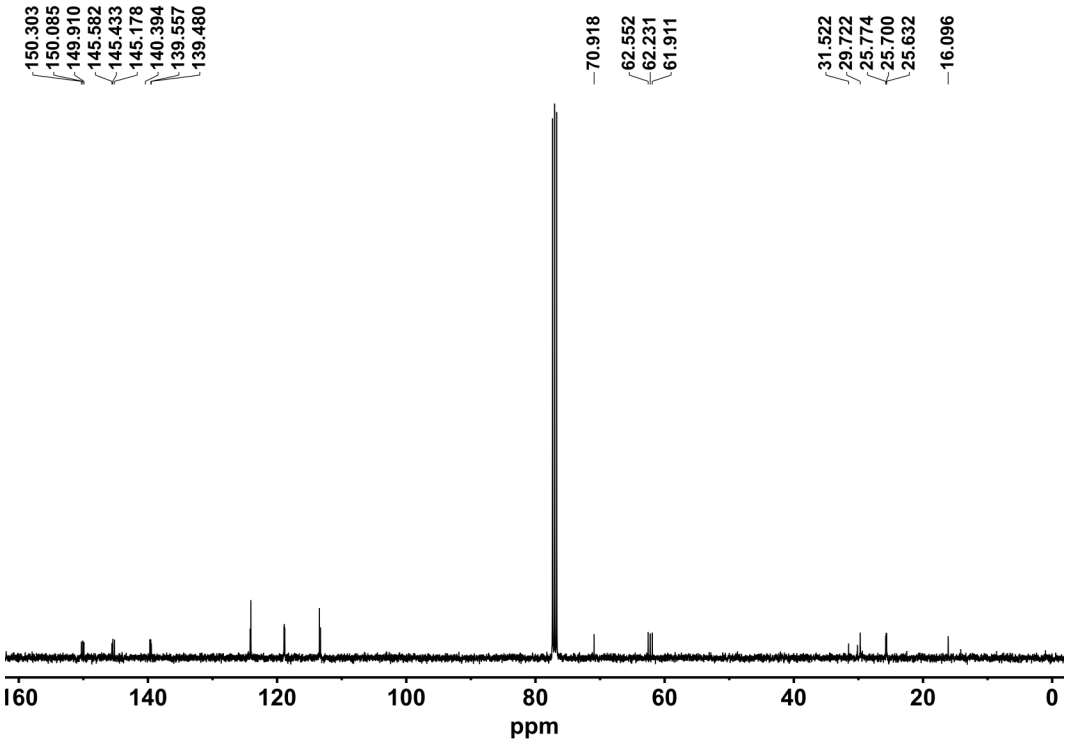

Fig. S18. ^{13}C NMR spectrum of C_1-**12** (101 MHz, 298 K, $CDCl_3$).

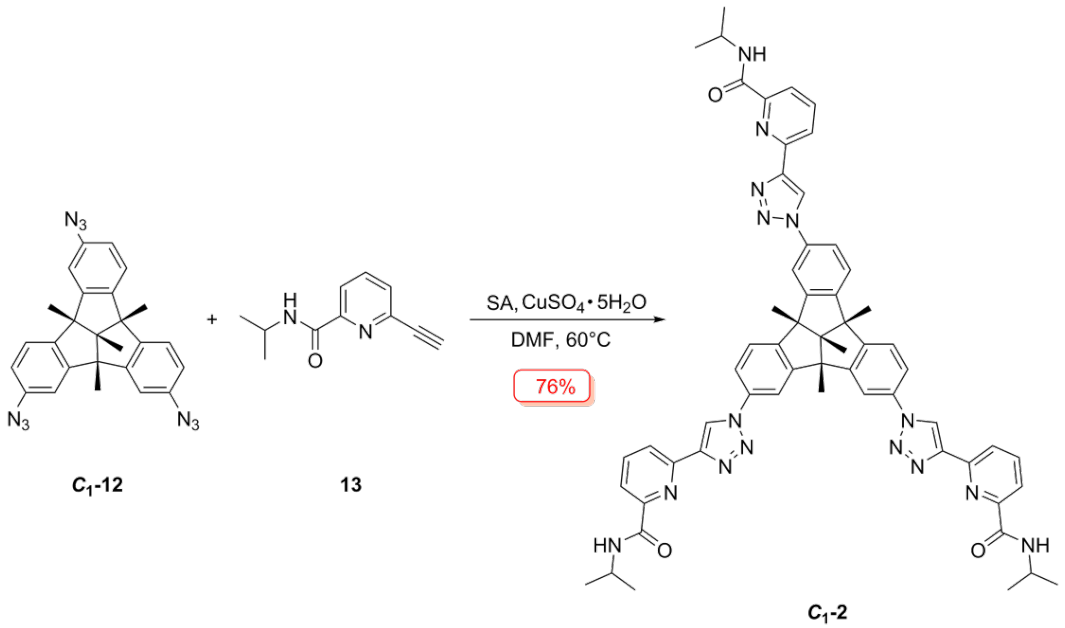

C_1-**12** (300 mg, 0.65 mmol, 1.0 equiv), **13** (405 mg, 2.15 mmol, 3.3 equiv), sodium ascorbate (SA, 271 mg, 1.37 mmol, 2.1 equiv) and $CuSO_4{\cdot}5H_2O$ (148 mg, 0.59 mmol, 0.9 equiv) were added into a solution of DMF (60 mL). The reaction mixture was stirred at 60 °C for 48 h. After that, the reaction solution was cooled to room temperature, and the solvent was removed under reduced pressure. Then, 50 mL of EDTA saturated aqueous solution was added and stirred for 1 h. The solution was extracted with mixed

organic solvents (50 mL × 3, DCM/MeOH v/v = 10/1), and the organic phase was washed with distilled water (30 mL × 2) and dried with anhydrous Na_2SO_4. The solvents were removed under reduced pressure to afford a crude product which was further purified chromatographically (SiO_2, DCM/MeOH, v/v = 100/1). White powder C_1-**2** was obtained after drying *in vacuo* (506 mg, 76%). Repeated attempts to separate the enantiomers *P*/*M*-**2** ended in failure, which may be attributed to the smaller structural difference of C_1-symmetric *P*/*M*-**2** relative to C_3-symmetric *P*/*M*-**1**.

^{1}H NMR (400 MHz, $CDCl_3$, 298 K) δ = δ 8.55 – 8.46 (m, 3H), 8.39 – 8.27 (m, 3H), 8.23 – 8.12 (m, 3H), 8.02 – 7.87 (m, 6H), 7.79 (t, *J* = 7.2 Hz, 3H), 7.69 – 7.54 (m, 6H), 4.37 – 4.23 (m, 3H), 1.95 – 1.74 (m, 9H), 1.52 (s, 3H), 1.35 – 1.22 (m, 18H). ^{13}C NMR (101 MHz, $CDCl_3$, 298 K) δ = 163.12, 163.09, 159.11, 150.29, 150.06, 150.01, 149.98, 149.33, 149.27, 149.19, 148.45, 148.44, 148.24, 148.19, 138.48, 138.41, 137.19, 137.05, 124.50, 124.31, 124.29, 123.05, 123.00, 122.96, 121.88, 121.81, 121.39, 121.29, 120.75, 120.51, 120.47, 120.30, 116.22, 116.18, 71.19, 63.13, 62.78, 62.56, 41.49, 26.93, 26.07, 25.83, 25.77, 22.87, 22.82, 16.20, 0.02. ESI-TOF-MS for $C_{59}H_{57}N_{15}O_3$ $[M + Na]^+$: calcd, m/z = 1046.4661; found, 1046.4666.

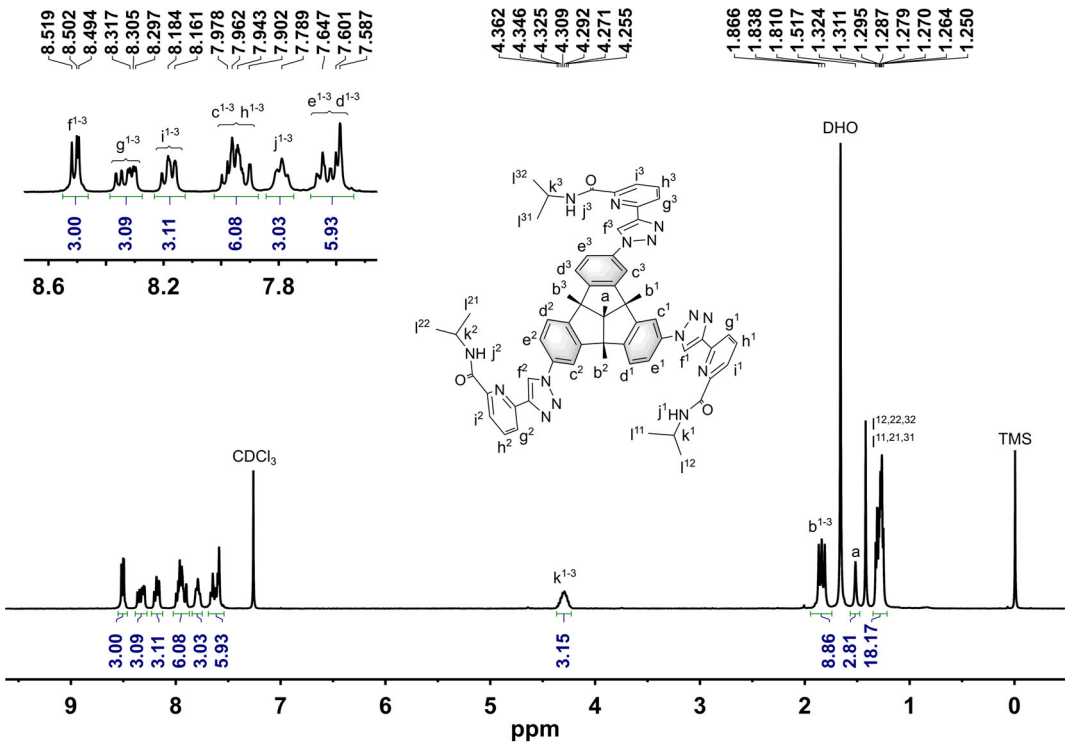

Fig. S19. ^{1}H NMR spectrum of C_1-**2** (400 MHz, 298 K, $CDCl_3$).

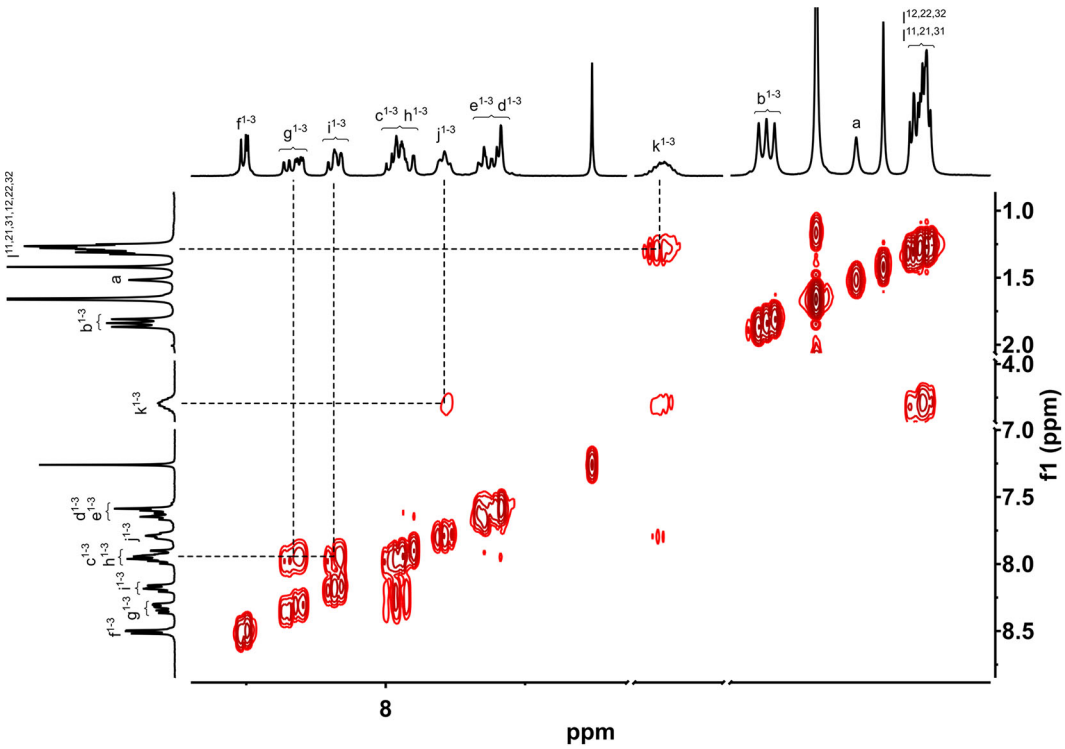

Fig. S20. Partial ^{1}H-^{1}H COSY spectrum of C_1-**2** (400 MHz, 298 K, $CDCl_3$).

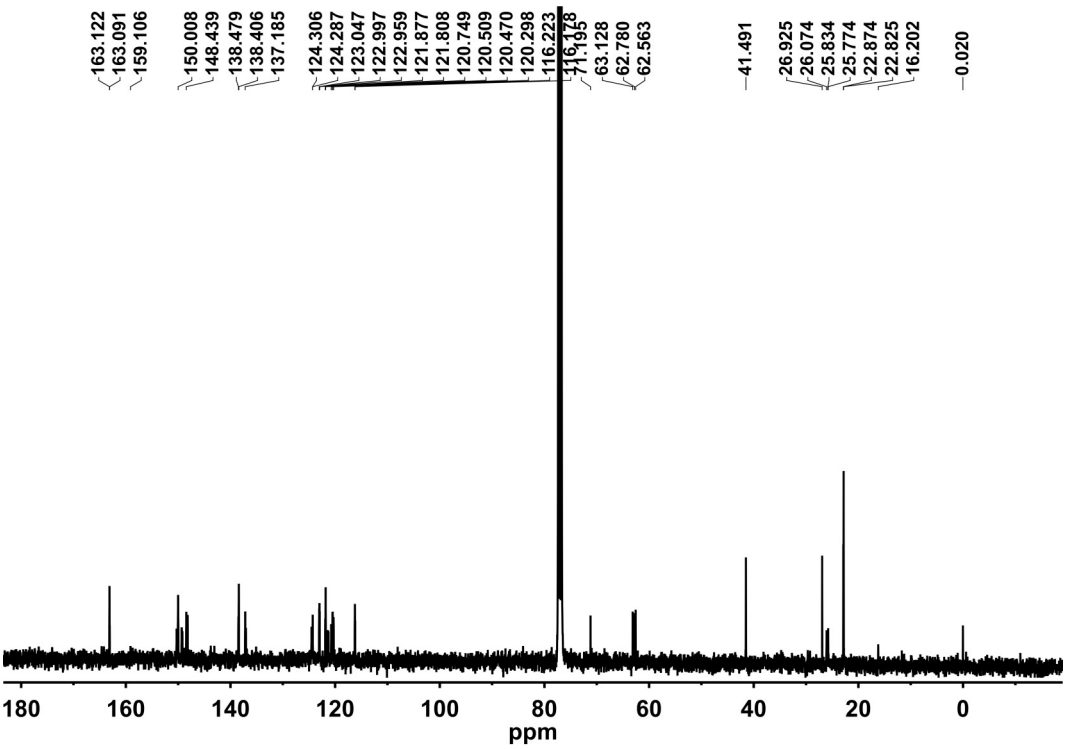

Fig. S21. ^{13}C NMR spectrum of C_1-**2** (101 MHz, 298 K, $CDCl_3$).

3.2 Synthesis of pseudo-cubic cages

3.2.1 Synthesis of cage *T*-**3**

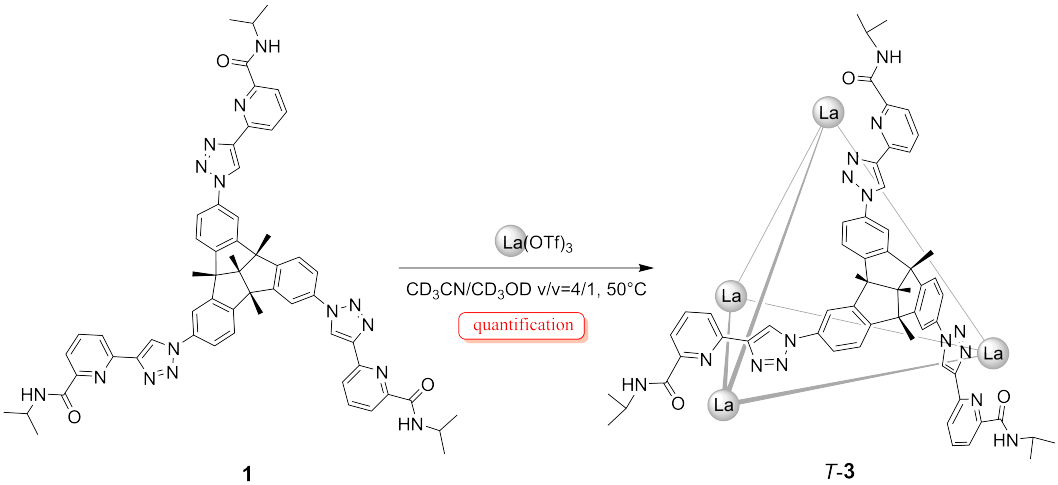

La(OTf)$_3$ (2.3 mg, 3.9 μmol) and **1** (4.0 mg, 3.9 μmol) were mixed in a solution of CD_3CN/CD_3OD (v/v 4/1, 500 μL). After stirring at 50 °C for 0.5 h, the white suspension gradually turned into a colorless solution that was characterized by NMR spectroscopy without further treatment. ^{1}H NMR spectrum showed that the assembly of **1** with La(OTf)$_3$ quantitatively formed *T*-symmetric cage **3**.

^{1}H NMR (400 MHz, 298 K, CD_3CN/CD_3OD v/v 4/1): δ = 9.65 (s, 12H, H_{11}), 8.59 (d, J = 8.1 Hz, 12H, H_{14}), 8.40 (t, J = 8.0 Hz, 12H, H_{15}), 8.09 (d, J = 7.9 Hz, 12H, H_{16}), 7.80 (s, 12H, H_{10}), 7.57 (d, J = 8.6 Hz, 12H, H_7), 6.88 (d, J = 8.5 Hz, 12H, H_8), 3.908 (m, 12H, H_{20}), 1.63 (s, 36H, H_4), 1.33 (s, 12H, H_1), 1.14 (d, J = 6.7 Hz, 36H, H_{22}), 0.86 (d, J = 6.6 Hz, 36H, H_{21}). ^{13}C NMR (101 MHz, 298 K, CD_3CN/CD_3OD v/v 4/1) δ 168.41, 151.45, 150.78, 150.35, 149.90, 149.06, 143.48, 137.09, 125.98, 124.03, 121.88, 119.77, 112.49, 73.08, 63.44, 43.89, 25.66, 23.23, 21.99, 14.86. High-resolution ESI-TOF-MS for *T*-**3**. The following picked signals are those at the highest intensities. m/z Calcd for [*T*-**3** – 8(OTf)]$^{8+}$ 656.0430, found 656.0439; Calcd for [*T*-**3** – 7(OTf)]$^{7+}$ 771.0423, found 771.0432; Calcd for [*T*-**3** – 6(OTf)]$^{6+}$ 924.3748, found 924.3763; Calcd for [*T*-**3** – 5(OTf)]$^{5+}$ 1139.0402, found 1139.0421; Calcd for [*T*-**3** – 4(OTf)]$^{4+}$ 1461.0384, found 1461.0411.

T-**3** (Δ_4-P_4 or Λ_4-M_4) was prepared by the same procedure except that racemic ligand C_3-**1** was replaced by chiral *P*-**1** or *M*-**1** (Fig. S25).

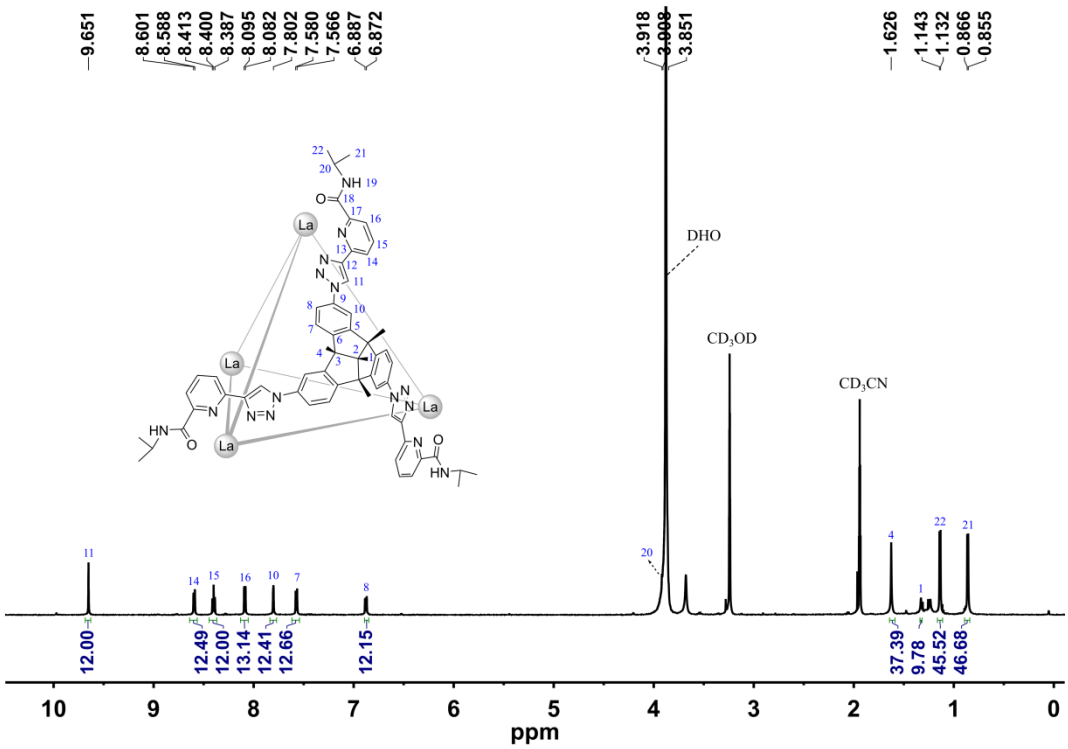

Fig. S22. ^{1}H NMR spectrum of *T*-**3** (400 MHz, 298 K, CD_3CN/CD_3OD v/v 4/1, [*T*-**3**] = 2.0 mM).

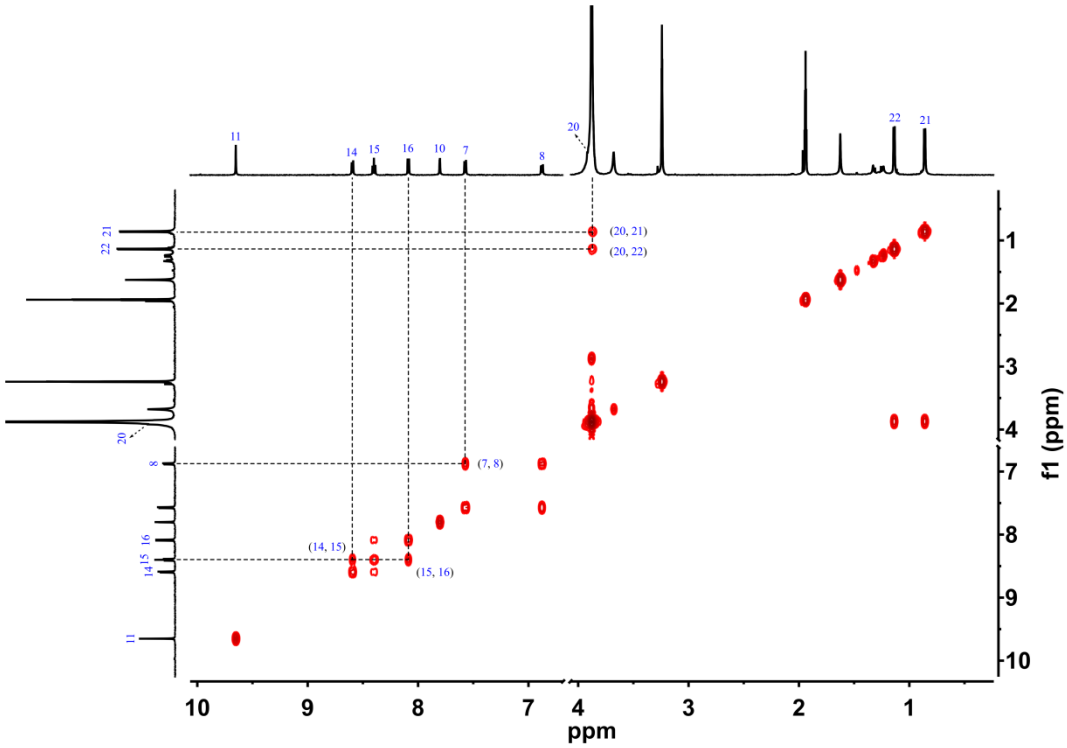

Fig. S23. Partial ^{1}H-^{1}H COSY spectrum of *T*-**3** (400 MHz, 298 K, CD_3CN/CD_3OD v/v 4/1, [*T*-**3**] = 2.0 mM).

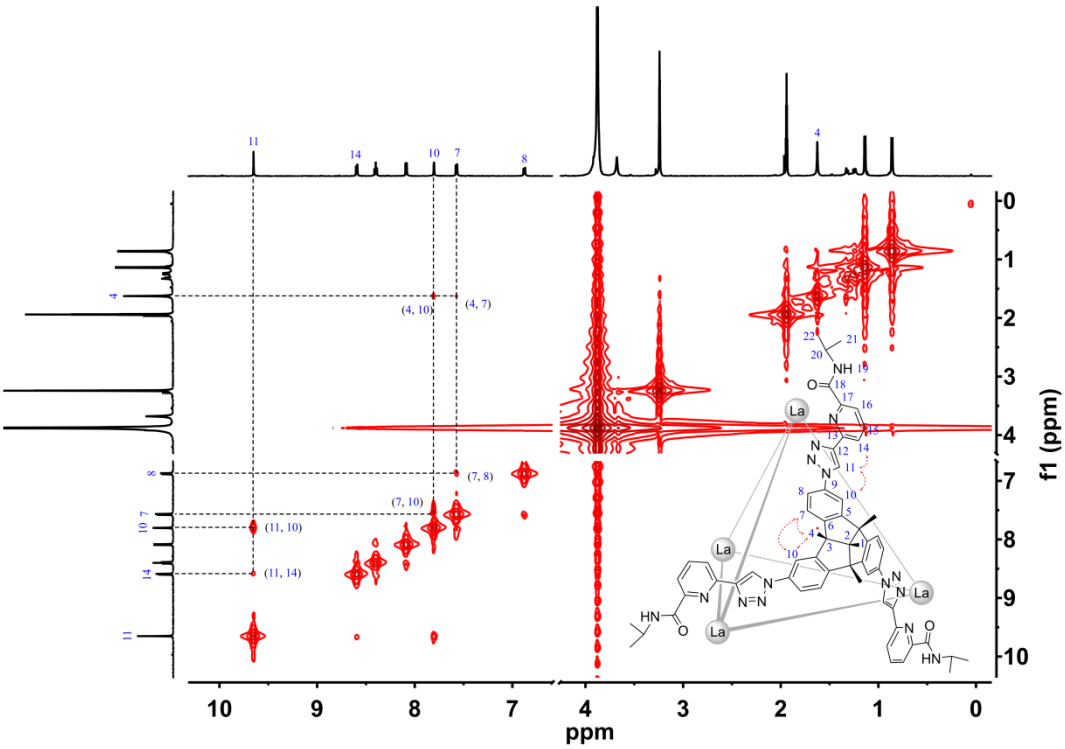

Fig. S24. Partial ^{1}H-^{1}H NOESY spectrum of *T*-**3** (400 MHz, 298 K, CD_3CN/CD_3OD v/v 4/1, [*T*-**3**] = 2.0 mM).

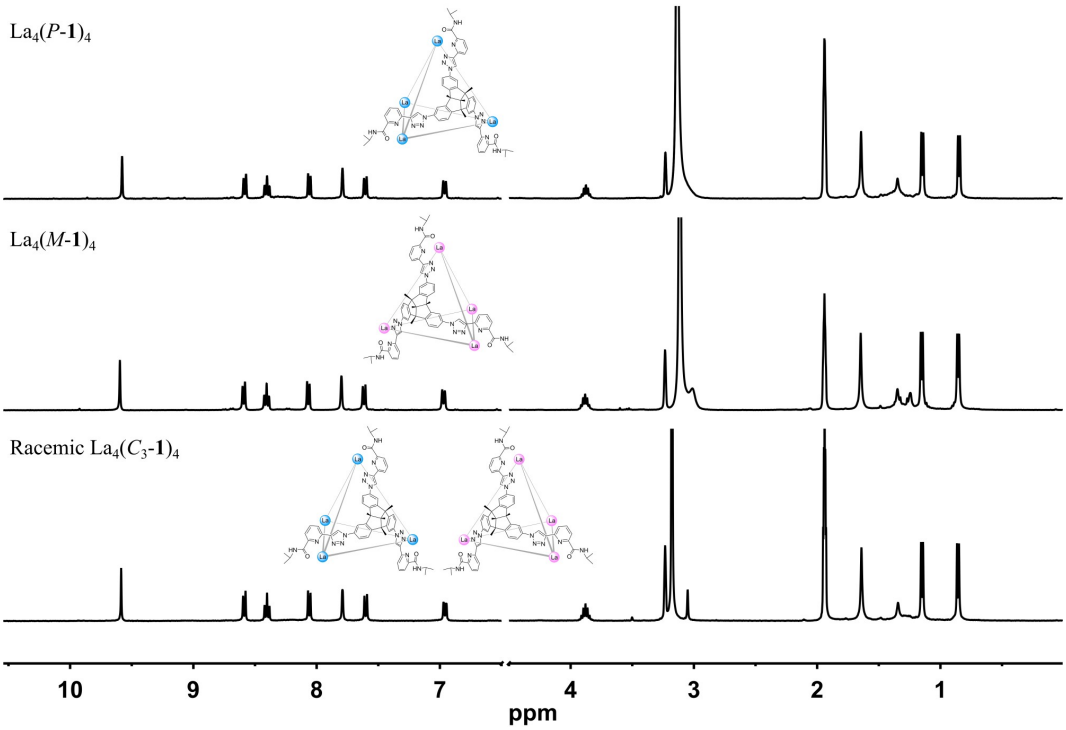

Fig. S25. Comparison of ^{1}H NMR spectra of racemic La_4(C_3-**1**)$_4$, homochiral La_4(*M*-**1**)$_4$ and La_4(*P*-**1**)$_4$ (400 MHz, 298 K, CD_3CN/MeOD v/v 4/1).

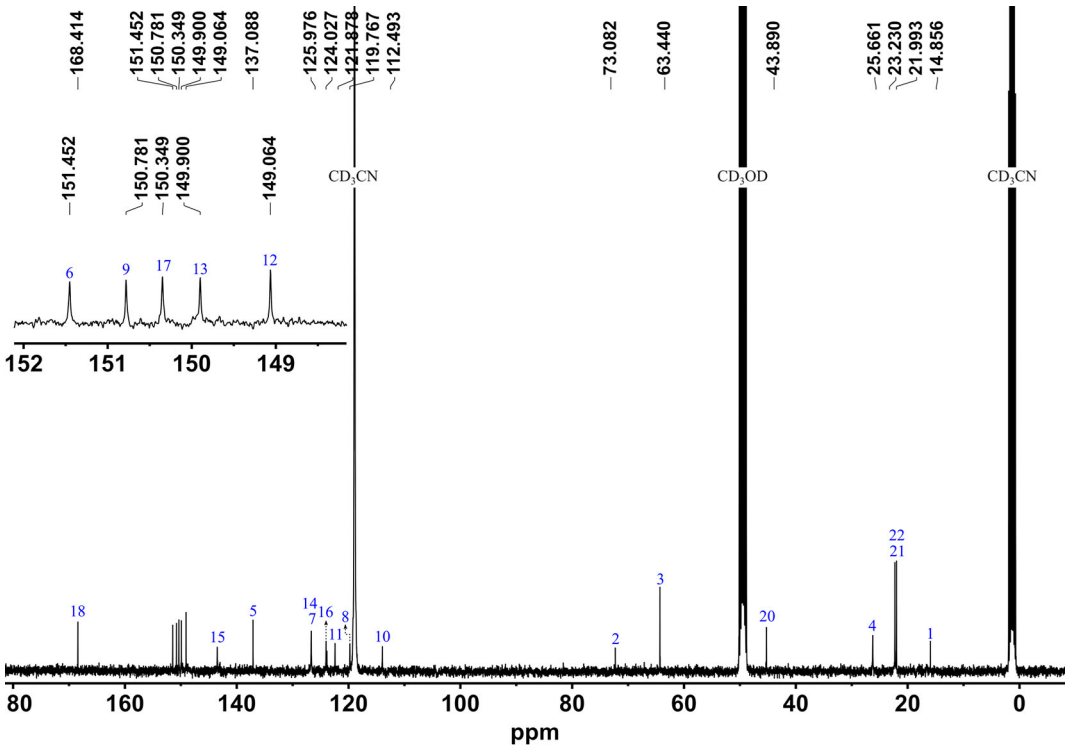

Fig. S26. ^{13}C NMR spectrum of *T*-**3** (400 MHz, 298 K, CD_3CN/CD_3OD v/v 4/1, [*T*-**3**] = 2.0 mM).

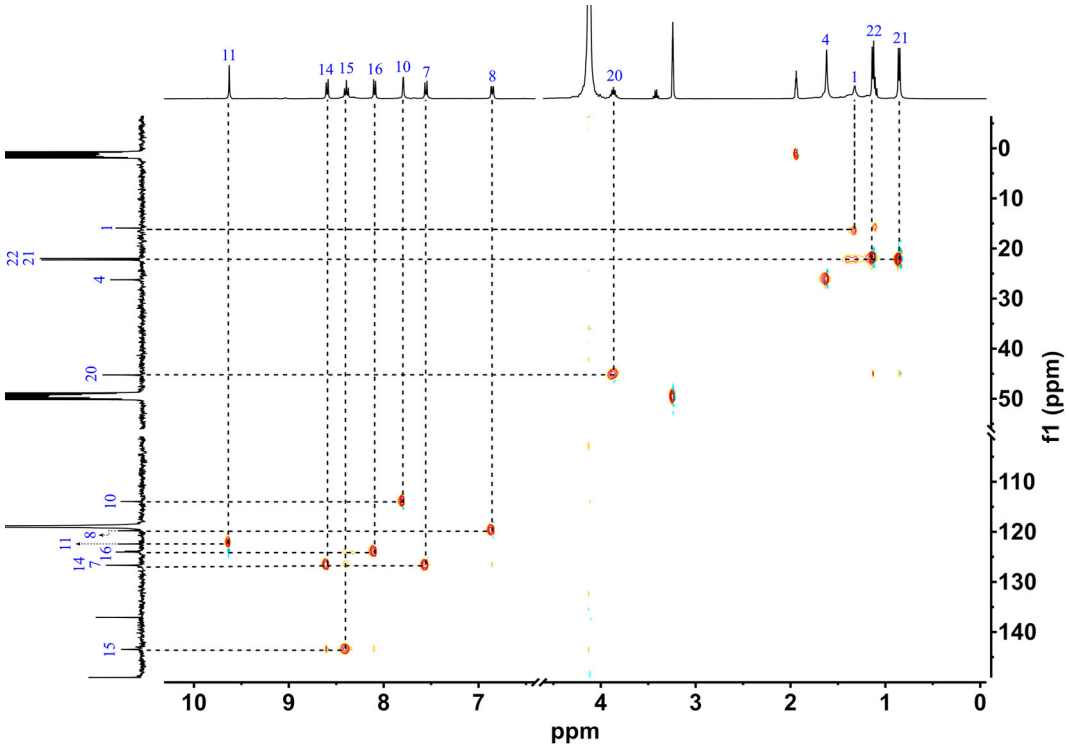

Fig. S27. Partial ^{1}H-^{13}C HSQC spectrum of *T*-**3** (400 MHz, 298 K, CD_3CN/CD_3OD v/v 4/1, [*T*-**3**] = 2.0 mM).

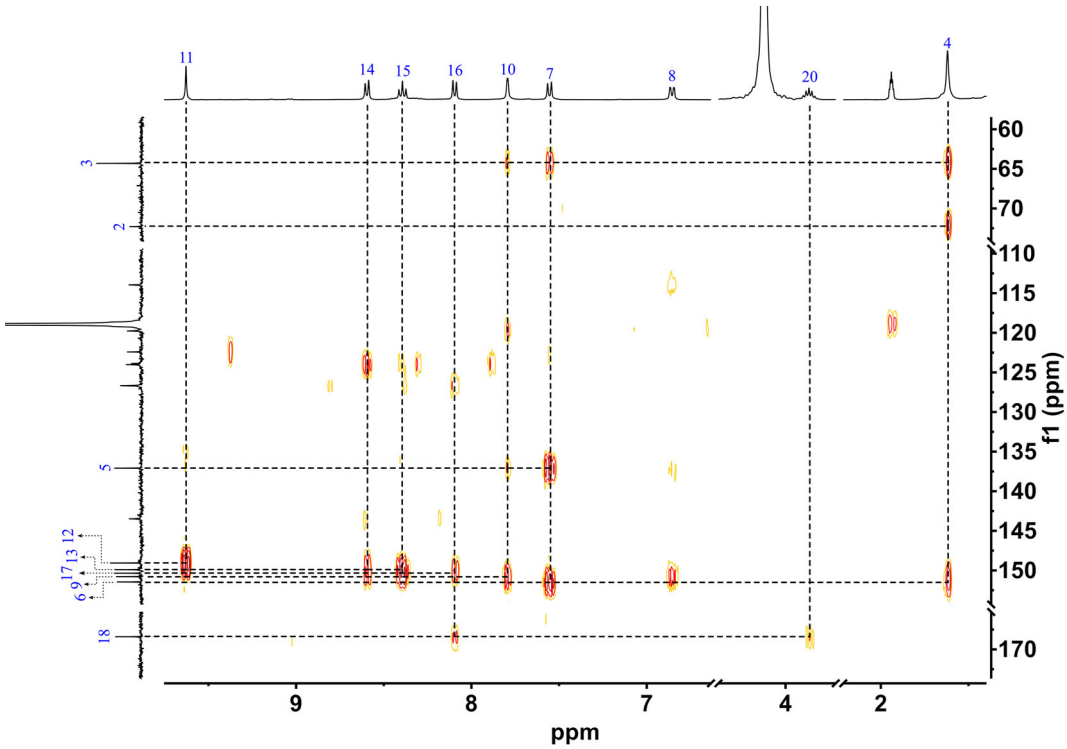

Fig. S28. Partial ^{1}H-^{13}C HMBC spectrum of *T*-**3** (400 MHz, 298 K, CD_3CN/CD_3OD v/v 4/1, [*T*-**3**] = 2.0 mM).

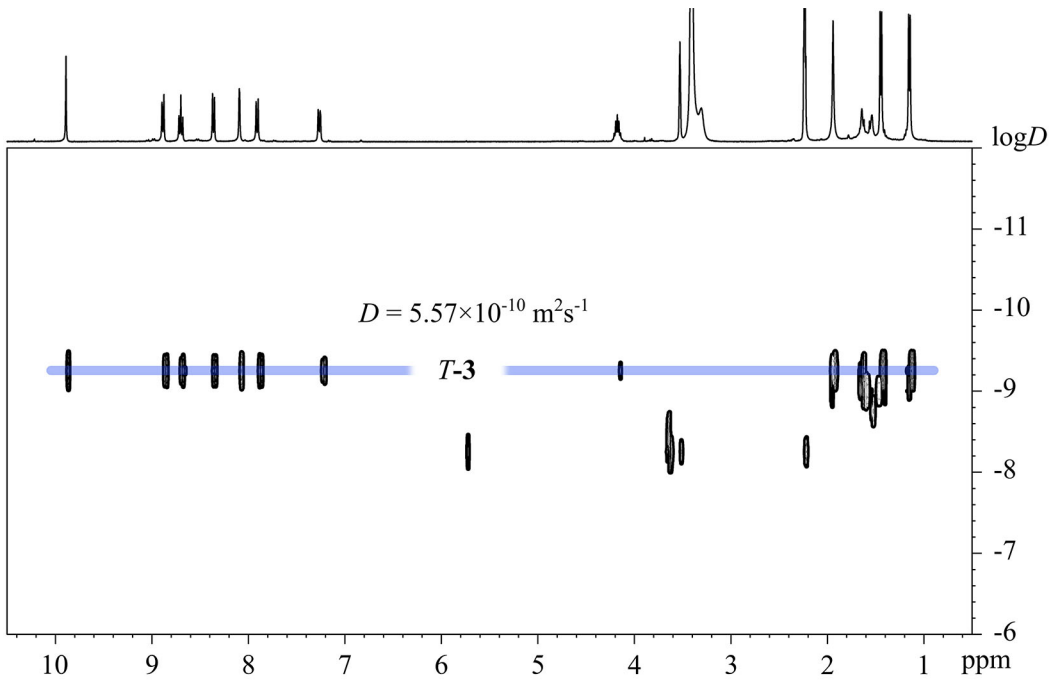

Fig. S29. ^{1}H DOSY spectrum of *T*-**3** (400 MHz, 298 K, CD_3CN/CD_3OD v/v 4/1, [*T*-**3**] = 2.0 mM). The hydrodynamic diameter of *T*-**3** was determined to be 2.3 nm.

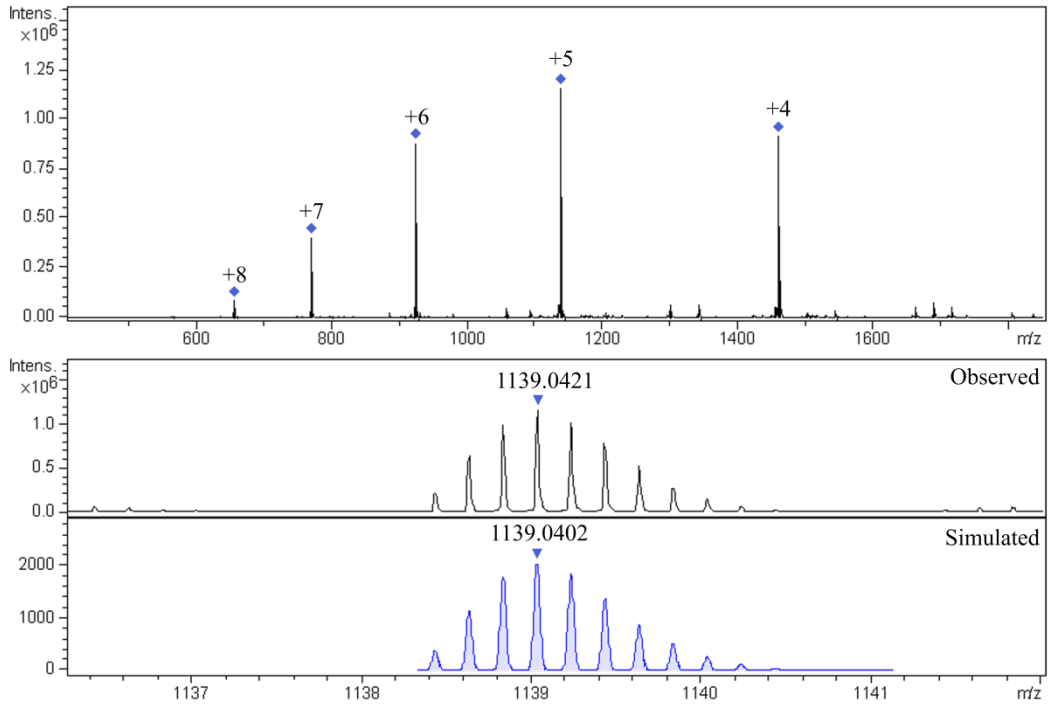

Fig. S30. High-resolution ESI-TOF-MS of *T*-**3** with the comparison of observed and simulated isotopic patterns of the peaks +5.

3.2.2 Synthesis of cage S_4-**4**

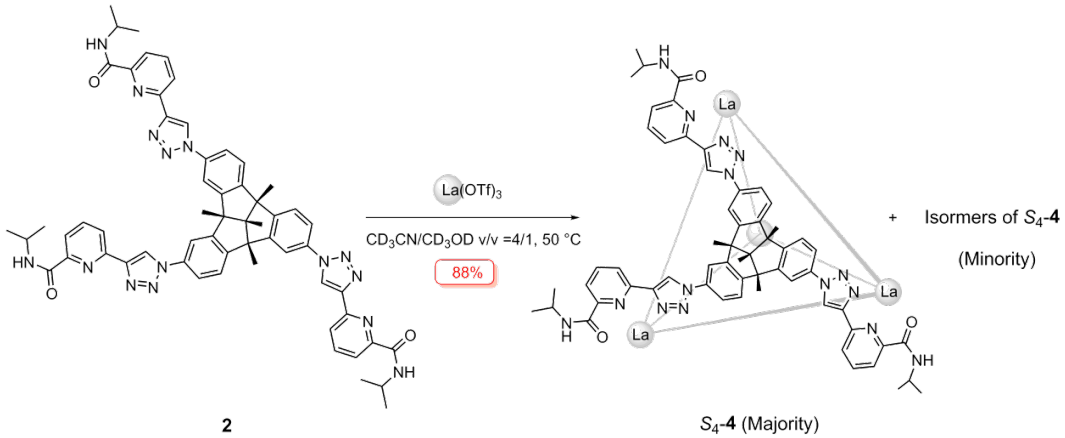

$La(OTf)_3$ (6.3 mg, 10.7 μmol) and **2** (11.0 mg, 10.7 μmol) were mixed in a solution of CD_3CN/CD_3OD (v/v 4/1, 500 μL). After stirring at 50 °C for 0.5 h, the white suspension gradually turned into a colorless solution that was characterized by NMR spectroscopy without further treatment. ^{1}H NMR spectrum showed that the assembly of **2** with $La(OTf)_3$ formed a mixed complex with S_4-symmetric cage **4** as the major product, and the NMR yield (88%) of S_4-**4** was determined by adding diethoxydimethylsilane as internal standard.

^{1}H NMR (400 MHz, 298 K, CD_3CN/CD_3OD v/v 4/1): δ = 9.56 (s, 4H, H_{51}), 9.43 (m, 8H, H_{33} and H_{15}), 8.76 (m, 8H, H_{36} and H_{54}), 8.53 (m, 12H, H_{18}, H_{37} and H_{55}), 8.33 (t, J = 8.0 Hz, 4H, H_{19}), 8.18 (m, 8H, H_{38} and H_{56}), 8.05 (s, 4H, H_{49}), 7.98 (d, J = 7.9 Hz,

4H, H_{20}), 7.87 (s, 4H, H_{31}), 7.67 (m, 8H, H_{13} and H_{46}), 7.45 (d, J = 8.5 Hz, 4H, H_{10}), 7.38 (d, J = 8.5 Hz, 4H, H_{28}), 7.04 (dd, J = 8.6, 1.9 Hz, 4H, H_{47}), 6.62 (dd, J = 8.5, 1.7 Hz, 4H, H_{11}), 6.33 (dd, J = 8.6, 1.7 Hz, 4H, H_{29}), 3.87 – 3.71 (m, 12H, H_{24}, H_{42} and H_{60}), 1.66 (m, 36H, H_6, H_8 and H_7), 1.37 (s, 12H), 1.18 – 1.03 (m, 36H, H_{25}, H_{43} and H_{61}), 0.74 (m, 36H, H_{26}, H_{44} and H_{62}). High-resolution ESI-TOF-MS for S_4-**4**. The following picked signals are those at the highest intensities. m/z Calcd for [S_4-**4** – 7(OTf)]$^{7+}$ 771.0423, found 771.0426; Calcd for [S_4-**4** – 6(OTf)]$^{6+}$ 924.3748, found 924.3758; Calcd for [S_4-**4** – 5(OTf)]$^{5+}$ 1139.0402, found 1139.0417; Calcd for [S_4-**4** – 4(OTf)]$^{4+}$ 1461.0384, found 1461.0401.

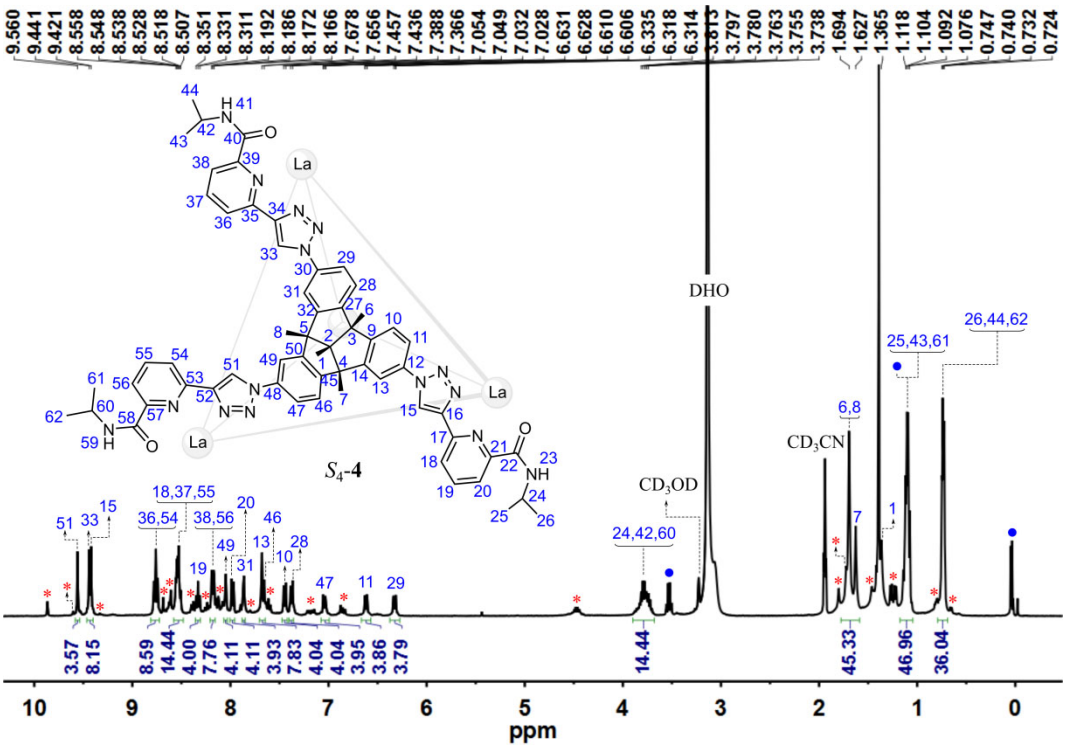

Fig. S31. ^{1}H NMR spectrum of S_4-**4** with minor isomers (400 MHz, 298 K, CD_3CN/CD_3OD v/v 4/1, [S_4-**4**] = 5.4 mM). (*: Isomers of S_4-**4**; ●: Inner standard, diethoxydimethylsilane)

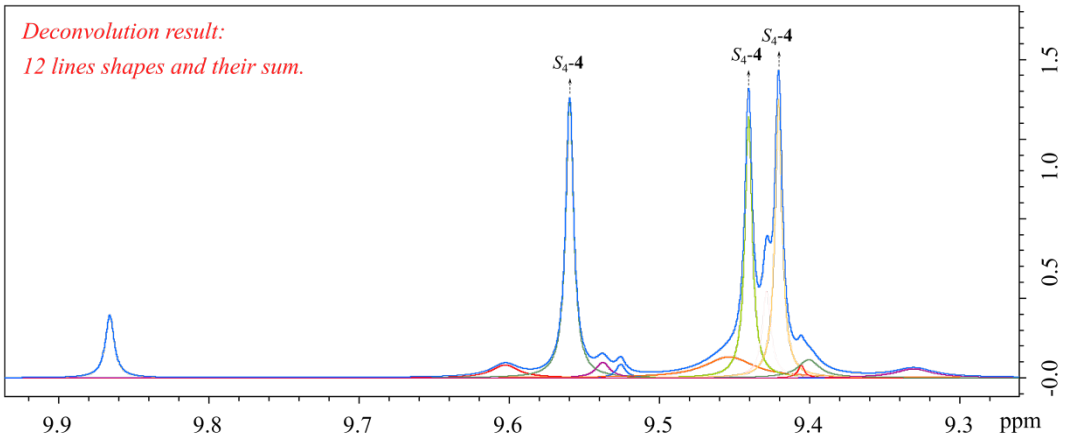

Fig. S32. Deconvolution result of the triazole region of ^{1}H NMR spectrum for S_4-**4** with

minor isomers (400 MHz, 298 K, CD_3CN/CD_3OD v/v 4/1, [S_4-**4**] = 5.4 mM). Multiple overlapping signals in the triazole region are consistent with the coexistence of at least three diastereomers in the mixture.

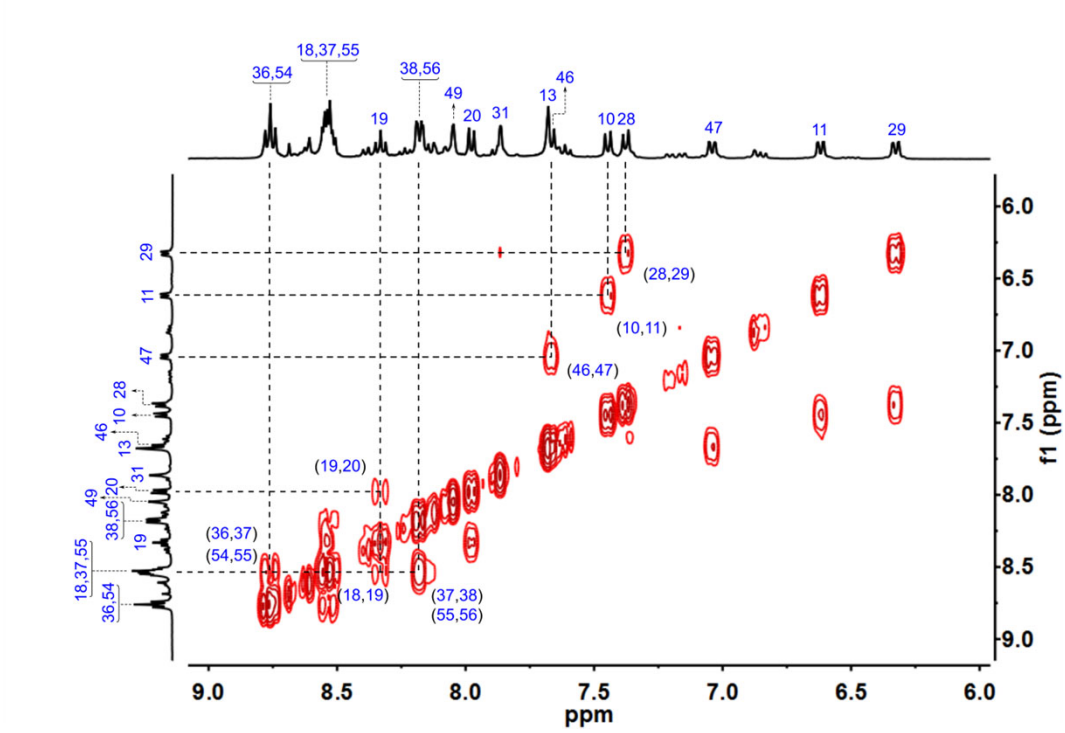

Fig. S33. Partial ^{1}H-^{1}H COSY spectrum of S_4-**4** with minor isomers (400 MHz, 298 K, CD_3CN/CD_3OD v/v 4/1, [S_4-**4**] = 5.4 mM).

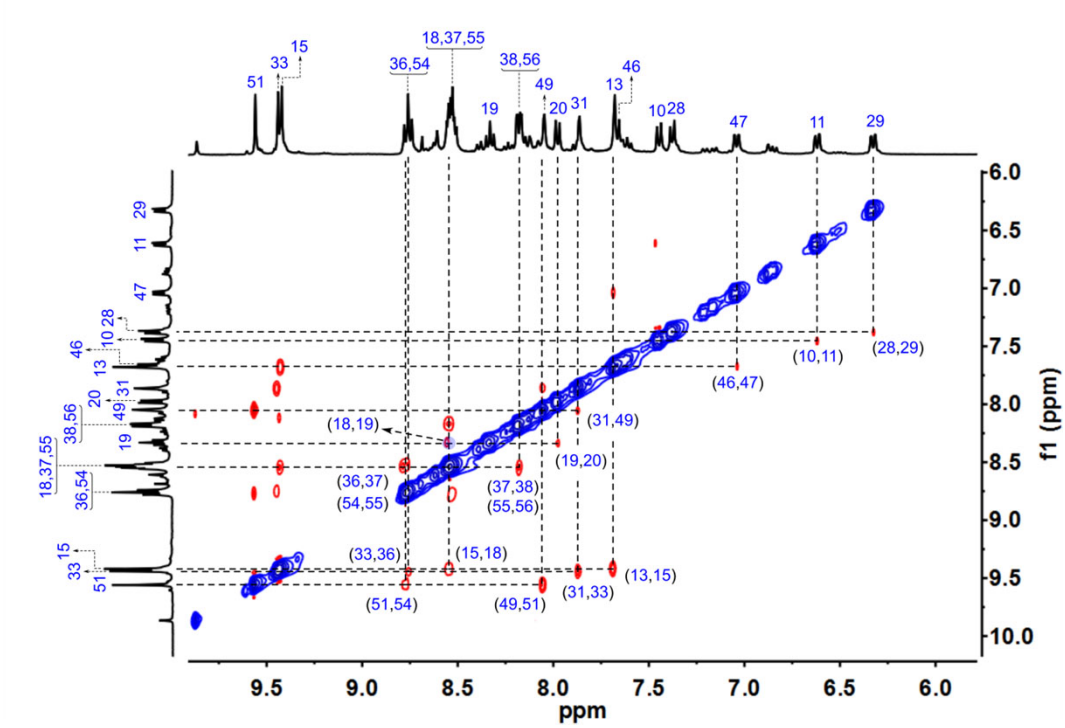

Fig. S34. Partial ^{1}H-^{1}H NOESY spectrum of S_4-**4** with minor isomers (400 MHz, 298 K, CD_3CN/CD_3OD v/v 4/1, [S_4-**4**] = 5.4 mM).

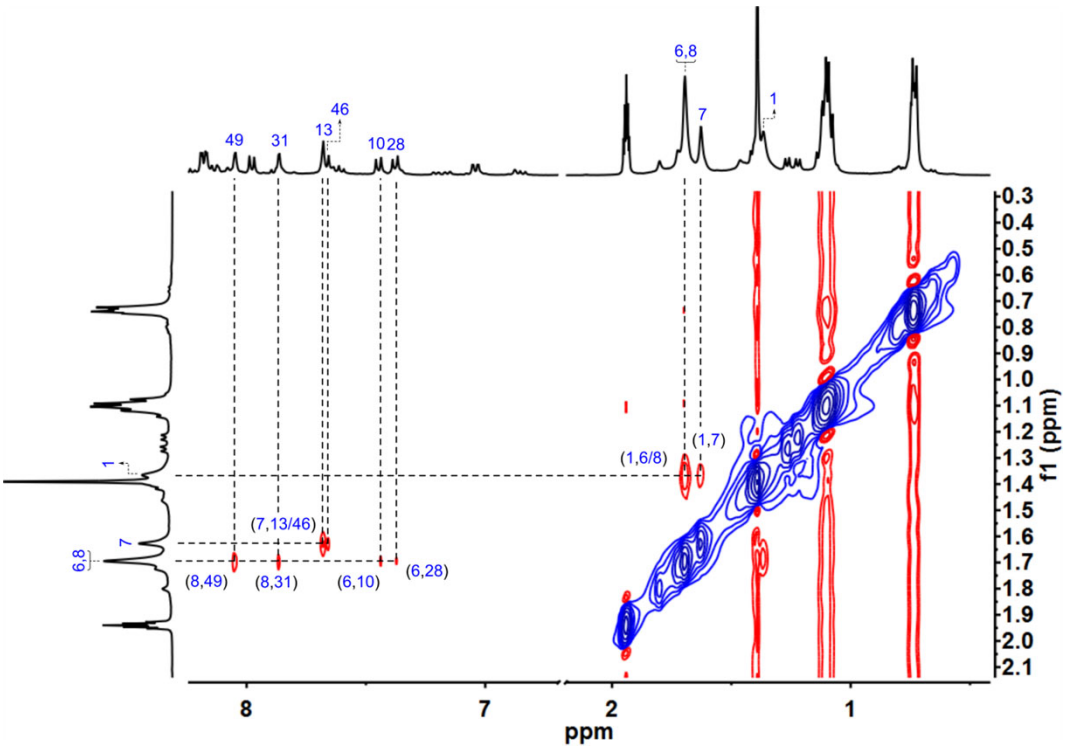

Fig. S35. Partial ^{1}H-^{1}H NOESY spectrum of S_4-**4** with minor isomers (400 MHz, 298 K, CD_3CN/CD_3OD v/v 4/1, [S_4-**4**] = 5.4 mM).

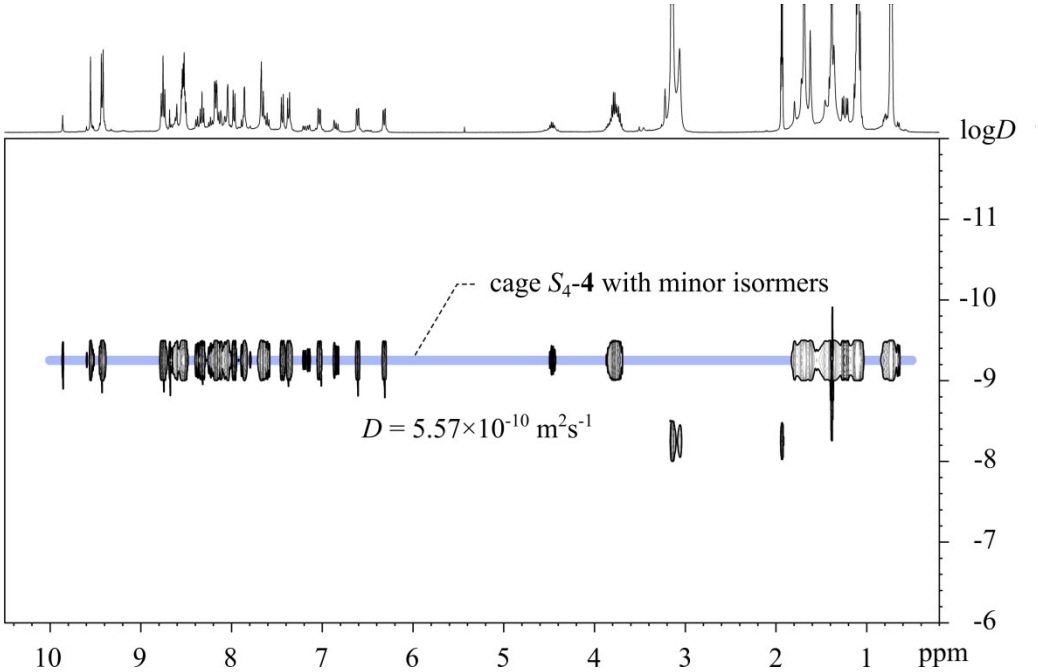

Fig. S36. ^{1}H DOSY spectrum of cage S_4-**4** with minor isomers (400 MHz, 298 K, CD_3CN/CD_3OD v/v 4/1, [S_4-**4**] = 5.4 mM). The hydrodynamic diameter of S_4-**4** was determined to be 2.2 nm.

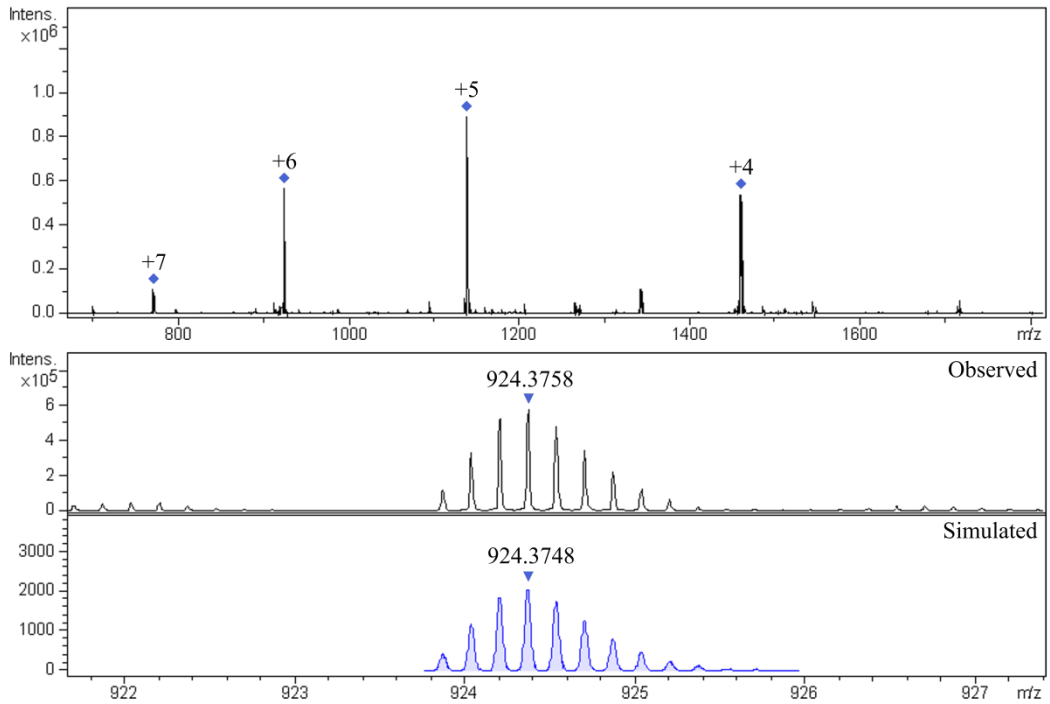

Fig. S37. High-resolution ESI-TOF-MS of S_4-**4** with the comparison of observed and simulated isotopic patterns of the peaks +6.

3.3 Host–guest complexes with fullerenes

3.3.1 Encapsulation of C_{60} with *T*-**3**

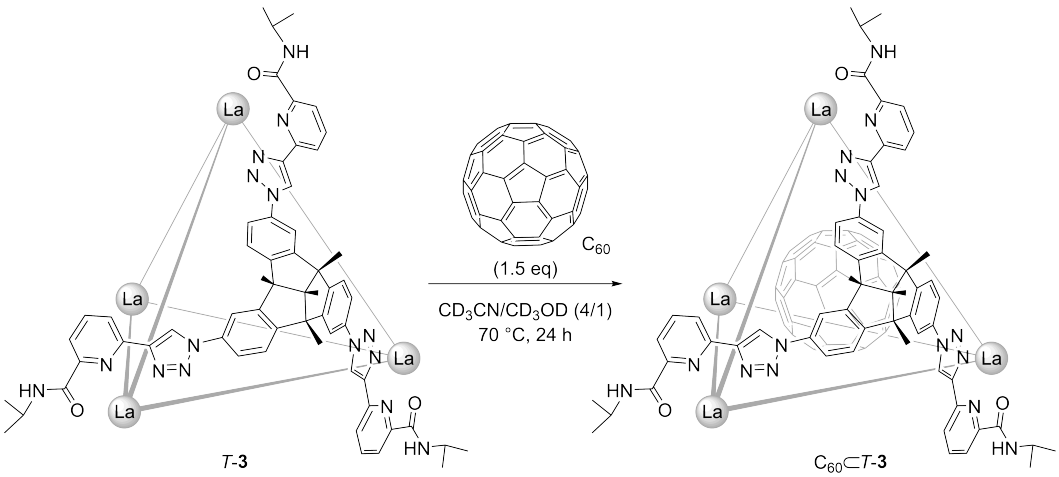

In situ self-assembly of C_{60}⊂*T*-**3**: $La(OTf)_3$ (3.5 mg, 5.9 μmol), *P*-**1** (6 mg, 5.9 μmol) and C_{60} (1.6 mg, 2.2 μmol) were mixed in a solution of CD_3CN/CD_3OD (v/v 4/1, 500 μL). After stirring at 70 °C for 24 h, the insoluble excess C_{60} was removed by centrifugation. The resulting solution was further characterized by NMR spectroscopy and high-resolution ESI-TOF-MS. ^{1}H NMR spectrum showed the quantitative

formation of $C_{60}\subset$*T*-**3** (Δ_4-P_4). The solvents were dried *in vacuo* to obtain a light purple powder. Yield ca. 10.5 mg, 99%.

^{1}H NMR (400 MHz, 298 K, CD_3CN/CD_3OD v/v 4/1): δ = 9.75 (s, 12H, H_{11}), 8.83 (d, J = 7.8 Hz, 12H, H_{14}), 8.47 (d, J = 7.7 Hz, 12H, H_{19}), 8.31 (t, J = 7.9 Hz, 12H, H_{15}), 8.08 (d, J = 7.7 Hz, 12H, H_{16}), 7.84 (d, J = 8.5 Hz, 12H, H_7), 7.70 (s, H_{10}), 7.39 (d, J = 6.3 Hz, 12H, H_8), 4.20 – 4.10 (m, 12H, H_{20}), 1.53 (s, 36H, H_4), 1.30 (d, J = 6.5 Hz, 36H, H_{22}), 1.24 (s, 12H, H_1), 1.10 (d, J = 6.5 Hz, 36H, H_{21}). ^{13}C NMR (101 MHz, 298 K, CD_3CN/CD_3OD v/v 4/1): δ = 168.71, 150.47, 150.36, 150.28, 149.76, 149.03, 142.95, 141.49 (encapsulated C_{60}), 137.82, 127.22, 126.03, 123.83, 123.67, 121.85, 120.65, 120.18, 113.01, 71.11, 63.50, 45.84, 31.58, 25.99, 21.83, 20.43. High-resolution ESI-TOF-MS for $C_{60}\subset$*T*-**3**. The following picked signals are those at the highest intensities. m/z Calcd for $[C_{60}\subset T\text{-}\mathbf{3} - 6(OTf)]^{6+}$ 1044.5419, found 1044.5410; Calcd for $[C_{60}\subset T\text{-}\mathbf{3} - 5(OTf)]^{5+}$ 1283.2407, found 1283.2407; Calcd for $[C_{60}\subset T\text{-}\mathbf{3} - 4(OTf)]^{4+}$ 1641.2890, found 1641.2892.

Encapsulation of C_{60} with preformed cage *T*-**3** (Δ_4-P_4): *T*-**3** (8 mg, 1.3 μmol) and C_{60} (1.4 mg, 2.0 μmol) were mixed in a solution of CD_3CN/CD_3OD (v/v 4/1, 500 μL). The mixture was stirred at 70 °C for 24 h and monitored by ^{1}H NMR.

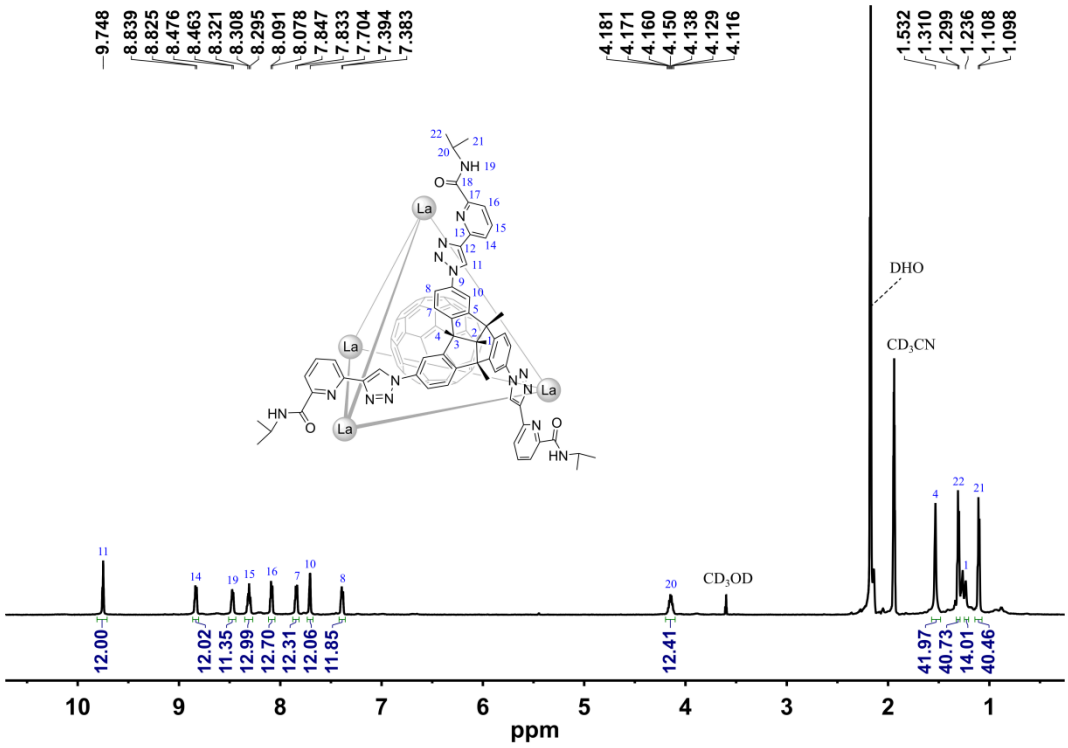

Fig. S38. ^{1}H NMR spectrum of $C_{60}\subset$*T*-**3** (400 MHz, 298 K, CD_3CN/CD_3OD v/v 4/1, $[C_{60}\subset T\text{-}\mathbf{3}]$ = 2.9 mM), where *T*-**3** is homochiral Δ_4-P_4.

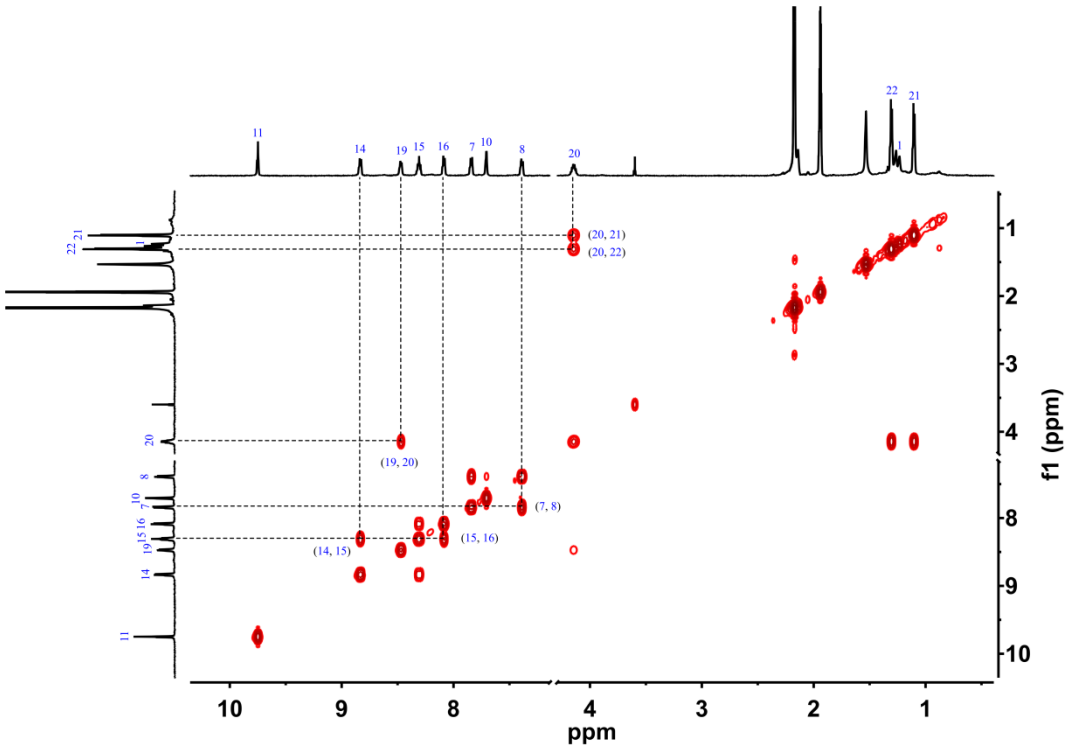

Fig. S39. Partial ^{1}H-^{1}H COSY spectrum of $C_{60}\subset$*T*-**3** (400 MHz, 298 K, CD_3CN/CD_3OD v/v 4/1, [$C_{60}\subset$*T*-**3**] = 2.9 mM), where *T*-**3** is homochiral Δ_4-P_4.

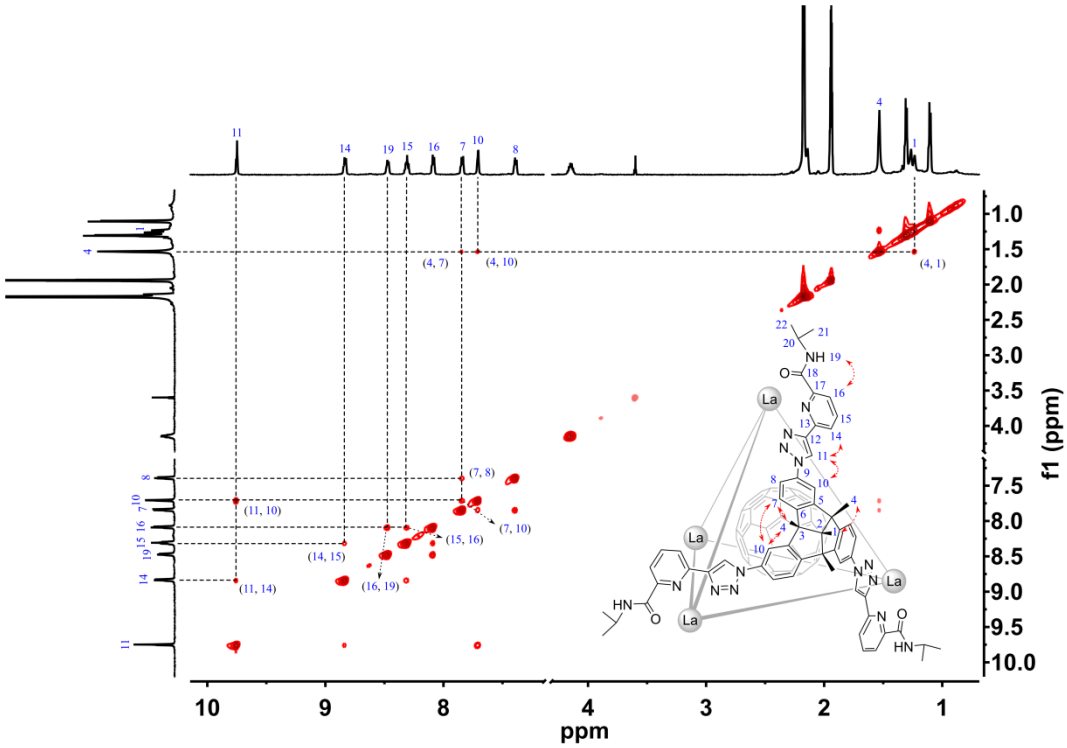

Fig. S40. Partial ^{1}H-^{1}H NOESY spectrum of $C_{60}\subset$*T*-**3** (400 MHz, 298 K, CD_3CN/CD_3OD v/v 4/1, [$C_{60}\subset$*T*-**3**] = 2.9 mM), where *T*-**3** is homochiral Δ_4-P_4.

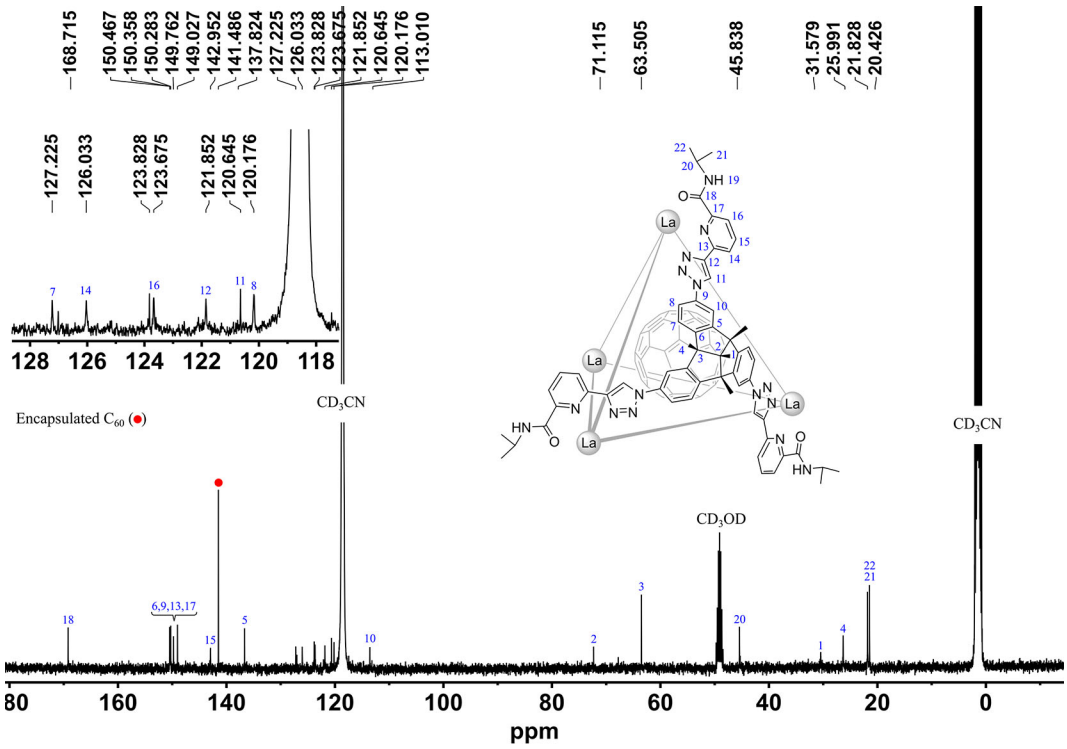

Fig. S41. ^{13}C NMR spectrum of $C_{60}\subset$*T*-**3** (400 MHz, 298 K, CD_3CN/CD_3OD v/v 4/1, [$C_{60}\subset$*T*-**3**] = 2.9 mM), where *T*-**3** is homochiral Δ_4-P_4.

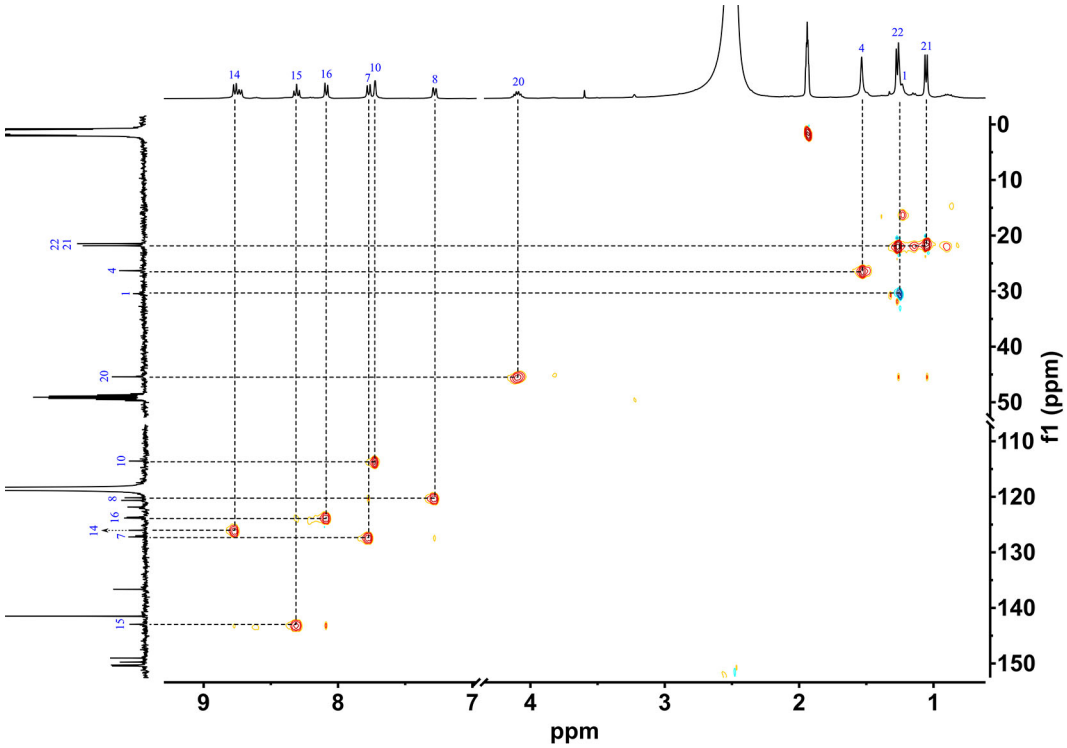

Fig. S42. Partial ^{1}H-^{13}C HSQC spectrum of $C_{60}\subset$*T*-**3** (400 MHz, 298 K, CD_3CN/CD_3OD v/v 4/1, [$C_{60}\subset$*T*-**3**] = 2.9 mM), where *T*-**3** is homochiral Δ_4-P_4.

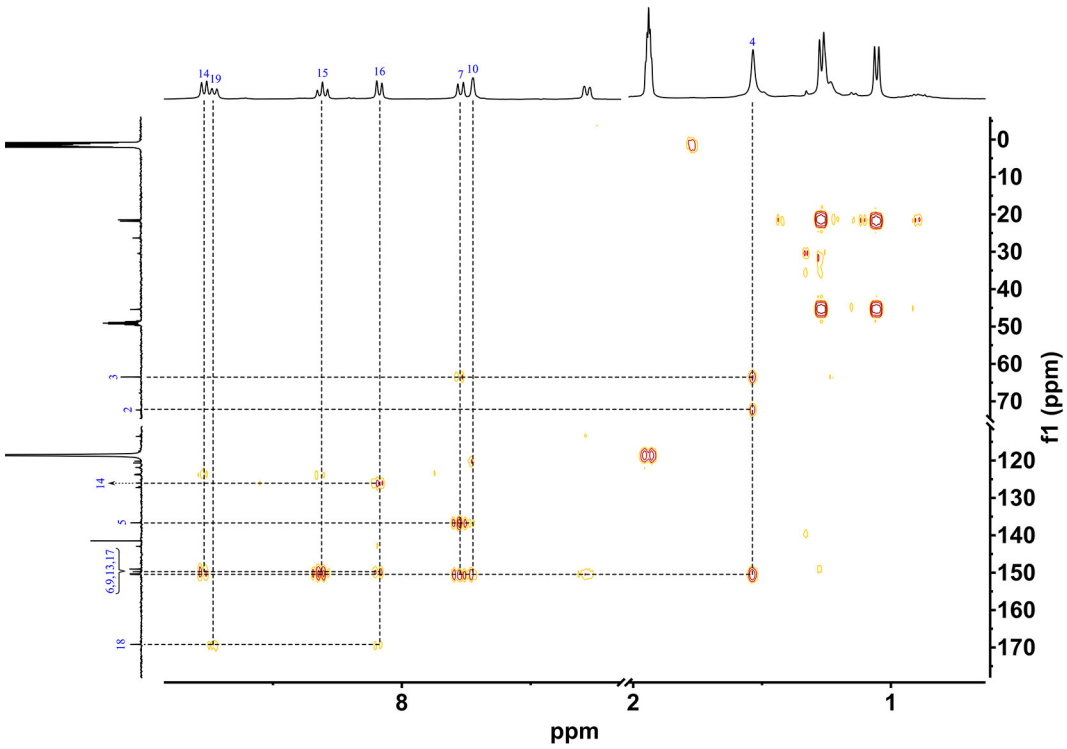

Fig. S43. Partial ^{1}H-^{13}C HMBC spectrum of $C_{60}\subset$*T*-**3** (400 MHz, 298 K, CD_3CN/CD_3OD v/v 4/1, [$C_{60}\subset$*T*-**3**] = 2.9 mM), where *T*-**3** is homochiral Δ_4-P_4.

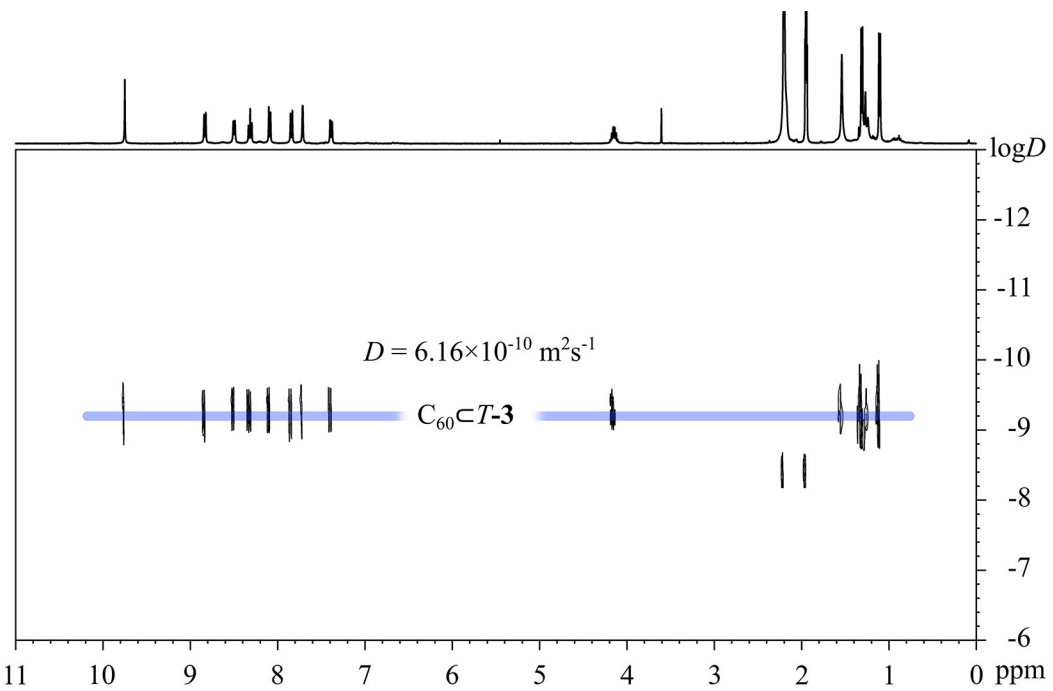

Fig. S44. ^{1}H DOSY spectrum of $C_{60}\subset$*T*-**3** (400 MHz, 298 K, CD_3CN/CD_3OD v/v 4/1, [$C_{60}\subset$*T*-**3**] = 2.9 mM), where *T*-**3** is homochiral Δ_4-P_4. The hydrodynamic diameter of $C_{60}\subset$*T*-**3** was determined to be 2.1 nm.

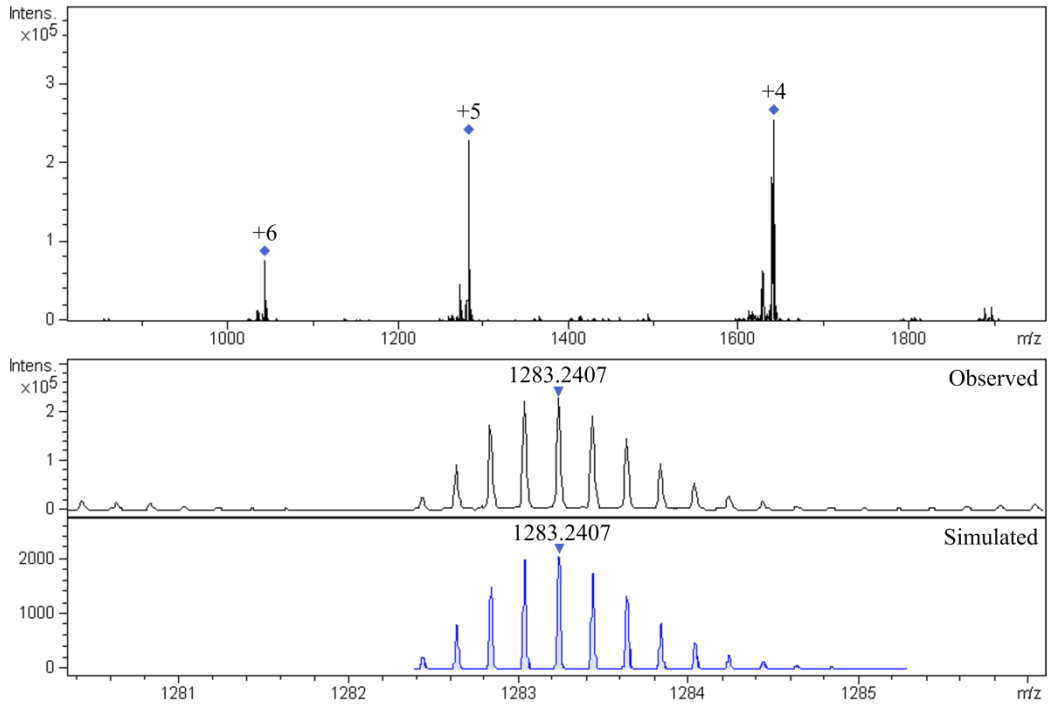

Fig. S45. High-resolution ESI-TOF-MS of C_{60}⊂*T*-**3** with the comparison of observed and simulated isotopic patterns of the peaks +5.

3.3.2 Encapsulation of C_{70} with *T*-**3**

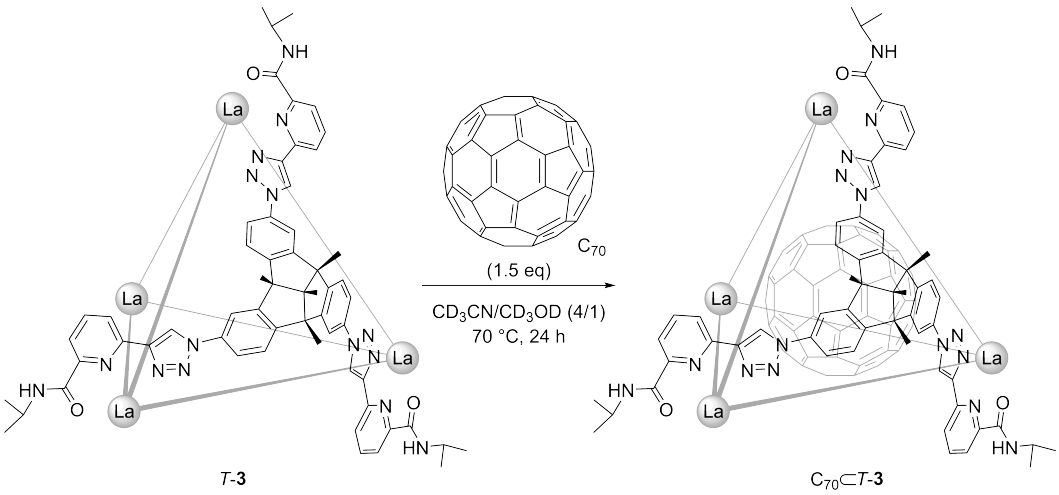

In situ self-assembly of C_{70}⊂*T*-**3**: $La(OTf)_3$ (3.5 mg, 5.9 μmol), *P*-**1** (6 mg, 5.9 μmol) and C_{70} (1.8 mg, 2.2 μmol) were mixed in a solution of CD_3CN/CD_3OD (v/v 4/1, 500 μL). After stirring at 70 °C for 24 h, the insoluble excess C_{70} was removed by centrifugation. The resulting solution was further characterized by NMR spectroscopy and high-resolution ESI-TOF-MS. ^{1}H NMR spectrum showed the quantitative formation of C_{70}⊂*T*-**3** (Δ_4-P_4). The solvents were dried *in vacuo* to obtain a light grey powder. Yield ca. 10.4 mg, 97%.

^{1}H NMR (400 MHz, 298 K, CD_3CN/CD_3OD v/v 4/1): δ = 9.57 (s, 12H, H_{11}), 8.70 (d, J = 8.0 Hz, 15H, H_{14} and H_{19}), 8.36 (t, J = 8.0 Hz, 12H, H_{15}), 8.06 (d, J = 8.0 Hz, 12H, H_{16}), 7.70 (s, 12H, H_{10}), 7.58 (d, J = 8.6 Hz, 12H, H_7), 6.97 (d, J = 10.0 Hz, 12H, H_8), 3.98 – 3.91 (m, 12H, H_{20}), 1.58 (s, 36H, H_4), 1.25 (s, 12H, H_1), 1.19 (d, J = 6.6 Hz, 36H, H_{22}), 0.94 (d, J = 6.6 Hz, 36H, H_{21}). ^{13}C NMR (101 MHz, 298 K, CD_3CN/CD_3OD v/v 4/1): δ = 168.75, 150.84 (encapsulated C_{70}), 150.14, 150.08, 149.63, 149.05, 148.73, 147.14 (encapsulated C_{70}), 145.82 (encapsulated C_{70}), 143.92 (encapsulated C_{70}), 142.83, 136.39, 129.27 (encapsulated C_{70}), 126.63, 125.87, 123.73, 123.13, 121.50, 120.59, 120.14, 112.83, 72.93, 63.31, 43.64, 31.90, 26.22, 21.79, 21.76. High-resolution ESI-TOF-MS for $C_{70}\subset$*T*-**3**. The following picked signals are those at the highest intensities. m/z Calcd for $[C_{70}\subset T\text{-}\mathbf{3} - 6(OTf)]^{6+}$ 1064.5422, found 1064.5415; Calcd for $[C_{70}\subset T\text{-}\mathbf{3} - 5(OTf)]^{5+}$ 1307.2408, found 1307.2403; Calcd for $[C_{70}\subset T\text{-}\mathbf{3} - 4(OTf)]^{4+}$ 1671.2891, found 1671.2883.

Encapsulation of C_{70} with preformed cage *T*-**3** (Δ_4-P_4): *T*-**3** (8 mg, 1.3 μmol) and C_{70} (1.7 mg, 2.0 μmol) were mixed in a solution of CD_3CN/CD_3OD (v/v 4/1, 500 μL). The mixture was stirred at 70 °C for 24 h and monitored by ^{1}H NMR.

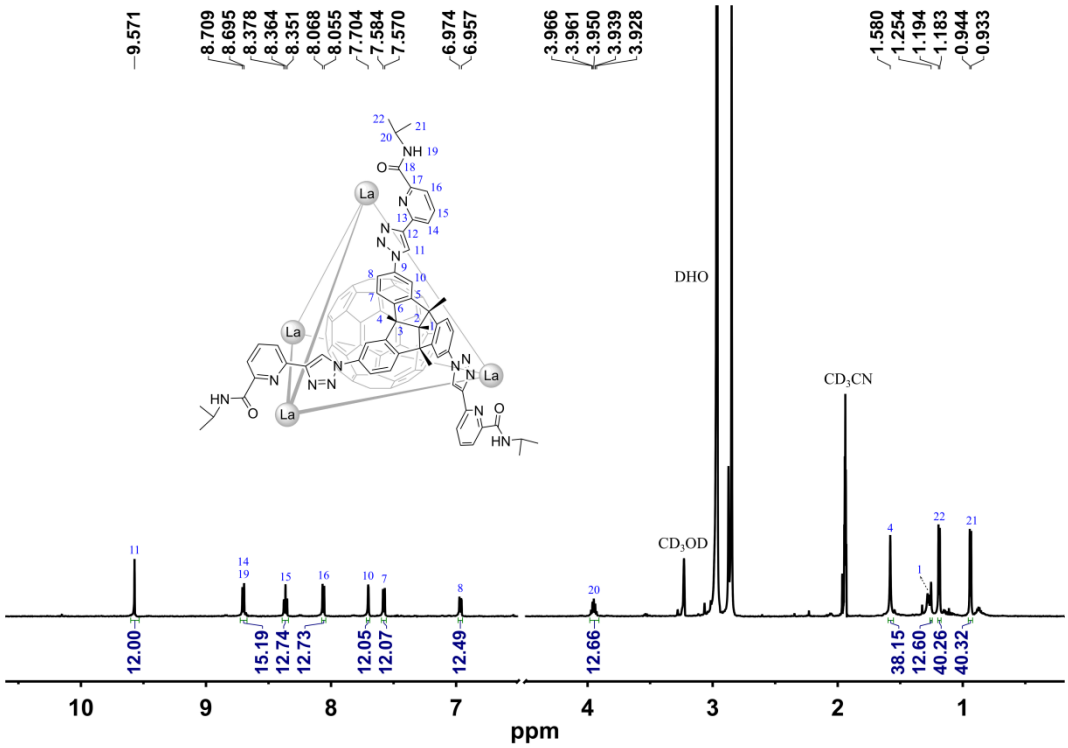

Fig. S46. ^{1}H NMR spectrum of $C_{70}\subset$*T*-**3** (400 MHz, 298 K, CD_3CN/CD_3OD v/v 4/1, $[C_{70}\subset T\text{-}\mathbf{3}]$ = 2.9 mM), where *T*-**3** is homochiral Δ_4-P_4.

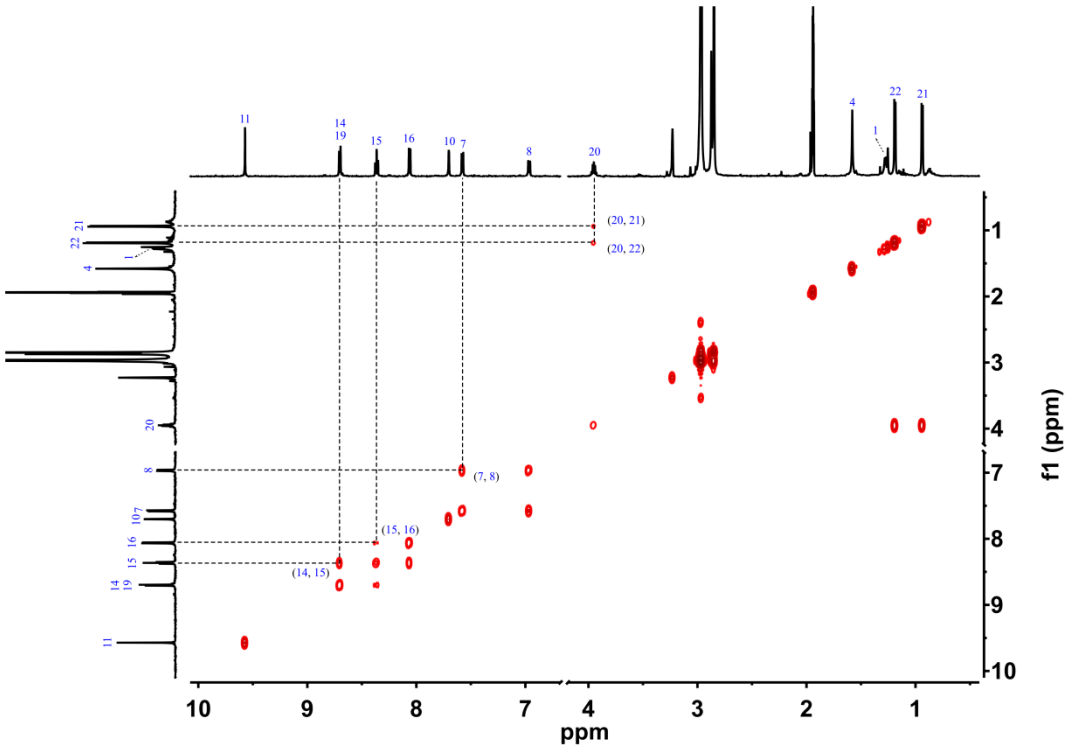

Fig. S47. Partial ^{1}H-^{1}H COSY spectrum of $C_{70}\subset$*T*-**3** (400 MHz, 298 K, CD_3CN/CD_3OD v/v 4/1, [$C_{70}\subset$*T*-**3**] = 2.9 mM), where *T*-**3** is homochiral Δ_4-P_4.

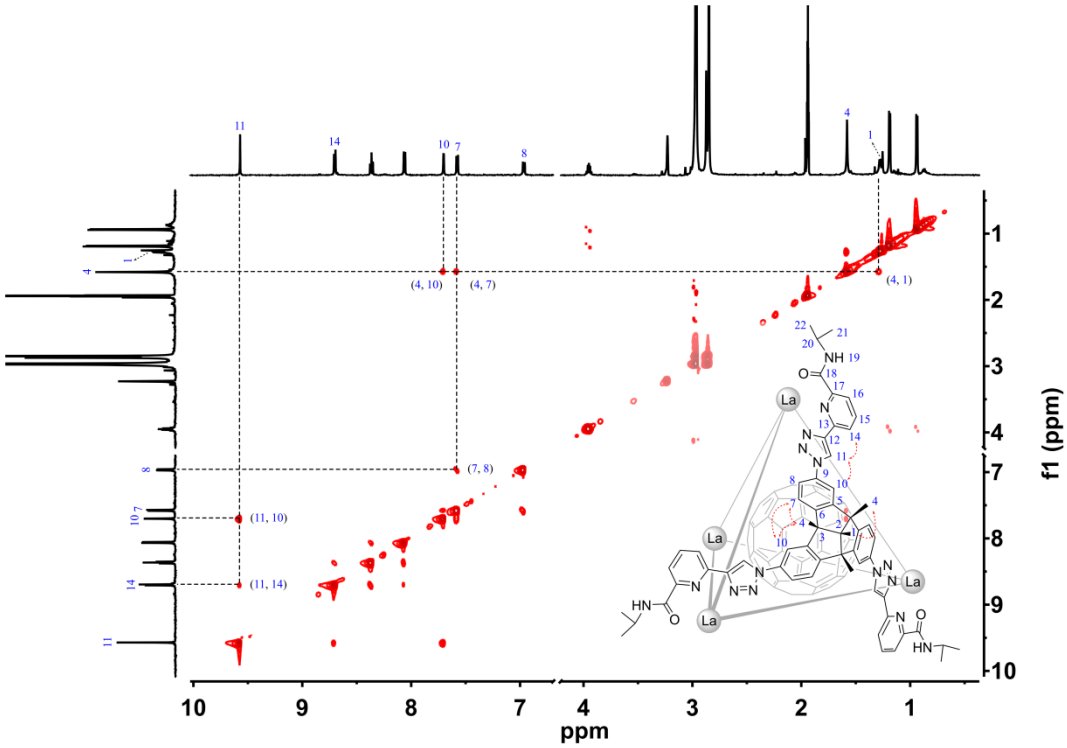

Fig. S48. Partial ^{1}H-^{1}H NOESY spectrum of $C_{70}\subset$*T*-**3** (400 MHz, 298 K, CD_3CN/CD_3OD v/v 4/1, [$C_{70}\subset$*T*-**3**] = 2.9 mM), where *T*-**3** is homochiral Δ_4-P_4.

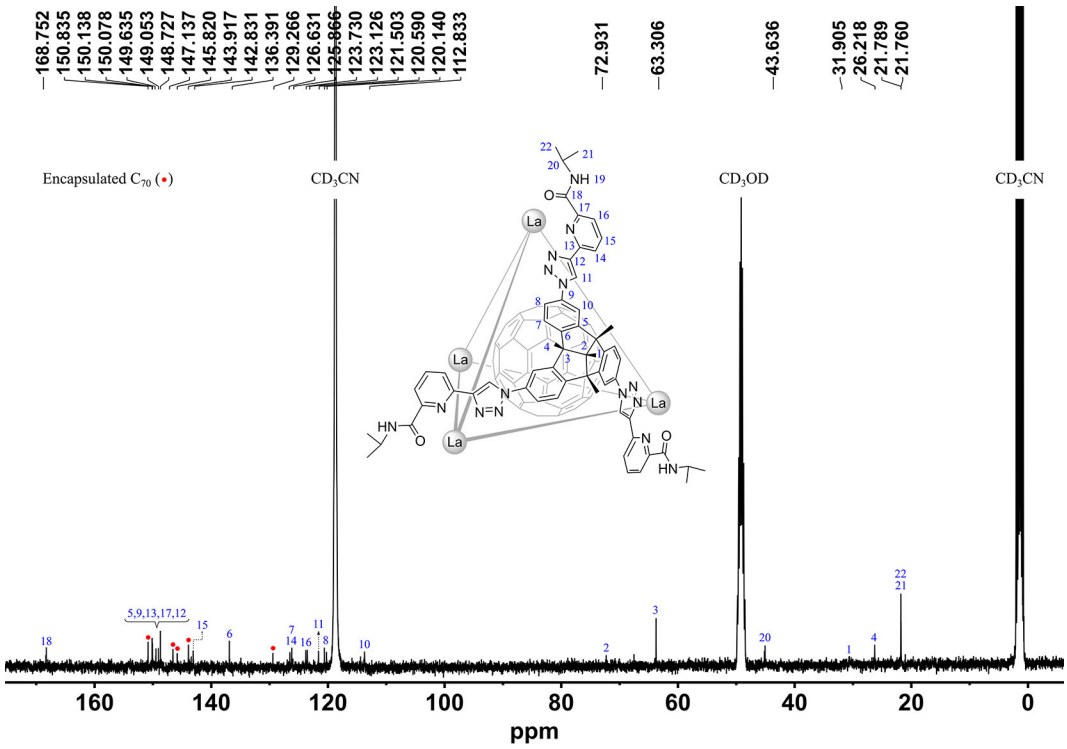

Fig. S49. ^{13}C NMR spectrum of $C_{70}\subset$*T*-**3** (400 MHz, 298 K, CD_3CN/CD_3OD v/v 4/1, [$C_{70}\subset$*T*-**3**] = 2.9 mM), where *T*-**3** is homochiral Δ_4-P_4. (●: encapsulated C_{70})

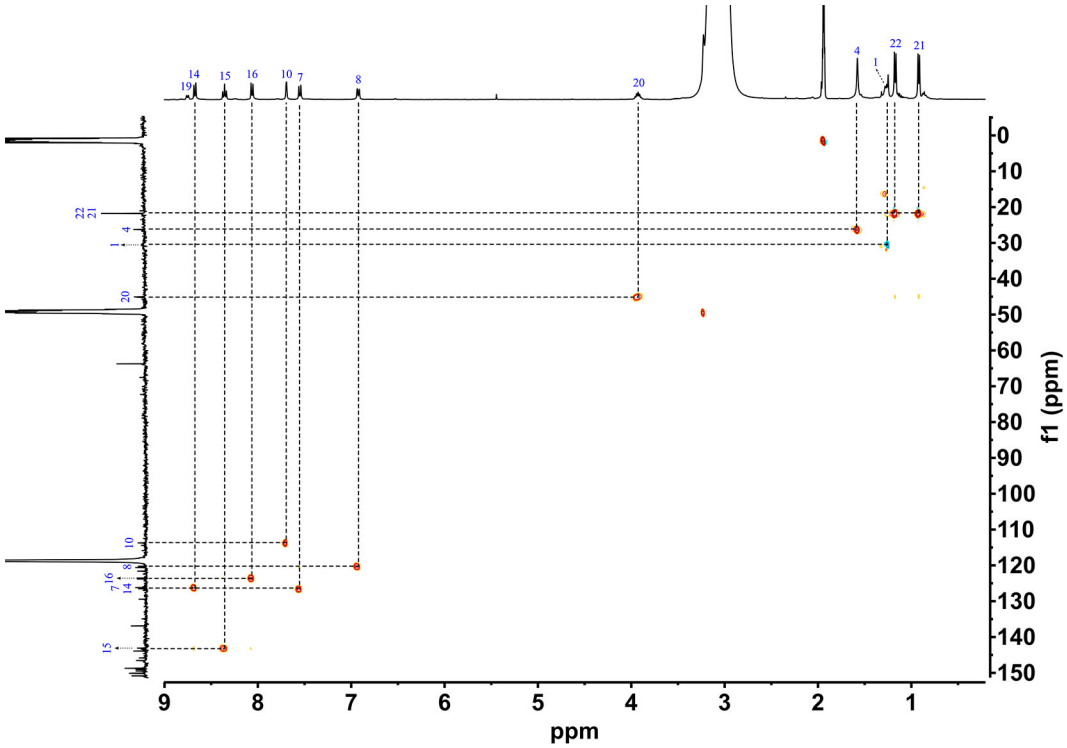

Fig. S50. Partial ^{1}H-^{13}C HSQC spectrum of $C_{70}\subset$*T*-**3** (400 MHz, 298 K, CD_3CN/CD_3OD v/v 4/1, [$C_{70}\subset$*T*-**3**] = 2.9 mM), where *T*-**3** is homochiral Δ_4-P_4.

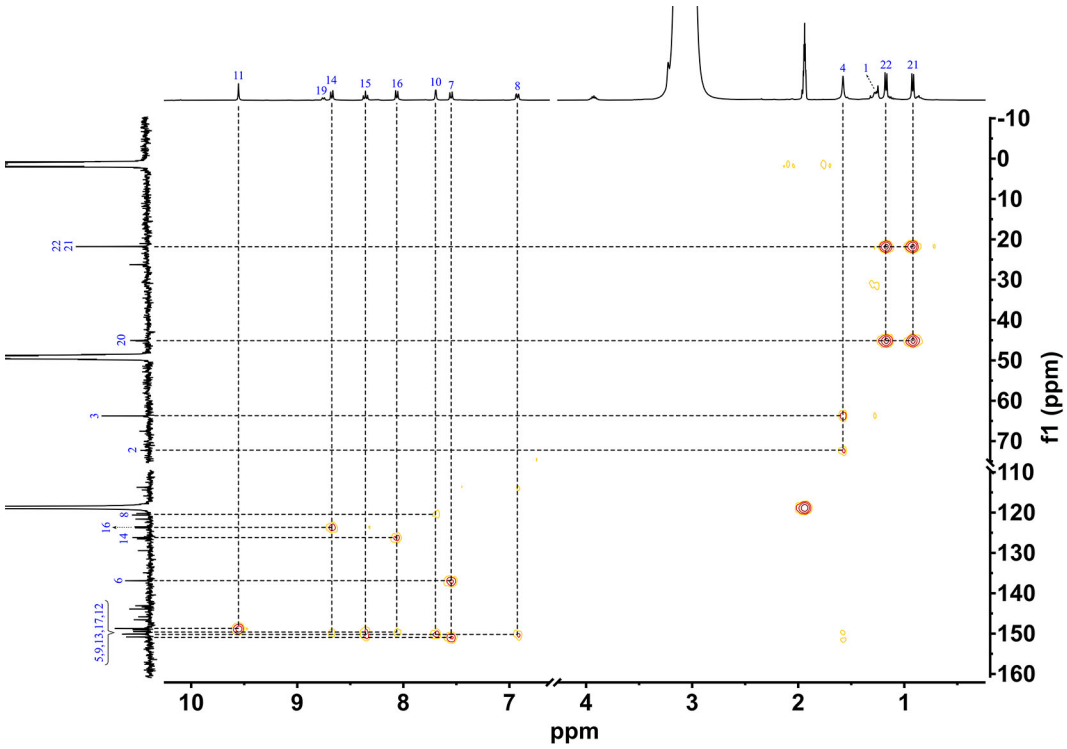

Fig. S51. Partial ^{1}H-^{13}C HMBC spectrum of $C_{70}\subset$*T*-**3** (400 MHz, 298 K, CD_3CN/CD_3OD v/v 4/1, [$C_{70}\subset$*T*-**3**] = 2.9 mM), where *T*-**3** is homochiral Δ_4-P_4.

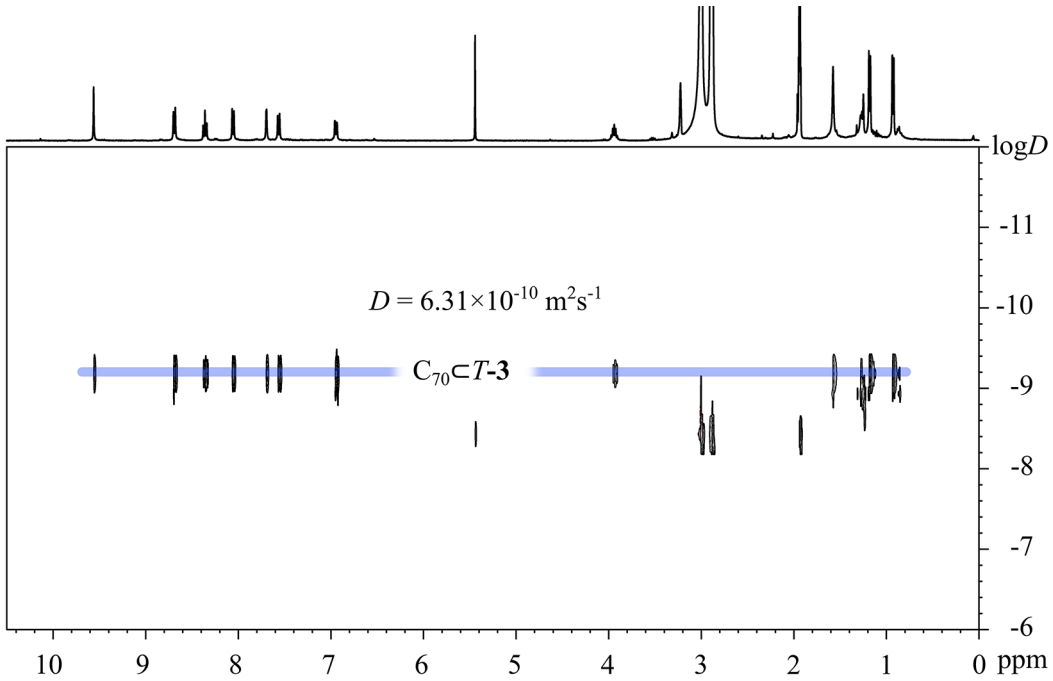

Fig. S52. ^{1}H DOSY spectrum of $C_{70}\subset$*T*-**3** (400 MHz, 298 K, CD_3CN/CD_3OD v/v 4/1, [$C_{70}\subset$*T*-**3**] = 2.9 mM), where *T*-**3** is homochiral Δ_4-P_4. The hydrodynamic diameter of $C_{70}\subset$*T*-**3** was determined to be 2.0 nm.

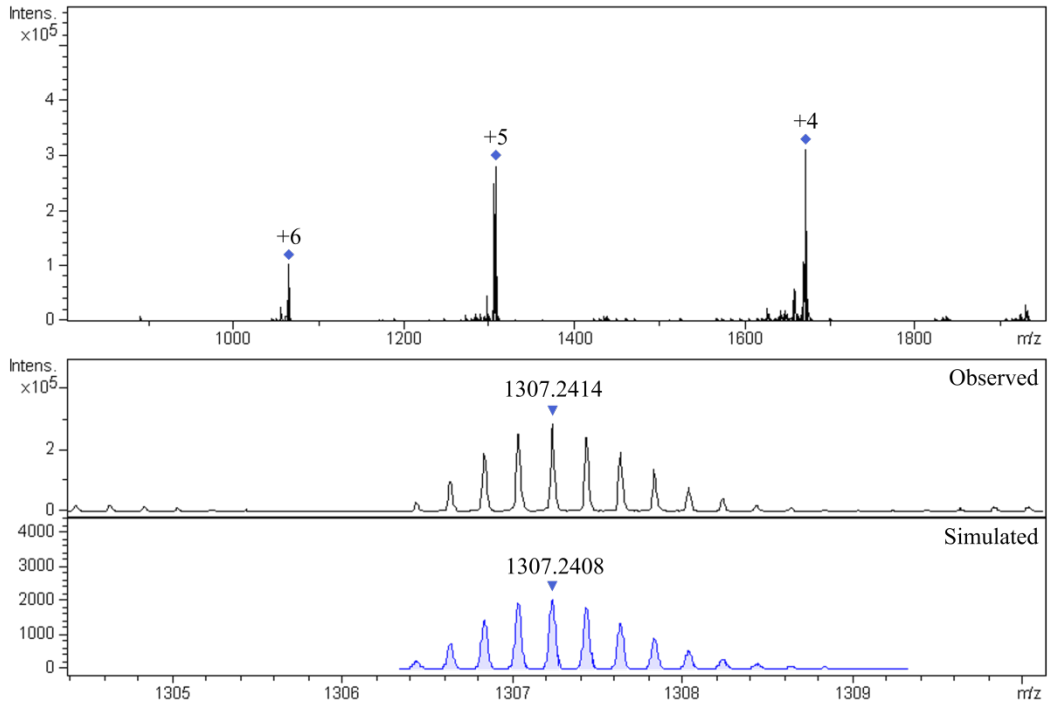

Fig. S53. High-resolution ESI-TOF-MS of C_{70}⊂*T*-**3** with the comparison of observed and simulated isotopic patterns of the peaks +5.

3.3.3 Encapsulation of D_2-C_{76} with *T*-**3**

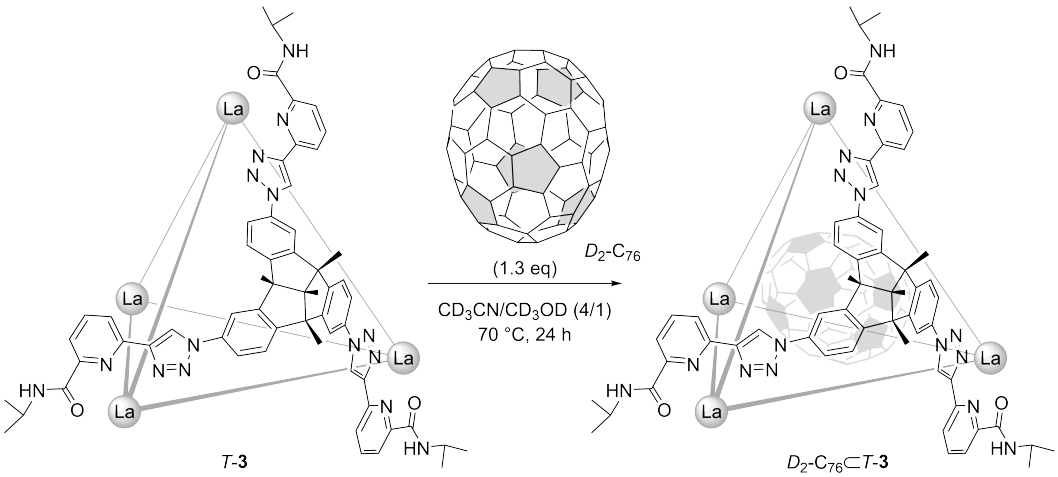

In situ self-assembly of D_2-C_{76}⊂*T*-**3**: La(OTf)$_3$ (1.3 mg, 2.2 μmol), *P*-**1** (2.3 mg, 2.2 μmol) and D_2-C_{76} (0.6 mg, 0.7 μmol) were mixed in a solution of CD_3CN/CD_3OD (v/v 4/1, 500 μL). After stirring at 70 °C for 24 h, the insoluble excess D_2-C_{76} was removed by centrifugation. The resulting solution was further characterized by NMR spectroscopy and high-resolution ESI-TOF-MS. ^{1}H NMR spectrum showed the quantitative formation of D_2-C_{76}⊂*T*-**3** (Δ_4-P_4). The solvents were dried *in vacuo* to obtain a light grey powder. Yield ca. 4.0 mg, 98%.

^{1}H NMR (400 MHz, 298 K, CD_3CN/CD_3OD v/v 4/1): δ = 9.55 (s, 12H, $H_{11/11}$), 9.54 (s, 12H, H_{11} and H_{11}), 8.67 (d, J = 7.9 Hz, 24H, H_{14} and H_{14}), 8.40 (t, J = 8.0 Hz, 24H, H_{15} and H_{15}), 8.05 (d, J = 7.9 Hz, 24H, H_{16} and H_{16}), 7.69 (s, 24H, H_{10} and H_{10}), 7.53 (m, 24H, H_7 and H_7), 6.87 (m, 24H, H_8 and H_8), 3.90 (m, 24H, H_{20} and H_{20}), 1.59 (s, 72H, H_4 and H_4), 1.30 (s, 24H, H_1 and H_1), 1.16 (d, J = 6.7 Hz, 72H, H_{22} and H_{22}), 0.90 (d, J = 6.6 Hz, 72H, H_{21} and H_{21}). The ^{13}C NMR signals were too weak to be measured. High-resolution ESI-TOF-MS for D_2-C_{76}⊂T-**3**. The following picked signals are those at the highest intensities. m/z Calcd for [D_2-C_{76}⊂T-**3** – 8(OTf)]$^{8+}$ 770.1684, found 770.1659; [D_2-C_{76}⊂T-**3** – 7(OTf)]$^{7+}$ 901.4713, found 901.4688; Calcd for [D_2-C_{76}⊂T-**3** – 6(OTf)]$^{6+}$ 1076.5419, found 1076.5390; Calcd for [D_2-C_{76}⊂T-**3** – 5(OTf)]$^{5+}$ 1321.6408, found 1321.6376; Calcd for [D_2-C_{76}⊂T-**3** – 4(OTf)]$^{4+}$ 1689.2891, found 1689.2840.

Encapsulation of D_2-C_{76} with preformed cage T-**3** (Δ_4-P_4): T-**3** (3.5 mg, 0.6 μmol) and D_2-C_{76} (0.6 mg, 0.7 μmol) were mixed in a solution of CD_3CN/CD_3OD (v/v 4/1, 500 μL). The mixture was stirred at 70 °C for 24 h and monitored by ^{1}H NMR.

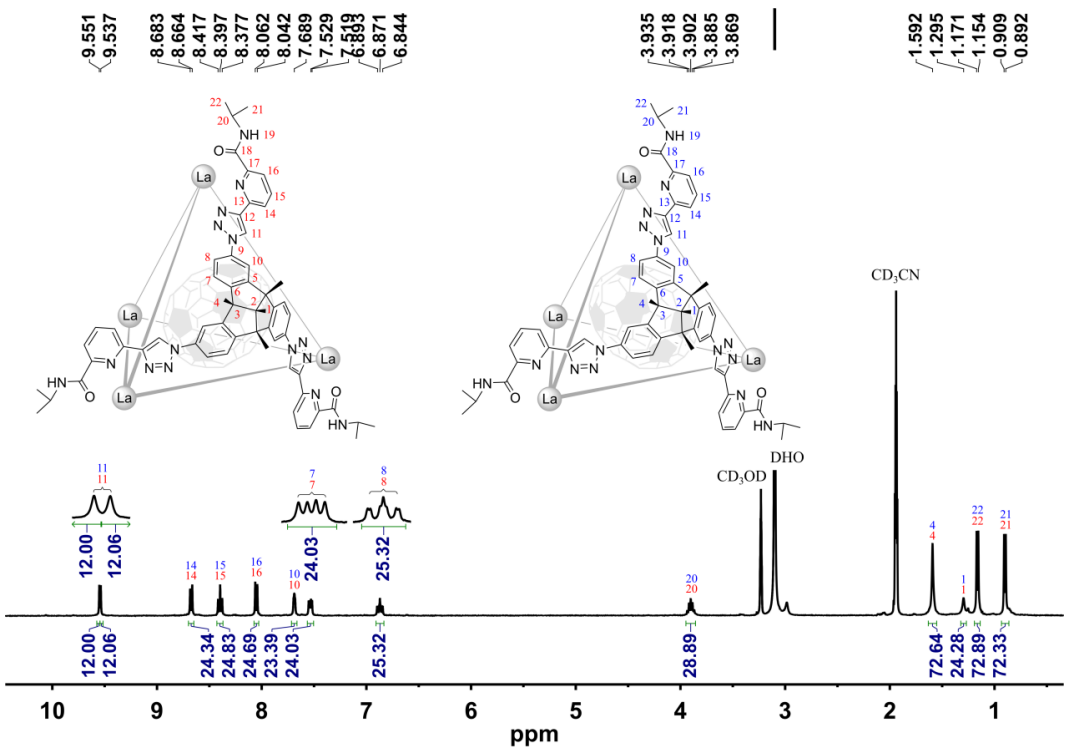

Fig. S54. ^{1}H NMR spectrum of D_2-C_{76}⊂T-**3** (400 MHz, 298 K, CD_3CN/CD_3OD v/v 4/1, [D_2-C_{76}⊂T-**3**] = 1.1 mM), where D_2-C_{76} is a pair of enantiomers and T-**3** is homochiral Δ_4-P_4.

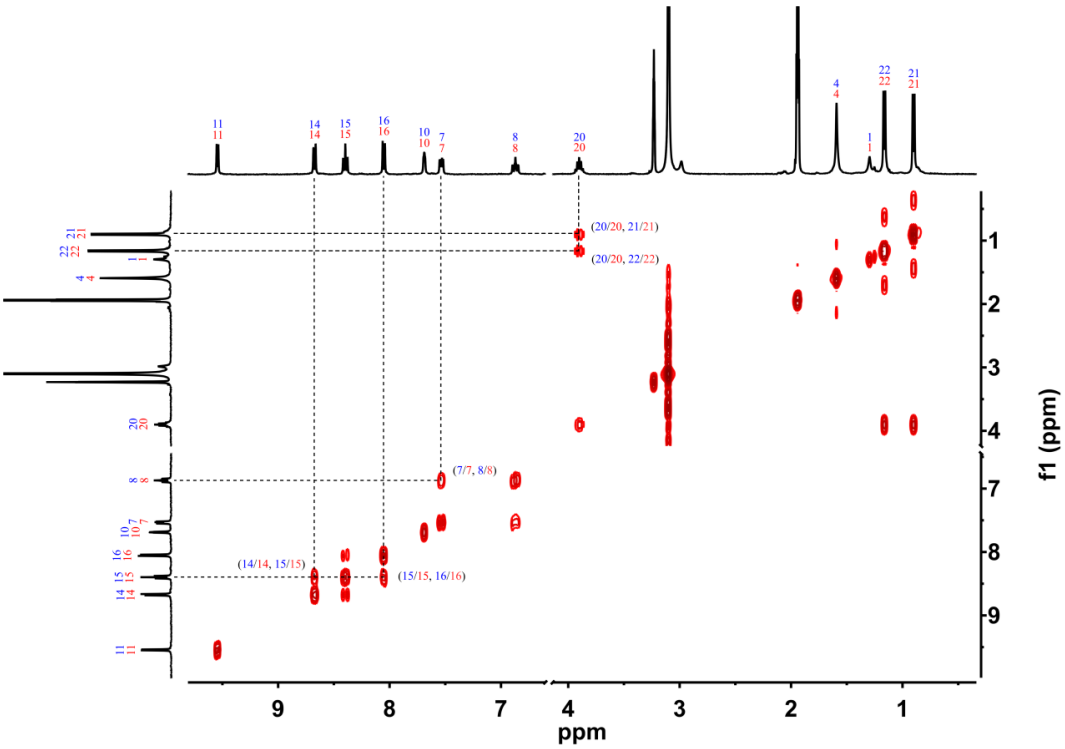

Fig. S55. Partial ^{1}H-^{1}H COSY spectrum of D_2-C_{76}⊂*T*-**3** (400 MHz, 298 K, CD_3CN/CD_3OD v/v 4/1, [D_2-C_{76}⊂*T*-**3**] = 1.1 mM), where D_2-C_{76} is a pair of enantiomers and *T*-**3** is homochiral Δ_4-P_4.

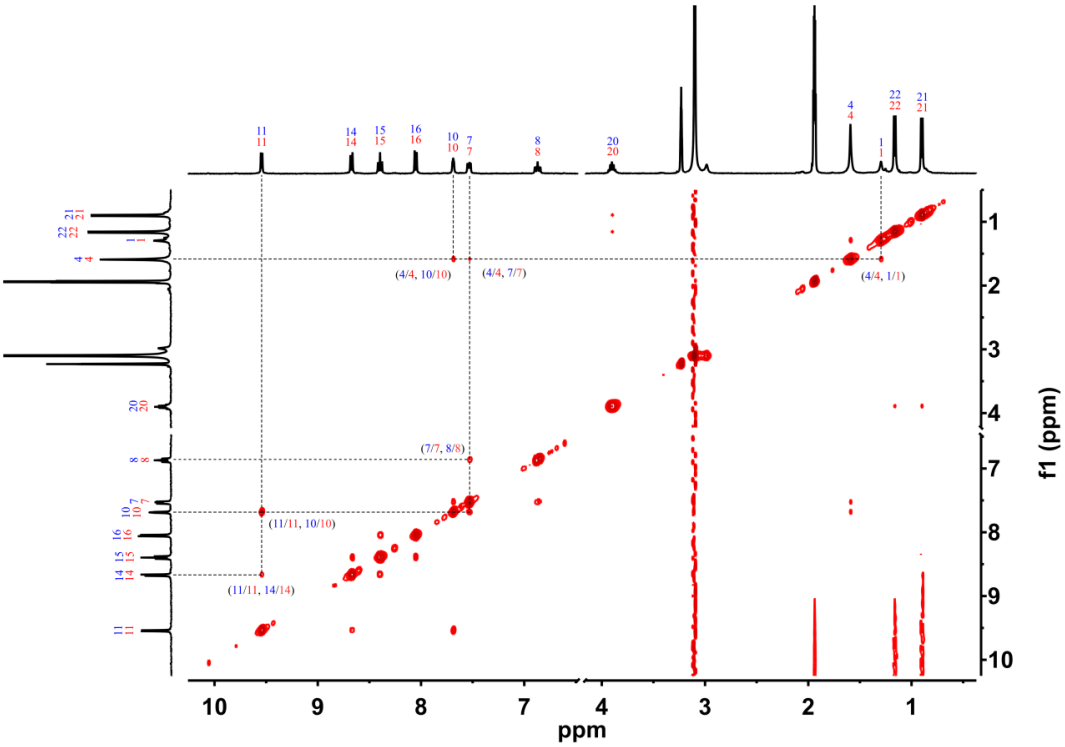

Fig. S56. Partial ^{1}H-^{1}H NOESY spectrum of D_2-C_{76}⊂*T*-**3** (400 MHz, 298 K, CD_3CN/CD_3OD v/v 4/1, [D_2-C_{76}⊂*T*-**3**] = 1.1 mM), where D_2-C_{76} is a pair of enantiomers and *T*-**3** is homochiral Δ_4-P_4.

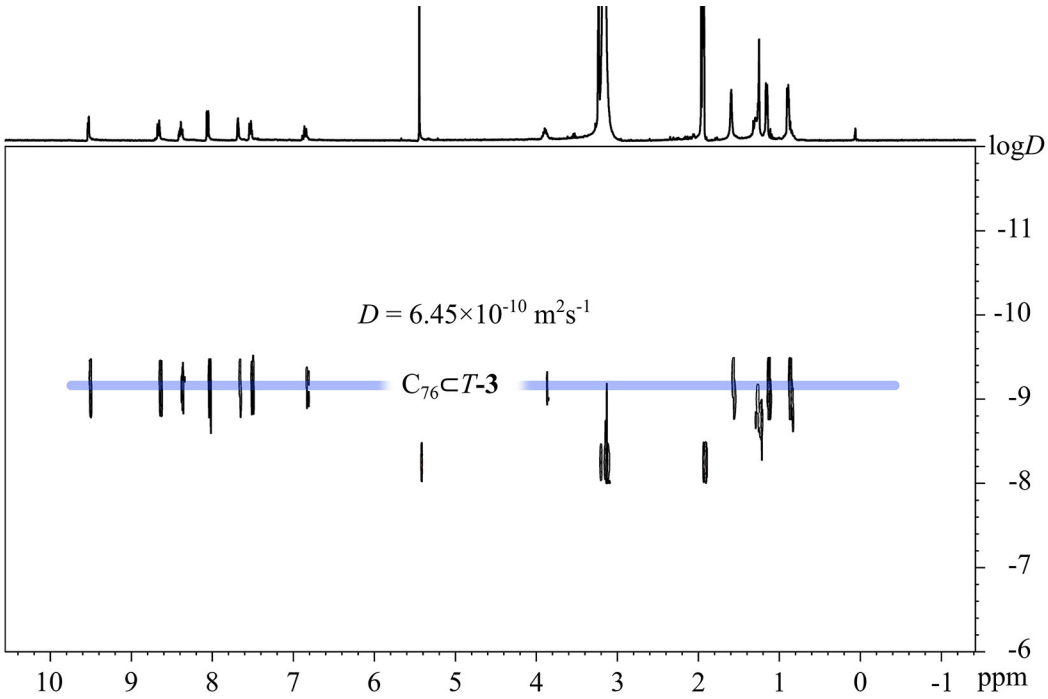

Fig. S57. ^{1}H DOSY spectrum of D_2-C_{76}⊂*T*-**3** (400 MHz, 298 K, CD_3CN/CD_3OD v/v 4/1, [D_2-C_{76}⊂*T*-**3**] = 1.1 mM), where D_2-C_{76} is a pair of enantiomers and *T*-**3** is homochiral Δ_4-P_4. The hydrodynamic diameter of D_2-C_{76}⊂*T*-**3** was determined to be 2.0 nm.

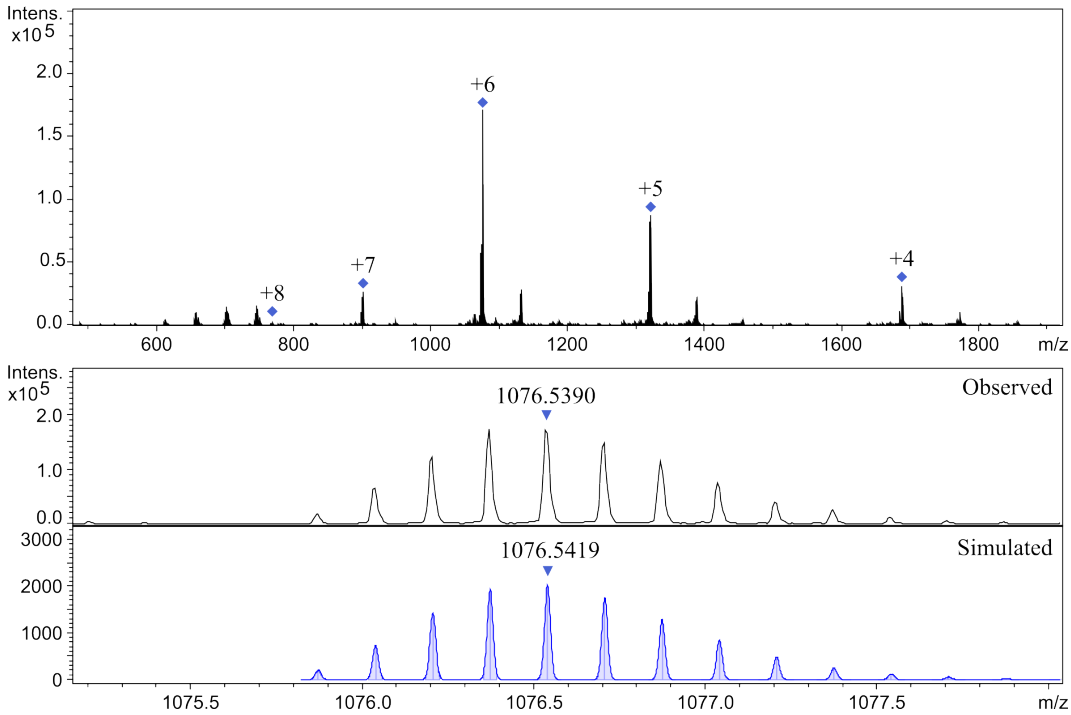

Fig. S58. High-resolution ESI-TOF-MS of D_2-C_{76}⊂*T*-**3** with the comparison of observed and simulated isotopic patterns of the peaks +6.

3.3.4 Encapsulation of C_{2v}-C_{78} with *T*-**3**

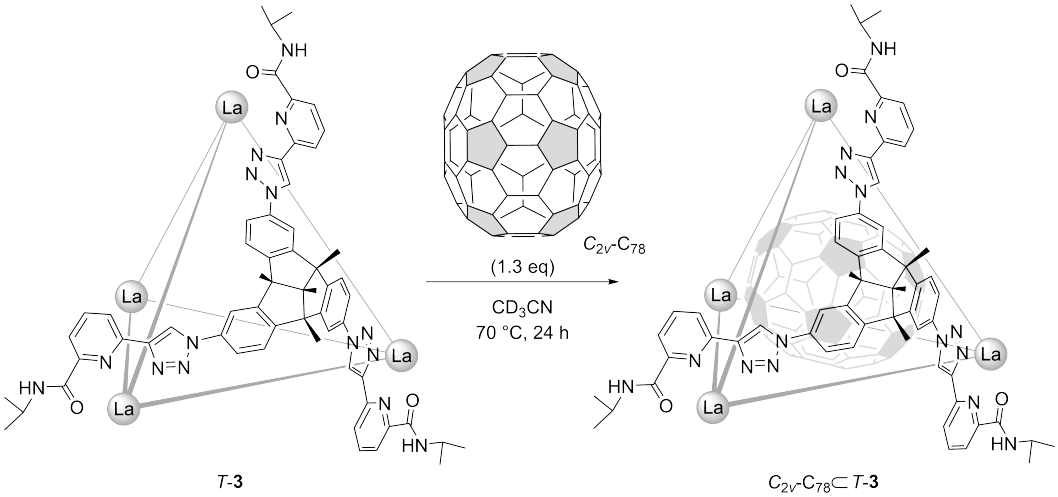

T-**3**

C_{2v}-$\mathrm{C}_{78}\subset T$-**3**

In situ self-assembly of C_{2v}-$\mathrm{C}_{78}\subset T$-**3**: $\mathrm{La(OTf)_3}$ (1.3 mg, 2.2 µmol), *P*-**1** (2.3 mg, 2.2 µmol) and C_{2v}-C_{78} (0.7 mg, 0.7 µmol) were mixed in a solution of $\mathrm{CD_3CN}$ (500 µL). After stirring at 70 °C overnight, the insoluble excess C_{2v}-C_{78} was removed by centrifugation. The resulting solution was further characterized by NMR spectroscopy and high-resolution ESI-TOF-MS. ^{1}H NMR spectrum showed the quantitative formation of C_{2v}-$\mathrm{C}_{78}\subset T$-**3** (Δ_4-P_4). The solvents were dried *in vacuo* to obtain a light grey powder. Yield ca. 3.9 mg, 97%.

^{1}H NMR (400 MHz, 298 K, $\mathrm{CD_3CN}$): δ = 9.56 (s, 12H, H_{11}), 8.77 (d, J = 8.0 Hz, 12H, H_{14}), 8.37-8.41 (m, 24H, H_{19} and H_{15}), 8.05 (d, J = 7.9 Hz, 12H, H_{16}), 7.71 (s, 11H, H_{10}), 7.67 (d, J = 8.6 Hz, 12H, H_7), 7.07 (d, J = 8.6 Hz, 12H, H_8), 3.97-4.00 (m, 12H, H_{20}), 1.57 (s, 36H, H_4), 1.30 (s, 12H, H_1), 1.21 (d, J = 6.5 Hz, 36H, H_{22}), 0.96 (d, J = 7.3 Hz, 36H, H_{21}). The ^{13}C NMR signals were too weak to be measured. High-resolution ESI-TOF-MS for C_{2v}-$\mathrm{C}_{78}\subset T$-**3**. The following picked signals are those at the highest intensities. m/z Calcd for $[C_{2v}\text{-}\mathrm{C}_{78}\subset T\text{-}\mathbf{3} - 7(\mathrm{OTf})]^{7+}$ 904.8999, found 904.8993; $[C_{2v}\text{-}\mathrm{C}_{78}\subset T\text{-}\mathbf{3} - 6(\mathrm{OTf})]^{6+}$ 1080.5419, found 1080.5413; Calcd for $[C_{2v}\text{-}\mathrm{C}_{78}\subset T\text{-}\mathbf{3} - 5(\mathrm{OTf})]^{5+}$ 1326.4408, found 1326.4399; Calcd for $[C_{2v}\text{-}\mathrm{C}_{78}\subset T\text{-}\mathbf{3} - 4(\mathrm{OTf})]^{4+}$ 1695.2891, found 1695.2870.

Encapsulation of C_{2v}-C_{78} with preformed cage *T*-**3** (Δ_4-P_4): *T*-**3** (3.5 mg, 0.6 µmol) and C_{2v}-C_{78} (0.7 mg, 0.7 µmol) were mixed in a solution of $\mathrm{CD_3CN}$ (500 µL). The mixture was stirred at 70 °C for 24 h and monitored by ^{1}H NMR.

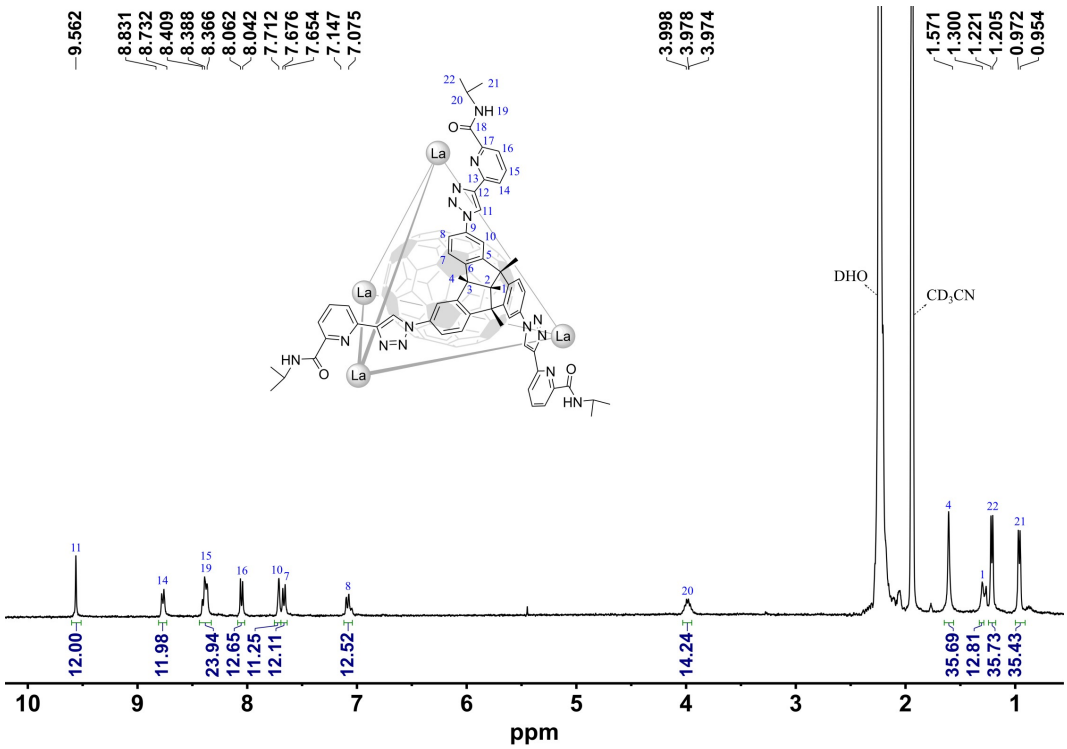

Fig. S59. ^{1}H NMR spectrum of C_{2v}-C_{78}⊂*T*-**3** (400 MHz, 298 K, CD_3CN, [C_{2v}-C_{78}⊂*T*-**3**] = 1.1 mM), where *T*-**3** is homochiral Δ_4-P_4.

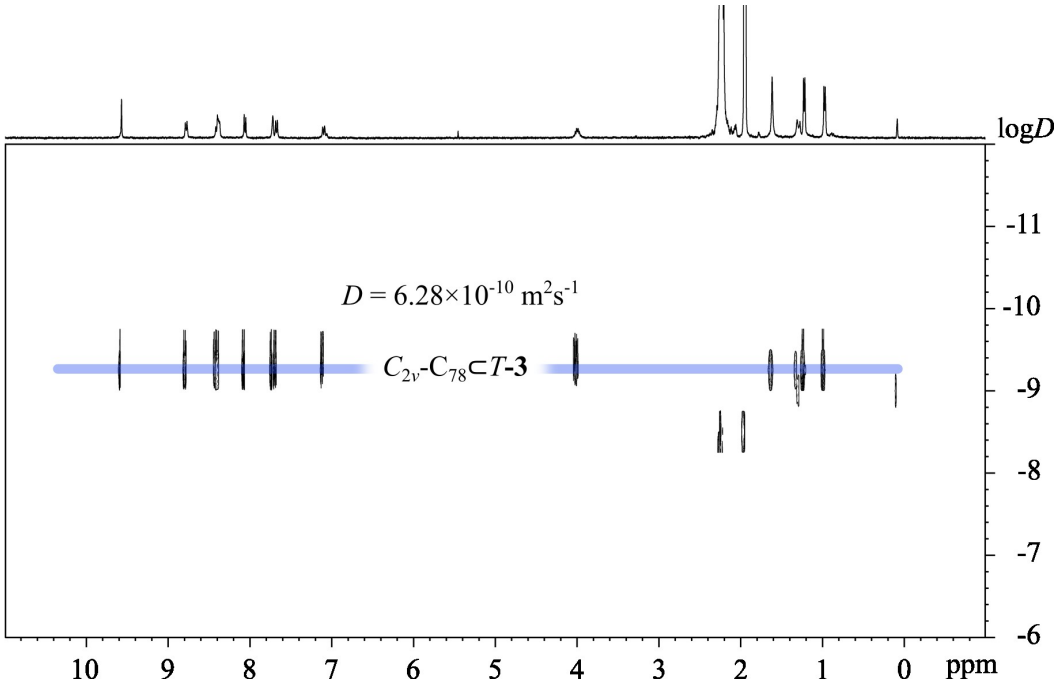

Fig. S60. ^{1}H DOSY spectrum of C_{2v}-C_{78}⊂*T*-**3** (400 MHz, 298 K, CD_3CN, [C_{2v}-C_{78}⊂*T*-**3**] = 1.1 mM), where *T*-**3** is homochiral Δ_4-P_4. The hydrodynamic diameter of C_{2v}-C_{78}⊂*T*-**3** was determined to be 2.1 nm.

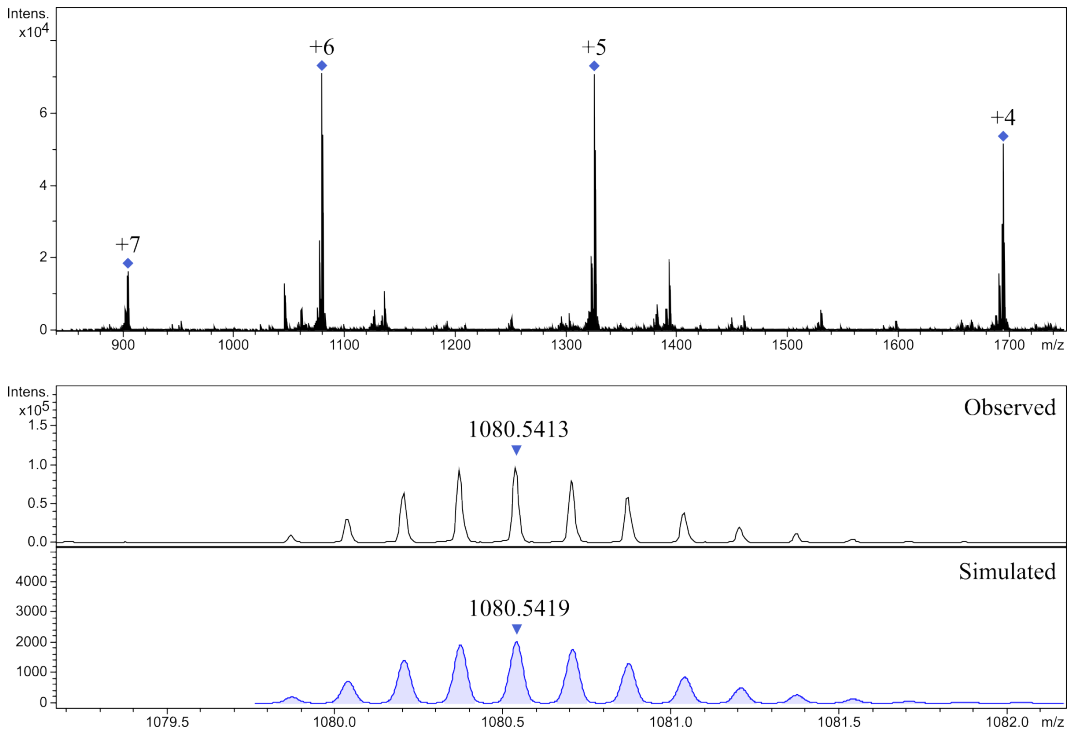

Fig. S61. High-resolution ESI-TOF-MS of C_{2v}-C_{78}⊂*T*-**3** with the comparison of observed and simulated isotopic patterns of the peaks +6.

3.3.5 Encapsulation of C_{2v}'-C_{78} with *T*-**3**

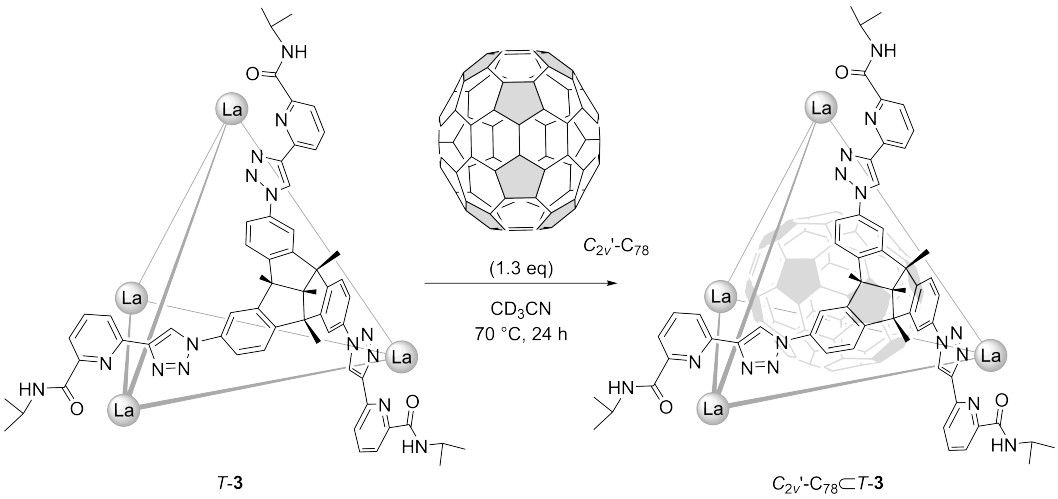

In situ self-assembly of C_{2v}'-C_{78}⊂*T*-**3**: $La(OTf)_3$ (1.3 mg, 2.2 μmol), *P*-**1** (2.3 mg, 2.2 μmol) and C_{2v}'-C_{78} (0.7 mg, 0.7 μmol) were mixed in a solution of CD_3CN (500 μL). After stirring at 70 °C for 24 h, the insoluble excess C_{2v}'-C_{78} was removed by centrifugation. The resulting solution was further characterized by NMR spectroscopy and high-resolution ESI-TOF-MS. ^{1}H NMR spectrum showed the quantitative formation of C_{2v}'-C_{78}⊂*T*-**3** (Δ_4-P_4). The solvents were dried *in vacuo* to obtain a light grey powder. Yield ca. 4.0 mg, 98%.

^{1}H NMR (400 MHz, 298 K, CD_3CN): δ = 9.55 (s, 12H, H_{11}), 8.75 (d, J = 7.9 Hz, 12H, H_{14}), 8.41 – 8.36 (m, 16H, H_{19} and H_{15}), 8.04 (d, J = 7.9 Hz, 12H, H_{16}), 7.71 (s, 12H, H_{10}), 7.65 (d, J = 8.6 Hz, 12H, H_7), 7.06 (d, J = 9.3 Hz, 12H, H_8), 4.01 – 3.93 (m, 12H, H_{20}), 1.57 (s, 36H, H_4), 1.30 (s, 12H, H_1), 1.20 (d, J = 7.3 Hz, 36H, H_{22}), 0.97 (d, J = 19.3 Hz, 36H, H_{21}). The ^{13}C NMR signals were too weak to be measured. High-resolution ESI-TOF-MS for C_{2v}'-C_{78}⊂*T*-**3**. The following picked signals are those at the highest intensities. m/z Calcd for [C_{2v}'-C_{78}⊂*T*-**3**-7(OTf)]$^{7+}$ 904.8999, found 904.8992; [C_{2v}'-C_{78}⊂*T*-**3**-6(OTf)]$^{6+}$ 1080.5419, found 1080.5409; Calcd for [C_{2v}'-C_{78}⊂*T*-**3**-5(OTf)]$^{5+}$ 1326.4408, found 1326.4393; Calcd for [C_{2v}'-C_{78}⊂*T*-**3**-4(OTf)]$^{4+}$ 1695.2891, found 1695.2876.

Encapsulation of C_{2v}'-C_{78} with preformed cage *T*-**3** (Δ_4-P_4): *T*-**3** (3.5 mg, 0.6 μmol) and C_{2v}'-C_{78} (0.7 mg, 0.7 μmol) were mixed in a solution of CD_3CN (500 μL). The mixture was stirred at 70 °C for 24 h and monitored by ^{1}H NMR.

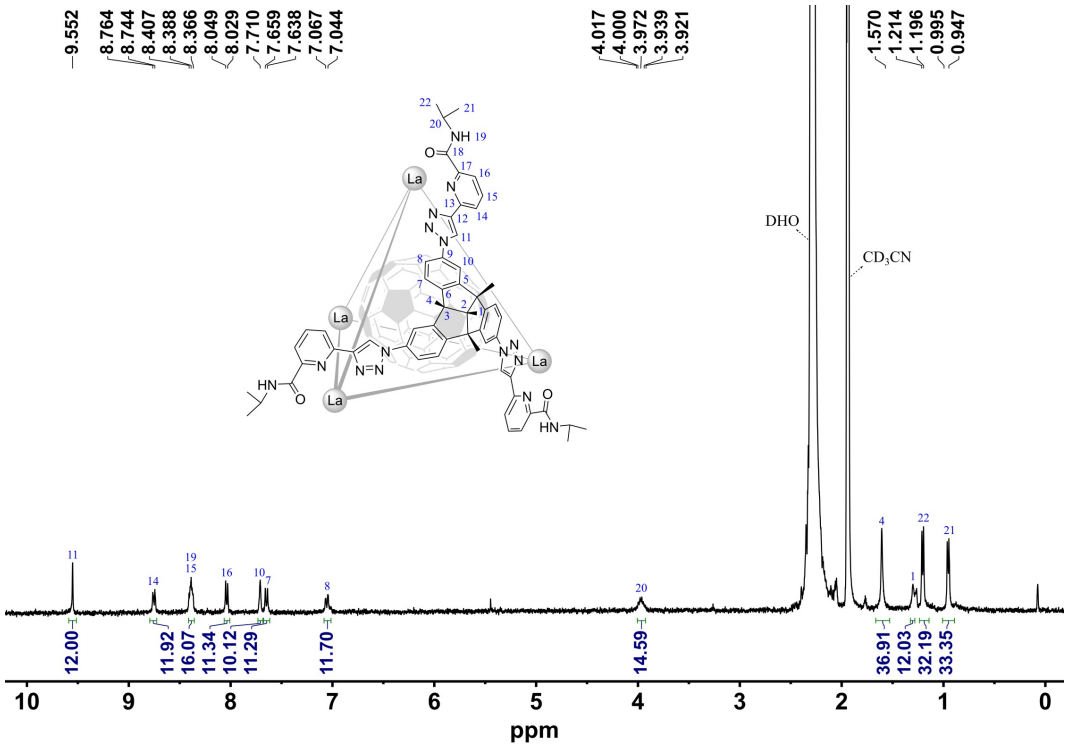

Fig. S62. ^{1}H NMR spectrum of C_{2v}'-C_{78}⊂*T*-**3** (400 MHz, 298 K, CD_3CN, [C_{2v}'-C_{78}⊂*T*-**3**] = 1.1 mM), where *T*-**3** is homochiral Δ_4-P_4.

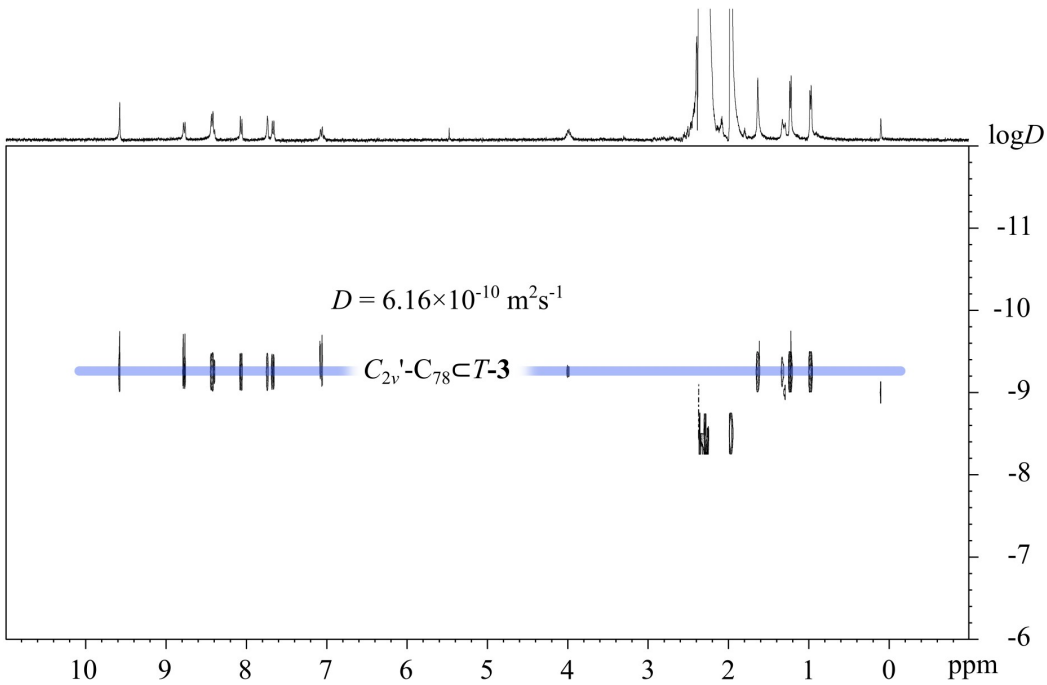

Fig. S63. ^{1}H DOSY spectrum of C_{2v}'-C_{78}⊂*T*-**3** (400 MHz, 298 K, CD_3CN, [C_{2v}'-C_{78}⊂*T*-**3**] = 1.1 mM), where *T*-**3** is homochiral Δ_4-P_4. The hydrodynamic diameter of C_{2v}'-C_{78}⊂*T*-**3** was determined to be 2.1 nm.

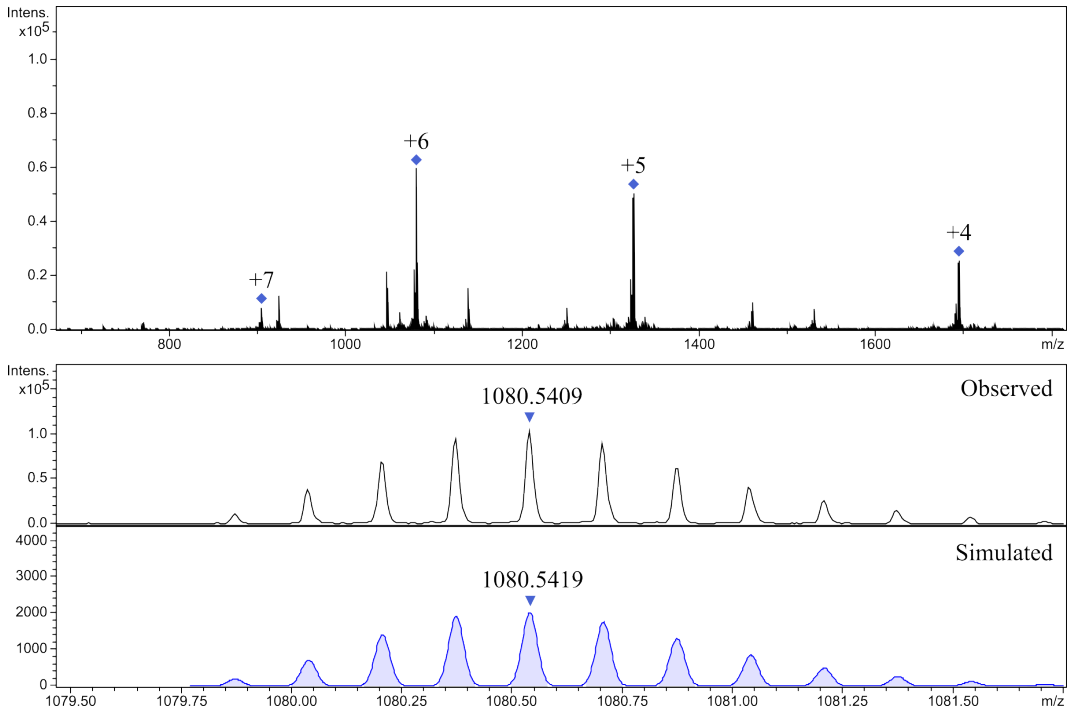

Fig. S64. High-resolution ESI-TOF-MS of C_{2v}'-C_{78}⊂*T*-**3** with the comparison of observed and simulated isotopic patterns of the peaks +6.

3.3.6 Encapsulation of C_{60} with S_4-**4**

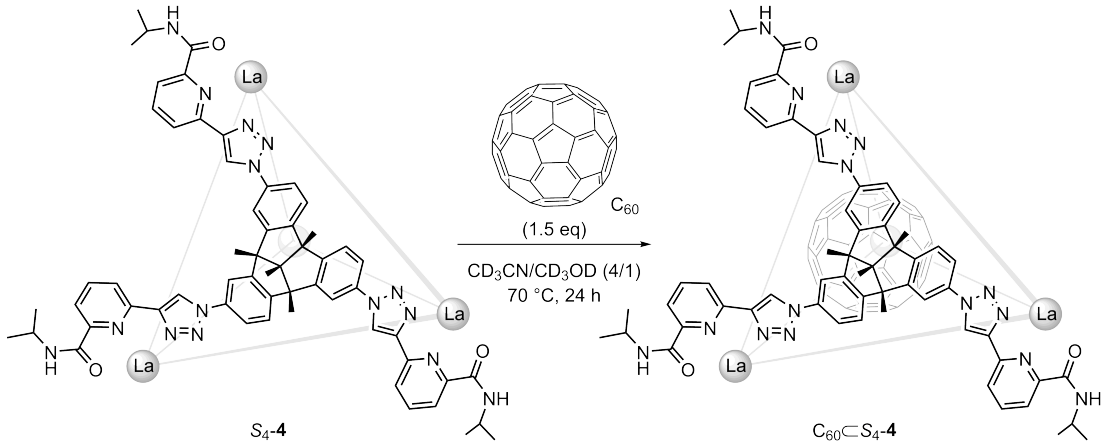

In situ self-assembly of $C_{60}\subset S_4$-**4**: La(OTf)$_3$ (6.9 mg, 11.7 μmol), C_1-**2** (12 mg, 11.7 μmol) and C_{60} (3.2 mg, 4.4 μmol) were mixed in a solution of CD_3CN/CD_3OD (v/v 4/1, 500 μL). After stirring at 70 °C for 24 h, the insoluble excess C_{60} was removed by centrifugation. The resulting solution was further characterized by NMR spectroscopy and high-resolution ESI-TOF-MS. ^{1}H NMR spectrum showed the quantitative formation of $C_{60}\subset S_4$-**4**. The solvents were dried *in vacuo* to obtain a light purple powder. Yield ca. 20.5 mg, 98%.

^{1}H NMR (400 MHz, 298 K, CD_3CN/CD_3OD v/v 4/1): δ = 9.45 (s, 4H, H_{51}), 9.36 (s, 4H, H_{15}), 9.29 (s, 4H, H_{33}), 8.92 (d, J = 8.0 Hz, 4H, H_{54}), 8.85 (d, J = 8.0 Hz, 4H, H_{36}), 8.65 (d, J = 7.9 Hz, 4H, H_{18}), 8.46 (m, 8H, H_{55} and H_{37}), 8.32 (t, J = 8.0 Hz, 4H, H_{19}), 8.09 (d, J = 8.0 Hz, 8H, H_{38} and H_{56}), 8.06 – 7.95 (m, 8H, H_{49} and H_{20}), 7.89 (s, 4H, H_{31}), 7.63 – 7.54 (m, 8H, H_{13} and H_{46}), 7.18 (m, 8H, H_{10} and H_{28}), 6.88 (d, J = 9.8 Hz, 4H, H_{47}), 6.43 (d, J = 8.4 Hz, 4H, H_{11}), 6.12 (d, J = 8.4 Hz, 4H, H_{29}), 3.90 – 3.77 (m, 12H, H_{24}, H_{42} and H_{60}), 1.67 – 1.49 (m, 36H, H_8, H_6 and H_7), 1.27 (s, 12H, H_1), 1.13 (m, 36H, H_{25}, H_{43} and H_{61}), 0.86 (m, 36H, H_{26}, H_{44} and H_{62}). ^{13}C NMR (101 MHz, 298 K, CD_3CN/CD_3OD v/v 4/1): δ = 167.8, 151.7, 151.2, 150.4, 149.9, 149.1, 148.5, 143.0, 141.6 (encapsulated C_{60}), 137.0, 136.5, 126.2, 123.7, 123.3, 123.2, 122.0, 121.5, 120.5, 114.8, 114.0, 113.7, 72.1, 65.2, 63.6, 62.5, 45.0, 27.5, 26.9, 23.9, 21.6, 16.1. High-resolution ESI-TOF-MS for $C_{60}\subset S_4$-**4**. The following picked signals are those at the highest intensities. m/z Calcd for $[C_{60}\subset S_4\text{-}\mathbf{4} - 6(OTf)]^{6+}$ 1044.5419, found 1044.5399; Calcd for $[C_{60}\subset S_4\text{-}\mathbf{4} - 5(OTf)]^{5+}$ 1283.2407, found 1283.2388; Calcd for $[C_{60}\subset S_4\text{-}\mathbf{4} - 4(OTf)]^{4+}$ 1641.2890, found 1641.2863.

Encapsulation of C_{60} with preformed cage S_4-**4** (majority): S_4-**4** (10 mg, 1.6 μmol) and C_{60} (1.7 mg, 2.4 μmol) were mixed in a solution of CD_3CN/CD_3OD (v/v 4/1, 500 μL). The mixture was stirred at 70 °C for 24 h and monitored by ^{1}H NMR.

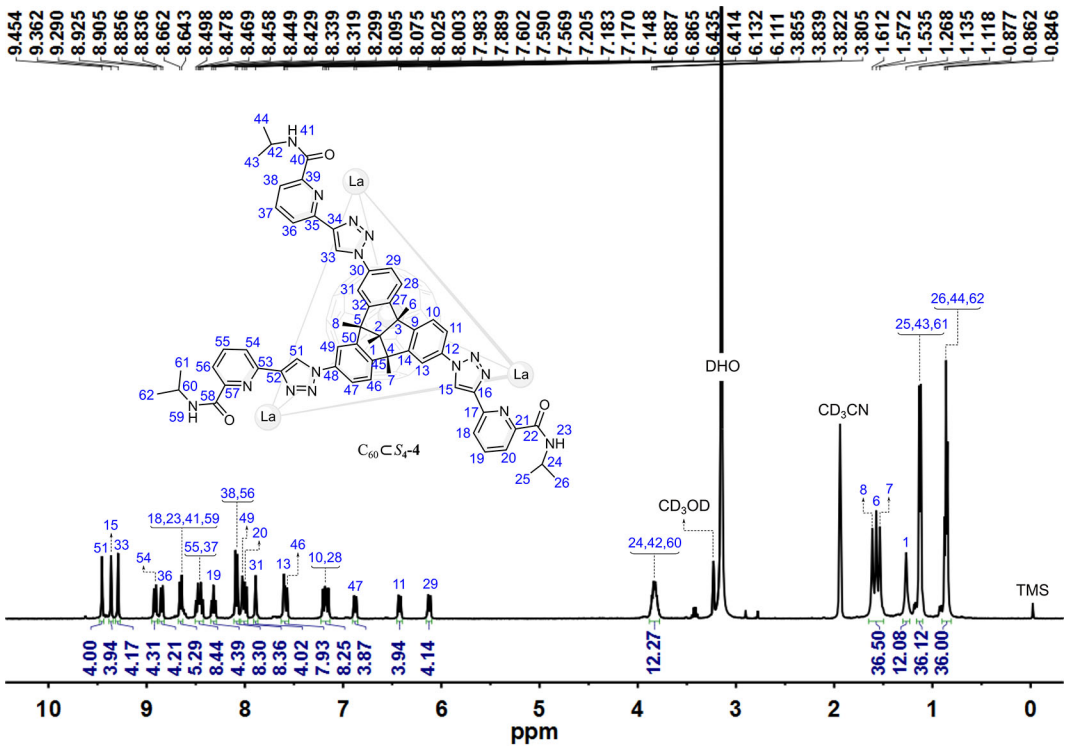

Fig. S65. ^{1}H NMR spectrum of $C_{60}\subset S_4$-**4** (400 MHz, 298 K, CD_3CN/CD_3OD v/v 4/1, [$C_{60}\subset S_4$-**4**] = 5.9 mM).

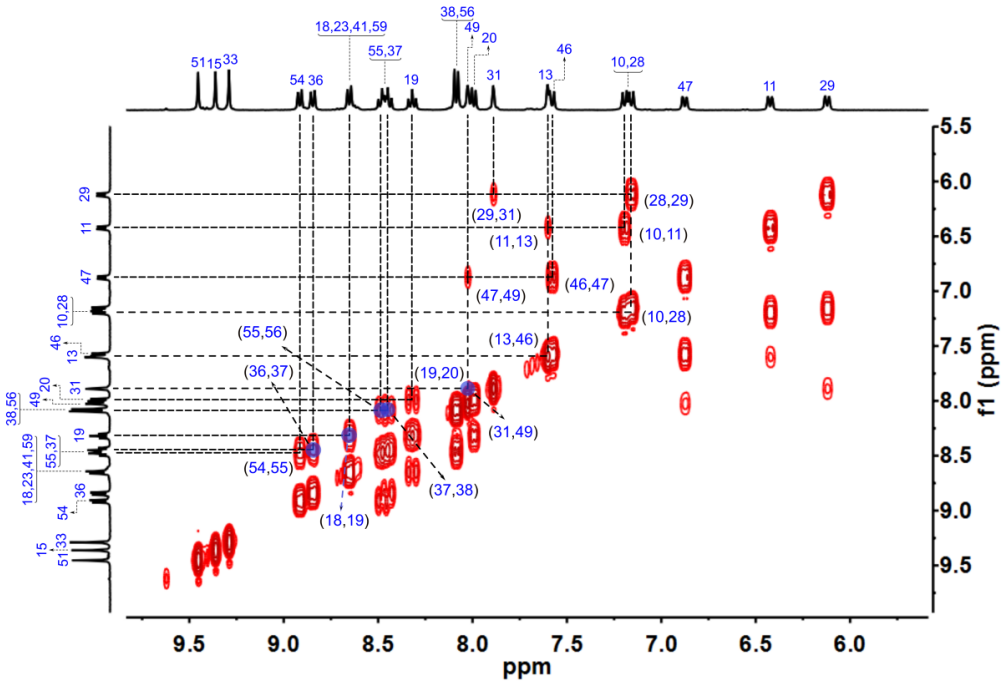

Fig. S66. ^{1}H-^{1}H COSY spectrum of $C_{60}\subset S_4$-**4** (400 MHz, 298 K, CD_3CN/CD_3OD v/v 4/1, [$C_{60}\subset S_4$-**4**] = 5.9 mM).

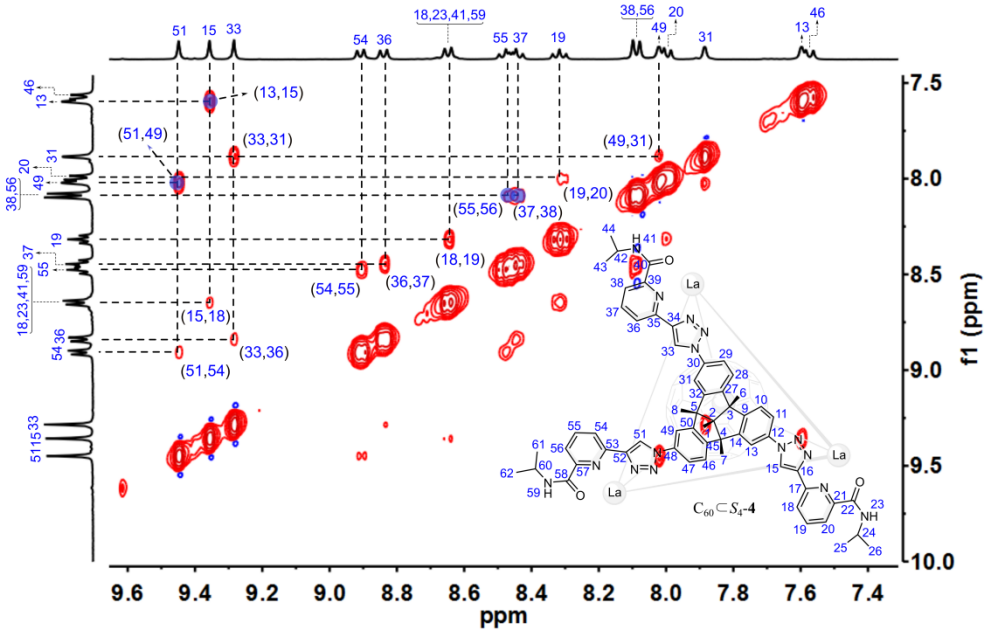

Fig. S67. Partial ^{1}H-^{1}H NOESY spectrum of $C_{60}\subset S_4$-**4** (400 MHz, 298 K, CD_3CN/CD_3OD v/v 4/1, [$C_{60}\subset S_4$-**4**] = 5.9 mM).

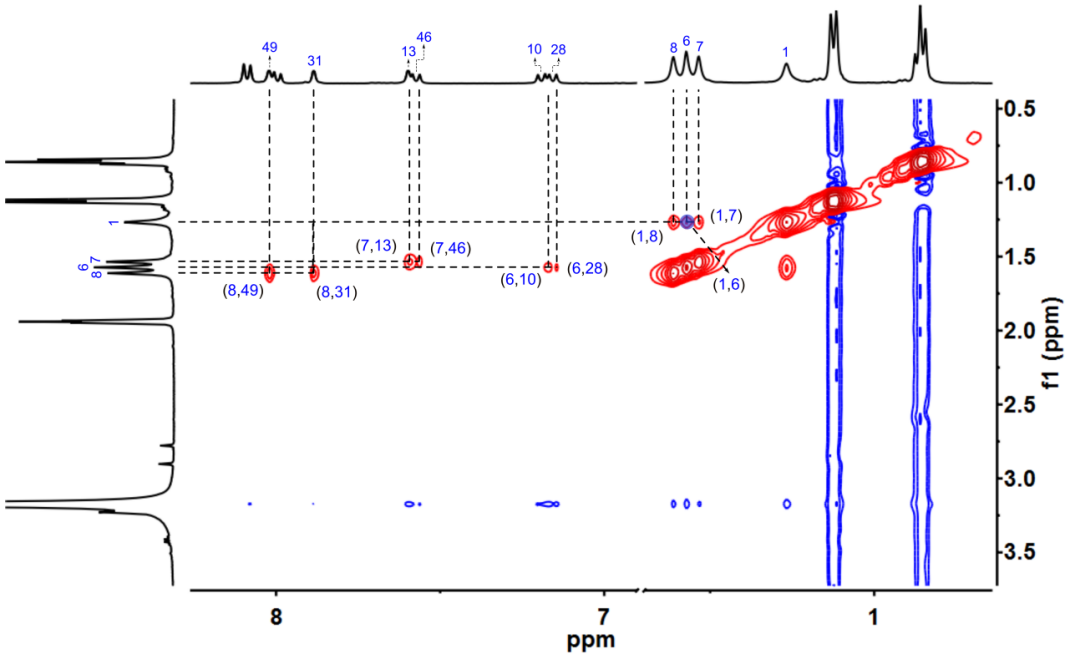

Fig. S68. Partial ^{1}H-^{1}H NOESY spectrum of $C_{60}\subset S_4$-**4** (400 MHz, 298 K, CD_3CN/CD_3OD v/v 4/1, [$C_{60}\subset S_4$-**4**] = 5.9 mM).

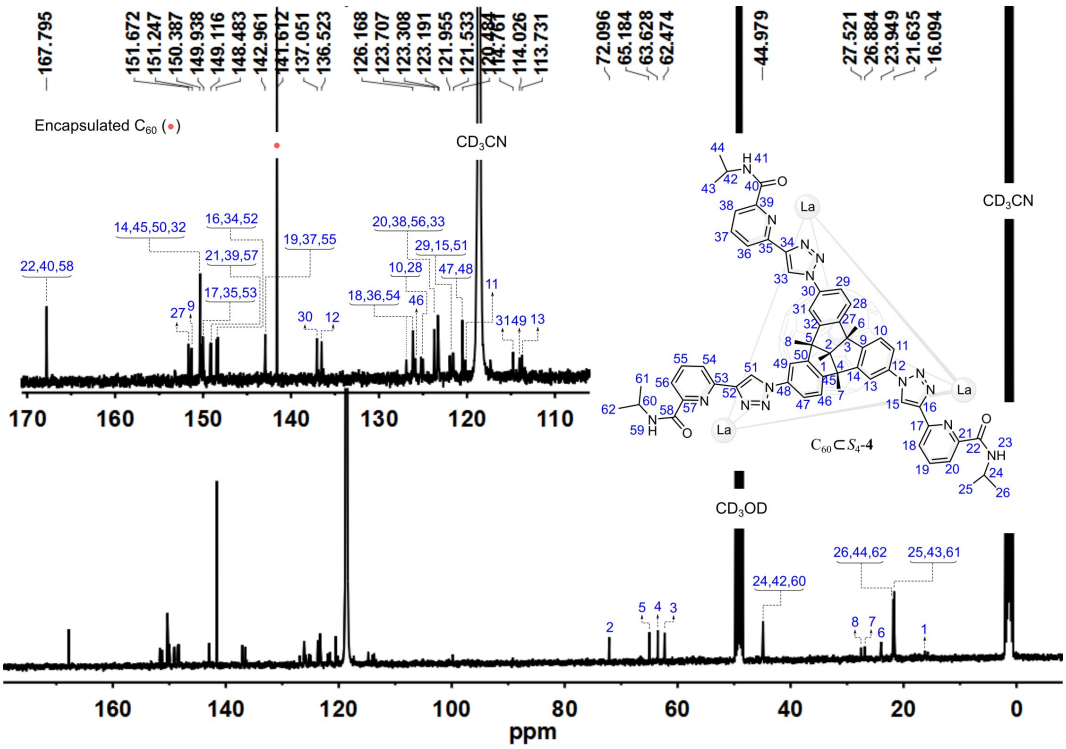

Fig. S69. ^{13}C NMR spectrum of $C_{60}\subset S_4$-**4** (400 MHz, 298 K, CD_3CN/CD_3OD v/v 4/1, [$C_{60}\subset S_4$-**4**] = 5.9 mM).

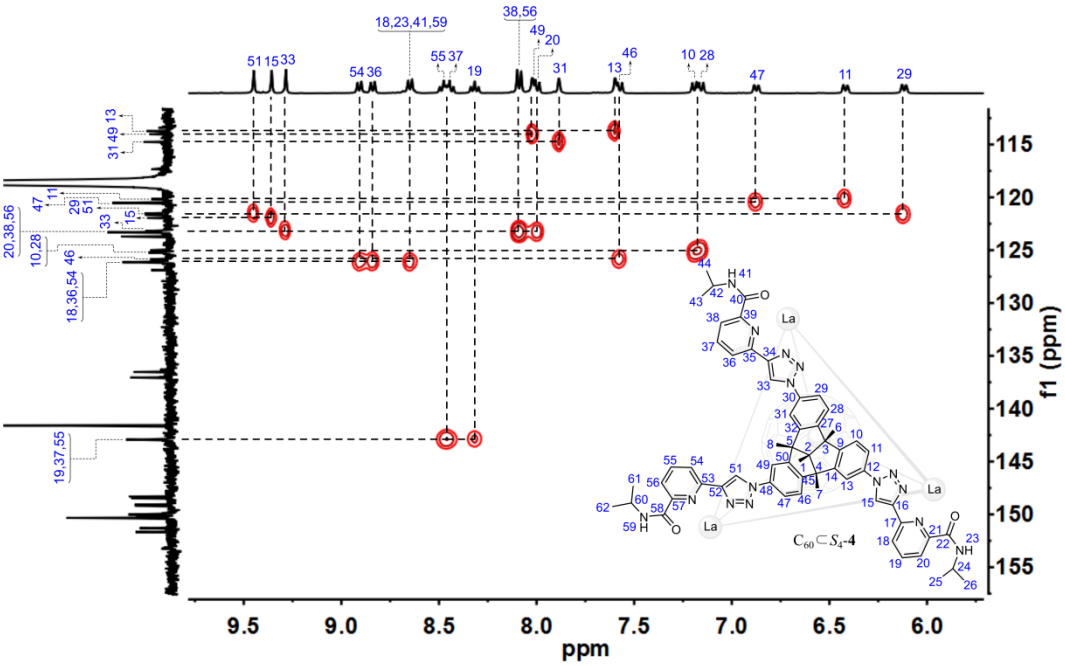

Fig. S70. Partial ^{1}H-^{13}C HSQC spectrum of $C_{60}\subset S_4$-**4** (400 MHz, 298 K, CD_3CN/CD_3OD v/v 4/1, [$C_{60}\subset S_4$-**4**] = 5.9 mM).

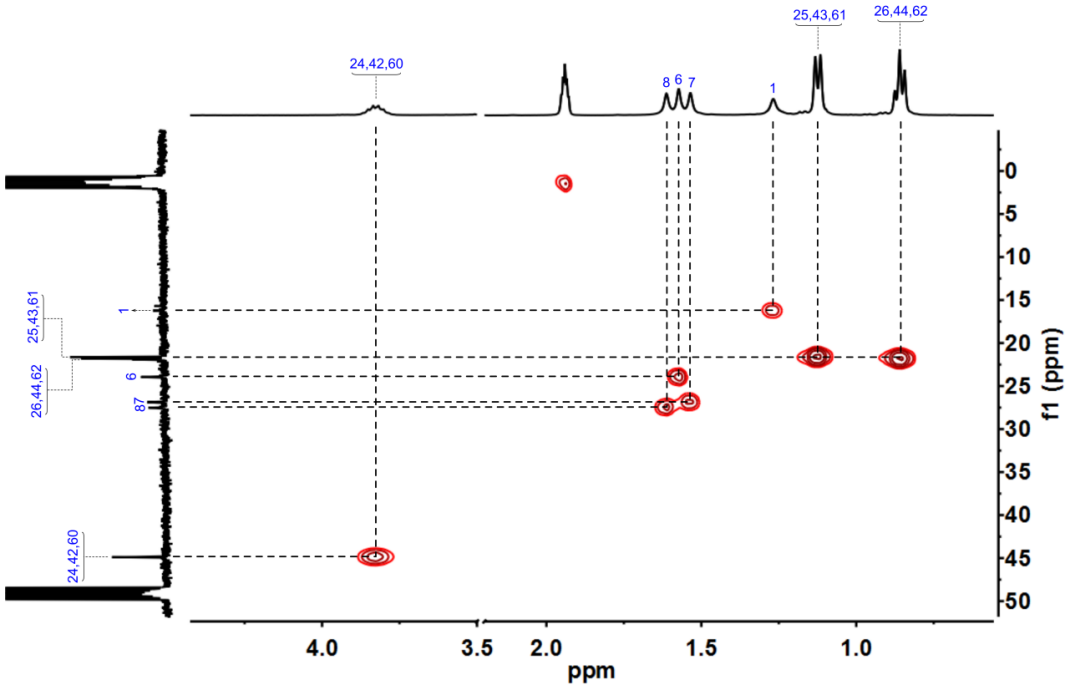

Fig. S71. Partial ^{1}H-^{13}C HSQC spectrum of $C_{60}\subset S_4$-**4** (400 MHz, 298 K, CD_3CN/CD_3OD v/v 4/1, [$C_{60}\subset S_4$-**4**] = 5.9 mM).

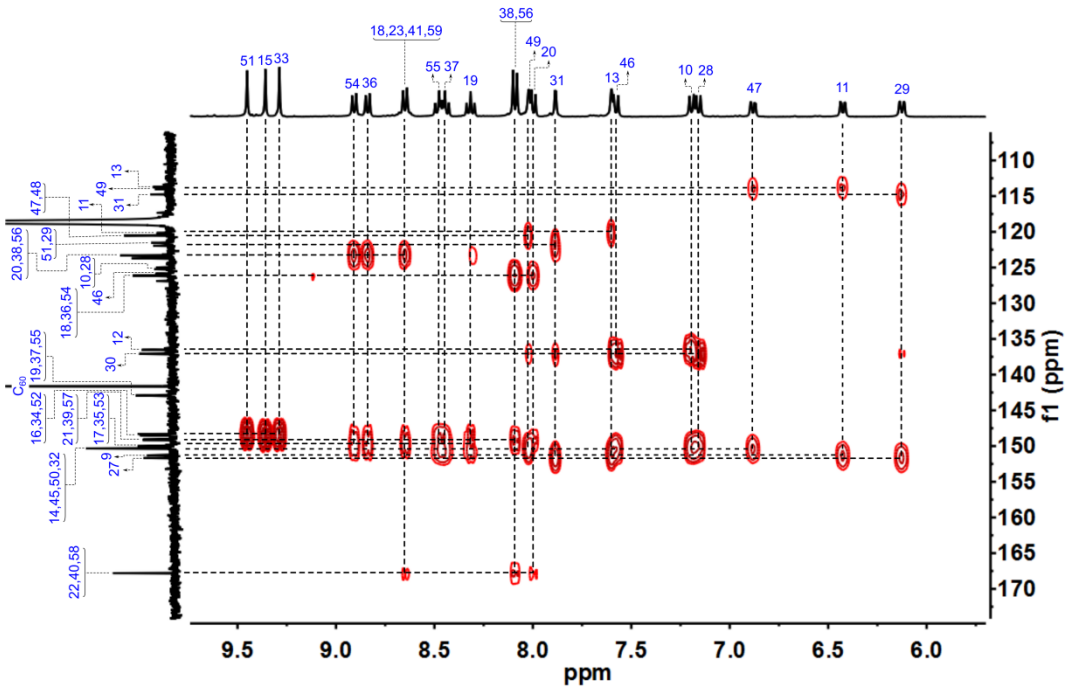

Fig. S72. Partial ^{1}H-^{13}C HMBC spectrum of $C_{60}\subset S_4$-**4** (400 MHz, 298 K, CD_3CN/CD_3OD v/v 4/1, [$C_{60}\subset S_4$-**4**] = 5.9 mM).

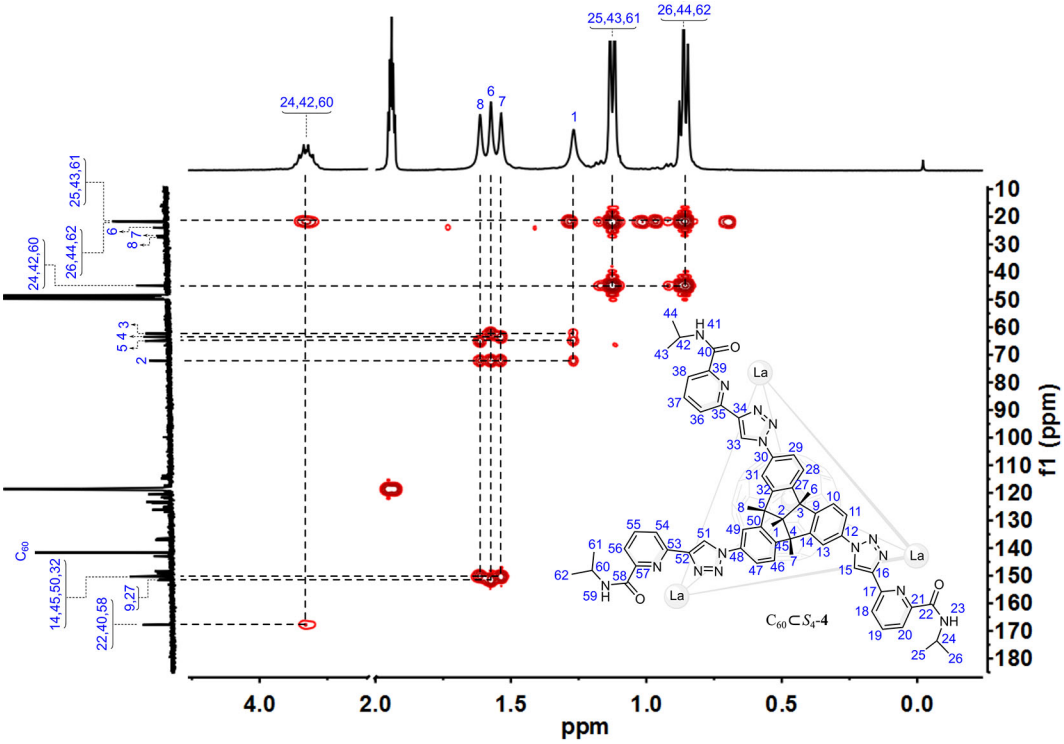

Fig. S73. Partial ^{1}H-^{13}C HMBC spectrum of $C_{60}\subset S_4$-**4** (400 MHz, 298 K, CD_3CN/CD_3OD v/v 4/1, [$C_{60}\subset S_4$-**4**] = 5.9 mM).

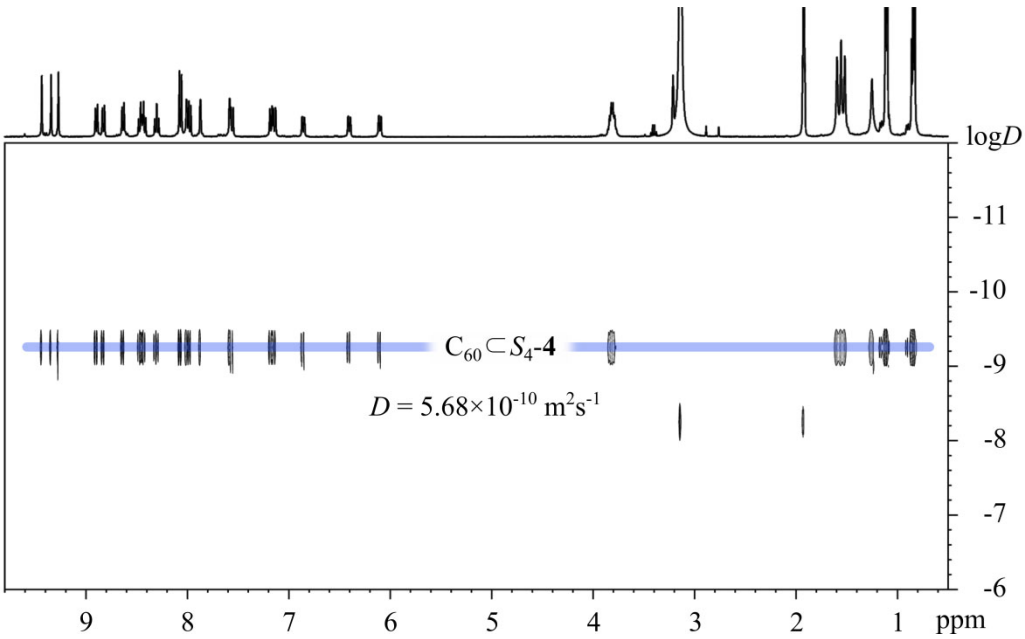

Fig. S74. ^{1}H DOSY spectrum of $C_{60}\subset S_4$-**4** (400 MHz, 298 K, CD_3CN/CD_3OD v/v 4/1, [$C_{60}\subset S_4$-**4**] = 5.9 mM). The hydrodynamic diameter of $C_{60}\subset S_4$-**4** was determined to be 2.2 nm.

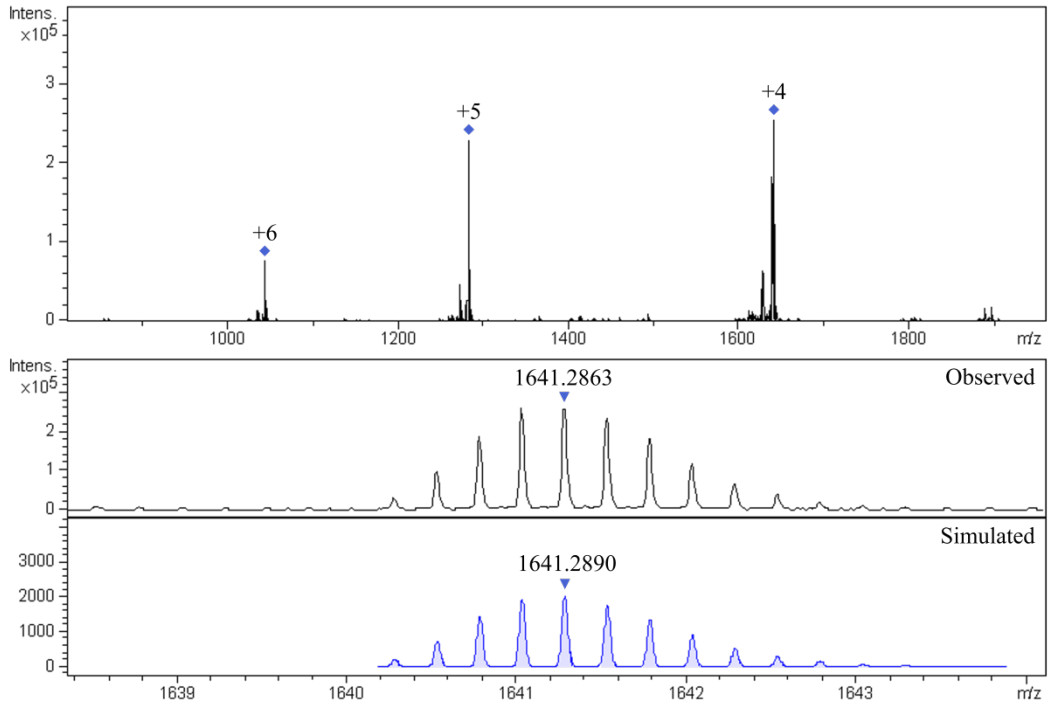

Fig. S75. High-resolution ESI-TOF-MS of $C_{60}\subset S_4$-**4** with the comparison of observed and simulated isotopic patterns of the peaks +4.

3.3.7 Encapsulation of C_{70} with S_4-**4**

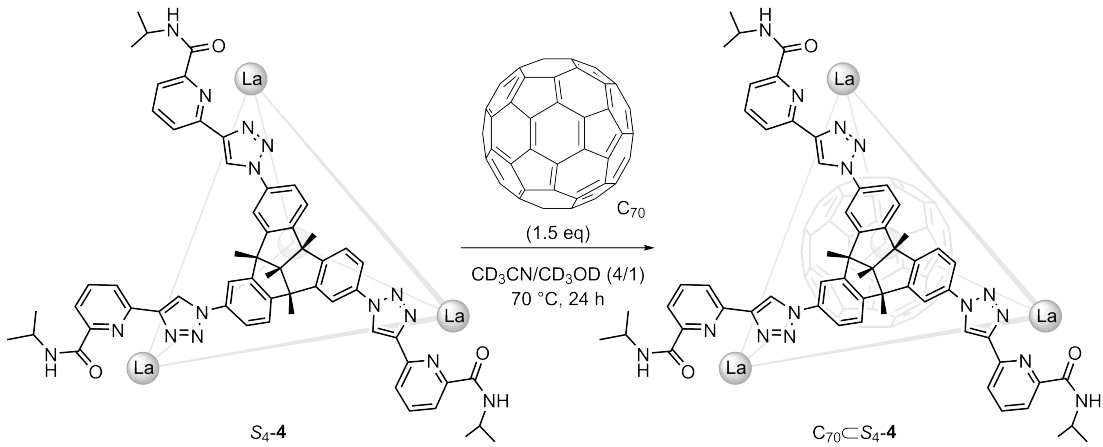

In situ self-assembly of $C_{70}\subset S_4$-**4**: $La(OTf)_3$ (6.9 mg, 11.7 μmol), C_1-**2** (12 mg, 11.7 μmol) and C_{70} (3.7 mg, 4.4 μmol) were mixed in a solution of CD_3CN/CD_3OD (v/v 4/1, 500 μL). After stirring at 70 °C for 24 h, the insoluble excess C_{70} was removed by centrifugation. The resulting solution was further characterized by NMR spectroscopy and high-resolution ESI-TOF-MS. ^{1}H NMR spectrum showed the quantitative formation of $C_{70}\subset S_4$-**4**. The solvents were dried *in vacuo* to obtain a brown powder. Yield ca. 20.3 mg, 95%.

^{1}H NMR (400 MHz, 298 K, CD_3CN/CD_3OD v/v 4/1): δ = 9.43 (s, 4H, H_{51}), 9.33 (s, 4H, H_{33}), 9.26 (s, 4H, H_{15}), 8.96 (d, J = 7.9 Hz, 4H, H_{54}), 8.88 (d, J = 7.9 Hz, 4H, H_{36}),

8.62 (d, J = 7.9 Hz, 4H, H_{18}), 8.48 (dt, J = 22.2, 8.0 Hz, 8H, H_{55} and H_{37}), 8.34 (t, J = 7.9 Hz, 4H, H_{19}), 8.09 (m, 12H, H_{38}, H_{56} and H_{49}), 8.00 (m, 8H, H_{31} and H_{20}), 7.44 (m, 8H, H_{13} and H_{46}), 7.16 (m, 8H, H_{28} and H_{10}), 6.67 (dd, J = 8.6, 1.6 Hz, 4H, H_{47}), 6.37 (dd, J = 8.6, 1.5 Hz, 4H, H_{11}), 6.16 (dd, J = 8.5, 1.6 Hz, 4H, H_{29}), 3.86 – 3.74 (m, 12H, H_{24}, H_{42} and H_{60}), 1.61 (m, 24H, H_8 and H_6), 1.53 (s, 12H, H_7), 1.27 (s, 12H, H_1), 1.18 – 1.07 (m, 36H, H_{25}, H_{43} and H_{61}), 0.85 (m, 36H, H_{26}, H_{44} and H_{62}). ^{13}C NMR (101 MHz, 298 K, CD_3CN/CD_3OD v/v 4/1): δ = 167.76, 152.05, 151.54, 150.51, 150.42, 150.33, 149.99, 149.66, 149.20 (encapsulated C_{70}), 148.59, 148.50, 146.68 (encapsulated C_{70}), 145.93 (encapsulated C_{70}), 143.99 (encapsulated C_{70}), 137.49, 136.67, 129.51 (encapsulated C_{70}), 126.94, 126.26, 125.75, 125.32, 124.97, 123.75, 123.36, 122.04, 121.89, 120.97, 120.57, 120.41, 115.80, 115.04, 114.05, 72.35, 65.29, 63.53, 62.31, 44.94, 28.27, 26.75, 21.98, 21.93, 21.91, 21.73, 21.69, 15.97. High-resolution ESI-TOF-MS for $C_{70}\subset S_4$-**4**. The following picked signals are those at the highest intensities. m/z Calcd for $[C_{70}\subset S_4\text{-}\mathbf{4} - 6(OTf)]^{6+}$ 1064.5419, found 1064.5422; Calcd for $[C_{70}\subset S_4\text{-}\mathbf{4} - 5(OTf)]^{5+}$ 1307.2408, found 1307.2414; Calcd for $[C_{70}\subset S_4\text{-}\mathbf{4} - 4(OTf)]^{4+}$ 1671.2891, found 1671.2897.

Encapsulation of C_{70} with preformed cage S_4-**4** (majority): S_4-**4** (10 mg, 1.6 μmol) and C_{70} (2.0 mg, 2.4 μmol) were mixed in a solution of CD_3CN/CD_3OD (v/v 4/1, 500 μL). The mixture was stirred at 70 °C for 24 h and monitored by ^{1}H NMR.

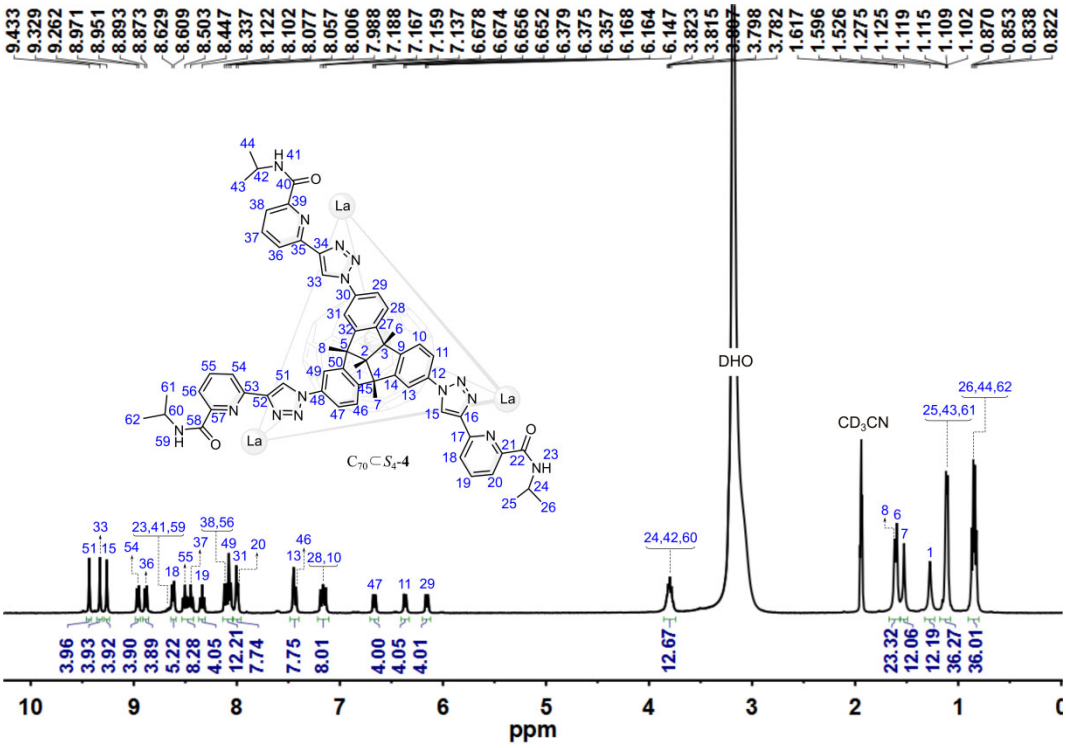

Fig. S76. ^{1}H NMR spectrum of $C_{70}\subset S_4$-**4** (400 MHz, 298 K, CD_3CN/CD_3OD v/v 4/1, $[C_{70}\subset S_4\text{-}\mathbf{4}]$ = 5.9 mM).

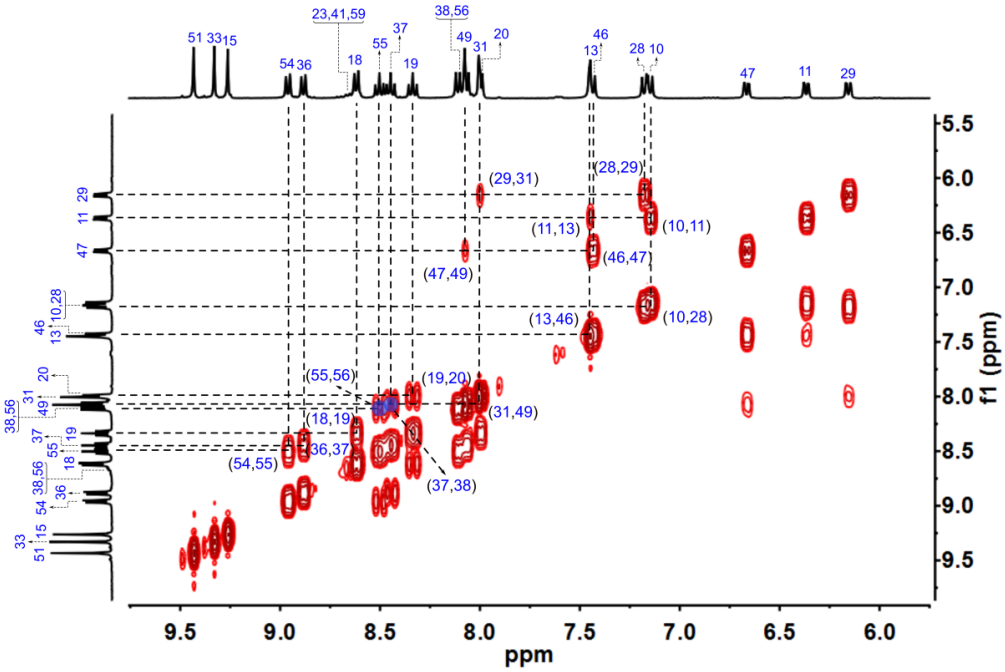

Fig. S77. ^{1}H-^{1}H COSY spectrum of $C_{70}\subset S_4$-**4** (400 MHz, 298 K, CD_3CN/CD_3OD v/v 4/1, [$C_{70}\subset S_4$-**4**] = 5.9 mM).

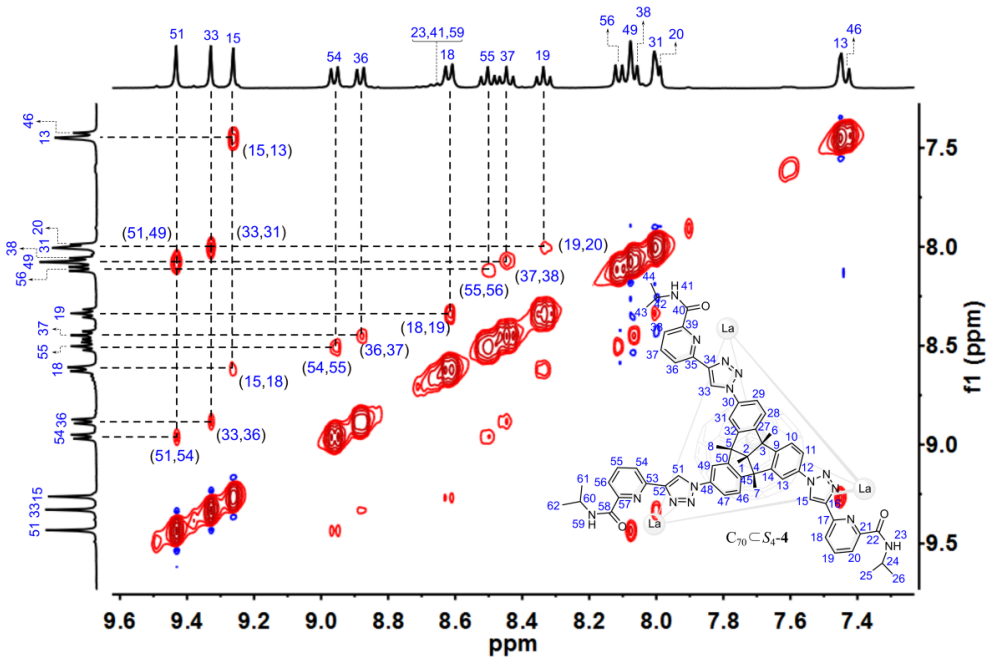

Fig. S78. Partial ^{1}H-^{1}H NOESY spectrum of $C_{70}\subset S_4$-**4** (400 MHz, 298 K, CD_3CN/CD_3OD v/v 4/1, [$C_{70}\subset S_4$-**4**] = 5.9 mM).

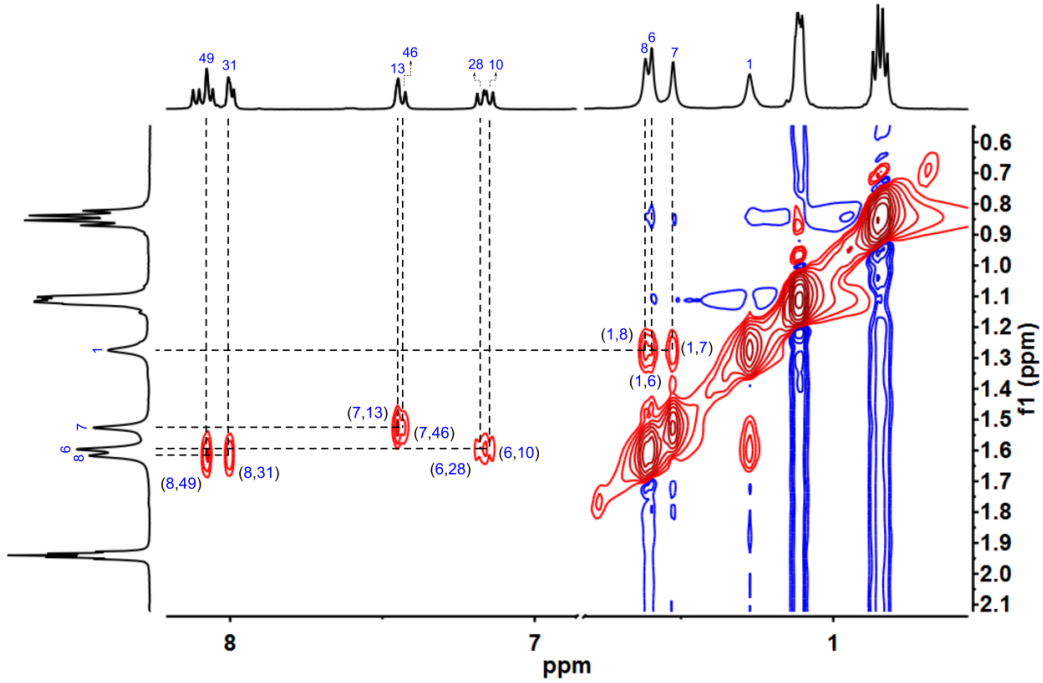

Fig. S79. Partial ^{1}H-^{1}H NOESY spectrum of $C_{70}\subset S_4$-**4** (400 MHz, 298 K, CD_3CN/CD_3OD v/v 4/1, [$C_{70}\subset S_4$-**4**] = 5.9 mM).

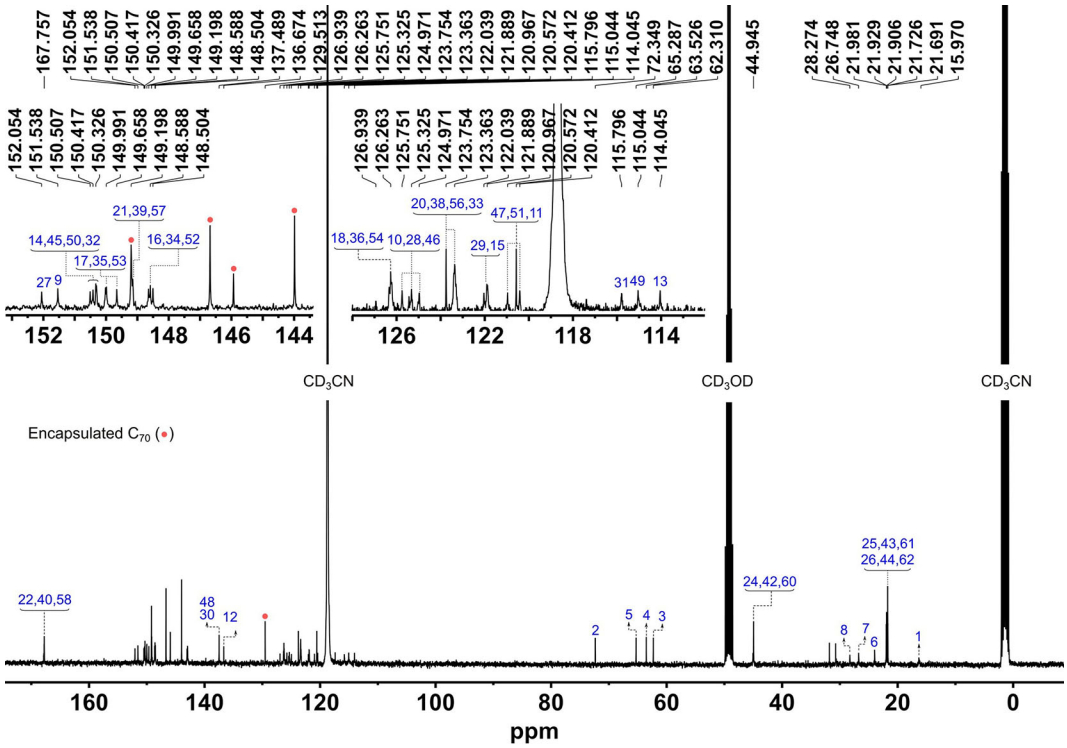

Fig. S80. ^{13}C NMR spectrum of $C_{70}\subset S_4$-**4** (400 MHz, 298 K, CD_3CN/CD_3OD v/v 4/1, [$C_{70}\subset S_4$-**4**] = 5.9 mM).

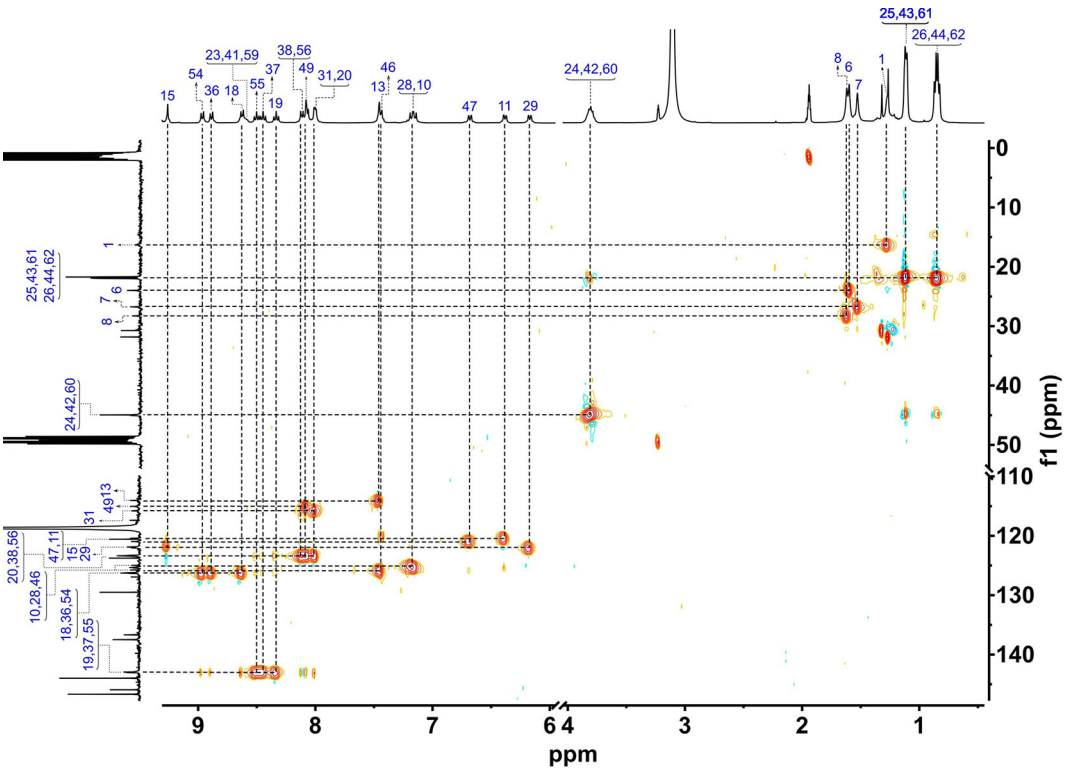

Fig. S81. Partial ^{1}H-^{13}C HSQC spectrum of $C_{70}\subset S_4$-**4** (400 MHz, 298 K, CD_3CN/CD_3OD v/v 4/1, [$C_{70}\subset S_4$-**4**] = 5.9 mM).

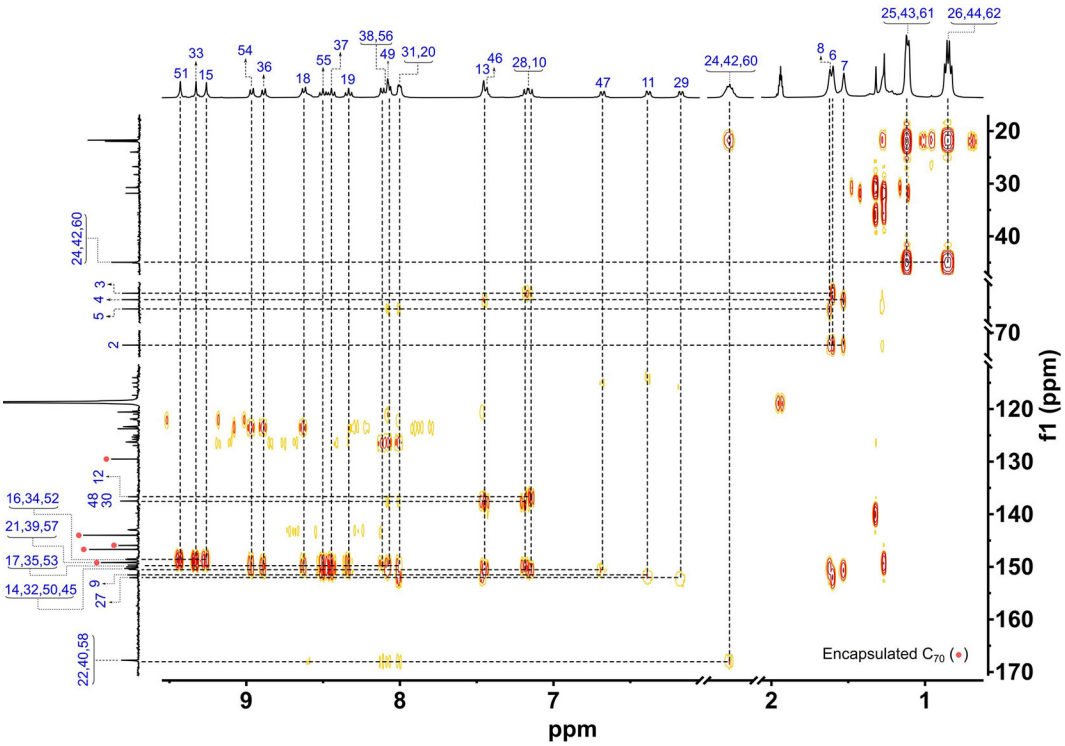

Fig. S82. Partial ^{1}H-^{13}C HMBC spectrum of $C_{70}\subset S_4$-**4** (400 MHz, 298 K, CD_3CN/CD_3OD v/v 4/1, [$C_{70}\subset S_4$-**4**] = 5.9 mM).

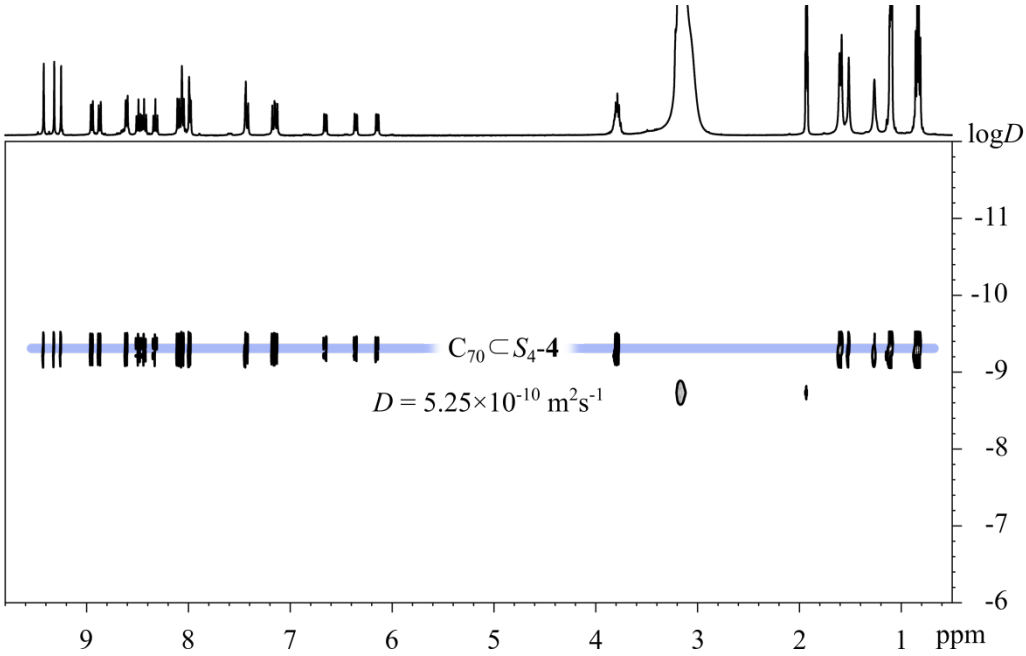

Fig. S83. ^{1}H DOSY spectrum of $C_{70}\subset S_4$-**4** (400 MHz, 298 K, CD_3CN/CD_3OD v/v 4/1, [$C_{70}\subset S_4$-**4**] = 5.9 mM). The hydrodynamic diameter of $C_{70}\subset S_4$-**4** was determined to be 2.4 nm.

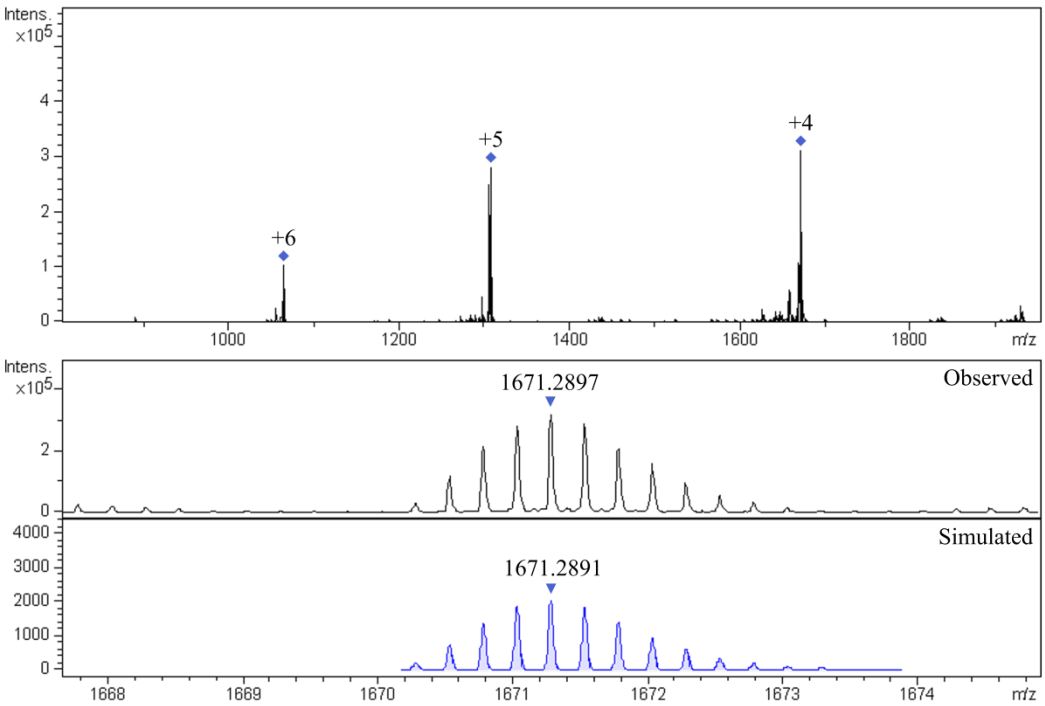

Fig. S84. High-resolution ESI-TOF-MS of $C_{70}\subset S_4$-**4** with the comparison of observed and simulated isotopic patterns of the peaks +4.

3.3.8 Encapsulation of D_2-C_{76} with S_4-**4**

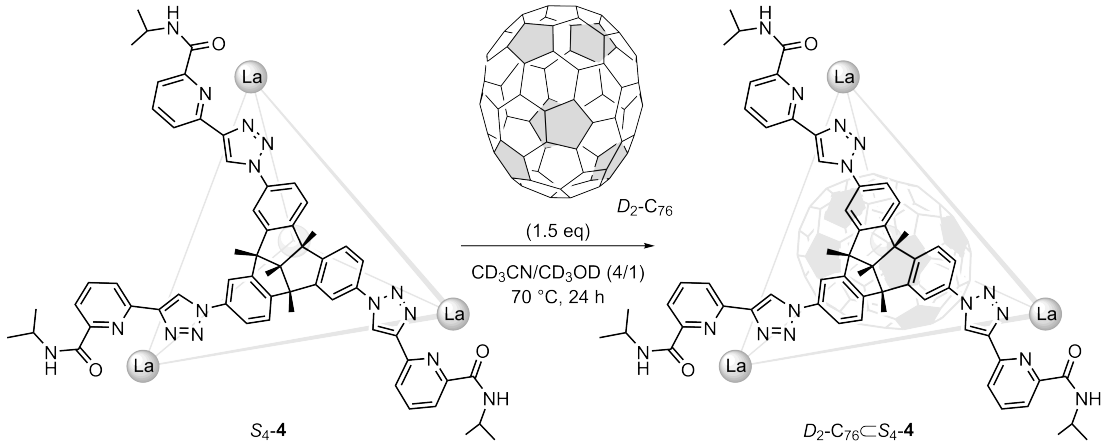

In situ self-assembly of D_2-C_{76}⊂S_4-**4**: La(OTf)$_3$ (2.3 mg, 3.9 μmol), C_1-**2** (4.0 mg, 3.9 μmol) and D_2-C_{76} (1.4 mg, 1.5 μmol) were mixed in a solution of CD_3CN/CD_3OD (v/v 4/1, 500 μL). After stirring at 70 °C for 24 h, the insoluble excess D_2-C_{76} was removed by centrifugation. The resulting solution was further characterized by NMR spectroscopy and high-resolution ESI-TOF-MS. ^{1}H NMR spectrum showed the quantitative formation of D_2-C_{76}⊂S_4-**4**. The solvents were dried *in vacuo* to obtain a brown powder. Yield ca. 6.8 mg, 94%.

^{1}H NMR (400 MHz, 298 K, CD_3CN/CD_3OD v/v 4/1): δ = 9.57 (s, 2H, $H_{51'}$), 9.52 (s, 2H, H_{51}), 9.47 (s, 2H, $H_{33'}$), 9.45 – 9.37 (m, 6H, $H_{15'}$, H_{15} and H_{33}), 8.84 (m, 8H, $H_{54'}$, $H_{36'}$, H_{54} and H_{36}), 8.68 (m, 6H, $H_{18'}$, and H_{18}), 8.50 (m, 8H, $H_{55'}$, H_{55}, $H_{37'}$ and H_{37}), 8.38 (dd, J = 15.7, 7.9 Hz, 4H, $H_{19'}$ and H_{19}), 8.16 (d, J = 7.8 Hz, 2H, $H_{56'}$), 8.10 (m, 8H, $H_{38'}$, H_{38}, $H_{36'}$ and H_{49}), 8.06 – 7.98 (m, 8H, $H_{49'}$, H_{31}, $H_{20'}$ and H_{20}), 7.91 (s, 2H, H_{31}), 7.55 (m, 8H, $H_{13'}$, H_{13}, $H_{46'}$ and H_{46}), 7.26 – 7.11 (m, 8H, $H_{28'}$, $H_{10'}$, H_{10} and H_{28}), 6.77 (m, 4H, $H_{47'}$ and H_{47}), 6.39 (m, 4H, $H_{11'}$ and H_{11}), 6.18 (d, J = 9.0 Hz, 2H, $H_{29'}$), 6.04 (d, J = 8.6 Hz, 2H, H_{29}), 3.87 – 3.74 (m, 12H, $H_{24'}$, H_{24}, $H_{42'}$, H_{42}, $H_{60'}$ and H_{60}), 1.59 (m, 36H, $H_{6'}$, H_6, $H_{7'}$, H_7, $H_{8'}$ and H_8), 1.28 (m, 12H, $H_{1'}$ and H_1), 1.12 (m, 36H, $H_{25'}$, H_{25}, $H_{43'}$, H_{43}, $H_{61'}$ and H_{61}), 0.92 – 0.74 (m, 36H, $H_{26'}$, H_{26}, $H_{44'}$, H_{44}, $H_{62'}$ and H_{62}). The ^{13}C NMR signals were too weak to be measured. High-resolution ESI-TOF-MS for D_2-C_{76}⊂S_4-**4**. The following picked signals are those at the highest intensities. m/z Calcd for [D_2-C_{76}⊂S_4-**4** – 7(OTf)]$^{7+}$ 901.4713, found 901.4694; Calcd for [D_2-C_{76}⊂S_4-**4** – 6(OTf)]$^{6+}$ 1076.5419, found 1076.5403; Calcd for [D_2-C_{76}⊂S_4-**4** – 5(OTf)]$^{5+}$ 1321.6408, found 1321.6397; Calcd for [D_2-C_{76}⊂S_4-**4** – 4(OTf)]$^{4+}$ 1689.2891, found 1689.2883.

Encapsulation of D_2-C_{76} with preformed cage S_4-**4** (majority): S_4-**4** (8 mg, 1.1 μmol) and D_2-C_{76} (1.6 mg, 1.7 μmol) were mixed in a solution of CD_3CN/CD_3OD (v/v 4/1, 500 μL). The mixture was stirred at 70 °C for 24 h and monitored by ^{1}H NMR.

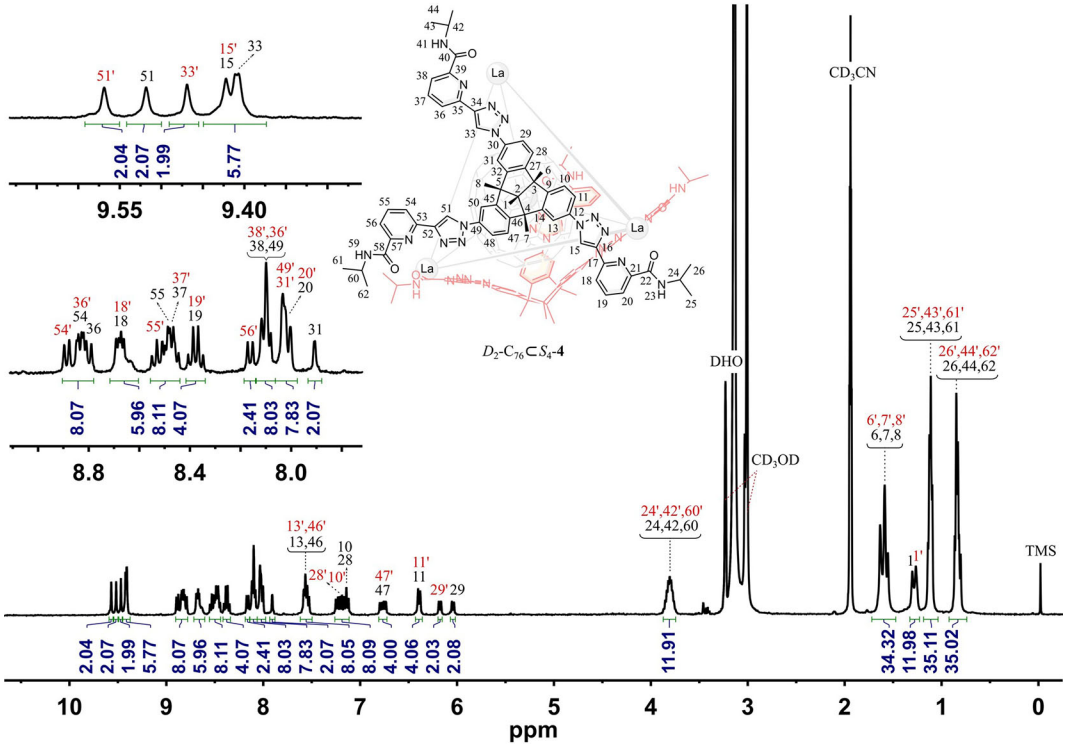

Fig. S85. ^{1}H NMR spectrum of D_2-C_{76}⊂S_4-**4** (400 MHz, 298 K, CD_3CN/CD_3OD v/v 4/1, [D_2-C_{76}⊂S_4-**4**] = 2.0 mM).

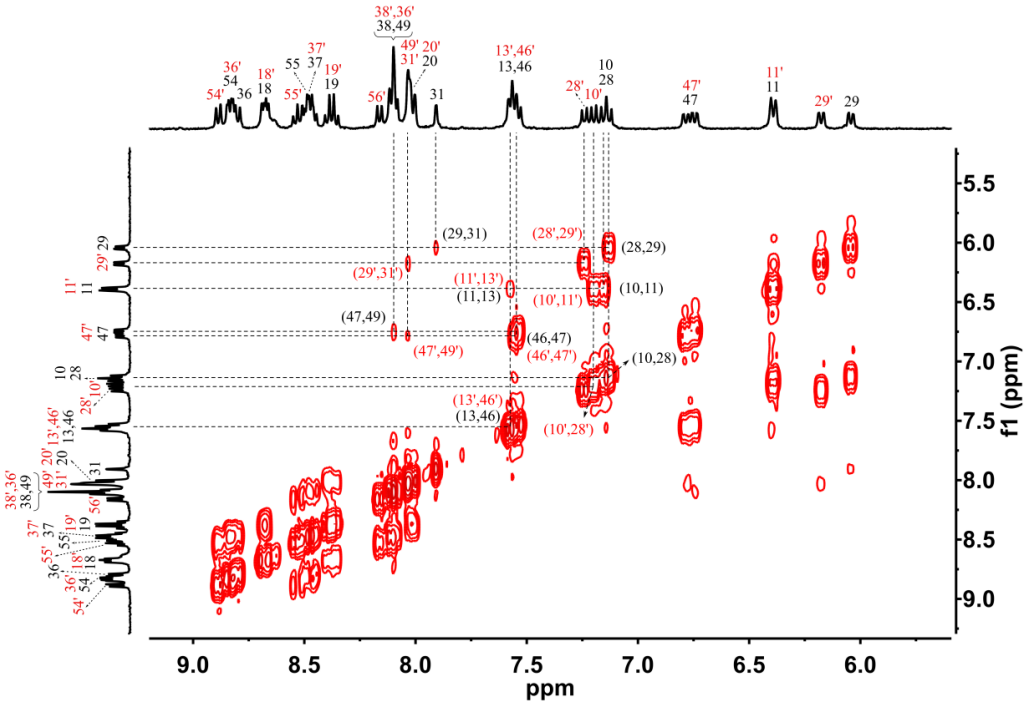

Fig. S86. Partial ^{1}H-^{1}H COSY spectrum of D_2-C_{76}⊂S_4-**4** (400 MHz, 298 K, CD_3CN/CD_3OD v/v 4/1, [D_2-C_{76}⊂S_4-**4**] = 2.0 mM).

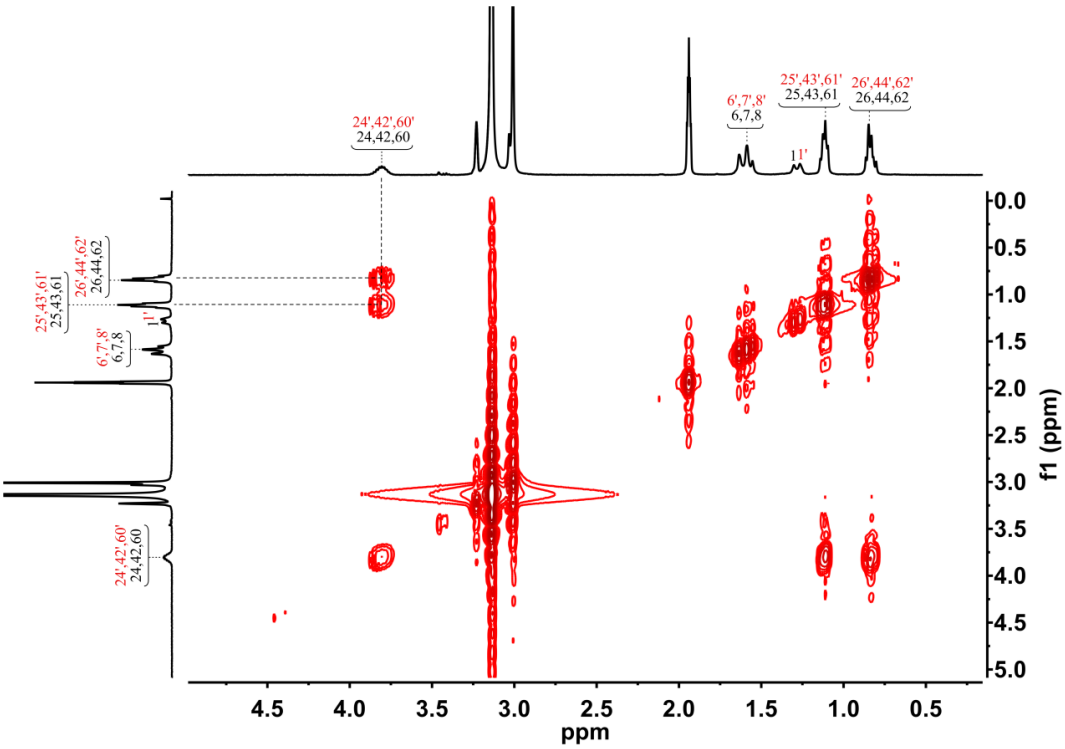

Fig. S87. Partial ^{1}H-^{1}H COSY spectrum of D_2-C_{76}⊂S_4-**4** (400 MHz, 298 K, CD_3CN/CD_3OD v/v 4/1, [D_2-C_{76}⊂S_4-**4**] = 2.0 mM).

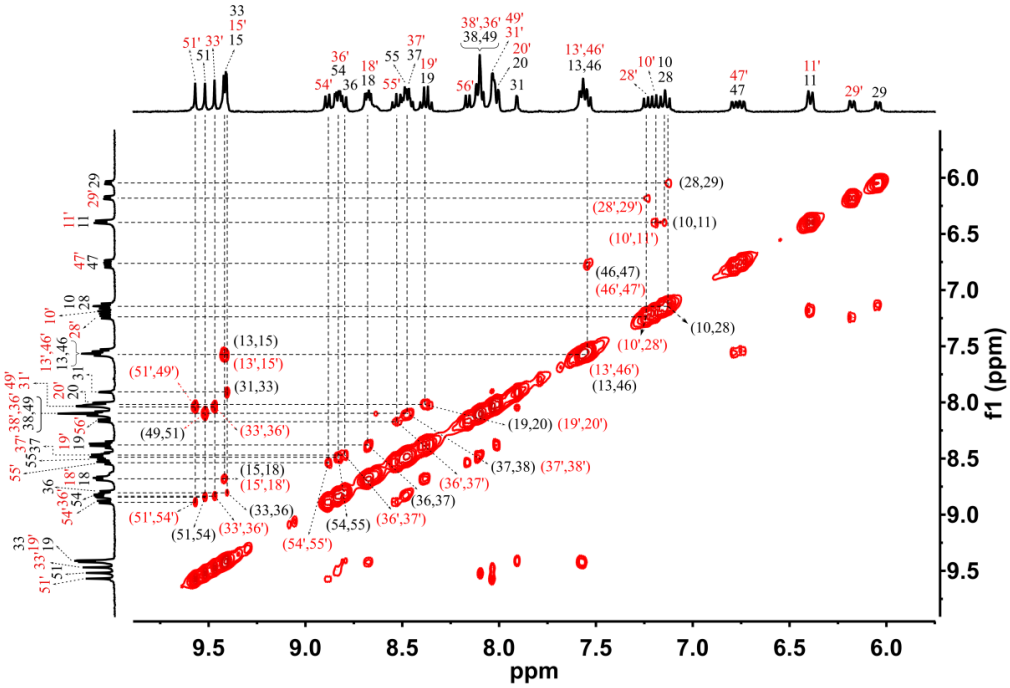

Fig. S88. Partial ^{1}H-^{1}H NOESY spectrum of D_2-C_{76}⊂S_4-**4** (400 MHz, 298 K, CD_3CN/CD_3OD v/v 4/1, [D_2-C_{76}⊂S_4-**4**] = 2.0 mM).

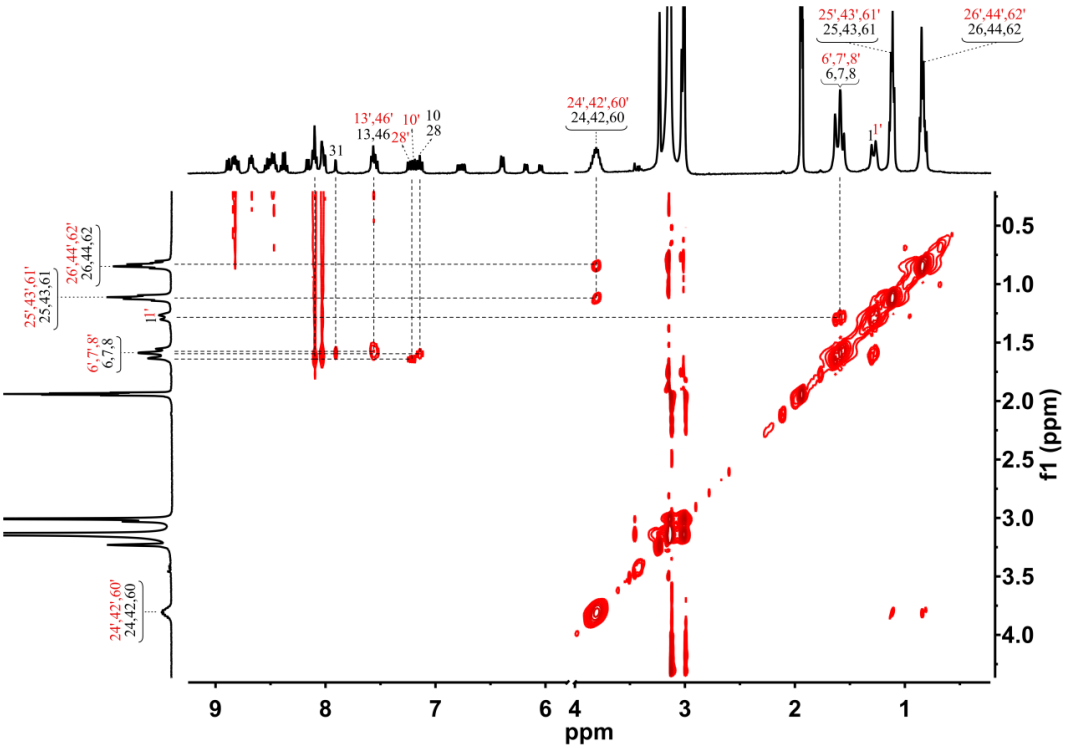

Fig. S89. Partial ^{1}H-^{1}H NOESY spectrum of D_2-C_{76}⊂S_4-**4** (400 MHz, 298 K, CD_3CN/CD_3OD v/v 4/1, [D_2-C_{76}⊂S_4-**4**] = 2.0 mM).

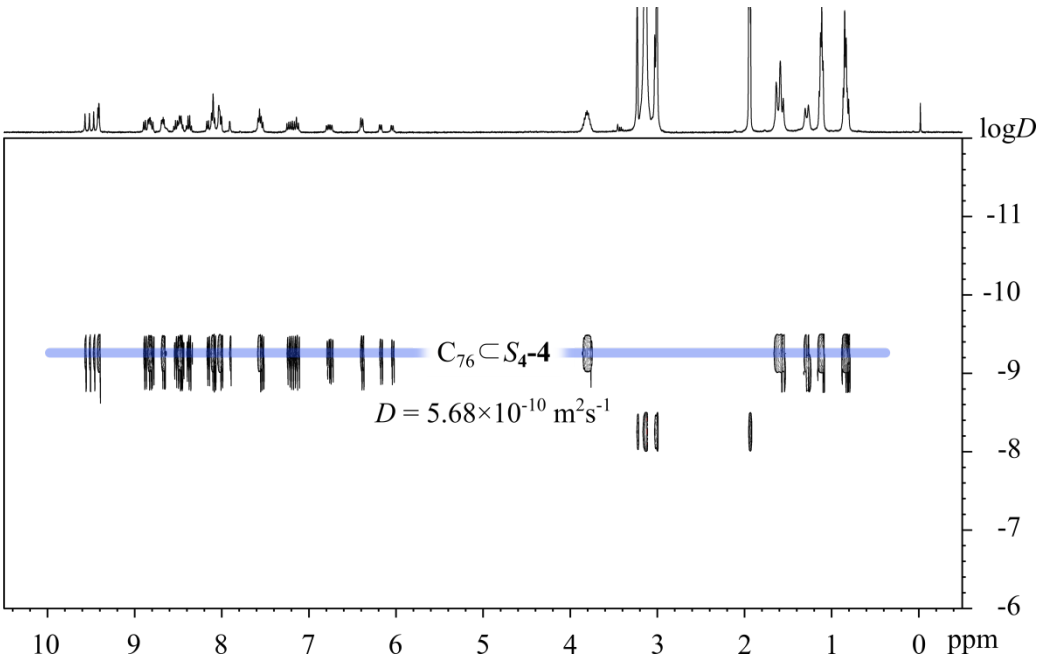

Fig. S90. ^{1}H DOSY spectrum of D_2-C_{76}⊂S_4-**4** (400 MHz, 298 K, CD_3CN/CD_3OD v/v 4/1, [D_2-C_{76}⊂S_4-**4**] = 2.0 mM). The hydrodynamic diameter of D_2-C_{76}⊂S_4-**4** was determined to be 2.2 nm.

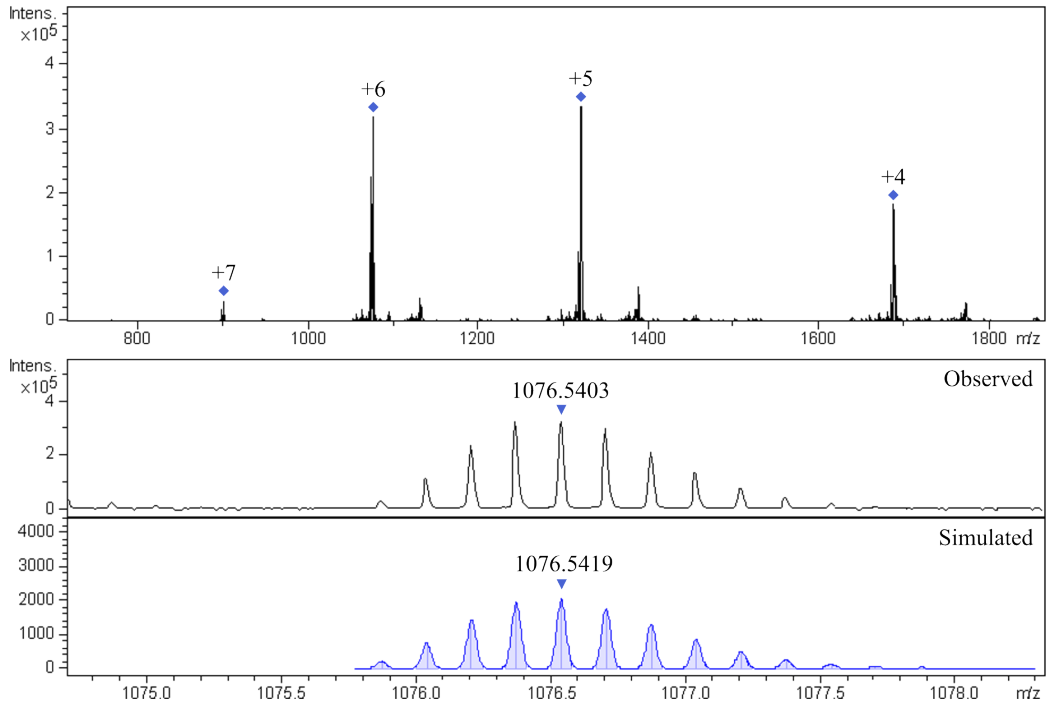

Fig. S91. High-resolution ESI-TOF-MS of D_2-C_{76}⊂S_4-**4** with the comparison of observed and simulated isotopic patterns of the peaks +6.

3.3.9 Encapsulation of C_{2v}-C_{78} with S_4-**4**

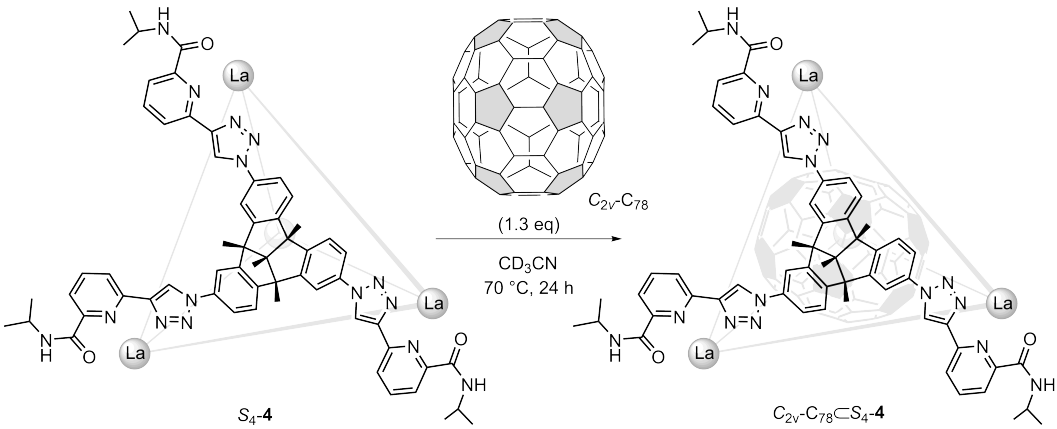

In situ self-assembly of C_{2v}-C_{78}⊂S_4-**4**: La(OTf)$_3$ (1.3 mg, 2.2 μmol), C_1-**2** (2.3 mg, 2.2 μmol) and C_{2v}-C_{78} (0.7 mg, 0.8 μmol) were mixed in a solution of CD_3CN (500 μL). After stirring at 70 °C for 24 h, the insoluble excess C_{2v}-C_{78} was removed by centrifugation. The resulting solution was further characterized by NMR spectroscopy and high-resolution ESI-TOF-MS. ^{1}H NMR spectrum showed the formation of a mixed host–guest complexes with S_4-symmetric (major) and C_2-symmetric (minor) C_{2v}-C_{78}⊂S_4-**4**. The solvents were dried *in vacuo* to obtain a brown powder. Yield ca. 3.9 mg, 95%.

^{1}H NMR (600 MHz, 298 K, CD_3CN) δ = 9.43 (s, 4H, H_{51}), 9.36 (s, 4H, H_{33}), 9.34 (s, 4H, H_{15}), 8.93 (d, J = 8.0 Hz, 4H, H_{54}), 8.89 (d, J = 7.9 Hz, 4H, H_{36}), 8.77 (d, J = 7.9 Hz, 4H, H_{18}), 8.49 – 8.44 (m, 8H, H_{55} and H_{37}), 8.35 (t, J = 8.0 Hz, 4H, H_{19}), 8.23 – 8.14 (m, 12H, H_{41}, H_{59} and H_{23}), 8.07 – 8.01 (m, 12H, H_{38}, H_{56} and H_{49}), 7.98 – 7.93 (m, 8H, H_{20} and H_{31}), 7.64 (d, J = 8.6 Hz, 4H, H_{46}), 7.61 (d, J = 2.1 Hz, 4H, H_{13}), 7.22 (dd, J = 8.6, 1.8 Hz, 8H, H_{28} and H_{10}), 6.99 (dd, J = 8.6, 2.2 Hz, 4H, H_{47}), 6.68 (dd, J = 8.5, 2.1 Hz, 4H, H_{11}), 6.35 (dd, J = 8.6, 2.1 Hz, 4H, H_{29}), 3.93 – 3.79 (m, 12H, H_{24}, H_{42} and H_{60}), 1.59 – 1.50 (m, 36H, H_8, H_7 and H_6), 1.26 (s, 12H, H_1), 1.15 – 1.12 (m, 36H, H_{25}, H_{43} and H_{61}), 0.88 – 0.84 (m, 36H, H_{26}, H_{44} and H_{62}). The ^{13}C NMR signals were too weak to be measured. High-resolution ESI-TOF-MS for C_{2v}-C_{78}⊂S_4-**4**. The following picked signals are those at the highest intensities. m/z Calcd for [C_{2v}-C_{78}⊂S_4-**4** – 6(OTf)]$^{6+}$ 1080.5419, found 1080.5397; Calcd for [C_{2v}-C_{78}⊂S_4-**4** – 5(OTf)]$^{5+}$ 1326.4408, found 1326.4362; Calcd for [C_{2v}-C_{78}⊂S_4-**4** – 4(OTf)]$^{4+}$ 1695.2891, found 1695.2791.

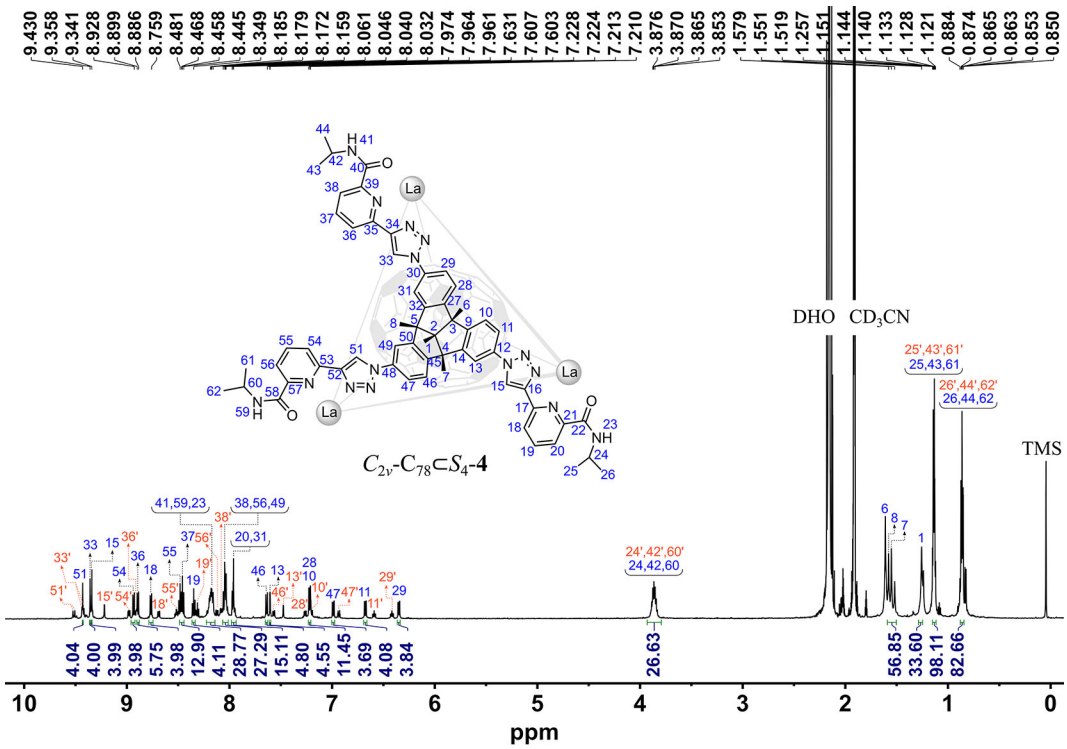

Fig. S92. ^{1}H NMR spectrum (600 MHz, 298 K, CD_3CN, [C_{2v}-C_{78}⊂S_4-**4**] = 1.0 mM) of C_2-symmetric C_{2v}-C_{78}⊂S_4-**4** (orange labels) and S_4-symmetric C_{2v}-C_{78}⊂S_4-**4** (bule labels).

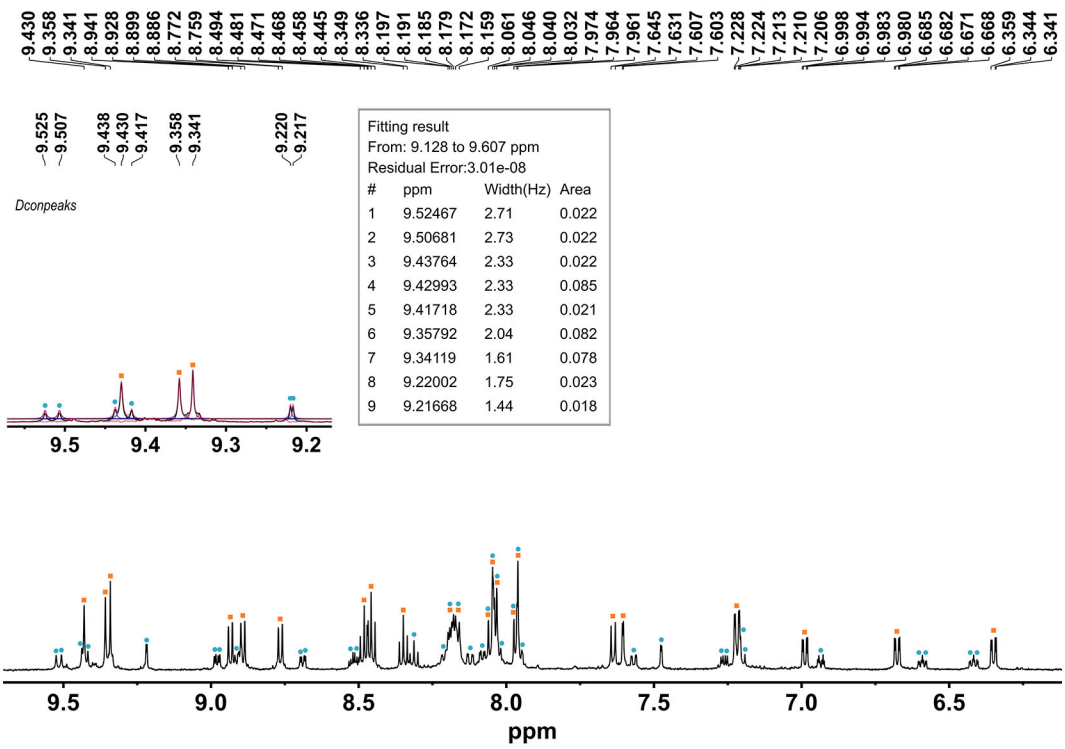

Fig. S93. Partial ^{1}H NMR spectrum of C_{2v}-C$_{78}$⊂S_4-**4** with inset showing the deconvolution result of the triazole region (600 MHz, 298 K, CD$_3$CN, [C_{2v}-C$_{78}$⊂S_4-**4**] = 1.0 mM). Multiple overlapping signals in the triazole region are consistent with the coexistence of C_2-symmetric C_{2v}-C$_{78}$⊂S_4-**4** (●) and S_4-symmetric C_{2v}-C$_{78}$⊂S_4-**4** (■).

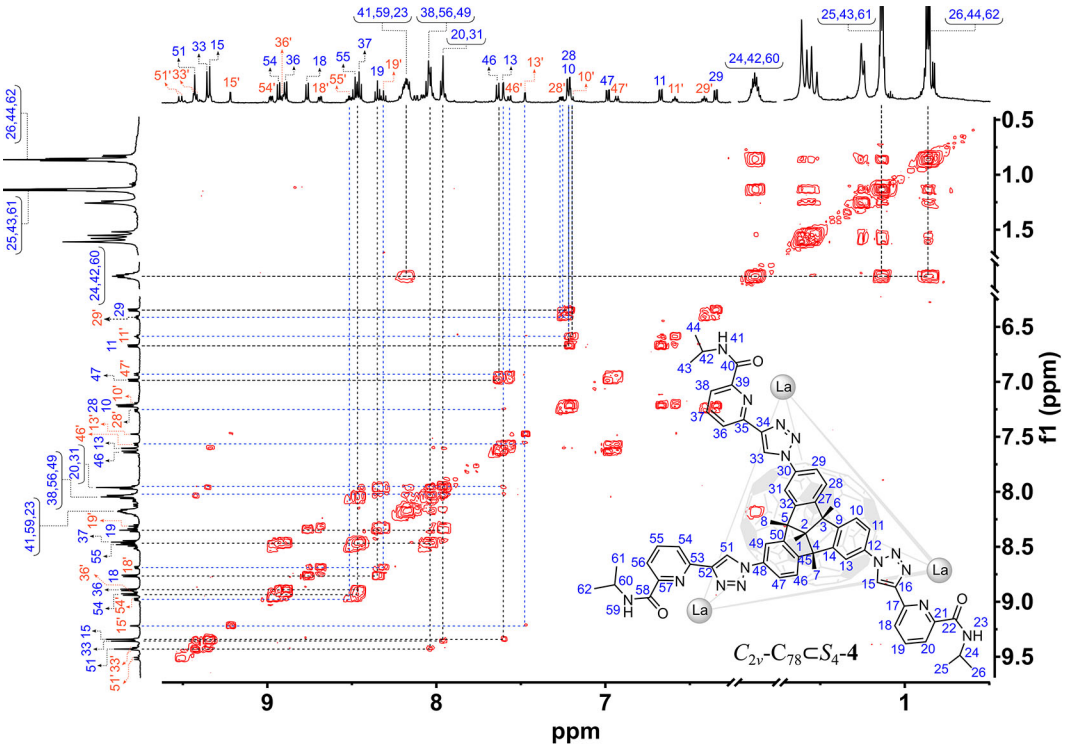

Fig. S94. Partial ^{1}H-^{1}H COSY spectrum of C_{2v}-C$_{78}$⊂S_4-**4** (600 MHz, 298 K, CD$_3$CN, [C_{2v}-C$_{78}$⊂S_4-**4**] = 1.0 mM).

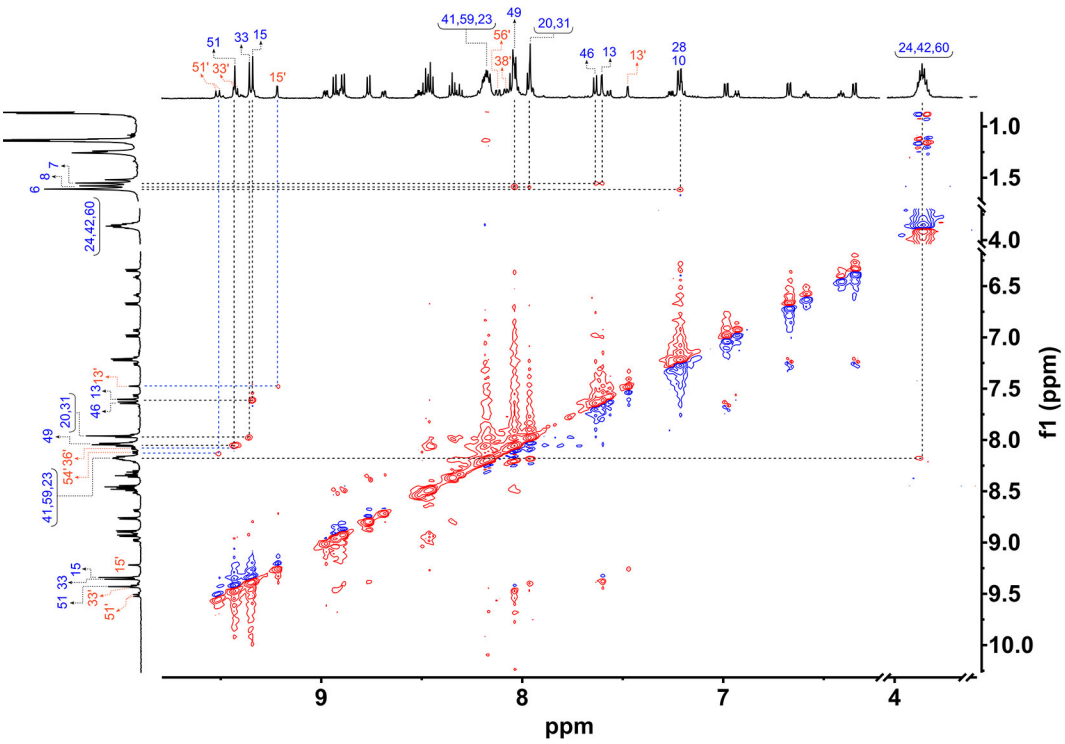

Fig. S95. Partial ^{1}H-^{1}H NOESY spectrum of C_{2v}-C_{78}⊂S_4-**4** (600 MHz, 298 K, CD_3CN, [C_{2v}-C_{78}⊂S_4-**4**] = 1.0 mM).

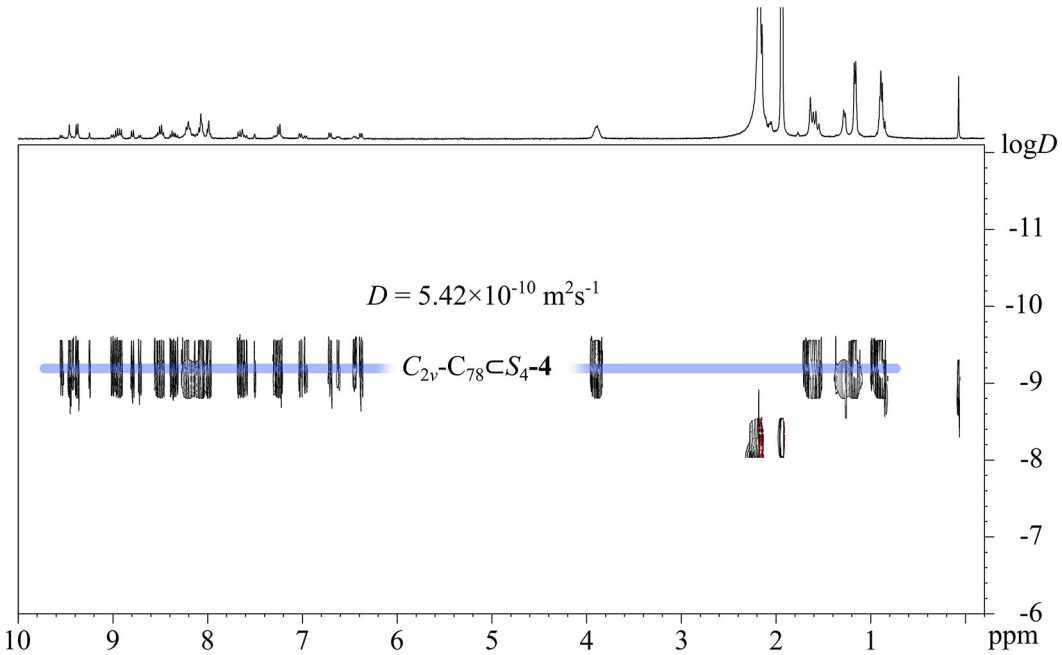

Fig. S96. ^{1}H DOSY spectrum of C_{2v}-C_{78}⊂S_4-**4** (400 MHz, 298 K, CD_3CN, [C_{2v}-C_{78}⊂S_4-**4**] = 1.0 mM). The hydrodynamic diameter of C_{2v}-C_{78}⊂S_4-**4** was determined to be 2.2 nm.

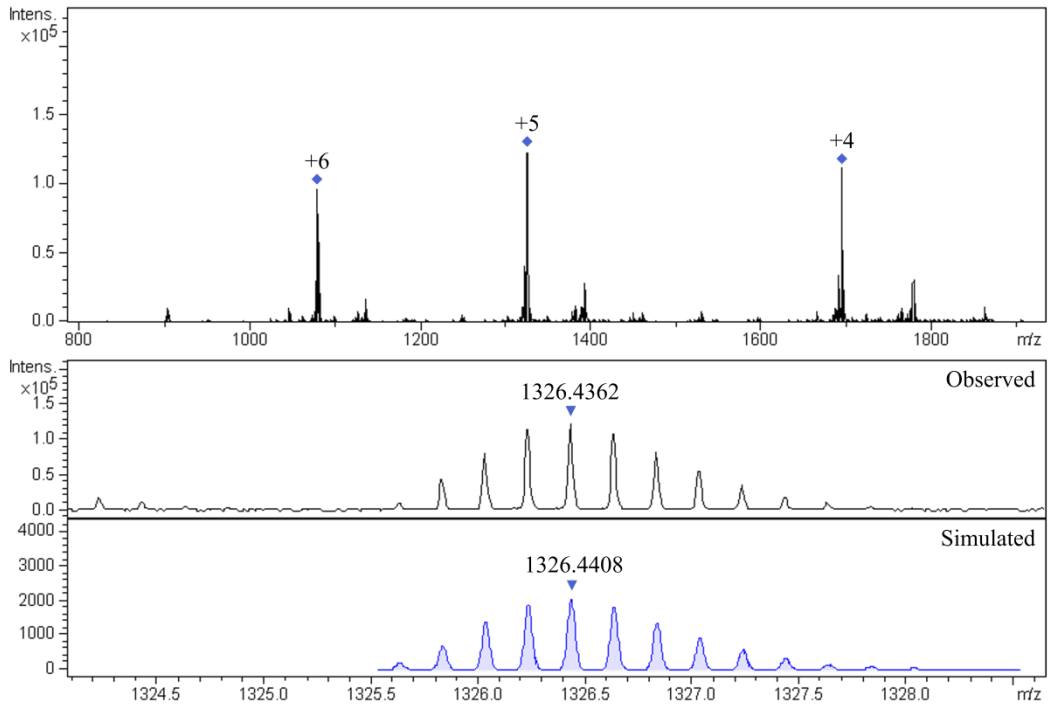

Fig. S97. High-resolution ESI-TOF-MS of C_{2v}-C_{78}⊂S_4-**4** with the comparison of observed and simulated isotopic patterns of the peaks +5.

3.3.10 Encapsulation of C_{2v}'-C_{78} with S_4-**4**

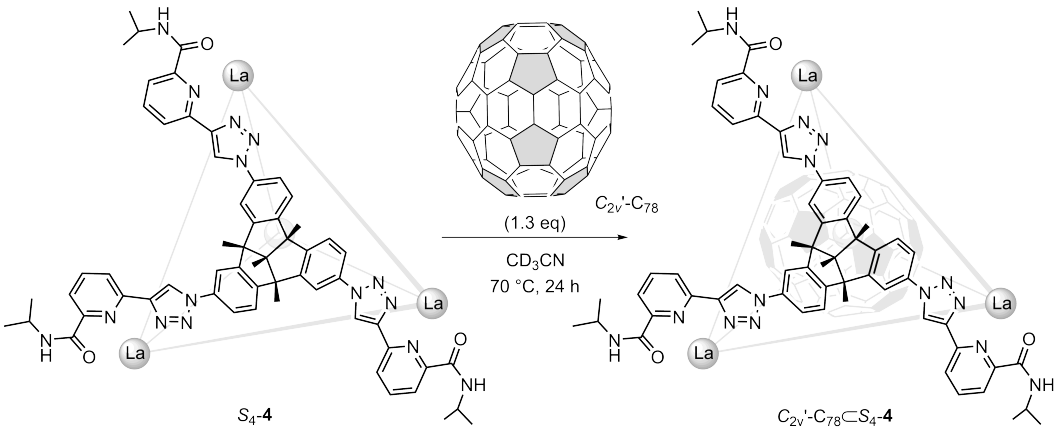

In situ self-assembly of C_{2v}'-C_{78}⊂S_4-**4**: $La(OTf)_3$ (1.3 mg, 2.2 μmol), C_1-**2** (2.3 mg, 2.2 μmol) and C_{2v}'-C_{78} (0.7 mg, 0.8 μmol) were mixed in a solution of CD_3CN (500 μL). After stirring at 70 °C for 24 h, the insoluble excess C_{2v}'-C_{78} was removed by centrifugation. The resulting solution was further characterized by NMR spectroscopy and high-resolution ESI-TOF-MS. ^{1}H NMR spectrum showed the quantitative formation of C_{2v}'-C_{78}⊂S_4-**4**. The solvents were dried *in vacuo* to obtain a brown powder. Yield ca. 3.8 mg, 93%.

^{1}H NMR (400 MHz, 298K, CD_3CN) δ = 9.41 (s, 4H, H_{51}), 9.38 (s, 4H, H_{33}), 9.33 (s, 4H, H_{15}), 8.91 (m, 8H, H_{54} and H_{36}), 8.78 (d, J = 8.1 Hz, 4H, H_{18}), 8.54 – 8.37 (m, 12H, H_{55}, H_{37} and H_{19}), 8.31 (m, 12H, H_{41}, H_{59} and H_{23}), 8.11 – 7.94 (m, 20H, H_{20}, H_{38}, H_{56} H_{49} and H_{31}), 7.63 (m, 8H, H_{46} and H_{13}), 7.18 (m, 8H, H_{28} and H_{10}), 6.89 (d, J = 8.3 Hz, 4H, H_{47}), 6.56 (d, J = 8.3 Hz, 4H, H_{11}), 6.22 (d, J = 8.4 Hz, 4H, H_{29}), 3.89 – 3.80 (m, 12H, H_{24}, H_{42} and H_{60}), 1.62 (m, 36H, H_6, H_7 and H_8), 1.30 (s, 12H, H_1), 1.15 (m, 36H, H_{25}, H_{43} and H_{61}), 0.88 (m, 36H, H_{26}, H_{44} and H_{62}). The ^{13}C NMR signals were too weak to be measured. High-resolution ESI-TOF-MS for C_{2v}'-C_{78}⊂S_4-**4**. The following picked signals are those at the highest intensities. m/z Calcd for [C_{2v}'-C_{78}⊂S_4-**4** – 6(OTf)]$^{6+}$ 1080.5419, found 1080.5415; Calcd for [C_{2v}'-C_{78}⊂S_4-**4** – 5(OTf)]$^{5+}$ 1326.4408, found 1326.4403; Calcd for [C_{2v}'-C_{78}⊂S_4-**4** – 4(OTf)]$^{4+}$ 1695.2891, found 1695.2893.

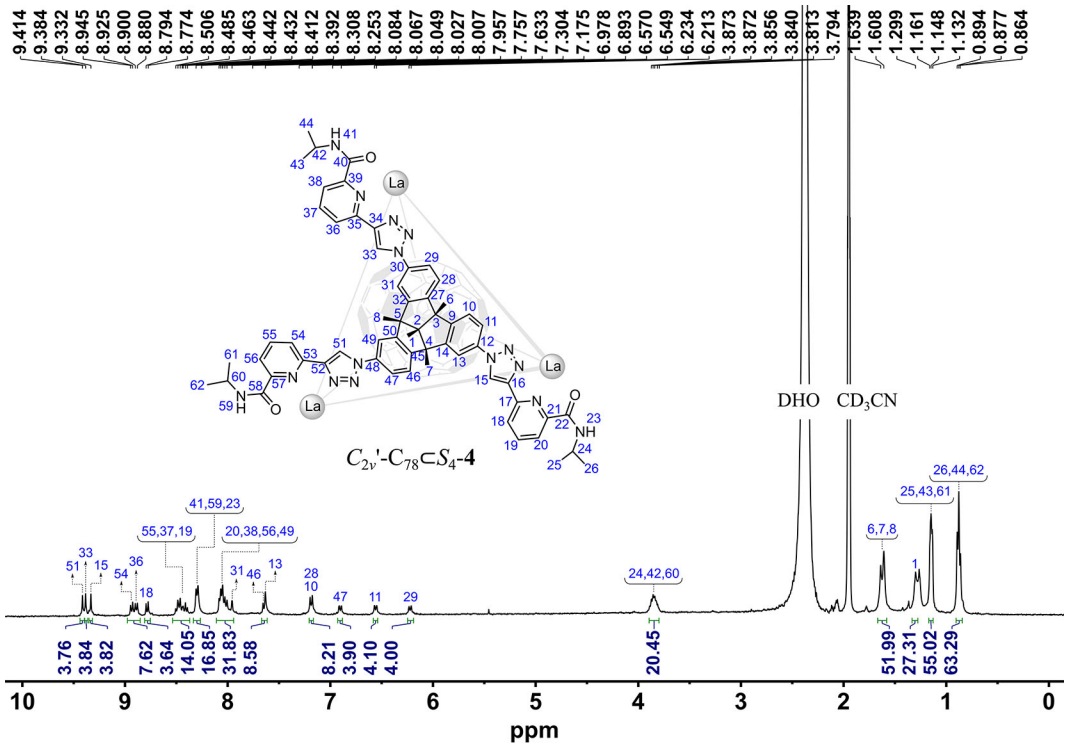

Fig. S98. ^{1}H NMR spectrum of C_{2v}'-C_{78}⊂S_4-**4** (400 MHz, 298 K, CD_3CN, [C_{2v}'-C_{78}⊂S_4-**4**] = 1.0 mM).

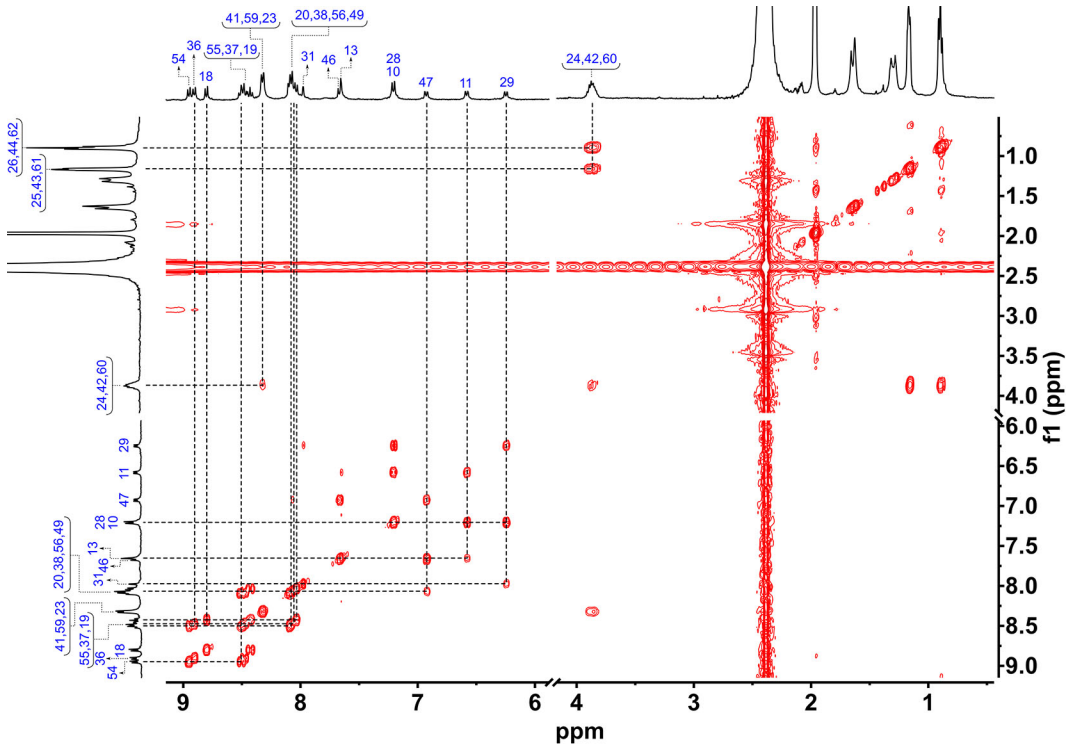

Fig. S99. Partial ^{1}H-^{1}H COSY spectrum of C_{2v}'-C$_{78}$⊂S_4-**4** (400 MHz, 298 K, CD$_3$CN, [C_{2v}'-C$_{78}$⊂S_4-**4**] = 1.0 mM).

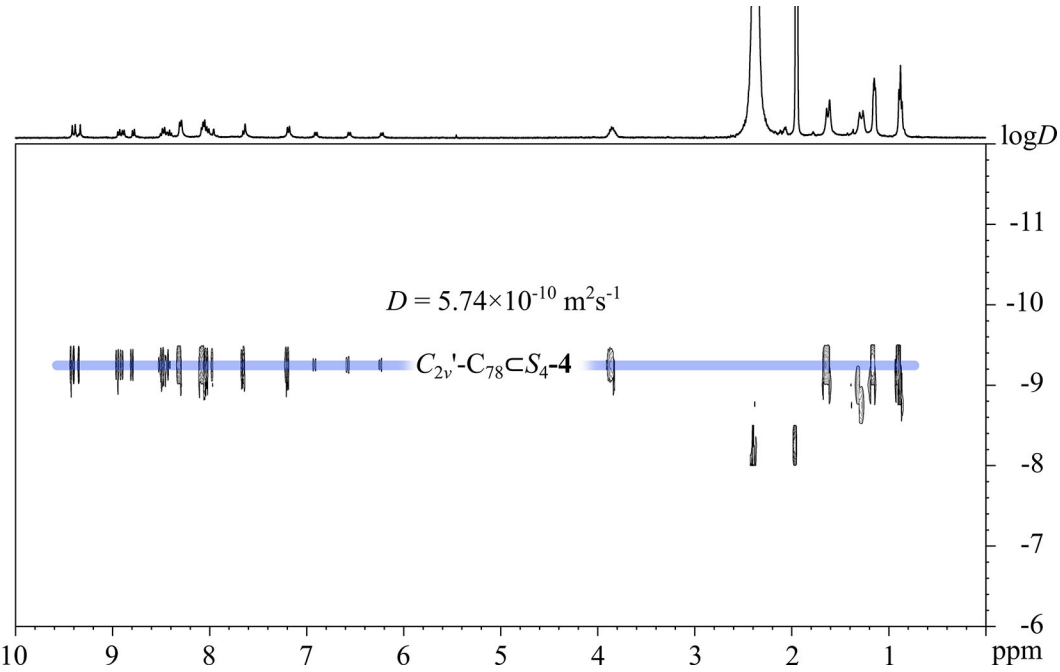

Fig. S100. ^{1}H DOSY spectrum of C_{2v}'-C$_{78}$⊂S_4-**4** (400 MHz, 298 K, CD$_3$CN, [C_{2v}'-C$_{78}$⊂S_4-**4**] = 1.0 mM). The hydrodynamic diameter of C_{2v}'-C$_{78}$⊂S_4-**4** was determined to be 2.2 nm.

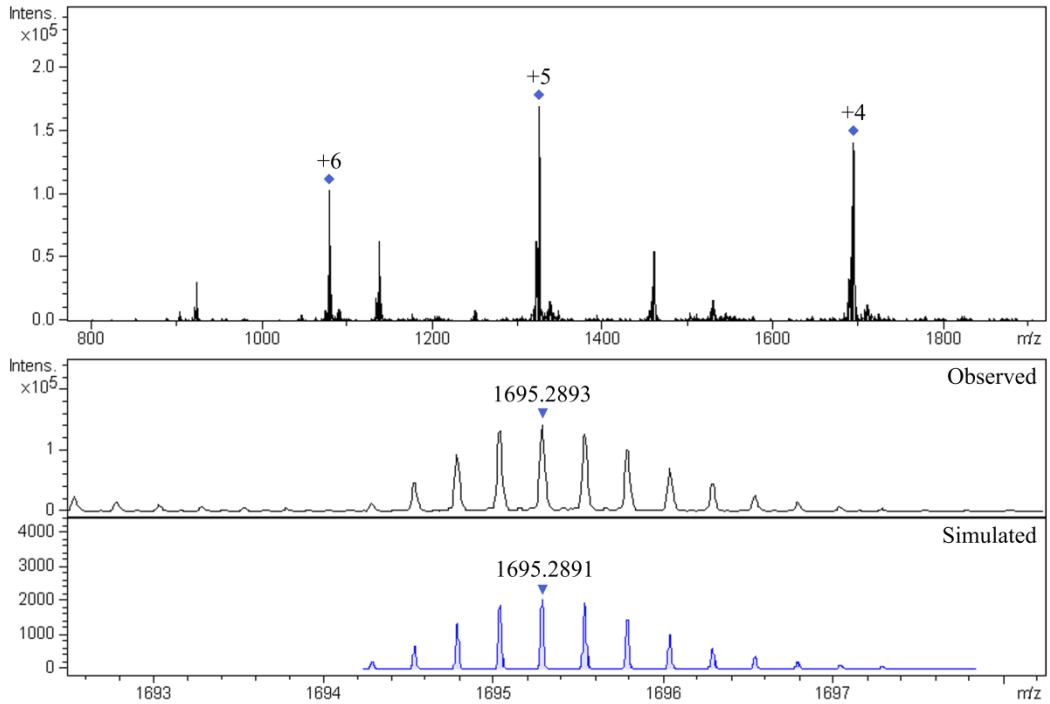

Fig. S101. High-resolution ESI-TOF-MS of C_{2v}'-$C_{78}\subset S_4$-**4** with the comparison of observed and simulated isotopic patterns of the peaks +4.

4. Assembly Behavior of Low-Symmetry Cage

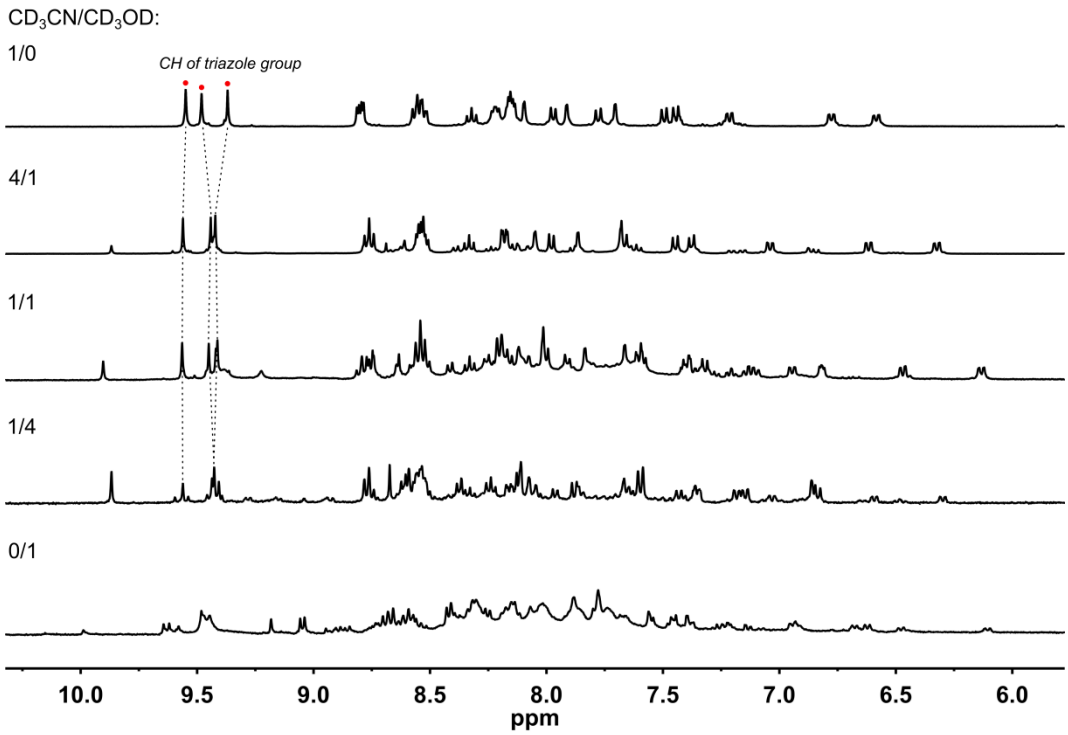

Fig. S102. ^{1}H NMR spectra of the self-assembly of C_1-**2** (3.9 mM) and La(OTf)$_3$ under variable solvent ratio conditions (400 MHz, 298 K, CD_3CN/MeOD v/v 1/0 to 0/1).

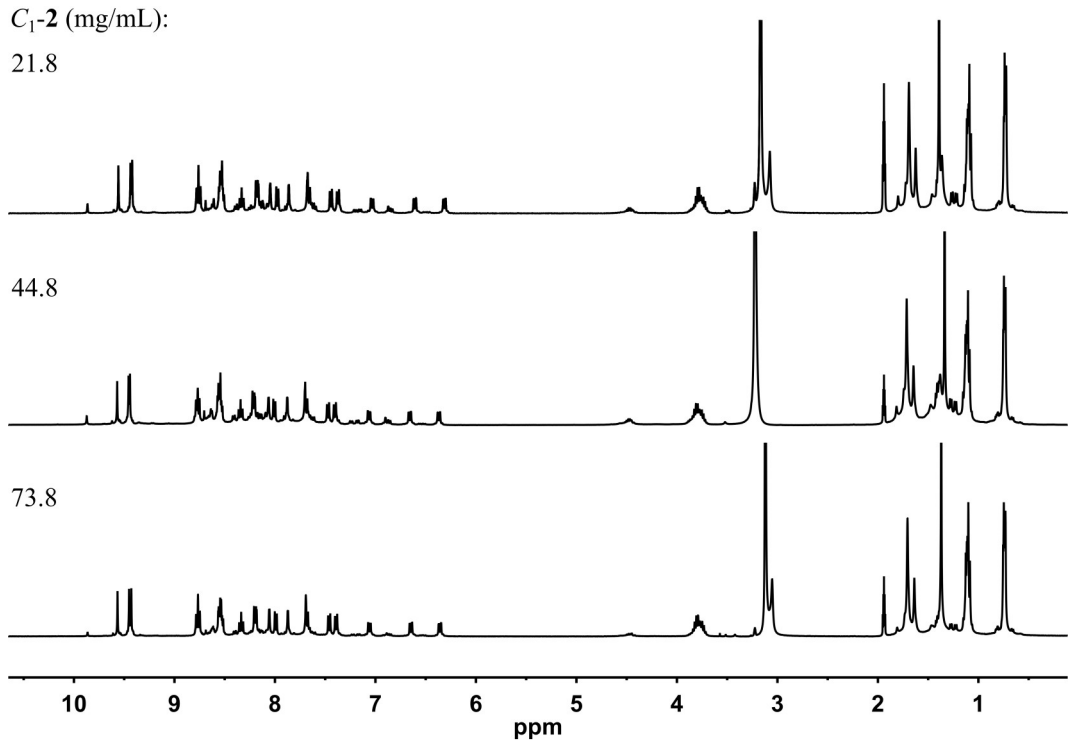

Fig. S103. ^{1}H NMR spectra of the self-assembly of C_1-**2** (3.9 mM) and La(OTf)$_3$ under variable ligand concentration conditions (400 MHz, 298 K, CD_3CN/MeOD v/v 4/1).

5. Conformation Analysis of *P*-2

Due to the free rotation of the C-N bond, *P*-**2** could theoretically generate eight possible conformations after coordinating with La^{3+} ion. Among them, when two TPA chelating arms close to each other adopt a back-to-back arrangement, *P*-**2** forms an anion binding cavity composed of two triazole C–H, two TBTQ C–H, and two pyridine C-H. These two conformations (*iii* and *iv*) resemble the triazolophane macrocycle reported by Flood's group.[S14] Thus, when *P*-**2** binds to a suitable anion, the anion acts as a template that drives the convergence of the dynamic library La_4(C_1-**2**)$_4$ to a single species.

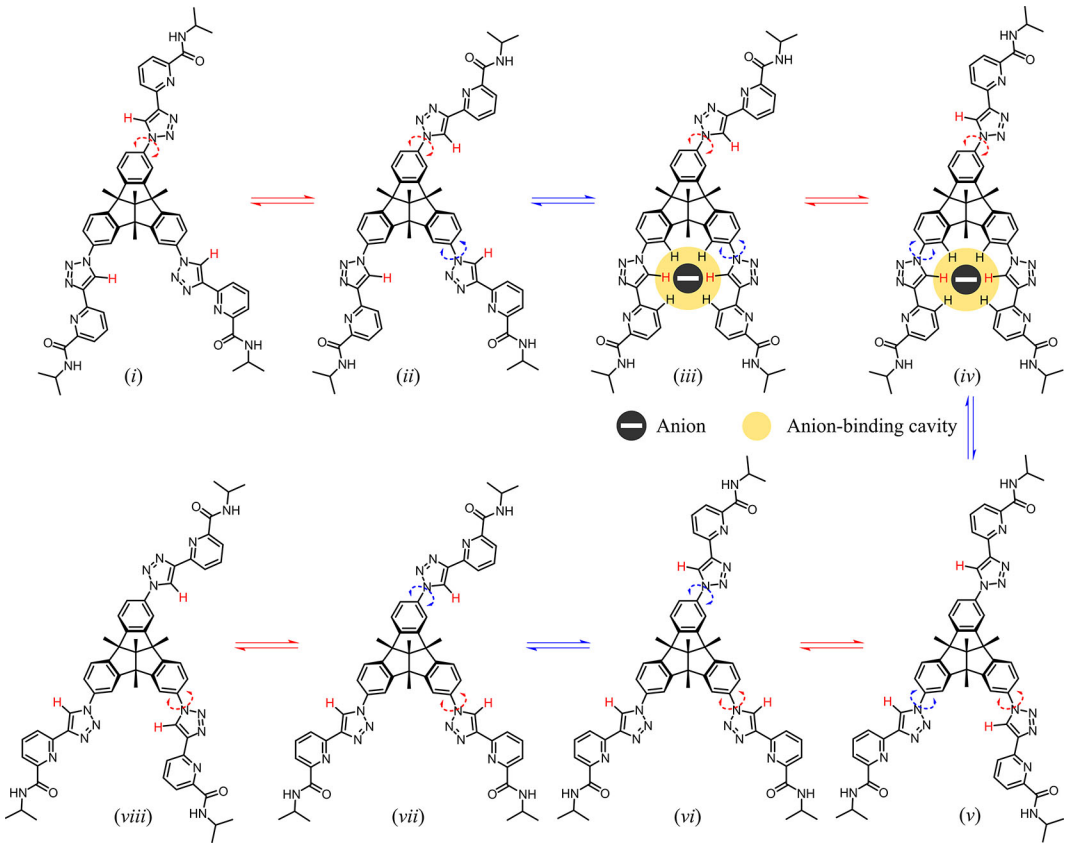

Fig. S104. Eight possible conformations of *P*-**2** after coordination with La^{3+} ion, where *iii* and *iv* conformations display anion-binding cavities.

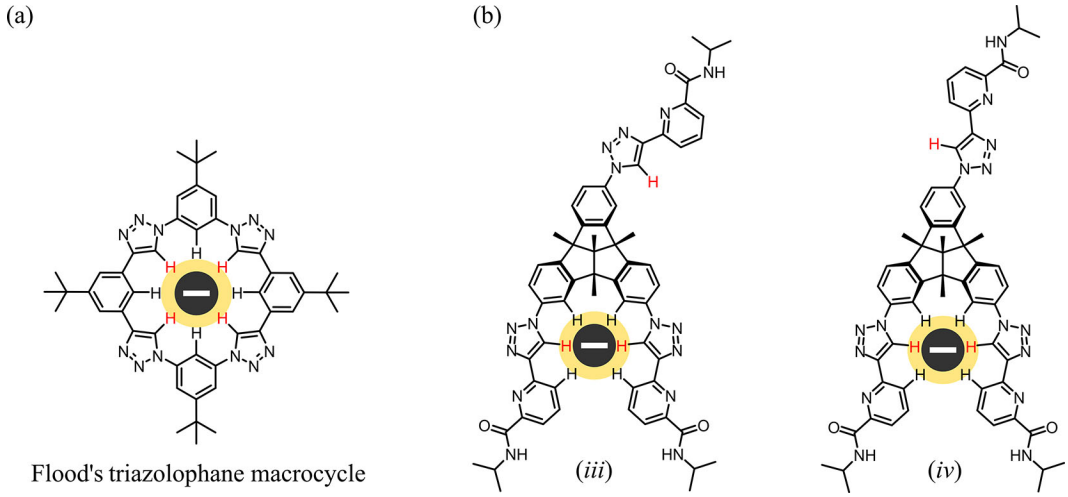

Fig. S105. (a) Flood's triazolophane macrocycle for anion recognition. (b) Two conformations of *P*-**2** display similar anion binding cavities.

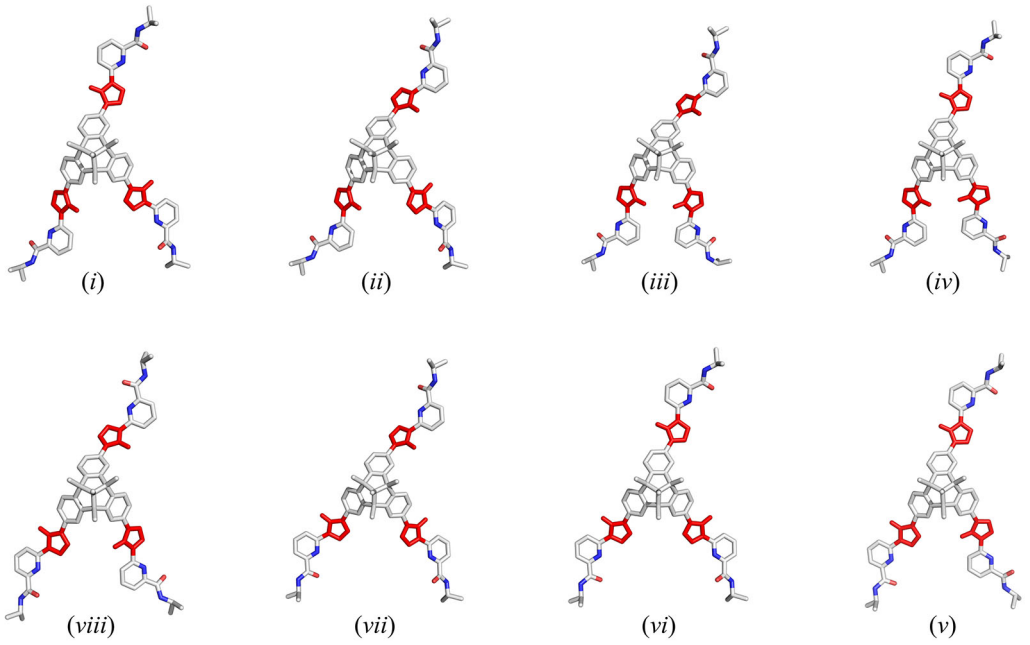

Fig. S106. Energy-optimized structures of eight conformations of *P*-**2** by using Materials Studio 7.0.

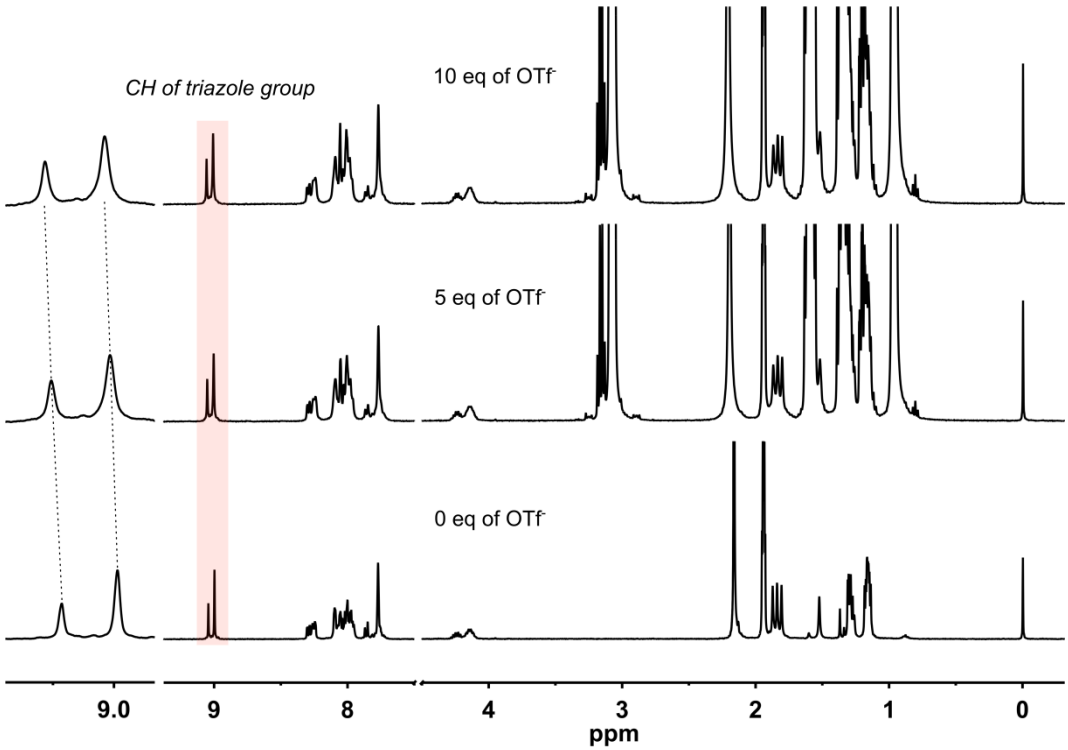

Fig. S107. ^{1}H NMR titration spectra (400 MHz, 298 K, CD_3CN) of C_1-**2** (3.9 mM) with different equiv of OTf^- anion.

6. Stereoisomer Analysis of Pseudo-Cubic Cages

6.1 Stereoisomers of $La_4(C_3\text{-}\mathbf{1})_4$

To analyze the potential isomers assembled by C_3-**1** and La^{III} ions, we abstracted the assemblies into brief pseudo-cubes. Each pseudo-cube consists of four metal coordination centers with the Δ/Λ configurations occupying opposite vertices, and four pyramidal ligands serving as the remaining four vertices, bridging three adjacent metal centers each. Theoretically, 25 combinations (Δ_4-P_4/M_4, Λ_4-P_4/M_4, Δ_4-P_3M/PM_3, Λ_4-P_3M/PM_3, Δ_4/Λ_4-P_2M_2, $\Delta_3\Lambda$-P_4/M_4, $\Delta\Lambda_3$-P_4/M_4, $\Delta_3\Lambda$-P_3M/PM_3, $\Delta\Lambda_3$-P_3M/PM_3, $\Delta_3\Lambda/\Delta\Lambda_3$-$P_2M_2$, $\Delta_2\Lambda_2$-P_4/M_4, $\Delta_2\Lambda_2$-P_3M/PM_3, $\Delta_2\Lambda_2$-P_2M_2) could be generated by integrating the P/M configuration of ligands and the Δ/Λ stereoconfiguration of metal centers. However, some combinations have many possible isomers depending on the distribution of metal coordination centers and chiral ligands. For example, $\Delta_3\Lambda$-P_3M could theoretically generate two isomers due to the different chemical environments of ligands at three *a* and one *b* positions (Fig. S108). Using an exhaustive method, we identified 36 possible isomers of $La_4(C_3\text{-}\mathbf{1})_4$ (Fig. S109).

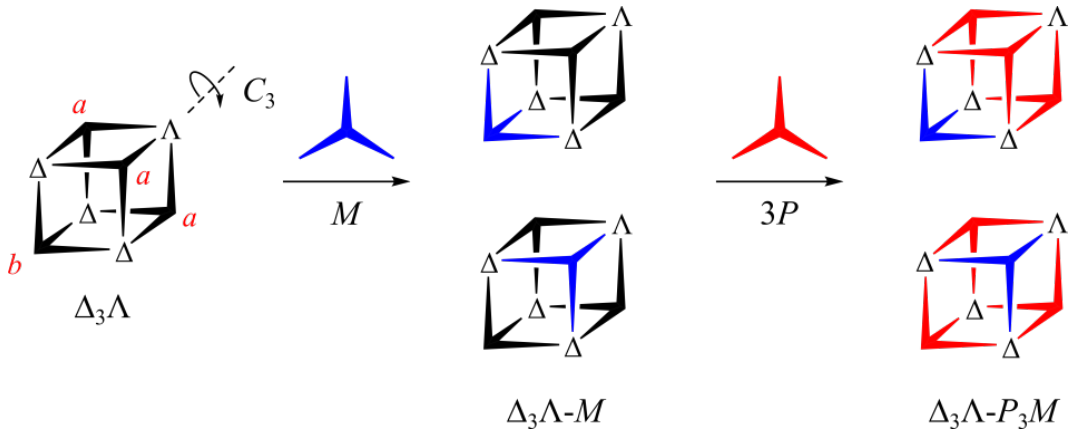

Fig. S108. Geometric analysis of potential isomers for $\Delta_3\Lambda$-P_3M based on symmetry operation.

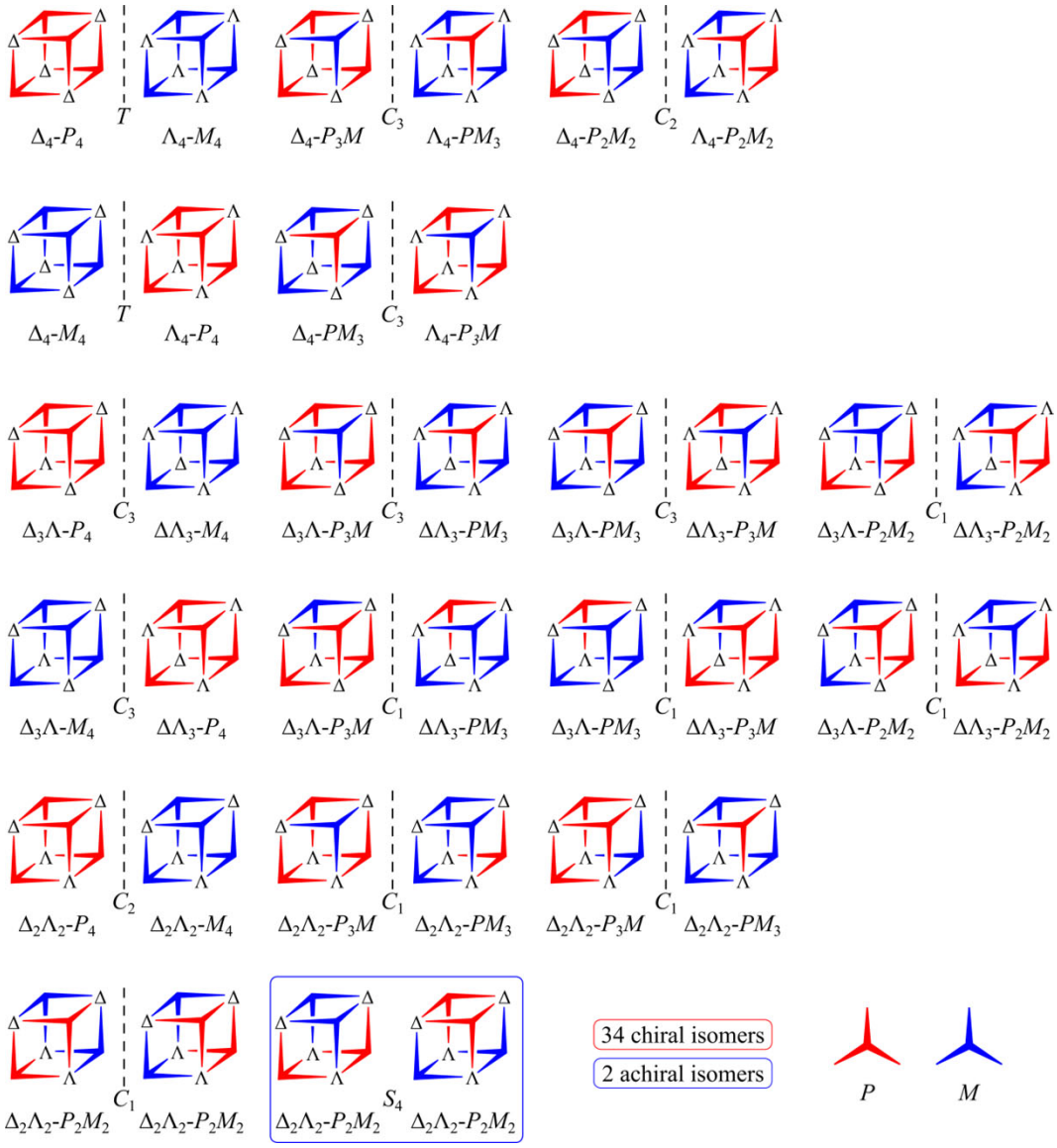

Fig. S109. Schematic structures of La$_4$(C_3-**1**)$_4$ illustrating 36 types of potential stereoisomers, of which 34 are chiral, and the remaining two are achiral (red schematic diagram represents propeller-like *P* configuration ligand C_3-**1**, while blue schematic diagram illustrates propeller-like *M* configuration ligand C_3-**1**; Δ/Λ, the chiral stereo-configuration of metal coordination centers).

6.2 Stereoisomers of La$_4$(C_1-**2**)$_4$

Like the isomer analysis of cage **3**, cage **4** was also simplified into a pseudo-cube. Unlike ligand **1** with C_3 symmetry, each C_1-symmetric ligand **2** might produce new isomers by rotating ca. ±120° along the opposite diagonal of the pseudo-cube. Furthermore, the rotational directionality of the ligand (*P*/*M*) and metal coordination center (Δ/Λ) would remain unchanged upon the symmetry operation. As a result, the number of isomers among the 25 combinations mentioned above between *P*/*M* and Δ/Λ would increase dramatically. To simplify the difficulty of isomer analysis, we split the

25 combinations into the following nine categories according to the number of isomers. A single representation from each class was sufficient to calculate the number of isomers by symmetry operation. In the case of fixed Δ/Λ metal vertices, the problem of painting *P*/*M* patterns on a pseudo-cube is similar to the mathematical classic polyhedron coloring problem, which can be calculated by Burnside's Lemme equation.

(1) Isomer analysis of Δ_4-P_4, Δ_4-M_4, Λ_4-P_4 and Λ_4-M_4

For Δ_4-P_4, we solved this problem by analyzing the symmetry elements of Δ_4: one identity operation (*E*), three C_2 rotational operations, four C_3 rotational operations, and the permutation groups of vertical patterns, as listed in the following Table S1.

Table S1. Calculation of the potential patterned pseudo-cube Δ_4-P_4 (inset indicating *T*-symmetric pseudo-cube Δ_4).

ΔΔΔΔ-P_4

T:

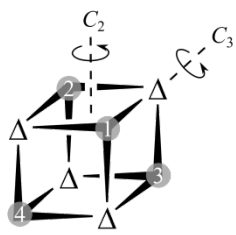

SE^i	PG^{ii}	SE^i	PG^{ii}	Types of painted cubes
E	(1)(2)(3)(4)	C_3^1	(134)(2)	
C_2^1	(12)(34)	C_3^2	(143)(2)	
C_2^1	(13)(24)	C_3^1	(124)(3)	$\frac{3^4 + 3 \times 3^2 + 8 \times 3^2}{1 + 3 + 8} = 15$
C_2^1	(14)(23)	C_3^2	(142)(1)	
C_3^1	(234)(1)	C_3^1	(123)(4)	
C_3^2	(243)(1)	C_3^2	(132)(4)	

(*i*): Symmetry elements (SE); (*ii*): Permutation groups (PG).

(2) Isomer analysis of Δ_4-P_3M, Δ_4-PM_3, Λ_4-P_3M and Λ_4-PM_3

For Δ_4-P_3M, when a *M* chiral ligand is first fixed to a specific pseudo-cube Δ_4 (four ligand positions are equivalent), the resulting Δ_4-*M* has C_1 symmetry, and it has only one identity operation (*E*). The permutation group is listed in the following Table S2.

Table S2. Calculation of the potential patterned pseudo-cube Δ_4-P_3M (inset indicating C_1-symmetric pseudo-cube Δ_4-*M*).

ΔΔΔΔ-P_3M

C_1:

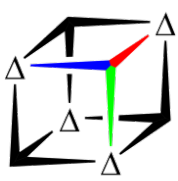

SE^i	PG^{ii}	Types of painted cubes
E	(1)(2)(3)	$\frac{3^3}{1} = 27$

(*i*): Symmetry elements (SE); (*ii*): Permutation groups (PG).

(3) Isomer analysis of Δ_4-P_2M_2 and Λ_4-P_2M_2

Since any ligand is adjacent to the remaining three ligands, we preferentially fix two *M* chiral ligands to a pseudo-cube Δ_4. Fig. S110 shows six possible arrangements for two adjacent *M* chiral ligands. Three of them show C_2 symmetry, and the others show C_1 symmetry. The combination of six M_2 patterns with a pseudo-cube Δ_4 gives three

C_2-symmetric and three C_1-symmetric Δ_4-M_2. The number of isomers of Δ_4-P_2M_2 can be simplified as the coloring problem of two P chiral ligands on six types of pseudo-cubes Δ_4-M_2. The permutation groups of vertical patterns are listed in the following Table S3-S4.

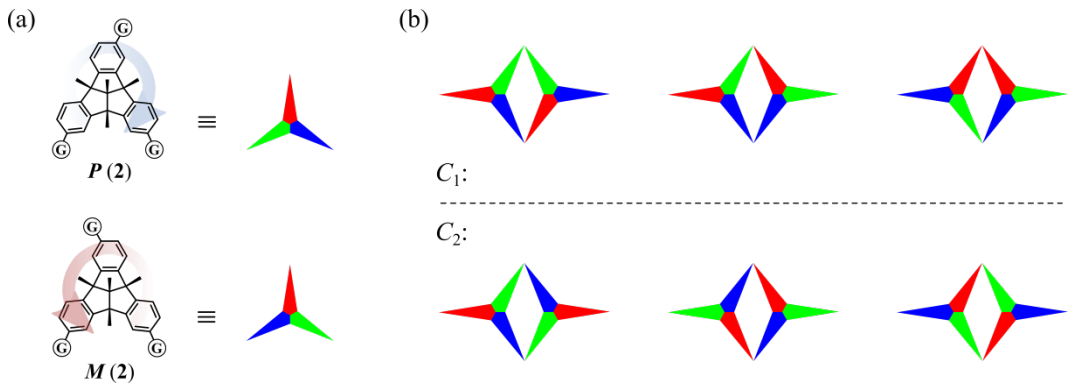

Fig. S110. (a) The P/*M* configuration ligands are represented by schematic diagrams with different color orders (G, cheating arms); (b) Six possible patterns of two adjacent *M* chiral ligands.

Table S3. Calculation of the potential patterned pseudo-cube Δ_4-P_2M_2 (inset indicating three C_2-symmetric pseudo-cubes Δ_4-M_2).

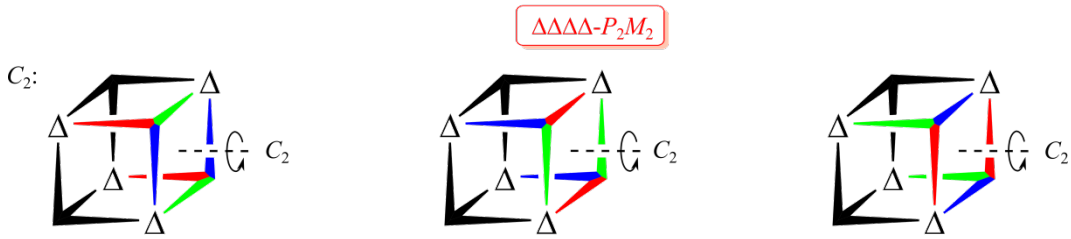

SE[i]	PG[ii]	Types of painted cubes
E	(1)(2)	$\frac{3^2+3^1}{1+1} \times 3 = 18$
C_2^1	(12)	

(*i*): Symmetry elements (SE); (*ii*): Permutation groups (PG).

Table S4. Calculation of the potential patterned pseudo-cube Δ_4-P_2M_2 (inset indicating three C_1-symmetric pseudo-cubes Δ_4-M_2).

$\Delta\Delta\Delta\Delta$-P_2M_2

C_1:

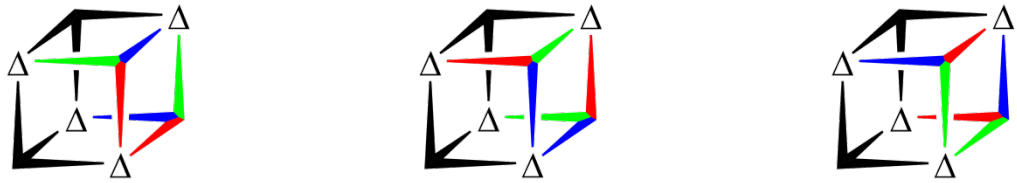

SE[i]	PG[ii]	Types of painted cubes
E	(1)(2)	$\frac{3^2}{1} \times 3 = 27$

(*i*): Symmetry elements (SE); (*ii*): Permutation groups (PG).

(4) Isomer analysis of $\Delta_3\Lambda$-P_4, $\Delta_3\Lambda$-M_4, $\Delta\Lambda_3$-P_4 and $\Delta\Lambda_3$-M_4

For $\Delta_3\Lambda$-P_4, we solved this problem by analyzing the symmetry elements of pseudo-cube $\Delta_3\Lambda$: one identity operation (E), one C_3 rotational operation, and the permutation groups of vertical patterns, as listed in the following Table S5.

Table S5. Calculation of the potential patterned pseudo-cube $\Delta_3\Lambda$-P_4 (inset indicating C_3-symmetric pseudo-cube $\Delta_3\Lambda$).

$\Delta\Delta\Delta\Lambda$-$P_4$

C_3:

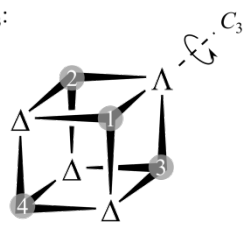

SE[i]	PG[ii]	Types of painted cubes
E	(1)(2)(3)(4)	$\frac{3^4 + 2 \times 3^2}{1 + 2} = 33$
C_3^1	(123)(4)	
C_3^2	(132)(4)	

(*i*): Symmetry elements (SE); (*ii*): Permutation groups (PG).

(5) Isomer analysis of $\Delta_3\Lambda$-P_3M, $\Delta_3\Lambda$-PM_3, $\Delta\Lambda_3$-P_3M and $\Delta\Lambda_3$-PM_3

Given the C_3 rotation axis of pseudo-cube $\Delta_3\Lambda$, ligand positions 1,2,3 are equivalent but not 4. Thus, six isomers with C_1 symmetry can be obtained by fixing one M chiral ligand on the pseudo-cube $\Delta_3\Lambda$. The number of isomers of $\Delta_3\Lambda$-P_3M can be simplified as the coloring problem of three P chiral ligands on six types of pseudo-cubes $\Delta_3\Lambda$-M. The resulting six $\Delta_3\Lambda$-M all exhibit one identity operation (E). The permutation operations are listed in the following Table S6.

Table S6. Calculation of the potential patterned pseudo-cube $\Delta_3\Lambda$-P_3M (inset indicating six C_1-symmetric pseudo-cubes $\Delta_3\Lambda$-M).

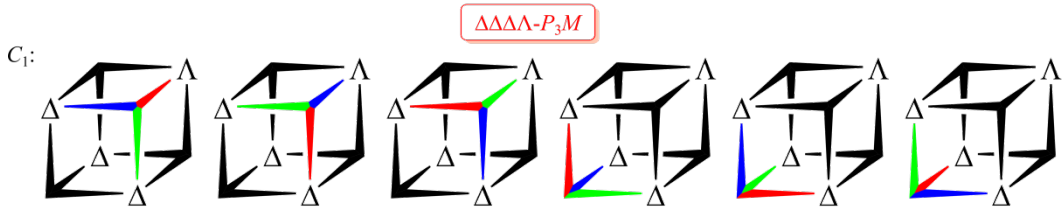

SE[i]	PG[ii]	Types of painted cubes
E	(1)(2)(3)	$\frac{3^3}{1} \times 6 = 162$

(*i*): Symmetry elements (SE); (*ii*): Permutation groups (PG).

(6) Isomer analysis of $\Delta_3\Lambda$-P_2M_2 and $\Delta\Lambda_3$-P_2M_2

In our previous analysis of Δ_4-P_2M_2 isomer, we mentioned six possible patterns (three with C_2 symmetry and three with C_1 symmetry) that result from combining two M chiral ligands. Here, when M_2 is attached to the pseudo-cube $\Delta_3\Lambda$, it must pass through one of the six edges (ABCDEF) of the embedded tetrahedron. Moreover, due to the C_3 symmetry of the pseudo-cube $\Delta_3\Lambda$, edges A, B and C (or D, E and F) are equivalent. Therefore, six possible $\Delta_3\Lambda$-M_2 isomers can be obtained by attaching three types of M_2 with C_2 symmetry. By immobilizing three types of M_2 with C_1 symmetry to the pseudo-cube $\Delta_3\Lambda$, we can get twelve possible $\Delta_3\Lambda$-M_2 isomers. The number of isomers for $\Delta_3\Lambda$-P_2M_2 can be simplified as a coloring problem of two P chiral ligands on eighteen types of pseudo-cubes $\Delta_3\Lambda$-M_2. The permutation groups of vertical patterns are listed in the following Table S7.

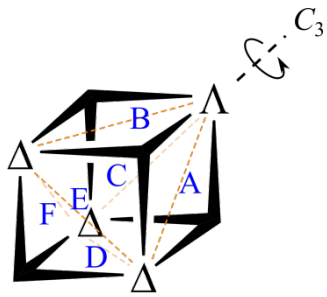

Table S7. Calculation of the potential patterned pseudo-cube $\Delta_3\Lambda$-P_2M_2 (inset indicating eighteen C_1-symmetric pseudo-cubes $\Delta_3\Lambda$-M_2).

$\Delta\Delta\Delta\Lambda$-$P_2M_2$

C_1:

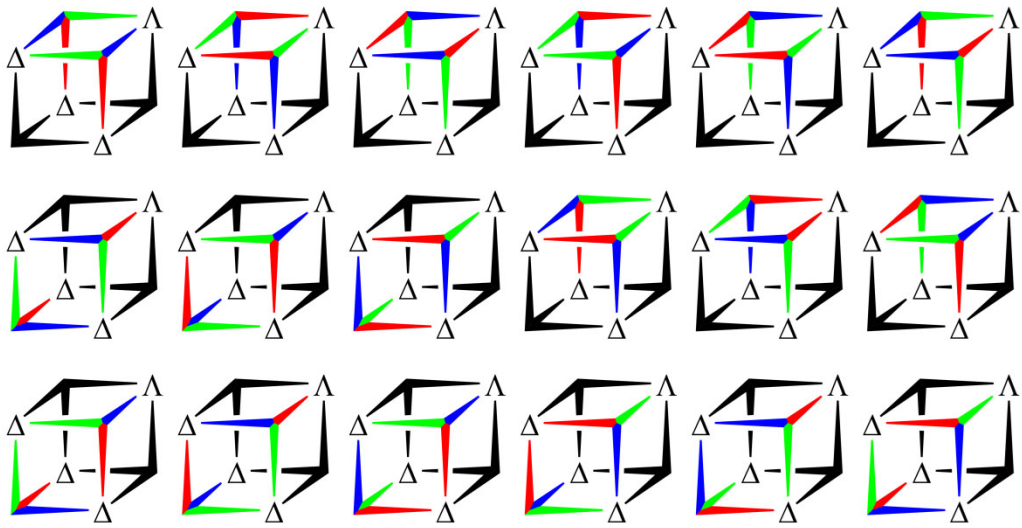

SE[i]	PG[ii]	Types of painted cubes
E	(1)(2)	$\frac{3^2}{1} \times 18 = 162$

(*i*): Symmetry elements (SE); (*ii*): Permutation groups (PG).

(7) Isomer analysis of $\Delta_2\Lambda_2$-P_4 and $\Delta_2\Lambda_2$-M_4

For $\Delta_2\Lambda_2$-P_4, we solved this problem by analyzing the symmetry elements of pseudo-cube $\Delta_2\Lambda_2$: one identity operation (E), one C_2 rotational operation, and the permutation groups of vertical patterns, as listed in the following Table S8.

Table S8. Calculation of the potential patterned pseudo-cube $\Delta_2\Lambda_2$-P_4 (inset indicating C_2-symmetric pseudo-cube $\Delta_2\Lambda_2$).

$\Delta\Delta\Lambda\Lambda$-$P_4$

C_2:

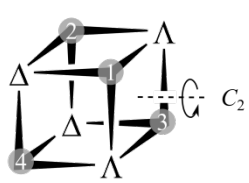

SE[i]	PG[ii]	Types of painted cubes
E	(1)(2)(3)(4)	$\frac{3^4 + 3^2}{1 + 1} = 45$
C_2^1	(13)(24)	

(*i*): Symmetry elements (SE); (*ii*): Permutation groups (PG).

(8) Isomer analysis of $\Delta_2\Lambda_2$-P_3M and $\Delta_2\Lambda_2$-PM_3

Given the C_2 rotation axis of pseudo-cube $\Delta_2\Lambda_2$, ligand positions 1, 3 (or 2, 4) are equivalent. By immobilizing one M chiral ligand on pseudo-cube $\Delta_2\Lambda_2$, we can generate six isomers of $\Delta_2\Lambda_2$-M. We can simplify the number of isomers for $\Delta_2\Lambda_2$-P_3M as a coloring problem of three P chiral ligands on six types of pseudo-cubes $\Delta_2\Lambda_2$-M. The permutation groups of vertical patterns are listed in the following Table S9.

Table S9. Calculation of the potential patterned pseudo-cube $\Delta_2\Lambda_2$-P_3M (inset indicating C_1-symmetric pseudo-cube $\Delta_2\Lambda_2$-M).

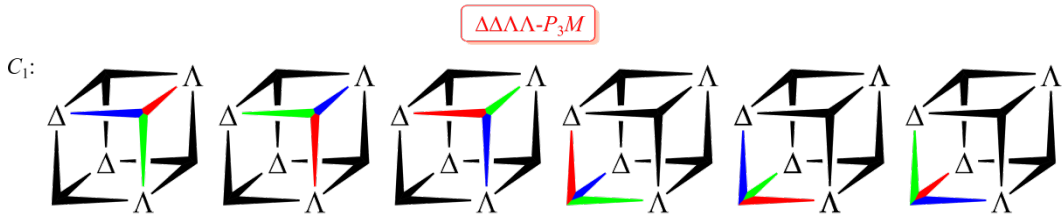

SE[i]	PG[ii]	Types of painted cubes
E	(1)(2)(3)	$\frac{3^3}{1} \times 6 = 162$

(*i*): Symmetry elements (SE); (*ii*): Permutation groups (PG).

(9) Isomer analysis of $\Delta_2\Lambda_2$-P_2M_2

Since the pseudo-cube $\Delta_2\Lambda_2$ has a C_2 rotation axis, the ligand positions 1 and 3 (or 2 and 4) are equivalent. To preserve the original C_2 rotation axis of the pseudo-cube $\Delta_2\Lambda_2$, three M_2 patterns with C_2 symmetry can be fixed along either edge A or F of the embedded tetrahedron, resulting in six possible C_2-symmetric $\Delta_2\Lambda_2$-M_2. On the other hand, placing six M_2 patterns on any of the other four edges (BCDE) can generate 42 possible C_1-symmetric $\Delta_2\Lambda_2$-M_2 isomers. The number of isomers for $\Delta_2\Lambda_2$-P_2M_2 can be simplified as a coloring problem of two P chiral ligands on six C_2-symmetric pseudo-cubes $\Delta_2\Lambda_2$-M_2 and 42 C_1-symmetric pseudo-cubes $\Delta_2\Lambda_2$-M_2. The permutation groups of vertical patterns are listed in the following Table S10-S11.

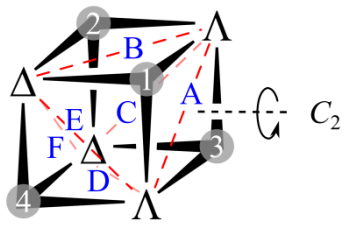

Table S10. Calculation of the potential patterned pseudo-cube $\Delta_2\Lambda_2$-P_2M_2 (inset indicating six C_2-symmetric pseudo-cubes $\Delta_2\Lambda_2$-M_2).

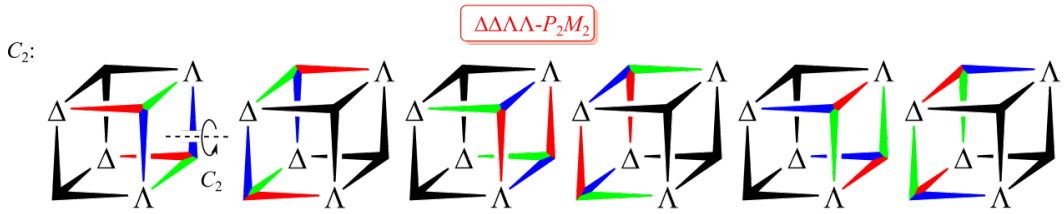

SE[i]	PG[ii]	Types of painted cubes
E	(2)(4)	$\frac{3^2 + 3^1}{1 + 1} \times 6 = 36$
C_2^1	(24)	

(*i*): Symmetry elements (SE); (*ii*): Permutation groups (PG).

Table S11. Calculation of the potential patterned pseudo-cube $\Delta_2\Lambda_2$-P_2M_2 (inset indicating 42 C_2-symmetric pseudo-cubes $\Delta_2\Lambda_2$-M_2).

$\Delta\Delta\Lambda\Lambda$-$P_2M_2$

C_1:

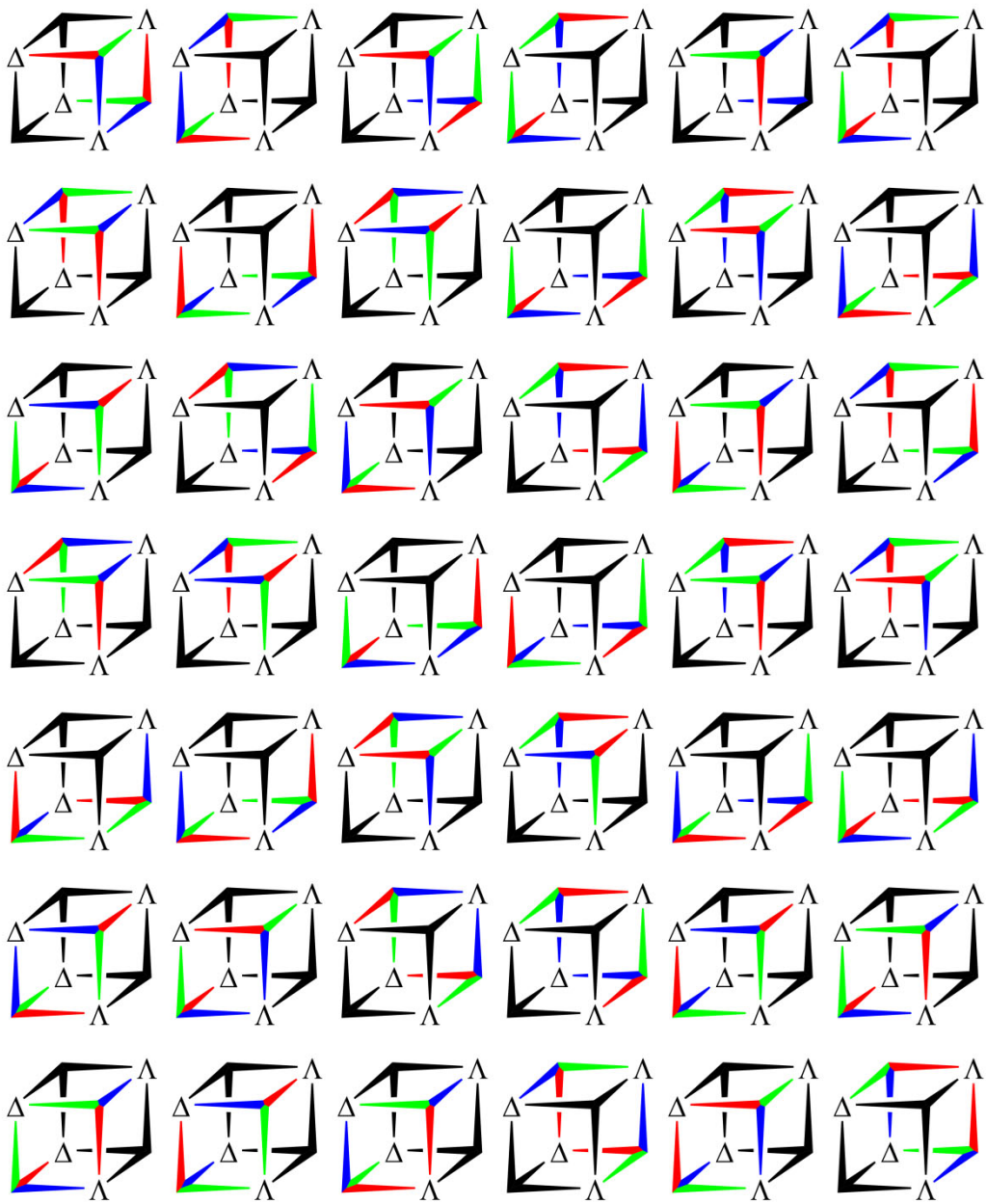

SE[i]	PG[ii]	Types of painted cubes
E	(1)(2)	$\frac{3^2}{1} \times 42 = 378$

(*i*): Symmetry elements (SE); (*ii*): Permutation groups (PG).

Table S12. Summary of the isomer number for $La_4(C_1\text{-}\mathbf{2})_4$.

	Δ_4	$\Delta_3\Lambda$	$\Delta_2\Lambda_2$	$\Delta\Lambda_3$	Λ_4
M_4	15	33	45	33	15
M_3P	27	162	162	162	27
M_2P_2	45	162	414	162	45
MP_3	27	162	162	162	27
P_4	15	33	45	33	15
sum			2190		

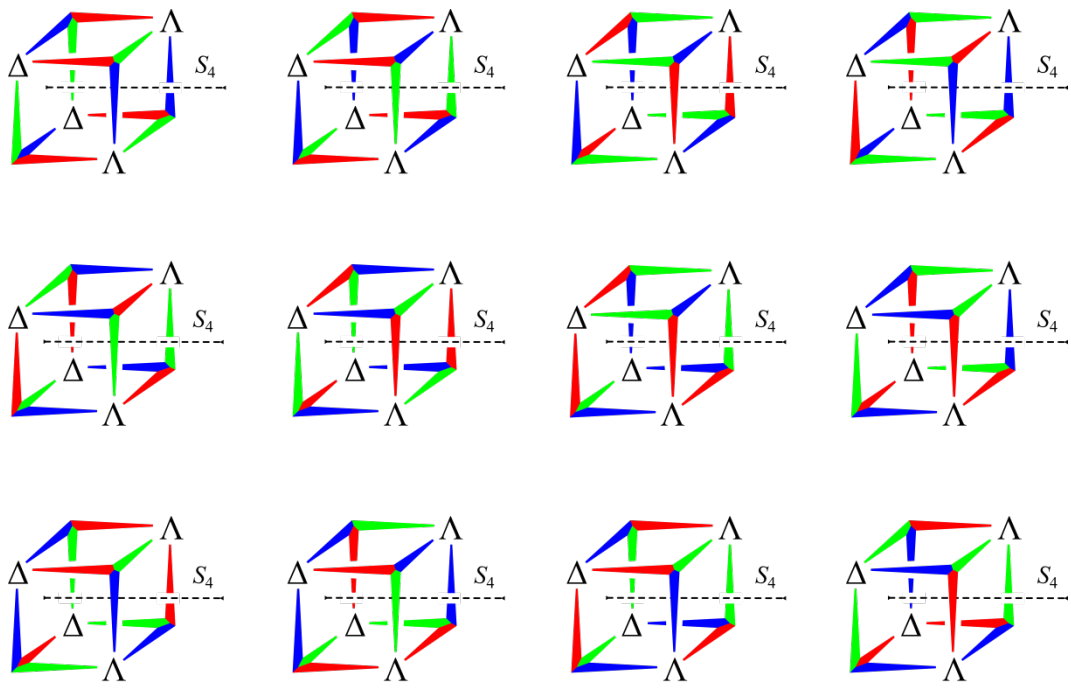

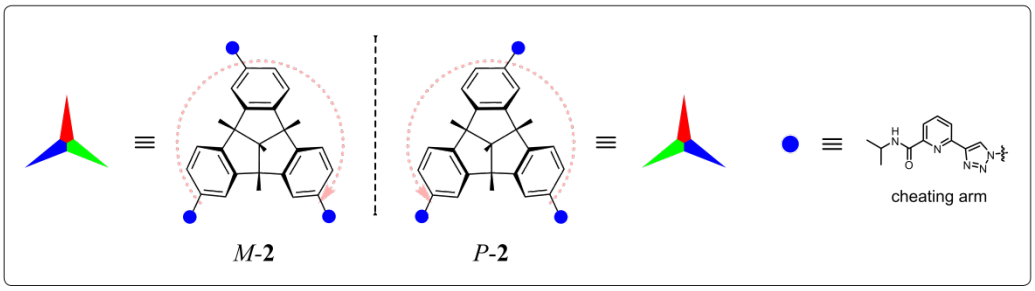

Fig. S111. 12 types of achiral mesomers $La_4(C_1\text{-}\mathbf{2})_4$ with S_4 symmetry.

7. Volume and Sphericity Calculation

The recognition ability of the host cavity for guest is closely related to the matching degree of volume and shape between them. To determine the molecular volumes (V_{mol}) of fullerene guests and the inner cavity volumes of the complexes before and after encapsulation, MoloVol calculations (https://molovol.com/)[S54] based on the crystal structures were performed using single probe mode. For fullerene molecules, the program parameters were set as follows: small probe radius: 1.2 Å; grid resolution: 0.2 Å; optimization depth: 4. For cage cavities, the program parameters were set as follows: small probe radius: 2.4 Å; grid resolution: 0.2 Å; optimization depth: 4. Additionally, sphericity[S15] was employed to reflect the shape of host cavity and guest. The concept of sphericity is a measure of how spherical an object is, which is defined as the ratio of the surface area of an equal-volume sphere to the actual surface area of the particle:

$$\psi = \frac{\pi^{1/3}(6V)^{2/3}}{A}$$

Where V is the molecular volume (V_{mol}) of fullerene guests or the cavity volume (V_c) of cage and A is the probe excluded surface (S_{excl}) of fullerene guests and the cage cavity. The detailed calculation results were shown in Table S13.

Table S13. Calculated volumes and sphericities of fullerenes and cages by MoloVol.

Guest/Cage	V_{mol}[1] / V_c[2] (Å^3)	S_{excl} (Å^2)	Ψ
C_{60} (I_h)	561	385	0.85
C_{70} (D_{5h})	652	434	0.84
C_{76} (D_2)	835	536	0.80
C_{78} (C_{2v})	859	549	0.80
C_{78} (C_{2v}')	861	550	0.80
T-**3**	810	444	0.95
S_4-**4**	1079	563	0.91
S_4-**4** (C_{60})	921	499	0.92
S_4-**4** (C_{70})	980	526	0.91

Note: [1]Molecular volume of fullerene; [2]Cavity volume of cage.

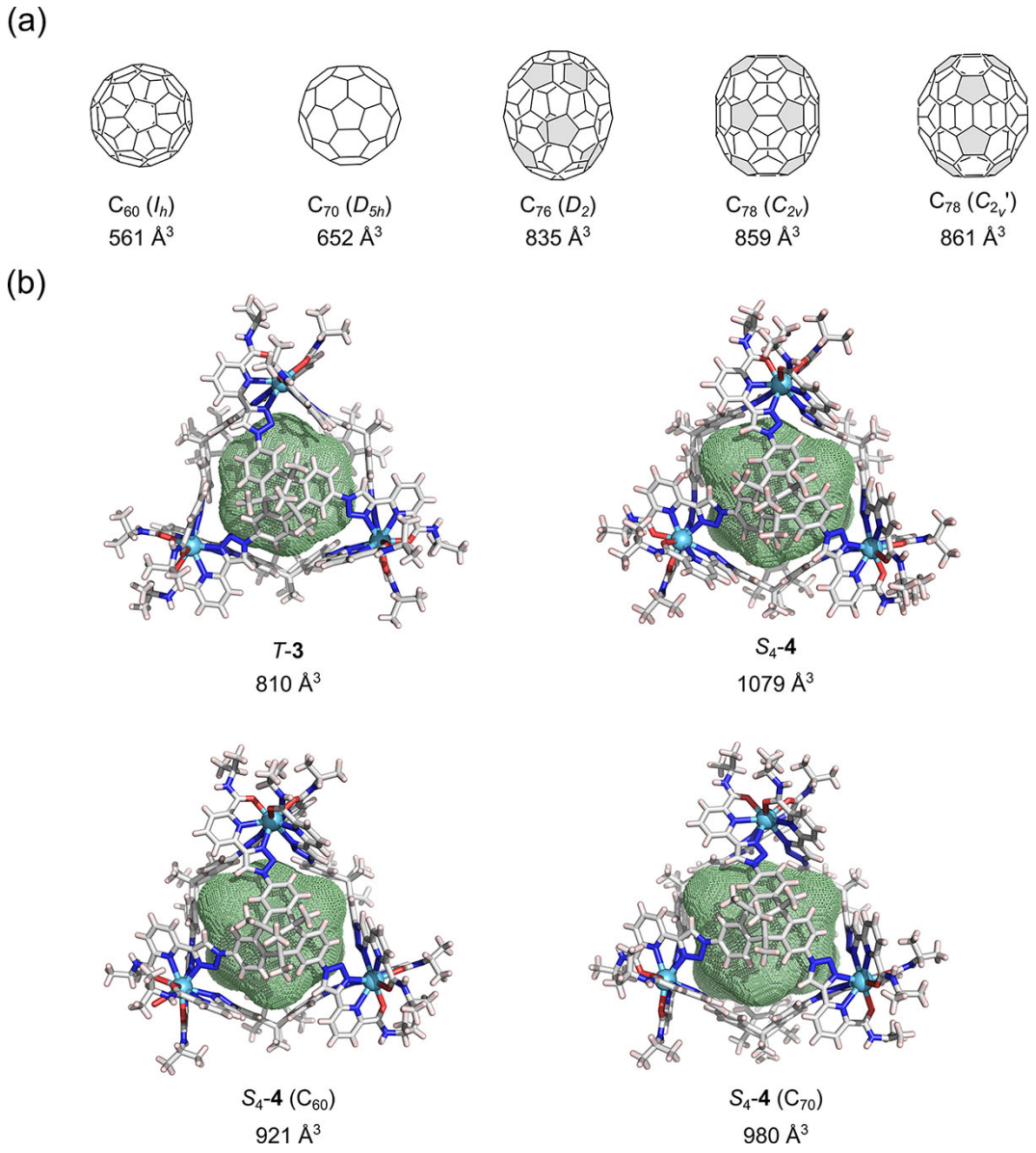

Fig. S112. MoloVol-calculated the molecular volumes of fullerene guests (a) and the inner void spaces (pale green mesh) of the pseudo-cubic cages (b) before and after encapsulating fullerene guests.

8. Enantioseparation and Configuration Assignment of *P*-1 and *M*-1

8.1 Chiral HPLC separation for C_3-**1**

HPLC analyses were performed on the SHIMADZU LC-20A instrument with a chiral Enantiopak®SDMP column (4.6*250 mm, 5μm). The racemic C_3-**1** was dissolved in pure ethanol and injected into the chiral analysis column (Injecting volume: 20 μL; Sample concentration: 0.3 mg/mL). The HPLC parameters were set as follows: Mobile phase: n-Hexane/EtOH = 55/45; Flow rate: 1 mL/min; Detecting wavelength: 254 nm.

Using the separation conditions established by HPLC, we further separated the racemic C_3-**1** on a Waters Prep 150 LC instrument with a chiral Enantiopak®SDMP column (10.0*250 mm, 5μm; Injecting volume: 2.5 mL; Sample concentration: 2.3 mg/mL) and obtained enantiomers *P*-**1** and *M*-**1**.

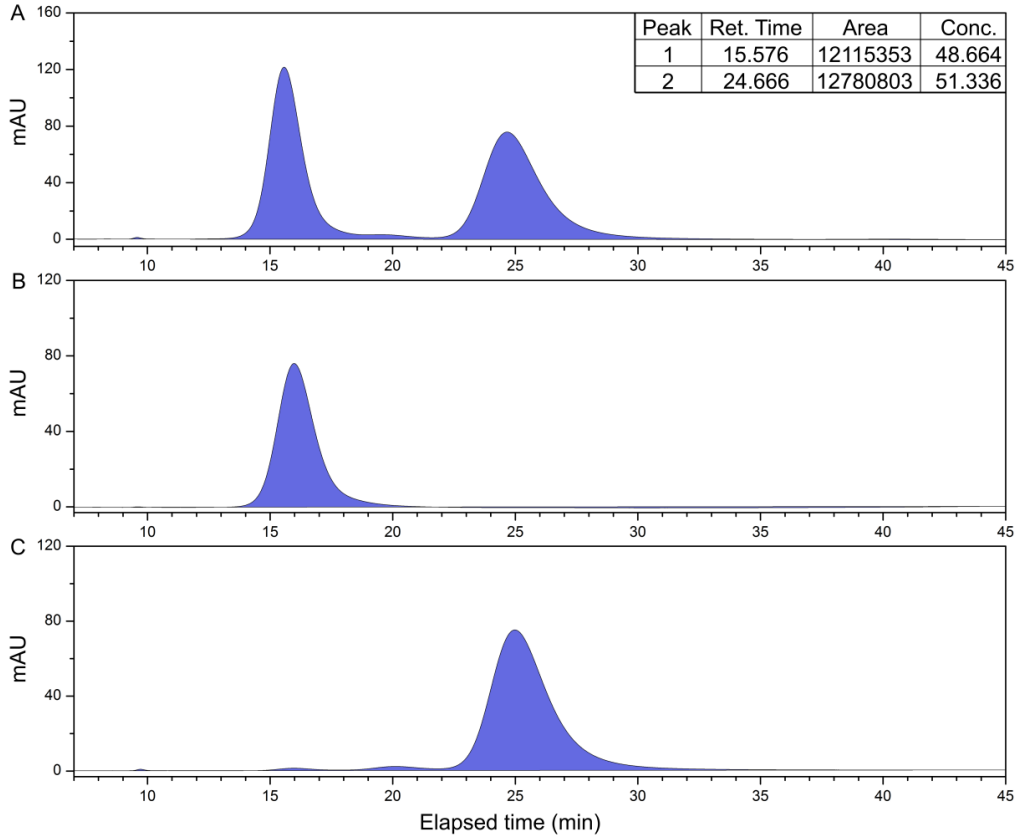

Fig. S113. (A) HPLC of racemic C_3-**1**. (B) HPLC of first fraction separated by Prep LC. (C) HPLC of second fraction separated by Prep LC.

8.2 Circular dichroism

The Circular dichroism (CD) spectra of *P*-**1** and *M*-**1** were recorded at room temperature on a MOS-450 circular dichroism spectrometer. The sample was dissolved in dichloromethane (2.0×10^{-5} M) and added into a quartz cell with 0.5 cm optical path length. Before the CD spectrum test, the baseline was corrected under the blank solvent condition.

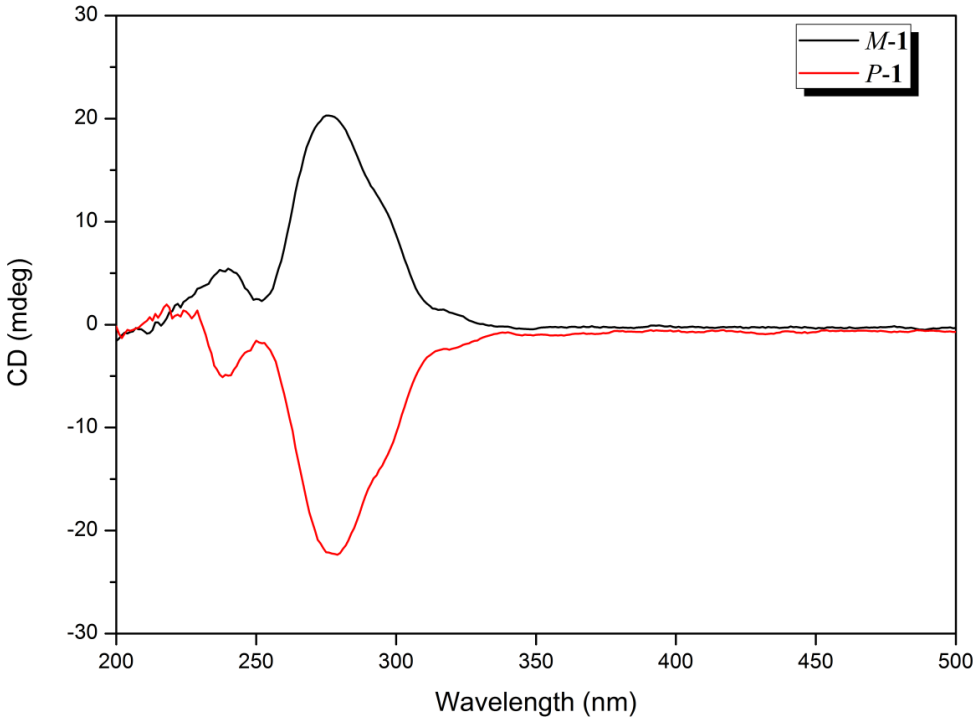

Fig. S114. CD spectra of *P*-**1** and *M*-**1** in DCM (2.0×10^{-5} M).

8.3 Absolute configuration determination by X-ray crystallography

The crystals of the second fraction of C_3-**1** separated by Prep LC were obtained through slow volatilization of the chloroform solution of the ligand, and the X-ray diffraction data were collected on a micro-focus metal jet diffractometer with Ga Kα radiation. Data reduction was performed with the CrysAlisPro package,[S2] and the Flack value was found to be 0.04(7), indicating that the absolute configuration *P* confirmed by X-ray diffraction was reliable. On the contrary, the first fraction of C_3-**1** can be determined to be of the *M* configuration.

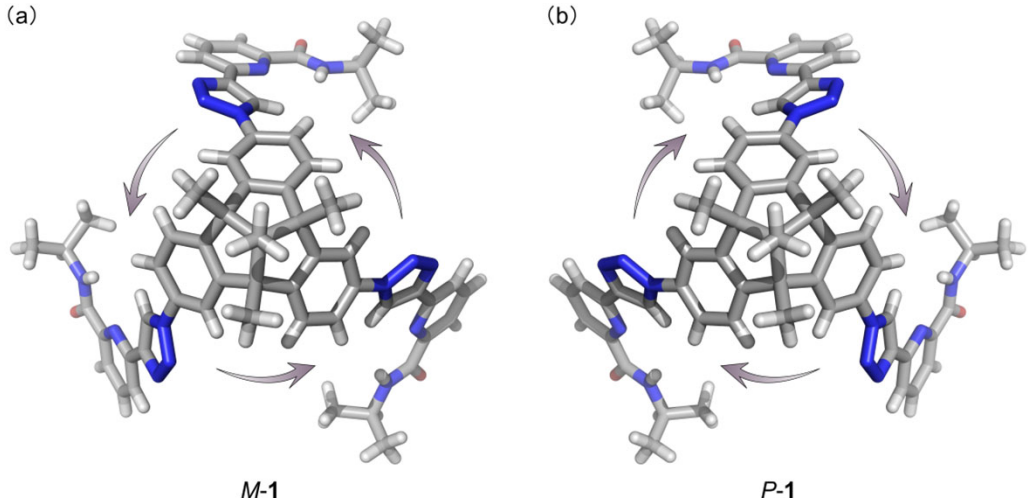

Fig. S115. (a) Energy-minimized structure of the first fraction of C_3-**1** with the *M* configuration. (b) Crystal structure of the second fraction of C_3-**1** with the *P* configuration (Solvent chloroform was removed for clarity).

9. Synthesis and Characterization of Fullerene Isomers

9.1 Preparation and isolation

A graphite rod, obtained through core drilling, was filled with graphite powder. Subsequently, the rods underwent annealing in a tube furnace at 1000°C for 12 hours under an argon atmosphere. They were then vaporized in a Krätschmer-Huffman-type fullerene generator, utilizing an arc current of 100 A, and operating under a helium atmosphere at 270 Torr. The resulting fullerene soot was collected and subjected to sonication in carbon disulfide for 1 hour. Following filtration, CS_2 was removed via a rotary evaporator. The remaining solid residue was dissolved in toluene and filtered. The separation and purification of C_{76}, C_{78}-I, and C_{78}-II were accomplished using a multi-stage HPLC process with toluene as the eluent. The initial stage employed a Buckyprep column (20 mm × 250 mm, Cosmosil Nacalai Tesque), and a fraction named Fr3 was collected (Fig. S116a). Fr3 was subsequently injected into another Buckyprep column (20 mm × 250 mm, Cosmosil Nacalai Tesque) for recycling separation, resulting in the final isolation of C_{76} (Fr3-1), C_{78}-I (Fr3-2), and C_{78}-II (Fr3-3) (Fig. S116b). The high purity of these compounds was verified by analytical HPLC chromatograms and mass spectra (Fig. S117).

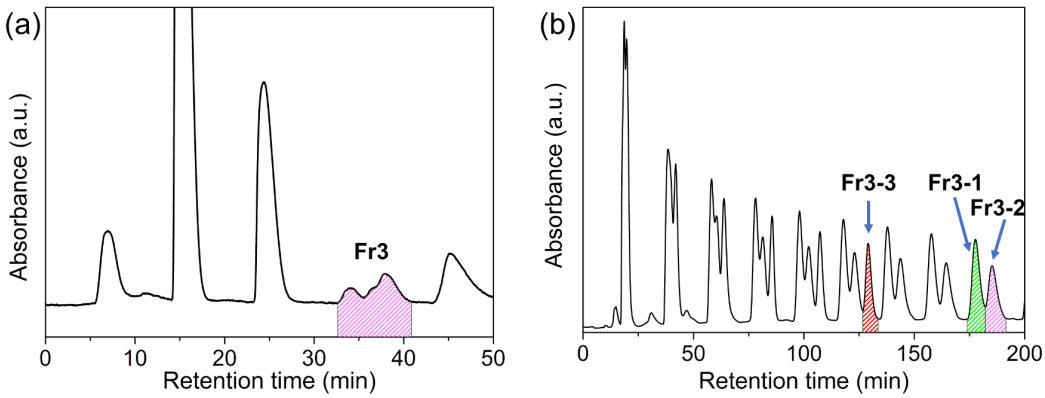

Fig. S116. (a) Isolation scheme of fullerene extract on a Buckyprep column. Conditions: 20 mL inject volume; 10 mL/min toluene flow; (b) Recycling HPLC chromatogram of Fr3 on a Buckyprep-M column. Conditions: 10 mL injection volume; 10 mL/min toluene flow. 330 nm detection wavelength.

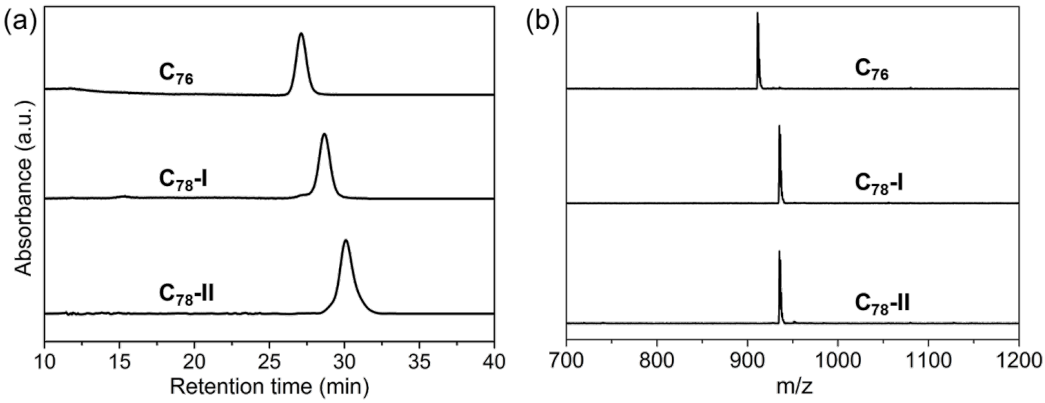

Fig. S117. (a) HPLC chromatograms and (b) LDI-TOF mass spectra of C_{76}, C_{78}-I, and C_{78}-II. HPLC conditions: Buckyprep column (∅ = 4.6 × 250 mm); 20 μL injection volume; 1 mL min^{-1} toluene flow; 330 nm detection wavelength; 40 °C.

9.2 Crystallographic characterizations

Black co-crystals of fullerenes and Ni^{II}(OEP) were obtained by layering a benzene solution of Ni^{II}(OEP) over a CS_2 solution of the respective fullerenes in a glass tube at 0 °C for 30 days. Single-crystal X-ray data were collected at a temperature of 100 K using a radiation wavelength of 0.71073 Å with a MarCCD detector at beamline BL17B in the Shanghai Synchrotron Radiation Facility (SSRF). For absorption corrections, a multi-scan method was employed. The crystal structures were solved using direct methods and refined using SHELXL-2014.[S58] Hydrogen atoms were placed at calculated positions and restrained with isotropic thermal parameters. Crystal data for C_{2v}(2)-C_{78} (C_{78}-I) and C_{2v}(3)-C_{78} (C_{78}-II) can be obtained free of charge from The Cambridge Crystallographic Data Centre with the CCDC reference number 2278920-2278921.

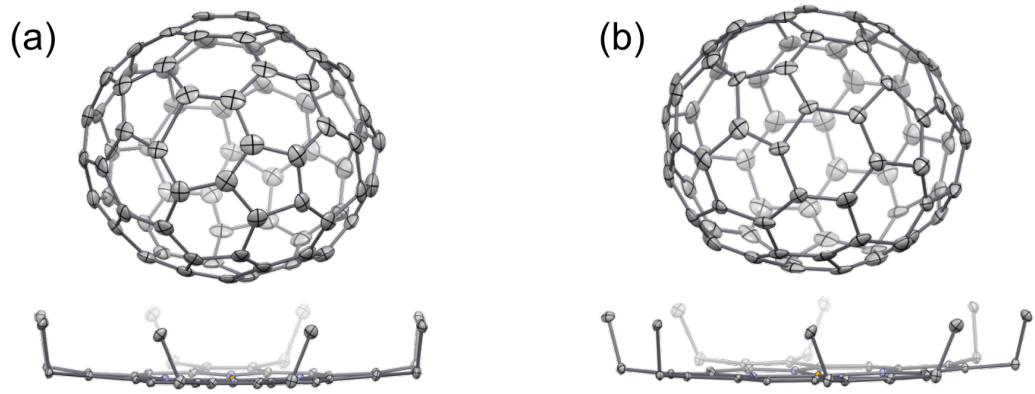

Fig. S118. ORTEP drawings of (a) C_{2v}(2)-C_{78}·Ni^{II}(OEP) and (b) C_{2v}(3)-C_{78}·Ni^{II}(OEP). Thermal contours are drawn at the 10 % probability level. Only one fullerene cage is shown, whereas solvent molecules and H atoms are omitted for clarity.

10. Comparison of Recognition Sensitivity for Higher Fullerene Isomers

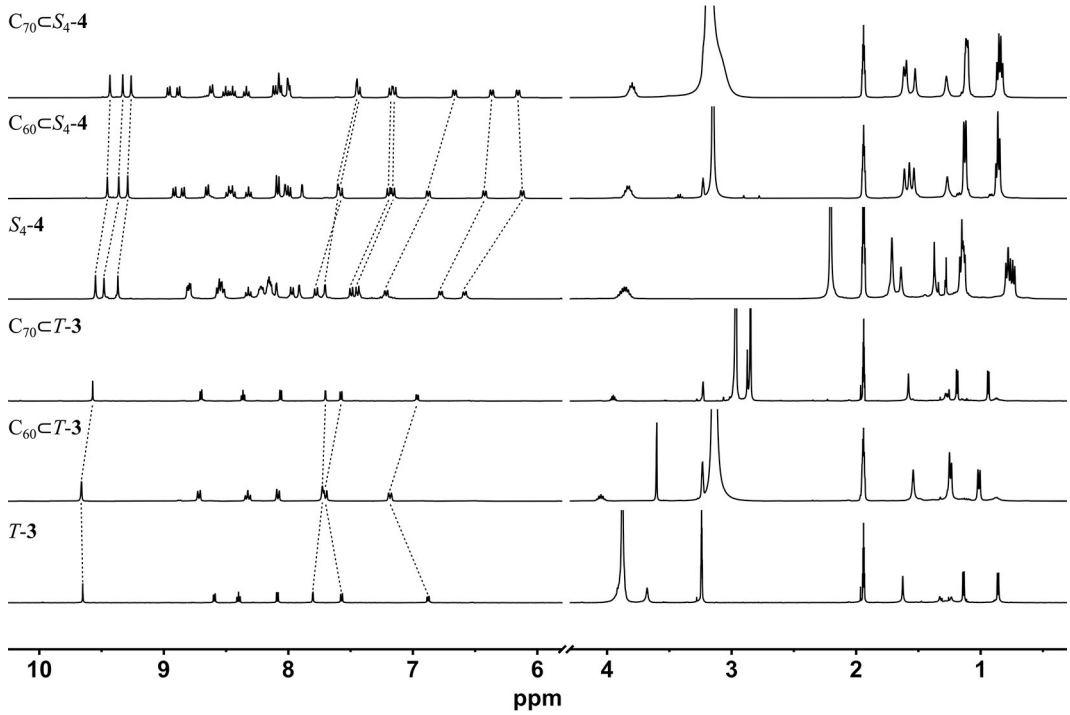

Fig. S119. ^{1}H NMR spectra (400 MHz, 298 K) of *T*-**3** (Δ_4-P_4) and S_4-**4** before and after encapsulating fullerene, where S_4-**4** empty is in a CD_3CN solution, and the others are in a mixed CD_3CN/CD_3OD (v/v 4/1) solution.

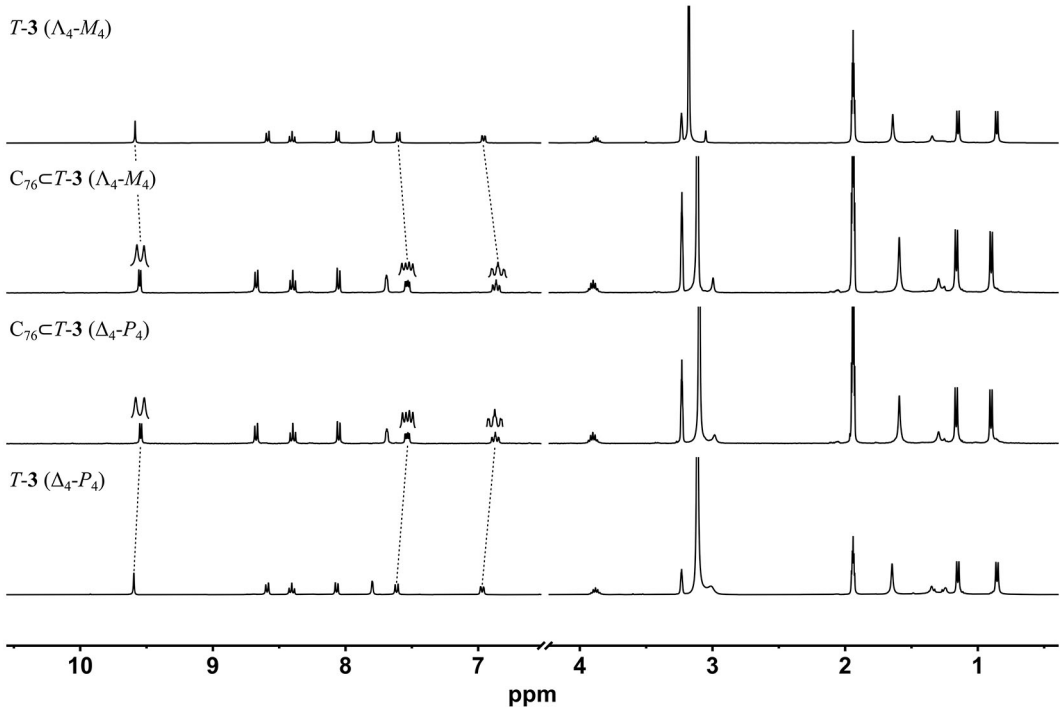

Fig. S120. Comparison of ^{1}H NMR spectra (400 MHz, 298 K, CD_3CN/CD_3OD, v/v 4/1) for *T*-**3** (Δ_4-P_4/Λ_4-M_4) before and after encapsulating C_{76} (D_2).

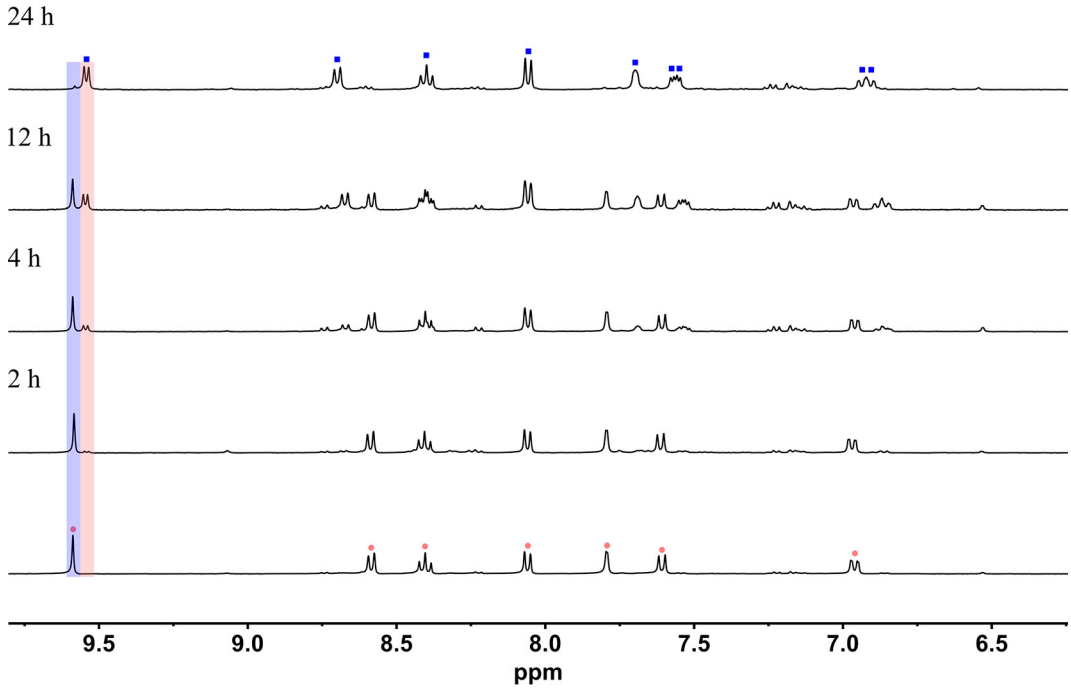

Fig. S121. ^{1}H NMR spectra (400 MHz, 298 K, CD_3CN/CD_3OD, v/v 4/1) tracking the encapsulation of C_{76} by *T*-**3** (Δ_4-P_4). (●: *T*-**3**; ■: $C_{76}\subset$*T*-**3**)

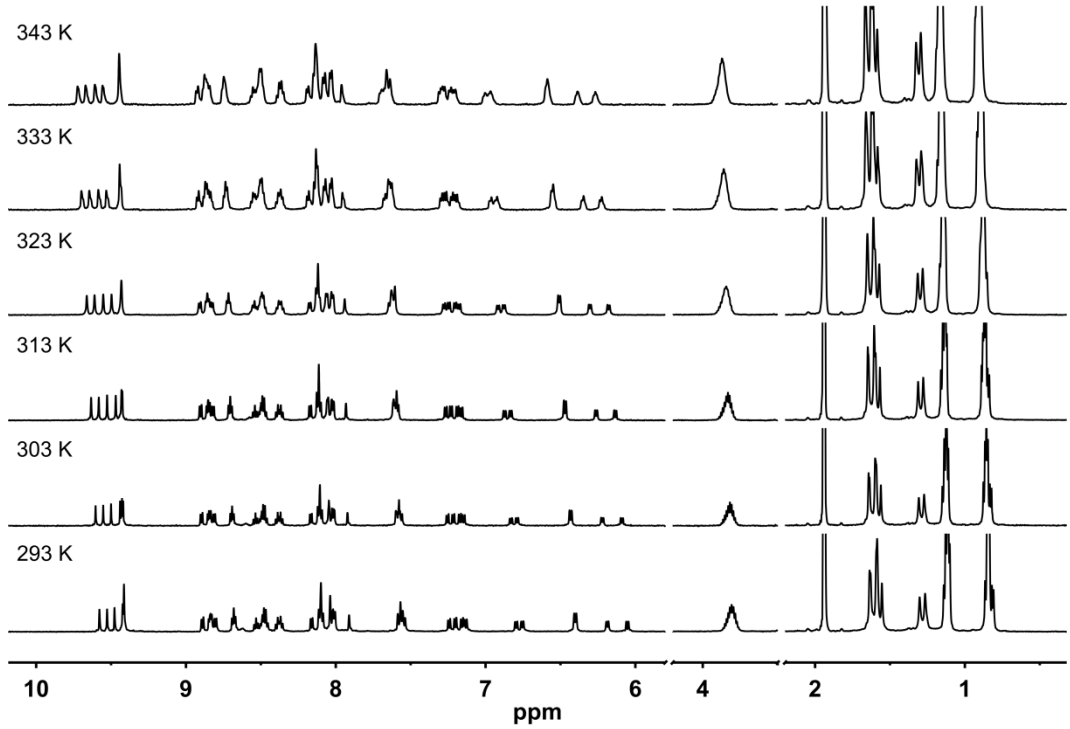

Fig. S122. VT-NMR spectra of $C_{76}\subset S_4$-**4** (600 MHz, 293-343 K, CD_3CN/MeOD = 4/1). VT-delay is set to 1200 s to ensure that the system reaches equilibrium.

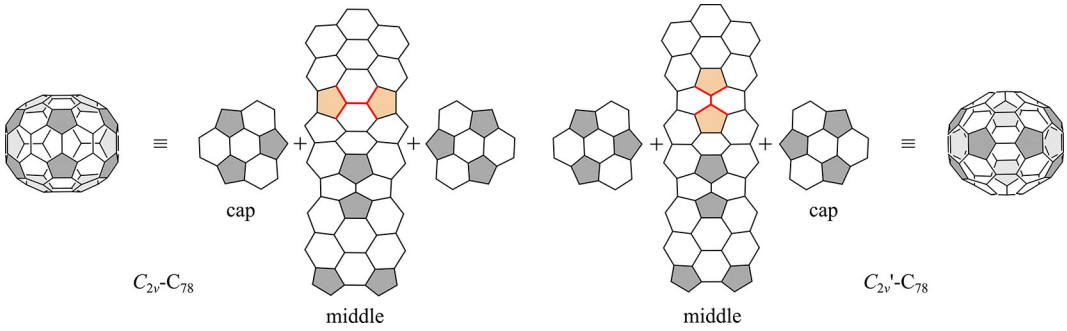

Fig. S123. Comparison of 2D and 3D structures of C_{2v}-C_{78} and C_{2v}'-C_{78}. The only differences are highlighted in red.

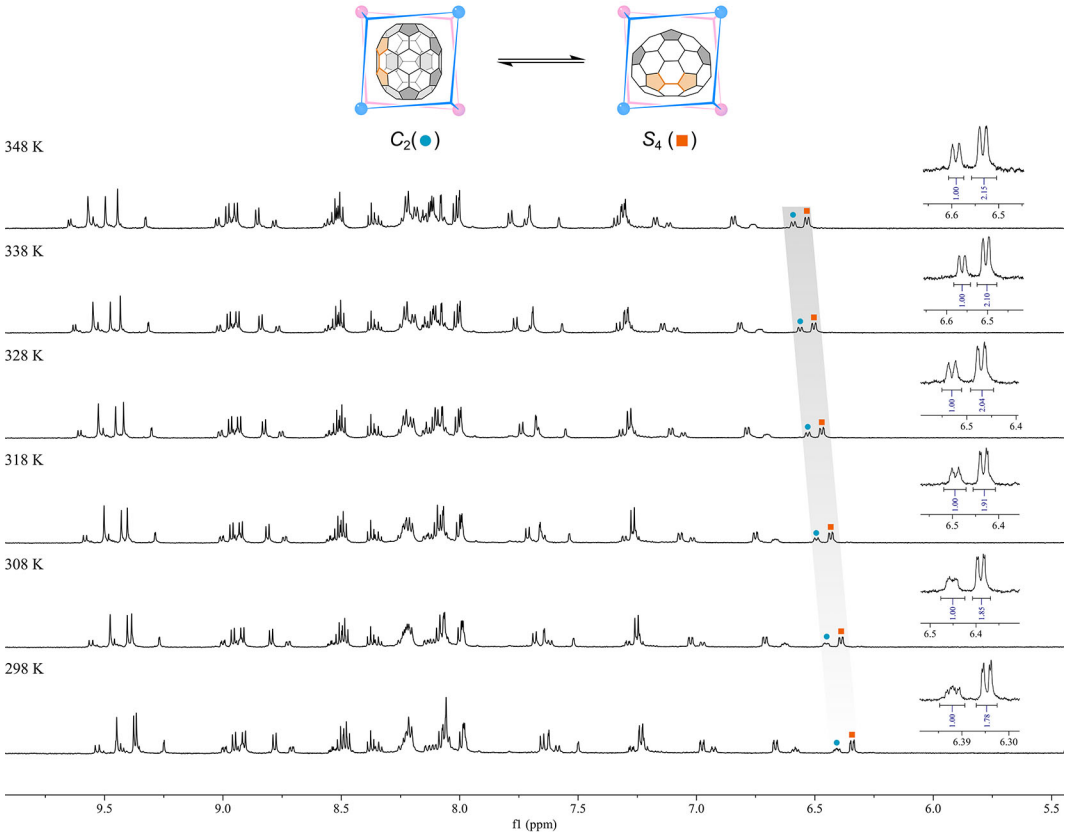

Fig. *S124*. VT-NMR stack plot (600 MHz, CD_3CN, [C_{2v}-C_{78}⊂S_4-**4**] = 1.0 mM) showing the effect of temperature on the equilibrium of C_{2v}-C_{78}⊂S_4-**4** (C_2) ⇌ C_{2v}-C_{78}⊂S_4-**4** (S_4). The proton signals on the TBTQ skeletons of C_2-symmetric C_{2v}-C_{78}⊂S_4-**4** (●) and S_4-symmetric C_{2v}-C_{78}⊂S_4-**4** (■) were integrated to determine the relative content. It can be observed that increase in temperature is conducive to the formation of S_4-symmetric C_{2v}-C_{78}⊂S_4-**4**.

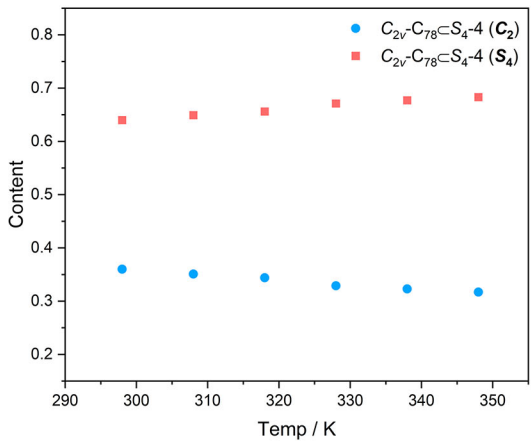

Temp (K)	C_{2v}-C_{78}⊂S_4-4 (C_2, %)	C_{2v}-C_{78}⊂S_4-4 (S_4, %)
298	36.0	64.0
308	35.1	64.9
318	34.4	65.6
328	32.9	67.1
338	32.3	67.7
348	31.7	68.3

Fig. *S125*. Distribution plots (left) and table (right) of C_2-symmetric C_{2v}-C_{78}⊂S_4-**4** and S_4-symmetric C_{2v}-C_{78}⊂S_4-**4** at various temperatures. The molar fractions at each temperature were calculated by ^{1}H NMR integral ratios for the proton signals on the TBTQ skeletons.

The thermodynamic parameters for the equilibrium of C_{2v}-C_{78}⊂S_4-**4** (C_2) ⇌ C_{2v}-C_{78}⊂S_4-**4** (S_4) can be obtained based upon van't Hoff equation:

$$\ln K = -\frac{\Delta H}{RT} + \frac{\Delta S}{R} \quad (1)$$

According to VT-NMR spectra, the equilibrium constant (K) at various temperature can be calculated by integral ratios. There is a linear relationship between 1/T and ln$K$ in equation 1. Therefore, the slope and intercept of the line can be obtained, and then corresponding thermodynamic parameters for encapsulation equilibrium are calculated as follows.

T (K)	K^a	1/T	ln$K$
298	1.78	0.00336	0.577
308	1.85	0.00325	0.615
318	1.91	0.00314	0.647
328	2.04	0.00305	0.713
338	2.10	0.00296	0.742
348	2.15	0.00287	0.765

a: Equilibrium constant of C_{2v}-C_{78}⊂S_4-4 (C_2) ⇌ C_{2v}-C_{78}⊂S_4-4 (S_4).

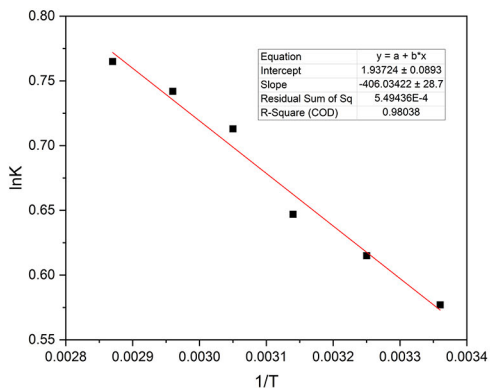

ΔH° (KJ/mol)	ΔS° (KJ/mol)	ΔG° (KJ/mol)
3.376	0.016	–1.392

Fig. *S126*. Left: Data for the equilibrium of C_{2v}-C_{78}⊂S_4-**4** (C_2) ⇌ C_{2v}-C_{78}⊂S_4-**4** (S_4) from VT-NMR. Right: The linear fitting of 1/T vs. lnK based on the van't Hoff equation and the calculated thermodynamic parameters of ΔH°, ΔS° and ΔG° (298 K).

11. Orientation Analysis of Host–Guest Complexes

11.1 Theoretical calculation of binding energy

To evaluate the potential relative orientation of S_4-**4** with respect to higher fullerenes (D_2-C_{76}, C_{2v}-C_{78}, and C_{2v}'-C_{78}), we performed binding energy (BE) calculations on the host – guest complexes using the forcite module in Materials Studio 7.0 by Accelrys software, Inc. The structures of these host – guest complexes were simulated by molecular mechanic modeling, utilizing the crystal data of $C_{70}\subset S_4$-**4** and fullerenes. The theoretical BE for each host – guest complex can be calculated by determining the energy of the host (E_H) after removing the guest and the energy of guest (E_G) after removing the host, followed by calculating the total energy of the host – guest complex (E_{HG}). Subsequently, the BE can be determined using the equation: BE = $E_{HG} - (E_H + E_G)$.

11.2 Binding energy of D_2-$C_{76}\subset S_4$-**4**

Affected by the host–guest interaction, the encapsulated host often experiences inevitable chemical shifts and even a reduction in symmetry, particularly when encapsulating guest molecules with lower symmetry. ^{1}H NMR analysis revealed that the proton signals of S_4-**4**, upon encapsulating D_2-C_{76}, transitioned from the original S_4 symmetry to C_2 symmetry, indicating restricted free rotation of D_2-C_{76} within the confined microenvironment of S_4-**4**. D_2-C_{76} has three perpendicular C_2 axes and varying sizes along these axes (*a*: 8.57 Å; *b*: 7.47 Å; *c*: 6.62 Å, excluding the van der Waals radii of carbon atoms). It can be inferred that one of the C_2 axes in D_2-C_{76} aligns with the S_4 axis of S_4-**4**, resulting in the host – guest complex exhibiting C_2 symmetry. For comparison, three potential scenarios were simulated, and the corresponding binding energies were calculated as follows.

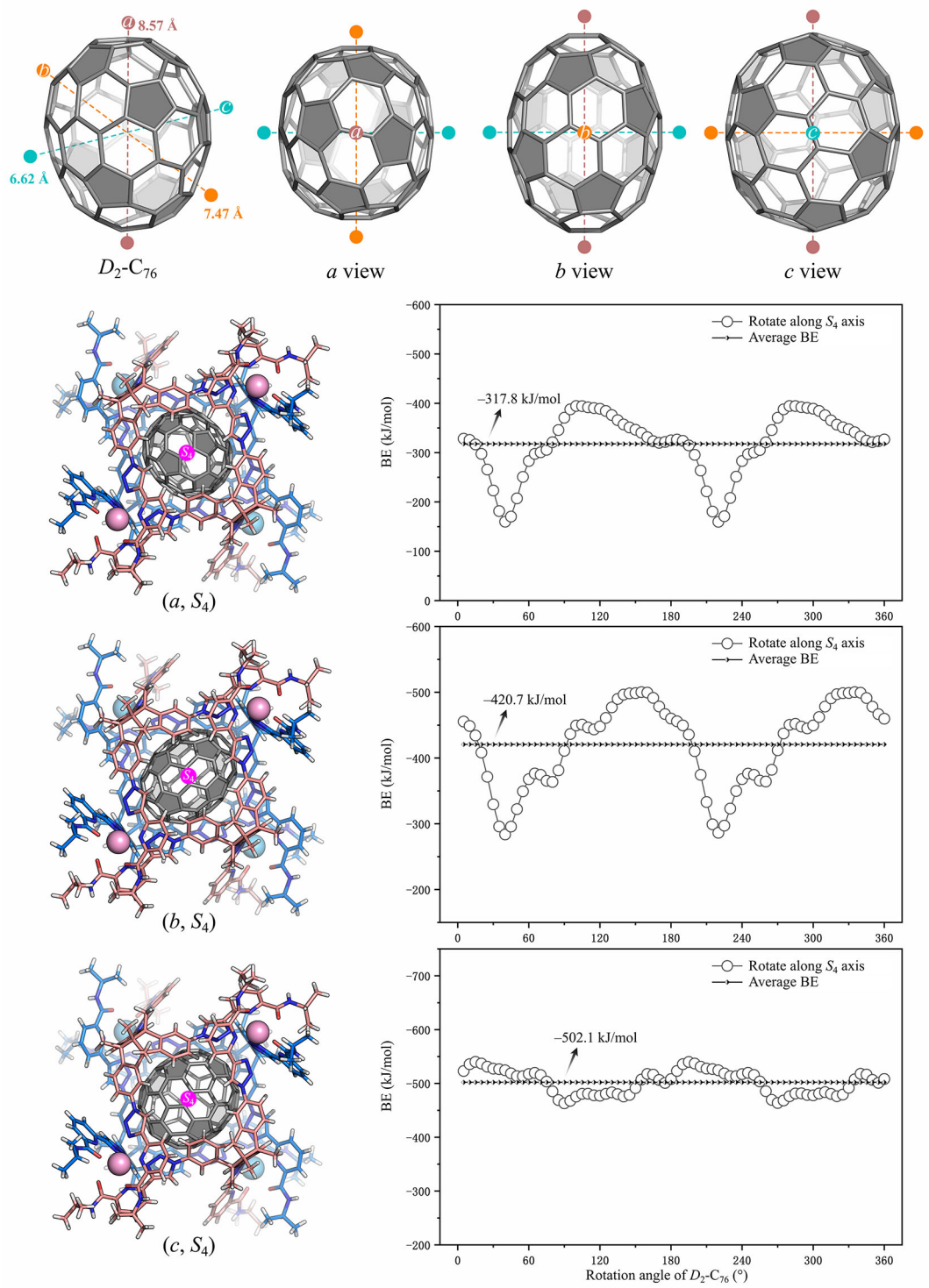

Fig. S127. (a) Different views of the crystal structure for D_2-C_{76} reported in the literature.[S16] (b) The theoretical BE vs. rotation angle of D_2-C_{76} for three relative orientations between D_2-C_{76} and S_4-**4**.

11.3 Binding energy of C_{2v}-C_{78}⊂S_4-**4**

^{1}H NMR analysis of C_{2v}-C_{78}⊂S_4-**4** revealed two sets of signals with distinct C_2 and S_4 symmetries. C_{2v}-C_{78} possesses the symmetry elements E, C_2 (d), and two vertical mirror planes σ_1 and σ_2. If the C_2 axis coincides with the S_4 axis of the host, it is plausible

that the complex would exhibit an overall C_2 symmetry, akin to that of $C_{76}\subset S_4$-**4**. Alternatively, one of the two mirrors could be perpendicular to the S_4 axis of the host, allowing the complex to exhibit S_4 symmetry. For comparison, three potential scenarios were simulated, and the corresponding binding energies were calculated as follows.

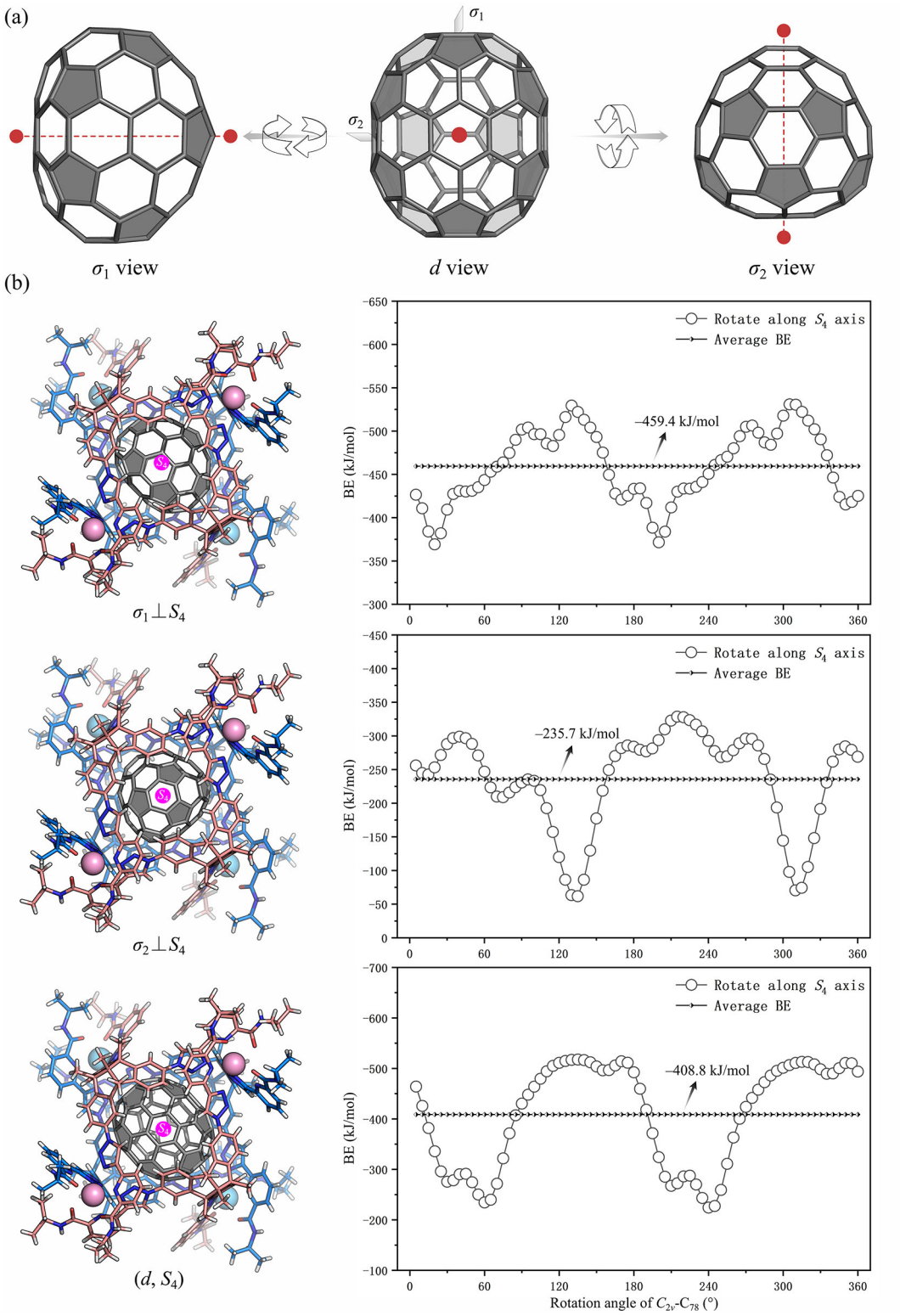

Fig. S128. (a) Three views of the crystal structure for C_{2v}-C_{78}. (b) The theoretical BE vs. rotation angle of C_{2v}-C_{78} for three possible combinations of C_{2v}-$C_{78}\subset S_4$-**4**.

11.4 Binding energy of C_{2v}'-C_{78}⊂S_4-**4**

Similar to the analysis of the relative orientation in C_{2v}-C_{78}⊂S_4-**4**, three scenarios for C_{2v}'-C_{78}⊂S_4-**4** were simulated, and the corresponding binding energies were calculated as follows.

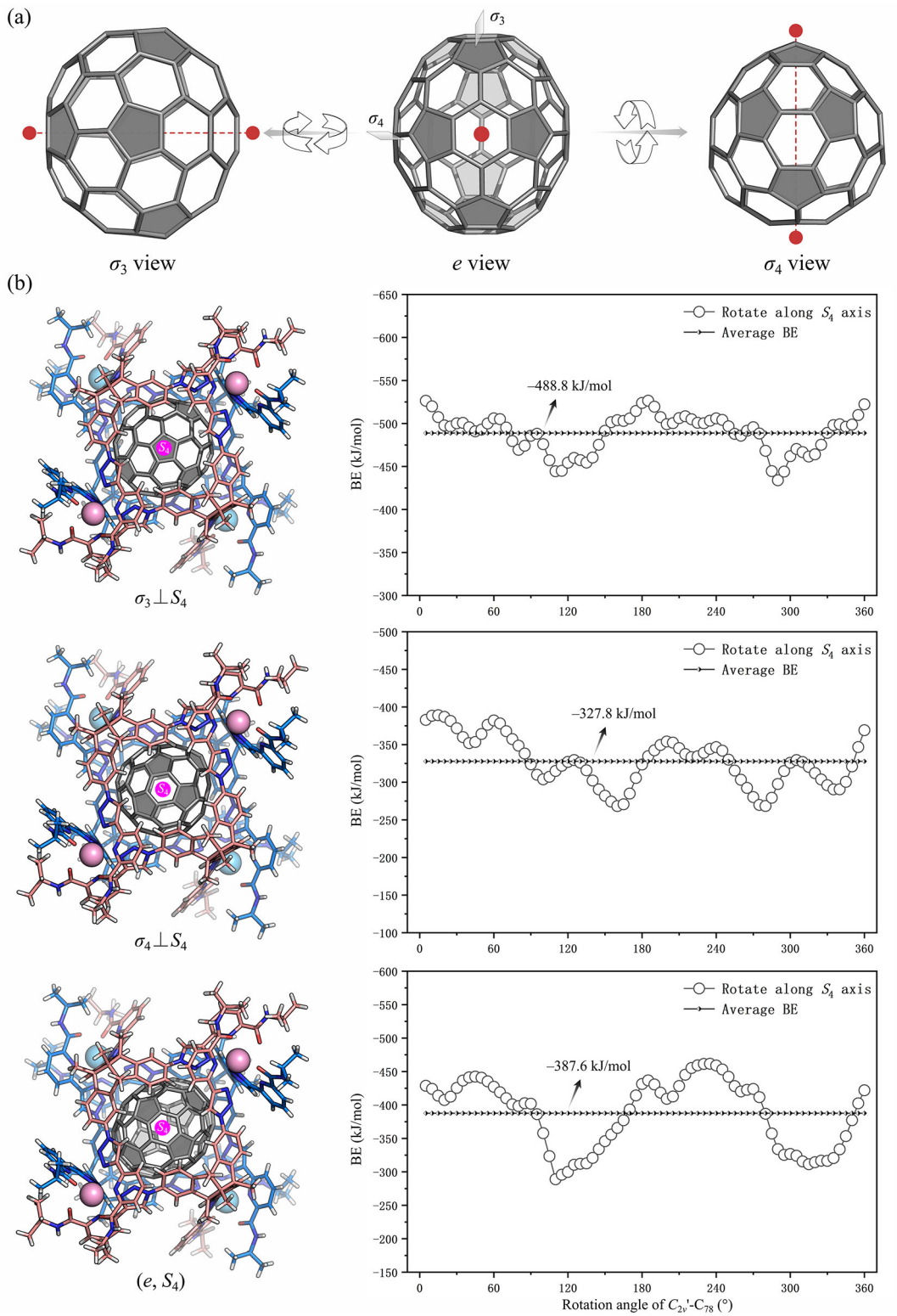

Fig. S129. (a) Three views of the crystal structure for C_{2v}'-C_{78}. (b) The theoretical BE vs. rotation angle of C_{2v}'-C_{78} for three possible combinations of C_{2v}'-C_{78}⊂S_4-**4**.

12. Analysis of Host–Guest Interactions

12.1 Quantitative analysis of host–guest interactions with Hirshfeld surfaces

To quantitatively assess and visually analyze the supramolecular interactions within the crystal structures of $C_{60}\subset S_4$-**4** and $C_{70}\subset S_4$-**4**, Hirshfeld surfaces analyses[S17,S18] were performed employing the CrystalExplorer software.[S19] The normalized contact distance (d_{norm}), which is based on d_e, d_i, and the van der Waals (*vdw*) radii of the atoms, given by Eq. (1), enables the identification of regions that hold particular importance to intermolecular interactions.[S20] Where d_e and d_i correspond to the nearest distances from points on the surface to external and internal atoms, respectively. The combination of d_e and d_i values in the form of a 2D fingerprint plot summarizes intermolecular contacts present in the crystal structure. During the calculation process, the fullerene guest molecules are selected and included in the surface.

$$d_{norm} = \frac{d_i - r_i^{vdw}}{r_i^{vdw}} + \frac{d_e - r_e^{vdw}}{r_e^{vdw}} \quad (2)$$

The Hirshfeld surfaces mapped with d_{norm} are illustrated in Fig. S130-S131, exhibiting the close intermolecular contacts near the guest molecules. The interaction between the host S_4-**4** and fullerene guests is clearly discernible on the Hirshfeld surfaces, manifesting as the bright white regions (Fig. S130b and S131b). The intermolecular interactions appear as distinct spikes in the 2D fingerprint plots (Fig. S130d and S131d). The C···C (~37%) and C···N (~23%) contacts are derived from the π···π stacking interaction of fullerenes with TBTQ skeletons and triazole groups, respectively. Notably, this π···π stacking interaction plays a pivotal role, constituting a significant portion (~ 60%) of the host–guest interaction. Following this, the CH···π (C···H contact, ~18%) interactions and the OTf⁻···π interactions (involving C···O and C···F contacts, ~22%) contribute to the overall interaction.

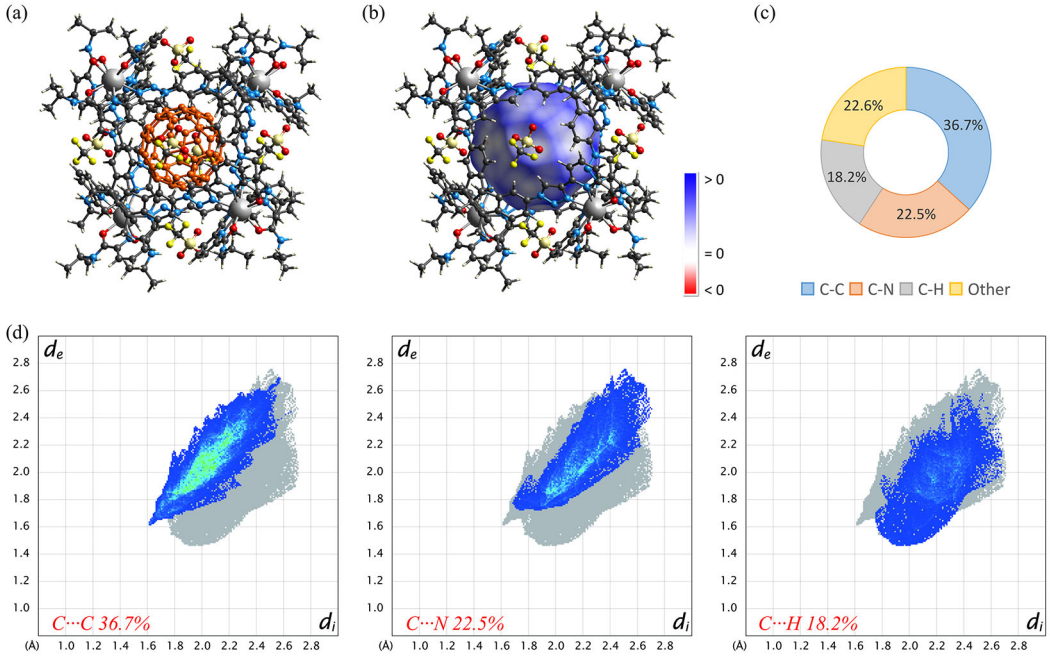

Fig. S130. (a) Crystal structure of $C_{60}\subset S_4$-**4**. (b) Hirshfeld surface of $C_{60}\subset S_4$-**4** mapped with d_{norm} showing the close intermolecular contacts near the guest C_{60} (Colour scheme: red highlights shorter contacts, white is used for contacts around the *vdw* separation, and blue is for longer contacts). (c) Relative contribution to the Hirshfeld surface for the various contacts between host S_4-**4** and guest C_{60}. (d) 2D fingerprint plots for $C_{60}\subset S_4$-**4** resolved into C···C (left), C···N (middle), and C···H (right) contacts.

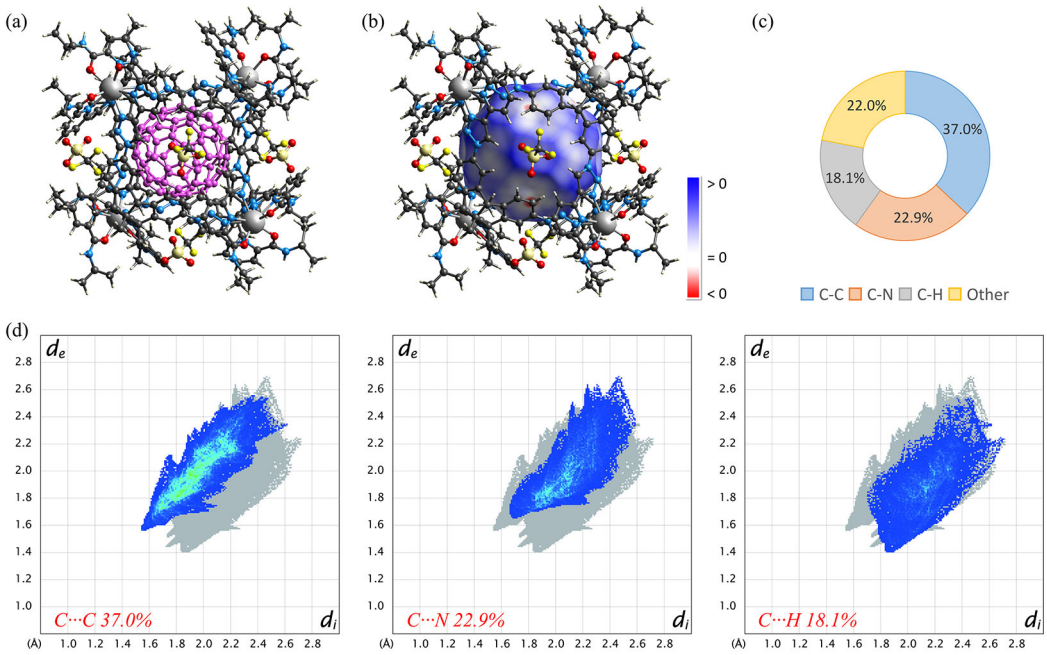

Fig. S131. (a) Crystal structure of $C_{70}\subset S_4$-**4**. (b) Hirshfeld surface of $C_{70}\subset S_4$-**4** mapped with d_{norm} showing the close intermolecular contacts near the guest C_{70}. (c) Relative contribution to the Hirshfeld surface for the various contacts between host S_4-**4** and guest C_{70}. (d) 2D fingerprint plots for $C_{70}\subset S_4$-**4** resolved into C···C (left), C···N (middle), and C···H (right) contacts.

12.2 Host–guest interactions analysis with IGM

The independent gradient model (IGM) analysis[S21] was conducted using the Multiwfn 3.8 program[S22] to explore the weak interactions between the host and guest. During the calculation process, the host–guest complex is split into two fragments (host and guest) to study their interactions. The contribution degree of atomic pair and atoms to the weak interaction is quantified as a percentage using the δg index. The molecular structure diagram, depicting the color-coded atomic δg index and δg_{inter} isosurface, was generated using the VMD 1.9.3 program.[S23] The color scale, ranging from red to orange (-0.8 to 0.2), effectively visualizes the δg index variations among different atoms. The smaller value of δg_{inter} isosurface is set to ensure the ideal visualization of the *vdw* interaction between the host and guest.

Hence, it is intuitively evident that the pseudo-cube cage exhibits apparent host–guest interactions with fullerene according to the IGM analysis. These interactions primarily originate from the π···π stacking and C-H···π interactions of TBTQ and triazole groups (highlighted in red) with the fullerenes. In the case of C_{60}⊂*T*-**3**, the isosurface of δg_{inter} displays high symmetry, aligning with the *T*-symmetric host. In contrast, the symmetry of the δg_{inter} isosurface in C_{60}⊂S_4-**4** is relatively lower, ascribed to the S_4-symmetric host.

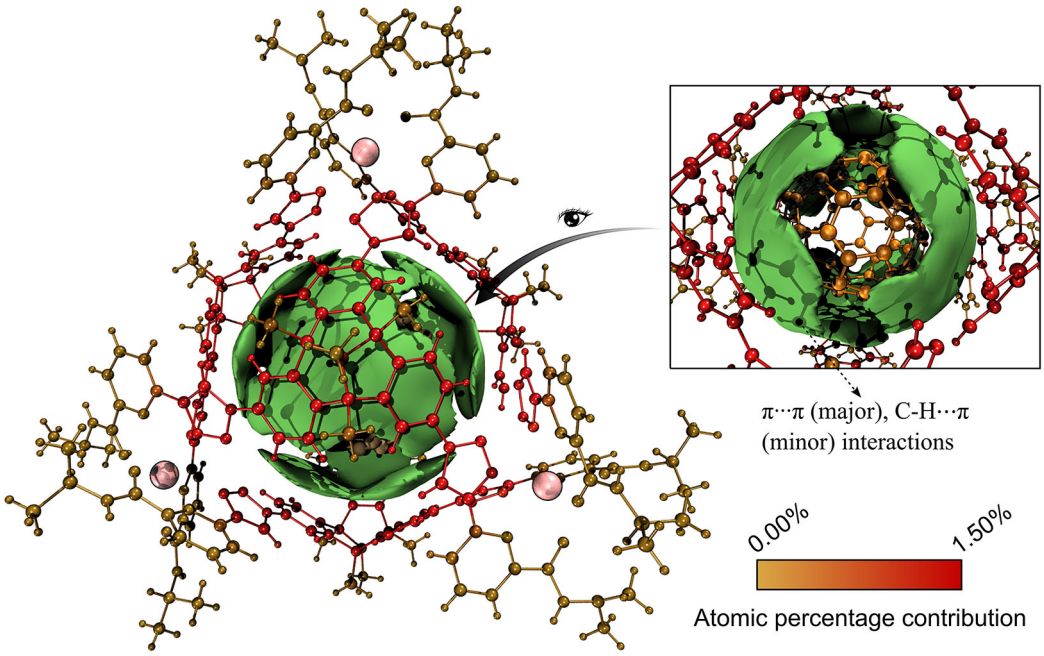

Fig. S132. IGM analysis for the simulated structure of C_{60}⊂*T*-**3** showing the π···π stacking and C-H···π interactions between host and guest (δg_{inter} = 0.0012). The percentage contribution of atomic pairs and atoms to the host–guest interactions is demonstrated by different colors.

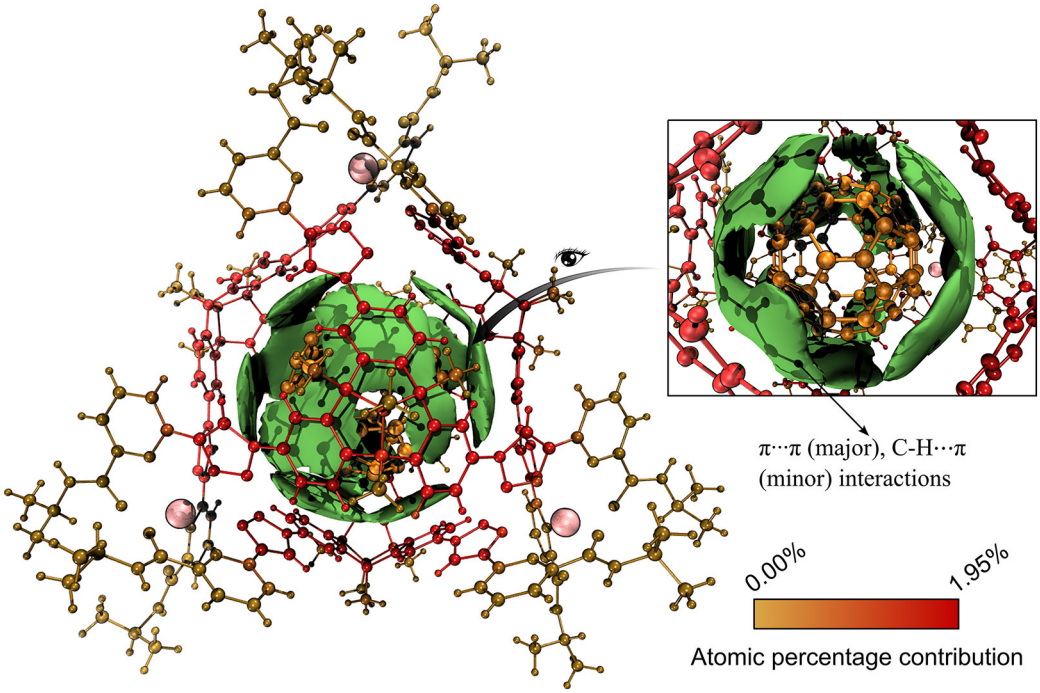

Fig. S133. IGM analysis for the crystal structure of C_{60}⊂S_4-**4** showing the π···π stacking and C-H···π interactions between host and guest (δg_{inter} = 0.0015). The percentage contribution of atomic pairs and atoms to the host–guest interactions is demonstrated by different colors.

13. Binding Constant Determination

13.1 General procedure

The binding constant (K_a) for the formation of the host-guest complex in CD_3CN was determined through NMR spectroscopy. The K_a value for the C_{60} guest was ascertained by directly encapsulating the guest with 1 equiv of the empty cage *T*-**3** or S_4-**4**. The binding constant for the equilibrium [C_{60} + H ⇌ C_{60}⊂H] was calculated using the Equation:

$$K_a(C_{60}) = \frac{[C_{60}\subset H]}{[C_{60}]\cdot[H]} \tag{3}$$

Here, H represents *T*-**3** or S_4-**4**. The saturated concentration of C_{60} (5.56×10^{-7} M at 298 K) in acetonitrile was established based on prior literature.[S24] For the remaining fullerenes (C_{70}, C_{76}, C_{2v}-C_{78}, C_{2v}'-C_{78}), competitive encapsulation experiments relative to 1 equiv of C_{60}⊂*T*-**3** or C_{60}⊂S_4-**4** were employed to evaluate the respective K_a values. The apparent binding constant for the equilibrium [C_{60}⊂H + C_n ⇌ C_n⊂H + C_{60}] was calculated using the Equation:

$$K' = \frac{[C_n\subset H]\cdot[C_{60}]}{[C_{60}\subset H]\cdot[C_n]} \tag{4}$$

$$\therefore \quad K_a(C_n) = K' \cdot K_a(C_{60}) \tag{5}$$

Here, n represents 70, 76, or 78. Considering the exceedingly low solubility of fullerenes in polar acetonitrile and for the sake of facilitating a comparative analysis of their relative binding capabilities, Equation 4 was simplified to $K' \approx [C_n \subset H]/[C_{60} \subset H]$. The mixture was heated at 70 °C for three days to ensure that it had reached equilibrium. Prior to NMR characterization, insoluble fullerenes were separated through centrifugation, with 1,3,5-trimethoxybenzene (TMB) serving as the internal standard to quantify the concentration of empty cages and host-guest complexes within the solution.

13.2 Binding constant for C_{60} guest

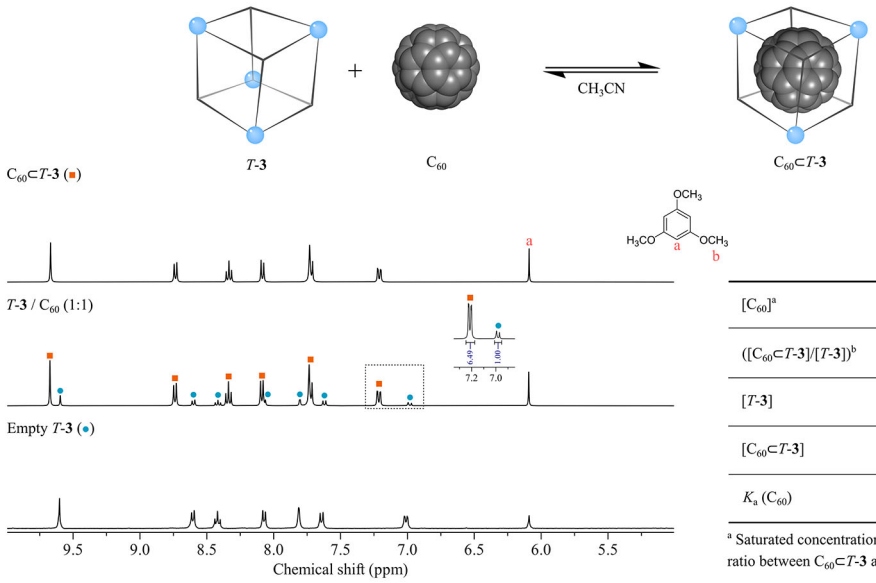

$[C_{60}]^a$	5.56×10^{-7} M
$([C_{60}\subset T\text{-}3]/[T\text{-}3])^b$	6.49
[*T*-**3**]	6.22×10^{-5} M
$[C_{60}\subset T\text{-}3]$	4.04×10^{-4} M
K_a (C_{60})	1.17×10^{7} M^{-1}

[a] Saturated concentration of C_{60} in CH_3CN; [b] Integral ratio between $C_{60}\subset T$-**3** and *T*-**3**.

Fig. S134. Partial ^{1}H NMR spectra (400 MHz, 298 K, CD_3CN) for the guest-binding equilibrium of [C_{60} + *T*-**3** ⇌ $C_{60}\subset T$-**3**] ([*T*-**3**]^o = 4.66×10^{-4} M, C_{60}, 1 equiv). K_a (C_{60}) = [$C_{60}\subset T$-**3**]/([C_{60}]· [*T*-**3**])

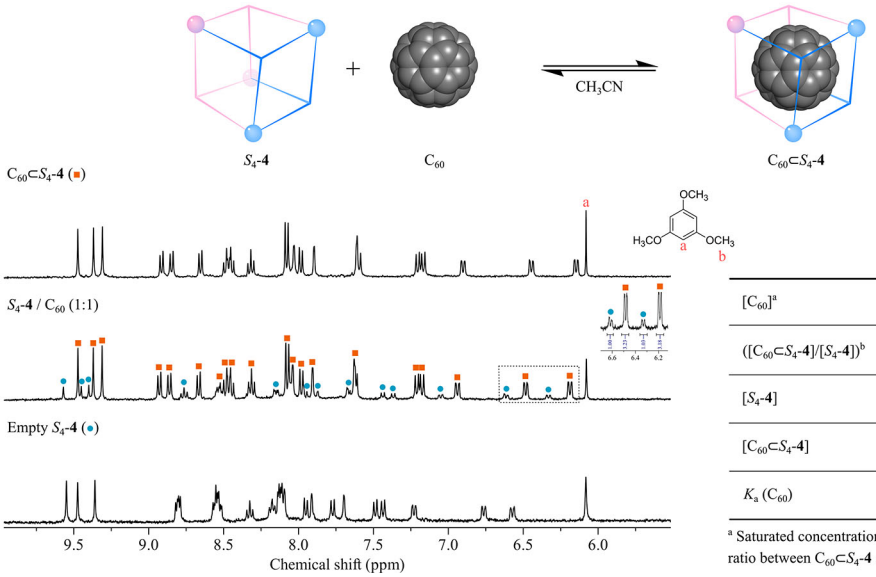

$[C_{60}]^a$	5.56×10^{-7} M
$([C_{60}\subset S_4\text{-}4]/[S_4\text{-}4])^b$	3.16
[S_4-**4**]	7.40×10^{-5} M
$[C_{60}\subset S_4\text{-}4]$	2.34×10^{-4} M
K_a (C_{60})	5.69×10^{6} M^{-1}

[a] Saturated concentration of C_{60} in CH_3CN; [b] Integral ratio between $C_{60}\subset S_4$-**4** and S_4-**4**.

Fig. S135. Partial ^{1}H NMR spectra (400 MHz, 298 K, CD_3CN) for the guest-binding equilibrium of [C_{60} + S_4-**4** ⇌ $C_{60}\subset S_4$-**4**] ([S_4-**4**]^o = 3.08×10^{-4} M, C_{60}, 1 equiv). K_a (C_{60}) = [$C_{60}\subset S_4$-**4**]/([C_{60}]· [S_4-**4**])

13.3 Binding constant for C_{70} guest

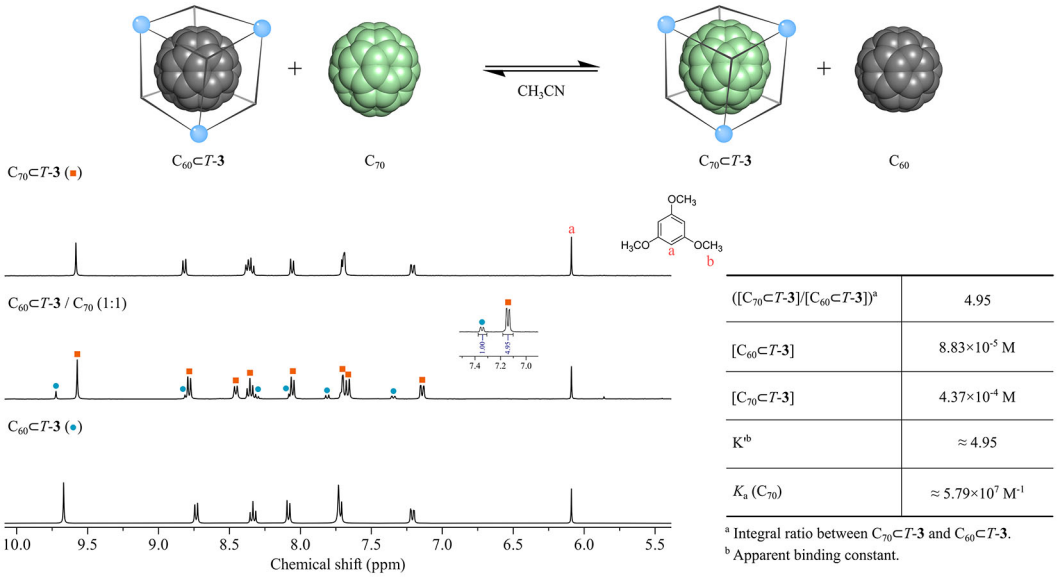

([C_{70}⊂*T*-**3**]/[C_{60}⊂*T*-**3**])[a]	4.95
[C_{60}⊂*T*-**3**]	8.83×10^{-5} M
[C_{70}⊂*T*-**3**]	4.37×10^{-4} M
K'[b]	≈ 4.95
K_a (C_{70})	≈ 5.79×10^{7} M^{-1}

[a] Integral ratio between C_{70}⊂*T*-**3** and C_{60}⊂*T*-**3**.
[b] Apparent binding constant.

Fig. S136. Partial ^{1}H NMR spectra (400 MHz, 298 K, CD_3CN) for the guest-binding equilibrium of [C_{60}⊂*T*-**3** + C_{70} ⇌ C_{70}⊂*T*-**3** + C_{60}] ([C_{60}⊂*T*-**3**]^o = 5.25×10^{-4} M, C_{70}, 1 equiv). K' = ([C_{70}⊂*T*-**3**]· [C_{60}])/([C_{60}⊂*T*-**3**]· [C_{70}]) ≈ [C_{70}⊂*T*-**3**]/[C_{60}⊂*T*-**3**]; K_a (C_{60}) = K'· K_a (C_{60})

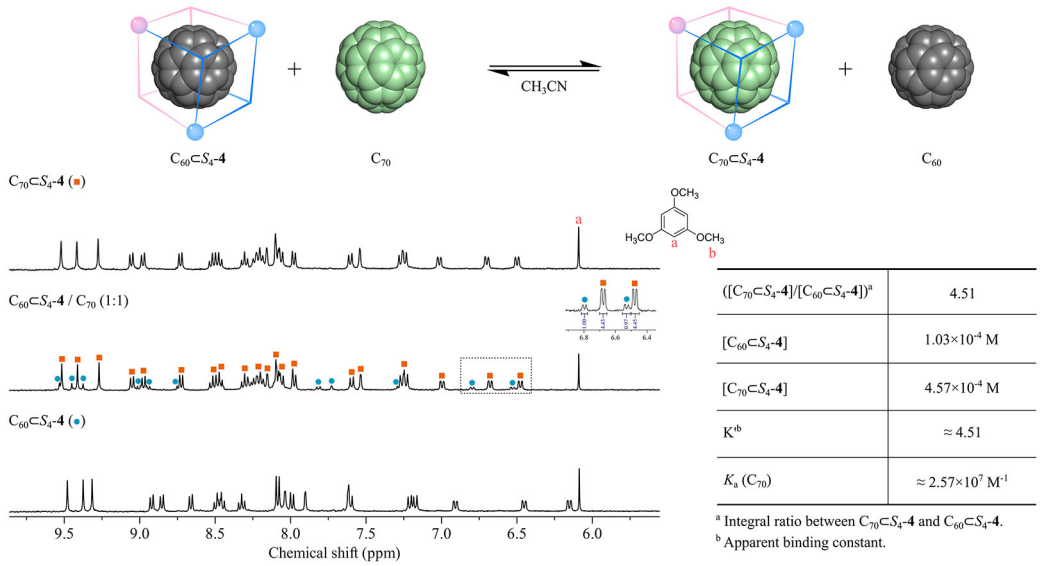

([C_{70}⊂S_4-**4**]/[C_{60}⊂S_4-**4**])[a]	4.51
[C_{60}⊂S_4-**4**]	1.03×10^{-4} M
[C_{70}⊂S_4-**4**]	4.57×10^{-4} M
K'[b]	≈ 4.51
K_a (C_{70})	≈ 2.57×10^{7} M^{-1}

[a] Integral ratio between C_{70}⊂S_4-**4** and C_{60}⊂S_4-**4**.
[b] Apparent binding constant.

Fig. S137. Partial ^{1}H NMR spectra (400 MHz, 298 K, CD_3CN) for the guest-binding equilibrium of [C_{60}⊂S_4-**4** + C_{70} ⇌ C_{70}⊂S_4-**4** + C_{60}] ([C_{60}⊂S_4-**4**]^o = 5.60×10^{-4} M, C_{70}, 1 equiv). K' = ([C_{70}⊂S_4-**4**]· [C_{60}])/([C_{60}⊂S_4-**4**]· [C_{70}]) ≈ [C_{70}⊂S_4-**4**]/[C_{60}⊂S_4-**4**]; K_a (C_{70}) = K'· K_a (C_{60})

13.4 Binding constant for C_{76} guest

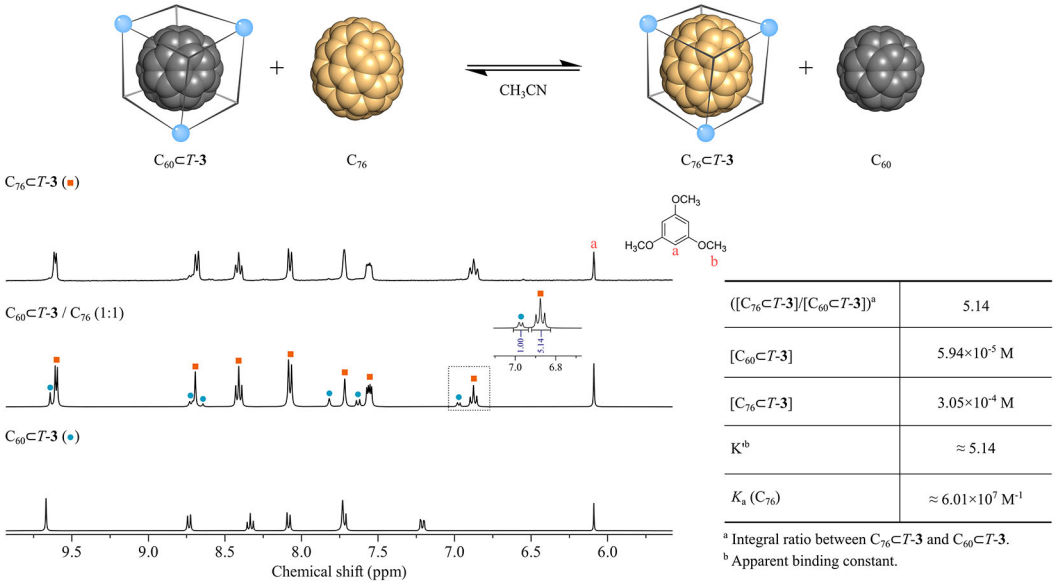

([C_{76}⊂*T*-**3**]/[C_{60}⊂*T*-**3**])[a]	5.14
[C_{60}⊂*T*-**3**]	5.94×10^{-5} M
[C_{76}⊂*T*-**3**]	3.05×10^{-4} M
K'[b]	≈ 5.14
K_a (C_{76})	≈ 6.01×10^{7} M^{-1}

[a] Integral ratio between C_{76}⊂*T*-**3** and C_{60}⊂*T*-**3**.
[b] Apparent binding constant.

Fig. S138. Partial ^{1}H NMR spectra (400 MHz, 298 K, CD_3CN) for the guest-binding equilibrium of [C_{60}⊂*T*-**3** + C_{76} ⇌ C_{76}⊂*T*-**3** + C_{60}] ([C_{60}⊂*T*-**3**]^o = 3.64×10^{-4} M, C_{76}, 1 equiv). K' = ([C_{76}⊂*T*-**3**]· [C_{60}])/([C_{60}⊂*T*-**3**]· [C_{76}]) ≈ [C_{76}⊂*T*-**3**]/[C_{60}⊂*T*-**3**]; K_a (C_{76}) = K'· K_a (C_{60})

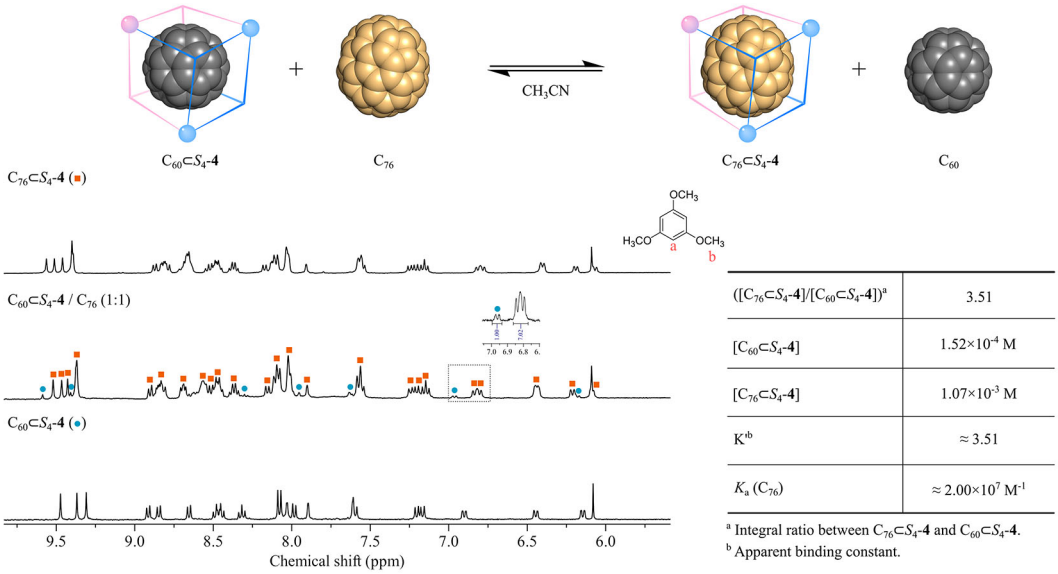

([C_{76}⊂S_4-**4**]/[C_{60}⊂S_4-**4**])[a]	3.51
[C_{60}⊂S_4-**4**]	1.52×10^{-4} M
[C_{76}⊂S_4-**4**]	1.07×10^{-3} M
K'[b]	≈ 3.51
K_a (C_{76})	≈ 2.00×10^{7} M^{-1}

[a] Integral ratio between C_{76}⊂S_4-**4** and C_{60}⊂S_4-**4**.
[b] Apparent binding constant.

Fig. S139. Partial ^{1}H NMR spectra (400 MHz, 298 K, CD_3CN) for the guest-binding equilibrium of [C_{60}⊂S_4-**4** + C_{76} ⇌ C_{76}⊂S_4-**4** + C_{60}] ([C_{60}⊂S_4-**4**]^o = 1.22×10^{-3} M, C_{76}, 1 equiv). K' = ([C_{76}⊂S_4-**4**]· [C_{60}])/([C_{60}⊂S_4-**4**]· [C_{76}]) ≈ [C_{76}⊂S_4-**4**]/[C_{60}⊂S_4-**4**]; K_a (C_{76}) = K'· K_a (C_{60})

13.5 Binding constant for C_{2v}-C_{78} guest

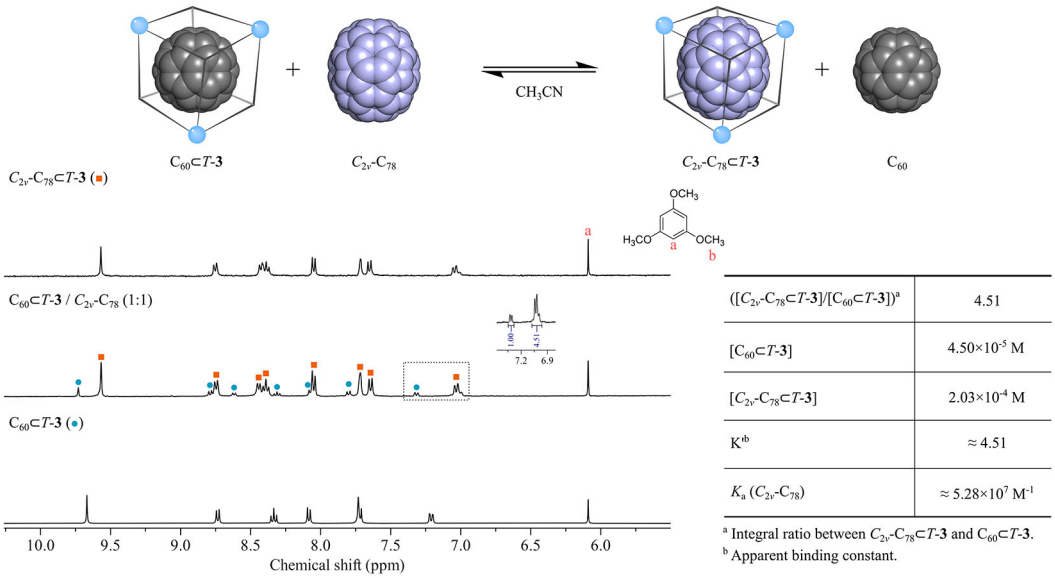

([C_{2v}-C_{78}⊂*T*-**3**]/[C_{60}⊂*T*-**3**])[a]	4.51
[C_{60}⊂*T*-**3**]	4.50×10^{-5} M
[C_{2v}-C_{78}⊂*T*-**3**]	2.03×10^{-4} M
K'[b]	≈ 4.51
K_a (C_{2v}-C_{78})	≈ 5.28×10^{7} M^{-1}

[a] Integral ratio between C_{2v}-C_{78}⊂*T*-**3** and C_{60}⊂*T*-**3**.
[b] Apparent binding constant.

Fig. S140. Partial ^{1}H NMR spectra (400 MHz, 298 K, CD_3CN) for the guest-binding equilibrium of [C_{60}⊂*T*-**3** + C_{2v}-C_{78} ⇌ C_{2v}-C_{78}⊂*T*-**3** + C_{60}] ([C_{60}⊂*T*-**3**]^o = 2.48×10^{-4} M, C_{2v}-C_{78}, 1 equiv). K' = ([C_{2v}-C_{78}⊂*T*-**3**]· [C_{60}])/([C_{60}⊂*T*-**3**]· [C_{2v}-C_{78}]) ≈ [C_{2v}-C_{78}⊂*T*-**3**]/[C_{60}⊂*T*-**3**]; K_a (C_{2v}-C_{78}) = K'· K_a (C_{60})

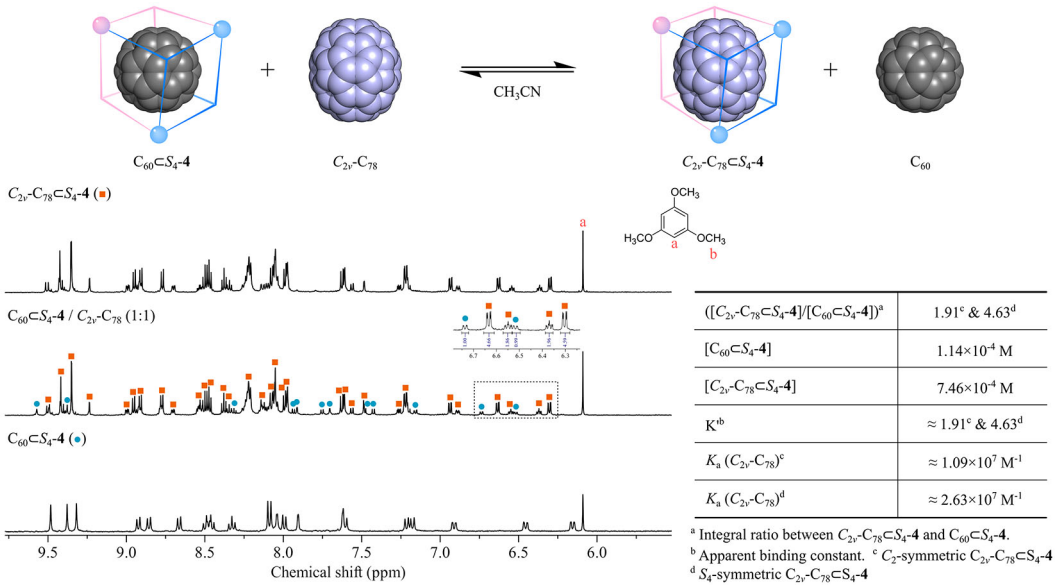

([C_{2v}-C_{78}⊂S_4-**4**]/[C_{60}⊂S_4-**4**])[a]	1.91[c] & 4.63[d]
[C_{60}⊂S_4-**4**]	1.14×10^{-4} M
[C_{2v}-C_{78}⊂S_4-**4**]	7.46×10^{-4} M
K'[b]	≈ 1.91[c] & 4.63[d]
K_a (C_{2v}-C_{78})[c]	≈ 1.09×10^{7} M^{-1}
K_a (C_{2v}-C_{78})[d]	≈ 2.63×10^{7} M^{-1}

[a] Integral ratio between C_{2v}-C_{78}⊂S_4-**4** and C_{60}⊂S_4-**4**.
[b] Apparent binding constant. [c] C_2-symmetric C_{2v}-C_{78}⊂S_4-**4**
[d] S_4-symmetric C_{2v}-C_{78}⊂S_4-**4**

Fig. S141. Partial ^{1}H NMR spectra (400 MHz, 298 K, CD_3CN) for the guest-binding equilibrium of [C_{60}⊂S_4-**4** + C_{2v}-C_{78} ⇌ C_{2v}-C_{78}⊂S_4-**4** + C_{60}] ([C_{60}⊂S_4-**4**]^o = 8.60×10^{-4} M, C_{2v}-C_{78}, 1 equiv). K' = ([C_{2v}-C_{78}⊂S_4-**4**]· [C_{60}])/([C_{60}⊂S_4-**4**]· [C_{2v}-C_{78}]) ≈ [C_{2v}-C_{78}⊂S_4-**4**]/[C_{60}⊂S_4-**4**]; K_a (C_{2v}-C_{78}) = K'· K_a (C_{60})

13.6 Binding constant for C_{2v}'-C_{78} guest

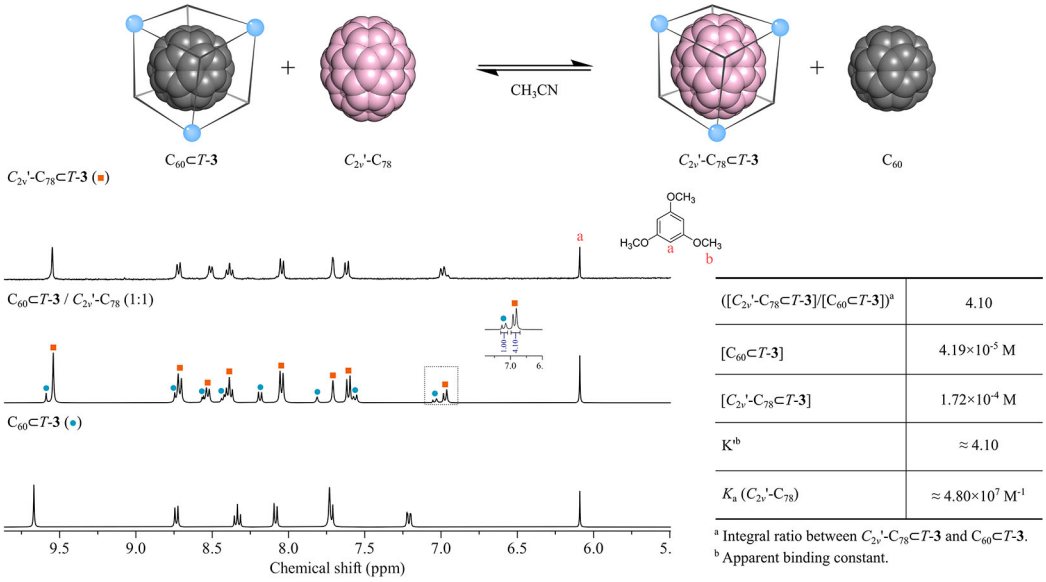

([C_{2v}'-C$_{78}$⊂*T*-**3**]/[C$_{60}$⊂*T*-**3**])[a]	4.10
[C$_{60}$⊂*T*-**3**]	4.19×10^{-5} M
[C_{2v}'-C$_{78}$⊂*T*-**3**]	1.72×10^{-4} M
K'[b]	≈ 4.10
K_a (C_{2v}'-C$_{78}$)	≈ 4.80×10^{7} M^{-1}

[a] Integral ratio between C_{2v}'-C$_{78}$⊂*T*-**3** and C$_{60}$⊂*T*-**3**.
[b] Apparent binding constant.

Fig. S142. Partial ^{1}H NMR spectra (400 MHz, 298 K, CD_3CN) for the guest-binding equilibrium of [C$_{60}$⊂*T*-**3** + C_{2v}'-C$_{78}$ ⇌ C_{2v}'-C$_{78}$⊂*T*-**3** + C$_{60}$] ([C$_{60}$⊂*T*-**3**]^o = 2.14×10^{-4} M, C_{2v}'-C$_{78}$, 1 equiv). K' = ([C_{2v}'-C$_{78}$⊂*T*-**3**]· [C$_{60}$])/([C$_{60}$⊂*T*-**3**]· [C_{2v}'-C$_{78}$]) ≈ [C_{2v}'-C$_{78}$⊂*T*-**3**]/[C$_{60}$⊂*T*-**3**]; K_a (C_{2v}'-C$_{78}$) = K'· K_a (C$_{60}$)

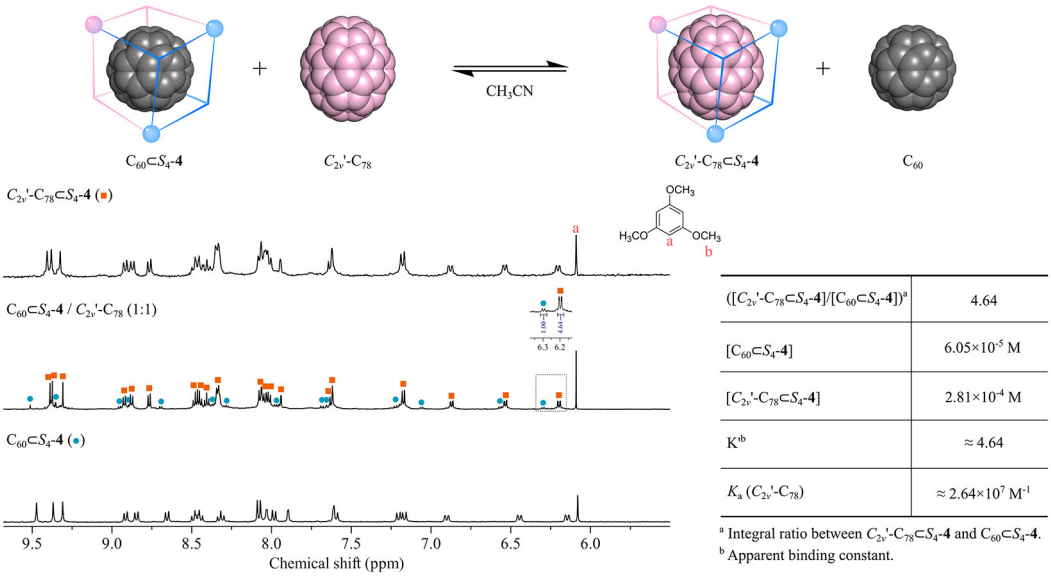

([C_{2v}'-C$_{78}$⊂S_4-**4**]/[C$_{60}$⊂S_4-**4**])[a]	4.64
[C$_{60}$⊂S_4-**4**]	6.05×10^{-5} M
[C_{2v}'-C$_{78}$⊂S_4-**4**]	2.81×10^{-4} M
K'[b]	≈ 4.64
K_a (C_{2v}'-C$_{78}$)	≈ 2.64×10^{7} M^{-1}

[a] Integral ratio between C_{2v}'-C$_{78}$⊂S_4-**4** and C$_{60}$⊂S_4-**4**.
[b] Apparent binding constant.

Fig. S143. Partial ^{1}H NMR spectra (400 MHz, 298 K, CD_3CN) for the guest-binding equilibrium of [C$_{60}$⊂S_4-**4** + C_{2v}'-C$_{78}$ ⇌ C_{2v}'-C$_{78}$⊂S_4-**4** + C$_{60}$] ([C$_{60}$⊂S_4-**4**]^o = 3.42×10^{-4} M, C_{2v}'-C$_{78}$, 1 equiv). K' = ([C_{2v}'-C$_{78}$⊂S_4-**4**]· [C$_{60}$])/([C$_{60}$⊂S_4-**4**]· [C_{2v}'-C$_{78}$]) ≈ [C_{2v}'-C$_{78}$⊂S_4-**4**]/[C$_{60}$⊂S_4-**4**]; K_a (C_{2v}'-C$_{78}$) = K'· K_a (C$_{60}$)

Table *S14*. Summary of the binding constants (K_a / M^{-1}) of *T*-**3** / S_4-**4** for fullerene guests

in CH_3CN.

Cage \ C_n	C_{60}[i]	C_{70}[ii]	C_{76}[ii]	C_{2v}-C_{78}[ii]	C_{2v}'-C_{78}[ii]
T-**3**	1.17×10^7	5.79×10^7	6.01×10^7	5.28×10^7	4.80×10^7
S_4-**4**	5.69×10^6	2.57×10^7	2.00×10^7	1.09×10^7[iii] 2.63×10^7[iv]	2.64×10^7

[i] The K_a values for the C_{60} guest were ascertained by directly encapsulating the guest with 1 equiv of the empty cage *T*-**3** or S_4-**4**. [ii] The K_a values for the C_n (n = 70, 76, 78) guest were evaluated by using competitive encapsulation experiments relative to 1 equiv of $C_{60}\subset$*T*-**3** or $C_{60}\subset S_4$-**4**. [iii] The K_a values for C_2-symmetric C_{2v}-$C_{78}\subset S_4$-**4**. [iv] The K_a values for S_4-symmetric C_{2v}-$C_{78}\subset S_4$-**4**.

14. Supplemental Figures and Tables for Crystal Data

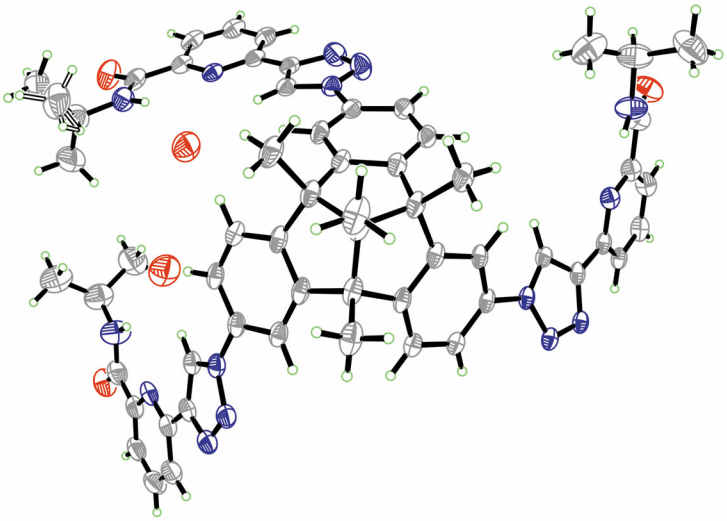

Fig. S144. Ortep-drawing of the asymmetric unit in the crystal structure of C_3-**1** at 30% probability level.

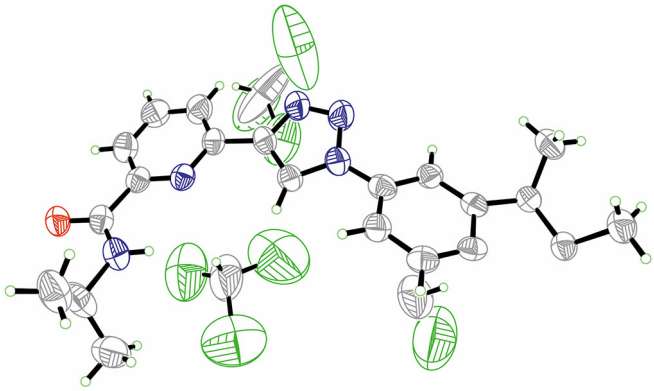

Fig. S145. Ortep-drawing of the asymmetric unit in the crystal structure of *P*-**1** at 30% probability level.

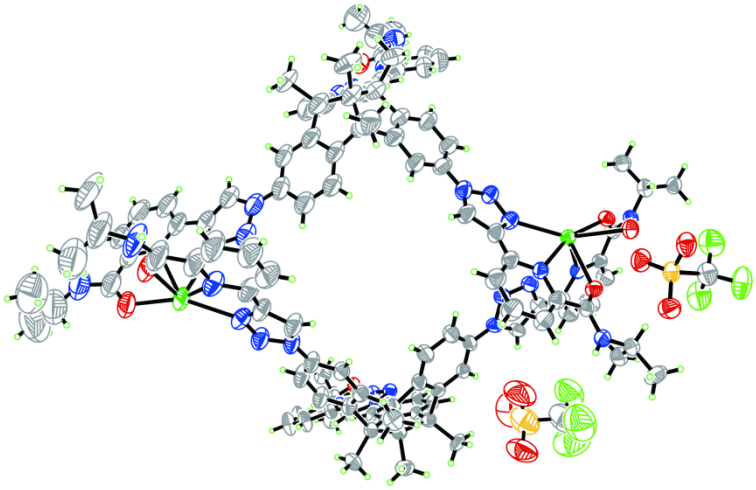

Fig. S146. Ortep-drawing of the asymmetric unit in the crystal structure of *T*-**3** at 30% probability level.

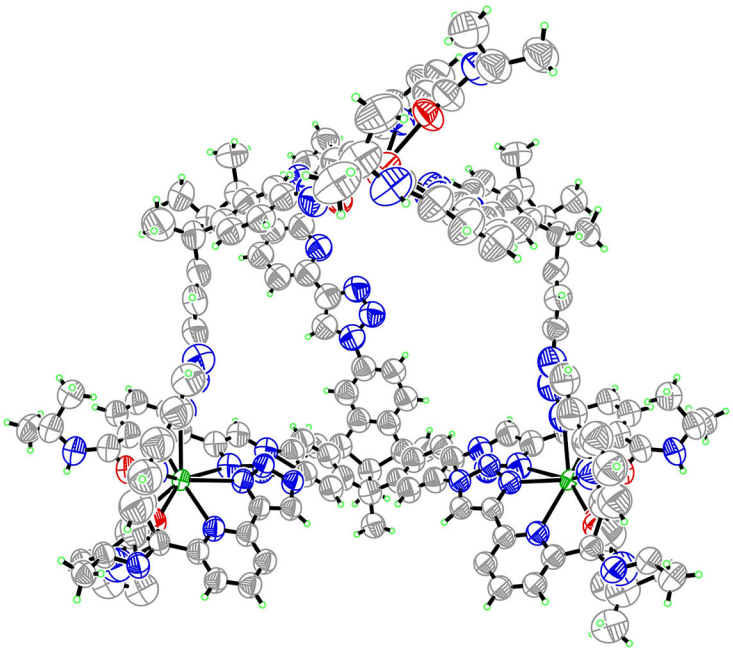

Fig. S147. Ortep-drawing of the asymmetric unit in the crystal structure of S_4-**4** at 30% probability level.

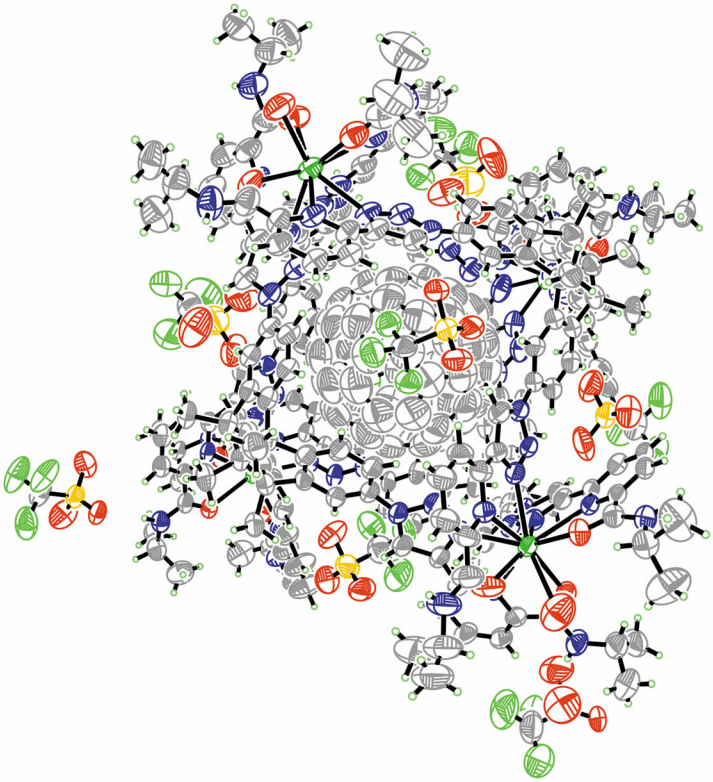

Fig. S148. Ortep-drawing of the asymmetric unit in the crystal structure of $C_{60}\subset S_4$-**4** at 30% probability level.

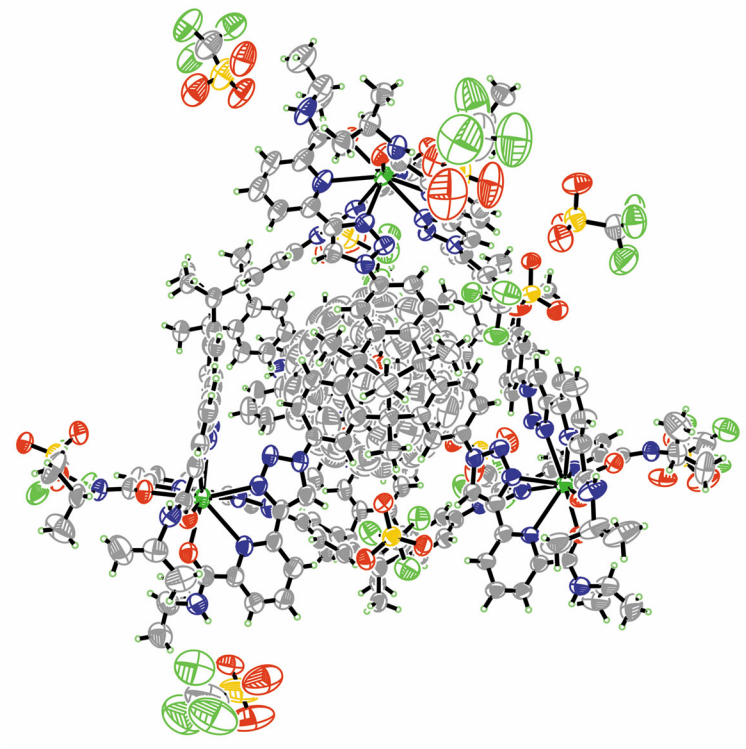

Fig. S149. Ortep-drawing of the asymmetric unit in the crystal structure of $C_{70}\subset S_4$-**4** at 30% probability level.

Table S15. Crystal data and structure refinement for C_3-**1**.

Identification code	C_3-**1** (2307962)
Empirical formula	$C_{59}H_{56}N_{15}O_5$
Formula weight	1055.19
Temperature	140(2) K
Wavelength	0.71073 Å
Crystal system	Triclinic
Space group	*P*-1
Unit cell dimensions	a = 9.276(4) Å α = 102.897(12)°
	b = 17.092(7) Å β = 90.871(12)°
	c = 20.259(8) Å γ = 105.056(12)°
Volume	3014(2) $Å^3$
Z	2
Density (calculated)	1.163 Mg/m^3
Absorption coefficient	0.078 mm^{-1}
F(000)	1110
Crystal size	0.2 x 0.15 x 0.1 mm^3
Theta range for data collection	2.291 to 25.027°.
Index ranges	-11<=h<=11, -20<=k<=20, -24<=l<=24
Reflections collected	82002
Independent reflections	10613 [R(int) = 0.1521]
Completeness to theta = 25.027°	99.7 %
Refinement method	Full-matrix least-squares on F^2
Data / restraints / parameters	10613 / 1249 / 722
Goodness-of-fit on F^2	1.104
Final R indices [I>2sigma(I)]	R_1 = 0.0942, wR_2 = 0.2849
R indices (all data)	R_1 = 0.1591, wR_2 = 0.3390
Extinction coefficient	n/a
Largest diff. peak and hole	0.798 and -0.438 e.$Å^{-3}$

Table S16. Crystal data and structure refinement for *P*-**1**.

Identification code	*P*-**1** (2307963)
Empirical formula	$C_{66}H_{64}Cl_{21}N_{15}O_3$
Formula weight	1859.77
Temperature	293(2) K
Wavelength	1.34139 Å
Crystal system	Trigonal
Space group	*R*3
Unit cell dimensions	a = 23.5481(9) Å α = 90°
	b = 23.5481(9) Å β = 90°
	c = 12.9841(5) Å γ = 120°
Volume	6235.3(5) $Å^3$
Z	3
Density (calculated)	1.486 Mg/m^3
Absorption coefficient	4.496 mm^{-1}
F(000)	2838
Crystal size	0.32 x 0.25 x 0.16 mm^3
Theta range for data collection	3.266 to 49.558°.
Index ranges	-26<=h<=26, -26<=k<=26, -14<=l<=14
Reflections collected	28757
Independent reflections	4248 [R(int) = 0.1529]
Completeness to theta = 49.558°	98.6 %
Refinement method	Full-matrix least-squares on F^2
Data / restraints / parameters	4155 / 31 / 316
Goodness-of-fit on F^2	1.468
Final R indices [I>2sigma(I)]	R_1 = 0.1572, wR_2 = 0.3689
R indices (all data)	R_1 = 0.1835, wR_2 = 0.3883
Extinction coefficient	n/a
Largest diff. peak and hole	0.747 and -0.463 e.$Å^{-3}$

Table S17. Crystal data and structure refinement for *T*-**3**.

Identification code	*T*-**3** (2307965)
Empirical formula	$C_{240}H_{226}F_{12}La_4N_{60}O_{26}S_4$
Formula weight	5278.70
Temperature	273(2) K
Wavelength	0.71073 Å
Crystal system	Orthorhombic
Space group	*Pccn*
Unit cell dimensions	a = 22.156(2) Å α = 90°
	b = 23.722(3) Å β = 90°
	c = 80.692(9) Å γ = 90°
Volume	42411(8) $Å^3$
Z	4
Density (calculated)	0.827 Mg/m^3
Absorption coefficient	0.465 mm^{-1}
F(000)	10776
Crystal size	0.42 x 0.36 x 0.28 mm^3
Theta range for data collection	5.92 to 20.810°.
Index ranges	-22<=h<=21, -23<=k<=23, -67<=l<=80
Reflections collected	77673
Independent reflections	21539 [R(int) = 0.2216]
Completeness to theta = 20.810°	97.0 %
Refinement method	Full-matrix least-squares on F^2
Data / restraints / parameters	21539 / 1945 / 1375
Goodness-of-fit on F^2	0.970
Final R indices [I>2sigma(I)]	R_1 = 0.1056, wR_2 = 0.2852
R indices (all data)	R_1 = 0.1576, wR_2 = 0.3254
Extinction coefficient	n/a
Largest diff. peak and hole	0.738 and -1.508 e.$Å^{-3}$

Table S18. Crystal data and structure refinement for **4**.

Identification code	**4** (2307964)
Empirical formula	$C_{240}H_{182}La_4N_{60}O_{12}$
Formula weight	4654.09
Temperature	278(2) K
Wavelength	0.71073 Å
Crystal system	Monoclinic
Space group	*C*2/*m*
Unit cell dimensions	a = 62.910(10) Å α = 90°
	b = 36.326(6) Å β = 125.26°
	c = 36.322(5) Å γ = 90°
Volume	67780(18) $Å^3$
Z	4
Density (calculated)	0.456 Mg/m^3
Absorption coefficient	0.272 mm^{-1}
F(000)	9464
Crystal size	0.41 x 0.32 x 0.25 mm^3
Theta range for data collection	2.060 to 14.737°
Index ranges	-44<=h<=45, -25<=k<=25, -25<=l<=25
Reflections collected	119381
Independent reflections	13201 [R(int) = 0.3270]
Completeness to theta = 14.737°	98.8 %
Refinement method	Full-matrix least-squares on F^2
Data / restraints / parameters	13201 / 5187 / 1613
Goodness-of-fit on F^2	1.568
Final R indices [I>2sigma(I)]	R_1 = 0.1580, wR_2 = 0.3955
R indices (all data)	R_1 = 0.2436, wR_2 = 0.4720
Extinction coefficient	n/a
Largest diff. peak and hole	1.083 and -0.763 e.$Å^{-3}$

Table S19. Crystal data and structure refinement for $C_{60}\subset S_4$-**4**.

Identification code	$C_{60}\subset S_4$-**4** (2307966)	
Empirical formula	$C_{304}H_{228}F_{24}La_4N_{60}O_{38}S_8$	
Formula weight	6597.54	
Temperature	293(2) K	
Wavelength	0.71073 Å	
Crystal system	Monoclinic	
Space group	*C*2/*c*	
Unit cell dimensions	a = 39.925(8) Å	α = 90°
	b = 41.557(8) Å	β = 95.23(3)°
	c = 41.117(8) Å	γ = 90°
Volume	67936(23) $Å^3$	
Z	8	
Density (calculated)	1.290 Mg/m^3	
Absorption coefficient	0.626 mm^{-1}	
F(000)	26784	
Crystal size	0.4 x 0.1 x 0.1 mm^3	
Theta range for data collection	0.709 to 23.019°.	
Index ranges	-30<=h<=43, -45<=k<=31, -45<=l<=45	
Reflections collected	86334	
Independent reflections	47013 [R(int) = 0.0624]	
Completeness to theta = 23.019°	99.2 %	
Refinement method	Full-matrix least-squares on F^2	
Data / restraints / parameters	47013 / 17225 / 3548	
Goodness-of-fit on F^2	1.353	
Final R indices [I>2sigma(I)]	R_1 = 0.1210, wR_2 = 0.3635	
R indices (all data)	R_1 = 0.1511, wR_2 = 0.3921	
Extinction coefficient	n/a	
Largest diff. peak and hole	1.786 and -1.427 e.$Å^{-3}$	

Table S20. Crystal data and structure refinement for $C_{70}\subset S_4$-**4**.

Identification code	$C_{70}\subset S_4$-**4** (2307967)	
Empirical formula	$C_{317}H_{227}F_{33}La_4N_{60}O_{45}S_{11}$	
Formula weight	7131.84	
Temperature	293(2) K	
Wavelength	0.71073 Å	
Crystal system	Monoclinic	
Space group	*C*2/*c*	
Unit cell dimensions	a = 40.408(8) Å	α = 90°
	b = 42.122(8) Å	β = 96.44(3)°
	c = 41.136(8) Å	γ = 90°
Volume	69574(24) $Å^3$	
Z	8	
Density (calculated)	1.362 Mg/m^3	
Absorption coefficient	0.639 mm^{-1}	
F(000)	28880	
Crystal size	0.25 x 0.2 x 0.15 mm^3	
Theta range for data collection	0.701 to 22.996°.	
Index ranges	0<=h<=44, 0<=k<=46, -44<=l<=44	
Reflections collected	47685	
Independent reflections	47685 [R(int) = 0.041]	
Completeness to theta = 22.996°	98.5 %	
Refinement method	Full-matrix least-squares on F^2	
Data / restraints / parameters	47685 / 13065 / 3835	
Goodness-of-fit on F^2	1.575	
Final R indices [I>2sigma(I)]	R_1 = 0.1224, wR_2 = 0.3696	
R indices (all data)	R_1 = 0.1437, wR_2 = 0.3877	
Extinction coefficient	n/a	
Largest diff. peak and hole	1.411 and -1.120 e.$Å^{-3}$	

Table S21. Crystal data and structure refinement for C_{2v}(2)-C_{78}·Ni^{II}(OEP)·2(C_6H_6).

Identification code	C_{2v}(2)-C_{78}·Ni^{II}(OEP)·2(C_6H_6)
CCDC	2278920
T, K	100(2)
λ, Å	0.71073
Color / Habit	black / block
Crystal size, mm	0.28×0.25×0.23
Empirical formula	$C_{126}H_{56}N_4Ni$
FW	1684.45
Crystal system	monoclinic
Space group	$C2/m$
a, Å	25.450(7)
b, Å	15.021(5)
c, Å	19.704(7)
α, deg	90
β, deg	92.312(11)
γ, deg	90
V, Å^3	7526(4)
Z	4
ρ, g/cm^3	1.487
μ, mm^{-1}	0.326
R_1 (all data)	0.0738
wR_2 (all data)	0.2395

Table S22. Crystal data and structure refinement for C_{2v}(3)-C_{78}·Ni^{II}(OEP)·2(C_6H_6).

Identification code	C_{2v}(3)-C_{78}·Ni^{II}(OEP)·2(C_6H_6)
CCDC	2278921
T, K	100(2)
λ, Å	0.71073
Color / Habit	black / block
Crystal size, mm	0.14×0.10×0.10
Empirical formula	$C_{126}H_{56}N_4Ni$
FW	1684.45
Crystal system	monoclinic
Space group	$C2/m$
a, Å	25.412(4)
b, Å	15.089(3)
c, Å	19.729(4)
α, deg	90
β, deg	93.213(4)
γ, deg	90
V, Å^3	7553(2)
Z	4
ρ, g/cm^3	1.481
μ, mm^{-1}	0.325
R_1 (all data)	0.0956
wR_2 (all data)	0.2826

15. References

S1. Maglic, J. B.; Lavendomme, R. MoloVol: an easy-to-use program for analyzing cavities, volumes and surface areas of chemical structures. *J. Appl. Crystallogr.* **2022**, *55*, 1033-1044.

S2. PyMOL 2.5 program, a user-sponsored molecular visualization system (https://pymol.org/2/).

S3. APEX III, Data collection software (version 2017.3).

S4. Agilent Technologies, CrysAlisPro v. 1.171.36.28, **2013**.

S5. Sheldrick, G. M. *Acta Crystallogr. Sect. A*, **2008**, *64*, 112.

S6. van der Sluis, P., and Spek, A.L. BYPASS: an effective method for the refinement of crystal structures containing disordered solvent regions. Acta Cryst. 1990, A46, 194-201.

S7. Spek, A. L. Single-Crystal Structure Validation with the Program PLATON. *J. Appl. Crystallogr.* **2003**, *36*, 7.

S8. T. K. Ronson, J. P. Carpenter and J. R. Nitschke, *Chem*. **2022**, 8, 557-568.

S9. D. Kratzert, J.J. Holstein, I. Krossing, *J. Appl. Cryst.* **2015**, *48*, 933-938.

S10. Kuck, D.; Lindenthal, T.; Schuster, A. Benzoanellated centropolyquinanes, 11. Synthesis of tribenzotriquinacene and some centro-substituted derivatives. *Chemische Berichte* **1992**, *125*, 1449-1460.

S11. Beaudoin, D.; Rominger, F.; Mastalerz, M. Efficient, Scalable syntheses of important intermediates in tribenzotriquinacene chemistry. *Synthesis-Stuttgart* **2015**, *47*, 3846-3848.

S12. Beaudoin, D.; Rominger, F.; Mastalerz, M. Synthesis and chiral Resolution of C_3-symmetric tribenzotriquinacenes. *Eur. J. Org. Chem.* **2016**, *2016*, 4470-4472.

S13. Guo, X.-Q.; Zhou, L.-P.; Cai, L.-X.; Sun, Q.-F. Self-assembled bright luminescent lanthanide-organic polyhedra for ratiometric temperature sensing. *Chem. Eur. J.* **2018**, *24*, 6936-6940.

S14. Y. Li, A. H. Flood, Pure C─H hydrogen bonding to chloride ions: a preorganized and rigid macrocyclic receptor. *Angew. Chem. Int. Ed*. **2008**, *47*, 2649-2652.

S15. Sabirov, D. S.; Garipova, R. R. The increase in the fullerene cage volume upon its chemical functionalization. *Fuller. Nano. Tub. Car. N*. **2019**, *27*, 702-709.

S16. Epple, L.; Amsharov, K. Y.; Jansen, M. Structures of the individual higher fullerene isomers C_{76}-D_2 and $C_{78}(2)$-C_{2v} in cocrystals with Ag- and Cu-tetraphenylporphyrines. *Fuller. Nano. Tub. Car. N*. **2009**, *17*, 67-77.

S17. M. A. Spackman and P. G. Byrom, *Chem. Phys. Lett.*, **1997**, *267*, 215–220;

S18. J. J. McKinnon, A. S. Mitchell and M. A. Spackman, *Chem.–Eur. J.*, **1998**, *4*, 2136–2141.

S19. Spackman, P. R.; Turner, M. J.; McKinnon, J. J.; Wolff, S. K.; Grimwood, D. J.; Jayatilaka, D.; Spackman, M. A. CrystalExplorer: a program for Hirshfeld surface analysis, visualization and quantitative analysis of molecular crystals. *J. Appl. Crystallogr.* **2021**, *54*, 1006-1011.

S20. M. A. Spackman, J. J. McKinnon, *CrystEngComm*. 2002, *4*, 378.

S21. Lefebvre, C.; Rubez, G.; Khartabil, H.; Boisson, J.-C.; Contreras-García, J.; Hénon, E. Accurately extracting the signature of intermolecular interactions present in the NCI plot of the reduced density gradient versus electron density. *Phys. Chem. Chem. Phys.* **2017**, *19*, 17928-17936.

S22. Lu, T.; Chen, F. Multiwfn: A multifunctional wavefunction analyzer. *J. Comput. Chem.* **2012**, *33*, 580-592.

S23. Humphrey, W.; Dalke, A.; Schulten, K. VMD: Visual molecular dynamics. *J. Mol. Graphics.* **1996**, *14*, 33-38.

S24. K. N. Semenov, N. A. Charykov, V. A. Keskinov, A. K. Piartman, A. A. Blokhin and A. A. Kopyrin, *J. of Chem. Eng. Data*. **2010**, *55*, 13-36.